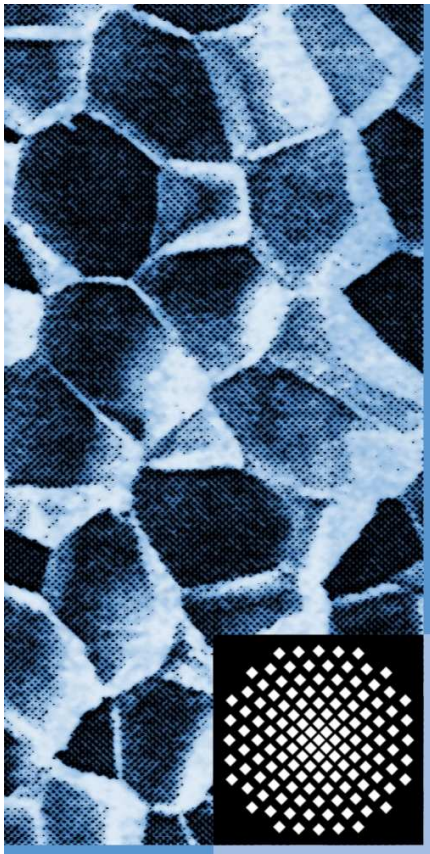

Universität Stuttgart
Germany

Institut für Mechanik (Bauwesen)
Lehrstuhl für Kontinuumsmechanik
Prof. Dr.-Ing. W. Ehlers

Damage in Multi-Phasic Materials Computed with the Extended Finite-Element Method

Hans-Uwe Rempler

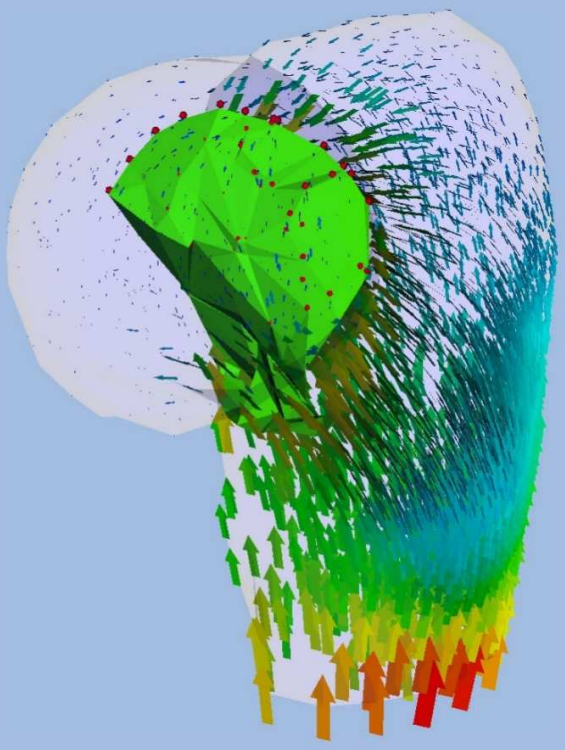

Report No.: II-23 (2012)

Damage in Multi-Phasic Materials Computed with the Extended Finite-Element Method

Von der Fakultät Bau- und Umweltingenieurwissenschaften und
dem Stuttgart Research Centre for Simulation Technology
der Universität Stuttgart zur Erlangung der Würde
eines Doktors der Ingenieurwissenschaften (Dr.-Ing.)
genehmigte Abhandlung

vorgelegt von

Dipl.-Ing. Hans-Uwe Rempler

aus

Mediasch

Hauptberichter:	Prof. Dr.-Ing. Wolfgang Ehlers
Mitberichter:	Prof. Dr.-Ing. Stefan Diebels

Tag der mündlichen Prüfung: 15. Juni 2012

Institut für Mechanik (Bauwesen) der Universität Stuttgart
Lehrstuhl für Kontinuumsmechanik
Prof. Dr.-Ing. W. Ehlers
2012

Report No. II-23
Institut für Mechanik (Bauwesen)
Lehrstuhl für Kontinuumsmechanik
Universität Stuttgart, Germany, 2012

Editor:
Prof. Dr.-Ing. W. Ehlers

Institut für Mechanik (Bauwesen)
Lehrstuhl für Kontinuumsmechanik
Universität Stuttgart
Pfaffenwaldring 7
70569 Stuttgart, Germany

ISBN 3 – 937399 – 24 – 0
(D 93 – Dissertation, Universität Stuttgart)

There is a theory which states that if ever anyone discovers exactly what the Universe is for and why it is here, it will instantly disappear and be replaced by something even more bizarre and inexplicable.

There is another theory which states that this has already happened.

Douglas Adams (1952 – 2001)

Acknowledgements

The work presented in this thesis was carried out in the years between 2005 and 2011, when I was a research associate at the Institute of Applied Mechanics (Civil Engineering), Chair of Continuum Mechanics, at the Universität Stuttgart. Numerous people contributed in many ways to the realisation of this work – all their support is most gratefully acknowledged.

First of all, I would like to thank my supervisor and teacher, Professor Wolfgang Ehlers, for giving me the opportunity to prepare my thesis at his institute. His research in the field of continuum mechanics built the important foundation for this work. I am also very grateful to Professor Stefan Diebels for taking the first co-chair in my promotion procedure in such a straightforward manner. The scientific cooperation with Professor Christian Wieners is gratefully acknowledged as an elementary contribution towards a deeper understanding of numerical solution techniques.

I would also like to thank the Stuttgart Research Centre for Simulation Technology for its support of my stay abroad at the Stanford University. There, Professor Ellen Kuhl welcomed me very warmly and gave me important input. Together with her kind and outgoing team, notably Serdar Göktepe, this stay will always be unforgettable for me as a wonderful experience.

As one can imagine, a lot of sweating has been done while preparing this thesis. Most of it in particular together with my former colleagues Martin Ammann, Ayhan Acartürk, Tobias Graf and Bernd Scholz, as they have been perfect lunch break sporting partners running around the University. Together with Ayhan Acartürk, David Koch, Maik Schenke, Fabian Welschinger, Ilona and Dominik Zimmermann, the intensive administration of the institute cluster, computers and network made a lot of fun, even though it has been pretty challenging to keep everything – more or less – constantly working. All my colleagues are thanked for creating a pleasant and friendly working atmosphere. In this nice working atmosphere, Sarah Gehrlicher and David Koch contributed directly to this work with their own diploma theses. My officemate Arndt Wagner helped me a lot with his eagle eye vision to identify even the smallest inaccuracies in all affairs. Despite occasionally long working hours, I could always count on the presence of Joel Méndez Diez, Irinia Komarova, Arzu and her brother Okan Avci for a warm and open conversation. Talking about long working hours, I must not forget to especially thank my very good friend Nils Karajan for his long-term friendship and his overall extensive support beginning as fellow students, roommates and finally officemates.

I deeply appreciate the long-term support from my parents which made it possible for me to accomplish all the steps necessary to reach this point in my life.

Finally, I would like to thank the most important person in my life, my beloved wife Sonja. I could always rely on her never ending understanding, patience and tolerance. This thesis would never have been possible without her limitless support.

Stuttgart, June 2012 Hans-Uwe Rempler

Contents

Deutsche Zusammenfassung

Mit Fokus auf gewachsenes, biologisches Gewebe ist es das Ziel der vorliegenden Arbeit, eine numerische Methodologie für die Simulation von Schädigungen in Mehrphasenmaterialien zu entwickeln. Dabei wird ein konsistentes numerisches Verfahren vorgestellt, welches diskontinuierliche Randwertprobleme (RWP) in einer nicht-linearen dreidimensionalen Umgebung simulieren kann. Repräsentative Beispiele aus dem Bereich biomechanischer Problemstellungen belegen die numerischen Möglichkeiten des vorgestellten Verfahrens. Gleichzeitig erfüllt dieses Verfahren die Anforderung der zukünftigen Erweiterbarkeit hin zu einer virtuellen, numerischen Laborumgebung. In einer solchen numerischen Laborumgebung können lebensbedrohliche Umstände bereits vor ihrem tatsächlichen Eintreten prognostiziert werden. Aufgrund der Allgemeingültigkeit der in dieser Arbeit verwendeten Methoden kann die daraus entwickelte Methodologie auch in völlig anderen Anwendungsbereichen angewandt werden, z. B. in der Bodenmechanik. In diesem Kontext sind Schädigungsmechanismen und -strukturen in letzter Zeit zu einer wichtigen Fragestellung im Bereich der CO_2-Sequestrierung geworden.

Die vorliegende Arbeit ist in vier Hauptkapitel untergliedert. Einleitung und Zusammenfassung rahmen die Arbeit ein. **Kapitel 1** führt die Motivation dieser Arbeit ein und gibt einen Überblick über den aktuellen Stand der Technik zu den hier behandelten Themengebieten. Zahlreiche Quellenangaben unterstützen den interessierten Leser bei einer begleitenden Literaturrecherche. Drei Anhänge liefern abschließend weitere Einblicke der zugrunde liegenden mathematischen, mechanischen und numerischen Details.

Die Grundlagen der Kontinuumsmechanik werden kurz in **Kapitel 2** diskutiert. Darin werden im Rahmen der Theorie Poröser Medien (TPM) grundlegende kontinuumsmechanische Prinzipe vorgestellt und ein thermodynamisch konsistentes Zweiphasen-Materialmodell entwickelt. Die hier zugrunde gelegten kontinuumsmechanischen Prinzipe haben ihren Ursprung in den klassischen Feldtheorien deformierbarer Körper. Im Allgemeinen wird jedoch davon ausgegangen, daß ein solcher Körper lediglich aus einem einzelnen, homogen verteilten Material bzw. einer Phase besteht. Die Annahme eines einphasigen Materials ist jedoch für viele Anwendungen nicht ausreichend. Nahezu alle Materialien sind – mehr oder minder – porös. Vor allem gewachsenes, biologisches Gewebe, dessen Beschreibung mit ein Schwerpunkt dieser Arbeit ist, muß als Mehrphasen-Material beschrieben werden. Biologisches Gewebe ist per se porös und durchsetzt von Blutgefäßen, Nervenbahnen und vielem mehr.
Aus historischer Sicht entstand die TPM aus der Kombination der Mischungstheorie mit dem Konzept der Volumenanteile. In der Mischungstheorie wird durch einen Homogenisierungsansatz über ein poröses Material die in der Regel unbekannte echte Mikrostruktur eines definierten Gebiets bzw. Kontinuums statistisch gemittelt. Die statistische Mittelung kann dabei als ein Verschmieren von mikroskopischen Informationen einzelner Konstituierenden interpretiert werden. Dabei bleibt die Information über die zugrundeliegende Mikrostruktur durch die Erweiterung der Mischungstheorie um das Konzept der Volumenanteile weiterhin erhalten. Die Volumenanteile sind das Maß des lokalen

Anteils einer einzelnen Konstituierenden in Relation zum gesamten Kontinuum. Somit ist ein Transfer der mechanischen Eigenschaften eines Mehrphasen-Kontiuums von der Mikroskala hin zur Makroskala möglich. Das makroskopische Modell besteht in Konsequenz aus mehreren superponierten, sprich, überlagerten und miteinander interagierenden Kontinua.
Bei der weiteren Entwicklung des kontinuumsmechanischen Materialmodells werden konstitutive Annahmen getroffen. Hierbei wird die Morphologie von biologischem Gewebe mit berücksichtigt. Da jedoch der Hauptfokus dieser Arbeit in der Entwicklung einer numerischen Methodologie zur Beschreibung des Schädigungsverhaltens von Mehrphasenmaterialien liegt, beschränkt sich das hier vorgestellte Materialmodell auf zwei Phasen. Dabei wird von einem vollständig mit Flüssigkeit gesättigten, porösen Festkörperskelett ausgegangen.
Als Voraussetzung der in den nächsten Kapiteln folgenden numerischen Diskretisierung schließt eine Diskussion über RWP die Einführung in die reguläre Kontinuumsmechanik ab. Das RWP beschreibt die bisher als stark definierte, kontinuumsmechanische Problemstellung in einer sogenannten schwachen, integralen Form. Es wird erkannt, daß durch die starke Kopplung der beiden Phasen infolge der interagierenden Kontinua zwei schwach formulierte Bilanzgleichungen notwendig sind; eine Massen- bzw. Volumenbilanz für das Porenfluid und eine Impulsbilanz des gesamten porösen Materials. Auf weitere, höhere Bilanzrelationen, wie z. B. die Energiebilanz, kann aufgrund der gewählten Konstitutivannahmen verzichtet werden.

Eine kurze Einführung in die theoretischen Grundlagen der Bruchmechanik erfolgt im ersten Teil von **Kapitel 3**. Diese theoretischen Grundlagen bilden quasi das Fundament für die folgende erweiterte kontinuumsmechanische Beschreibung des Schädigungsverhaltens von Mehrphasenmaterialien. Die Grundlagen der Bruchmechanik werden auf Basis von linear elastischem Materialverhalten und mit der Einschränkung auf den zweidimensionalen Raum hergeleitet. Als Ergebnis der Herleitungen können dazu begleitend die klassischen Bruchmechanik-Themengebiete Spannungsintensitätsfaktoren, Energiefreisetzungsrate, J-Integral und letztlich die Kohäsivzonentheorie diskutiert werden. Obwohl diese Themengebiete durch die zugrundeliegenden Einschränkungen nur begrenzte Gültigkeit aufweisen, ist deren Verständnis für die Erweiterung der Bruchmechanik hin zum dreidimensionalen, diskontinuierlichen Mehrphasenmaterial elementar.
Der zweite Teil des Kapitels befaßt sich mit der Eingliederung der Bruchmechanik-Grundlagen in einen kontinuumsbruchmechanischen Kontext. Eine detaillierte Betrachtung der kinematischen Zusammenhänge motiviert die Einführung einer kohäsiven, gemittelten Bruchfläche. Die eineindeutige geometrische Beschreibung der Bruchfläche ermöglicht in Konsequenz die Definition von modifizierten Bilanzgleichungen. Diese modifizierten Bilanzgleichungen beinhalten auch jeweils einen diskontinuierlichen Anteil; sie werden schwach, im Sinne eines RWP, für die im nächsten Kapitel beschriebene Diskretisierung umformuliert. Als Abschluß des dritten Kapitels ergibt die Untersuchung der Lokalisierung von Diskontinuitäten ein geeignetes Rißausbreitungskriterium für das Festkörperskelett.

Kapitel 4 stellt die numerische Umsetzung von Schädigungsprozessen für das vorherig entwickelte Zweiphasen-Materialmodell vor. Die numerische Umsetzung erfolgt auf Basis der Finite-Elemente-Methode (FEM). Zunächst wird die FEM allgemein anhand der

räumlichen und zeitlichen Diskretisierung der schwach formulierten Bilanzgleichungen des RWP aus Kapitel 2 praktiziert. Die zeitliche Diskretisierung erfolgt dabei über einen impliziten Lösungsansatz. Das sich ergebende, stark gekoppelte Gleichungssystem wird im Rahmen eines Ein-Schritt-Verfahrens gelöst. Danach wird der diskontinuierliche Anteil der modifizierten Bilanzgleichungen aus Kapitel 3 durch eine Erweiterung der FEM betrachtet. Das Grundprinzip dieser Erweiterung – auch bekannt als „extended Finite-Element Method“ (XFEM) – wird zunächst anhand eines Beispiels aus dem Bereich von elastisch-inelastischem Materialverhalten eingeführt. Jenes Beispiel führt vorab zu der Entwicklung einer weiteren numerischen Methode, der sogenannten „augmented Finite-Element Method“ (AugFEM).
Als Konsequenz der diskontinuierlichen Diskretisierung des RWP ist ein besonderes Augenmerk auf die numerische Integration zu richten. Die schwachen, modifizierten Bilanzgleichungen müssen für die erfolgreiche Lösung des Gleichungssystems konsistent numerisch integriert werden. Dazu werden die lokalen Informationen über den elementweisen Durchgang der Bruchfläche, sprich, die Diskontinuität, mittels des aus der dreidimensionalen Computervisualisierung bekannten „Marching Cubes Algorithm“ (MCA) berechnet. Diese lokale Berechnung erfordert leistungsfähige Techniken für die globale numerische Nachverfolgung der Diskontinuitäten. Im Rahmen dieses Kapitels werden zwei dieser Techniken vorgestellt. Die erste basiert auf vektorwertigen Level-Set-Funktionen und wird für die einfache Lokalisierung eines Bruchs verwendet. Somit wird sie in dieser Arbeit auf den zweidimensionalen Raum beschränkt. Um dieser zweidimensionalen Einschränkung zu entgehen, wird alternativ der „Global Tracking Algorithm“ (GTA) vorgestellt. Durch dessen Verwendung wird aber auch gleichzeitig das Gleichungsystem um eine dritte Bilanzgleichung erweitert. Diese kann aufgrund der Charakteristik einer schwachen Kopplung in einem gestaffelten Lösungsverfahren im Nachlauf zu den ersten beiden Bilanzgleichungen gelöst werden. Ein kurzes exemplarisches Beispiel zur numerischen Implementierung des GTA in Kombination mit dem MCA schließt dieses Kapitel ab.

Das letzte Hauptkapitel, **Kapitel 5**, präsentiert numerische Beispiele, die auf Basis der theoretischen Aspekte aus den vorangegangenen Kapiteln berechnet sind. Sämtliche numerische Beispiele wurden mit dem institutseigenen FEM Programm PANDAS simuliert. Dazu wurde das Programm im Rahmen dieser Arbeit um AugFEM, XFEM, MCA, GTA und vektorwertige Level-Set Funktionalitäten erweitert. Dazu begleitend wurde ein zusätzliches Lösungsverfahren zur gestaffelten Lösung schwach gekoppelter Bilanzgleichungen implementiert. In diesem Kapitel der numerischen Beispiele belegen zunächst numerische Studien zur AugFEM die Wirksamkeit der Methode. Dazu werden die Ergebnisse der AugFEM zur numerischen Berechnung von elasto-viskoplastischem Materialverhalten mit den Ergebnisse aus der Standard-FEM verglichen. In dem anschließenden zweidimensionalen numerischen Beispiel wird der Flüssigkeitsaustausch innerhalb einer Rißöffnung eines hydrierten Gewebequerschnitts simuliert. Dieses Beispiel bezieht sich auf die globale numerische Nachverfolgung von Diskontinuitäten mittels vektorwertiger Level-Set-Funktionen. Final befassen sich dreidimensionale Beispiele mit der Problemstellung einer Fraktur eines menschlichen Oberschenkelhalsknochens. Diese Simulationen sind an einer Echt-Geometrie des menschlichen Oberschenkels durchgeführt und validieren die in dieser Arbeit entwickelte numerische Methodologie. Alle vorausgehend diskutierten numerischen

Aspekte sind in diesem letzten Beispiel implementiert.

Die vorliegende Arbeit ist in **Kapitel 6** zusammengefaßt. Die Vorteile der entwickelten Methodologie sowie eventuelle Einschränkungen werden darin reflektiert. Ein Ausblick beschreibt sinnvolle Erweiterungen und zukünftige Anwendungen.

Einige der mathematischen Aspekte dieser Arbeit werden in ausgewählten Regeln der Tensorrechnung im **Appendix A** angeschnitten. **Appendix B** beinhaltet mechanische Details, die den Rahmen der Hauptkapitel gesprengt hätten. Dennoch sind diese Details für ein grundlegendes Verständnis der behandelten Themen von besonderem Interesse. **Appendix C** stellt numerische Algorithmen für die praktische Umsetzung der vorgestellten numerischen Methodologie zur Verfügung; darin sind auch drei Programm-Quelltexte enthalten, die der Einfachheit halber in die Programmiersprache PYTHON übersetzt wurden.

Chapter 1:
Introduction and Overview

1.1 Motivation

Material failure is in general a critical situation. It is accompanied with reduced load capacities. Thus, buildings, structures, configurations, etc. tend to collapse and by that loose their designated purpose. This can result in catastrophic consequences. Therefore, a reliable prediction of damage processes is necessary. Consequently, the structural information of crack configurations is of essential interest. The structural information of cracks is usually determined under the assumption of homogeneous, single-phase materials. Certainly, not all materials consist of just one single phase only. Actually, nearly all materials are – more or less – porous materials. Especially grown, biological tissue needs to be regarded as a multi-phasic material. Every biological tissue consists of structural cells, blood vessels, nerves and much more. Tissue rupture, or fracture, respectively, can become a direct hazard to life and living. So, these damage processes are of great interest. Interstitial fluid has to be taken into account when regarding living tissue. As a consequence, damage can result in fluid leaking, sucking, or exchange. This can become a serious danger for, e. g., internal organs.

Figure 1.1: Spleen rupture.

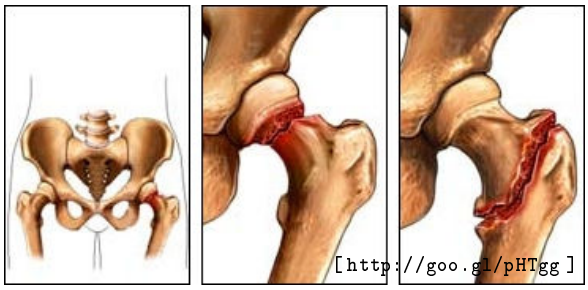

Figure 1.2: Human femur fracture.

The Theory of Porous Media (TPM) is capable of a macroscopic description of multi-phasic continua. Therein, the information about the underlying microstructure is obtained by the concept of volume fractions. Thus, the material microstructure can remain unknown. Furthermore, the TPM postulates fully coupled, thermodynamically consistent balance equations for multiple constituents. These characteristics make the TPM the ideal approach to describe biological tissue as immiscible multi-phasic aggregates. Nowadays, it has become common practise to compute material behaviour numerically. Therein, the Finite-Element Method (FEM) has proven to be well-suited for the numerical approximation of differential balance equations. But, the FEM is limited in the simulation of material failure. Thus, the extended FEM (XFEM) was lately developed to overcome this restriction. The XFEM bears the advantage that the finite-element mesh does not need to honour the geometric shape of discontinuities. On this basis, especially when targeting three-dimensional (3-d) problems, efficient finite-elements are crucial for a correct discretisation. Moreover, sophisticated

tracking techniques are necessary to exploit the advantage of XFEM damage simulations.

With focus on – but not limited to – grown, biological materials, the aim of this monograph is the development of a numerical methodology for the simulation of damage in multi-phasic materials. Therein, the goal is to present a consistent numerical method for the simulation of discontinuous boundary-value problems (BVP) within a 3-d non-linear setting. Representative examples from the field of bio-mechanical problems should reflect the numerical capabilities of the presented method. Furthermore, the numerical capabilities should meet requirements for a future extension towards a numerical laboratory. The numerical laboratory could then be designed to predict life-threatening circumstances. Due to the generality of the used methods, the presented methodology could also be used in – only at first sight – totally different application areas, e. g., soil mechanics. Damage processes and structures have always been of high interest in engineering applications. Lately, this has become an important question in the context of CO_2 sequestration.

1.2 State of the Art

The use of the TPM assures a thermodynamically consistent continuum-mechanical framework. Classic continuum-mechanical field theories are comprehensively reflected in the fundamental works of *Chadwick* [36], *Gurtin* [91], *Haupt* [98, 99], *Malvern* [133], and *Maugin* [135]. The context of multi-phasic materials evolved from its first phenomenological approach by *Biot* [12] to the Theory of Mixtures (TM), cf. *Bowen* [26], and *Truesdell & Toupin* [185]. The TM was extended by the concept of volume fractions to basically define the TPM, see *Bowen* [27, 28], until it's current understanding, cf. *de Boer* [16, 17], *de Boer & Ehlers* [18], and *Ehlers* [53, 55, 58]. Based on the TPM, a geometrically and materially non-linear model describing the dynamical behaviour of a saturated binary porous medium has been presented by *Diebels & Ehlers* [45]. The TPM has been successfully adopted for the modelling of biomaterials in, e. g., *Ehlers & Markert* [64], *Ehlers et al.* [65], and *Karajan* [116]. The continuum-mechanical model discussed herein for biological tissue considers isotropic and hyperelastic material properties for the porous solid matrix. The concept of hyperelasticity allows the derivation of the effective stress tensor from a strain-energy density function, cf. *Ogden* [149]. However, the original *Ogden*-type strain-energy function is not capable to account for a compaction point, see *Odgen* [148]. Thus, it is not directly applicable to porous media. Therefore, the strain-energy function is extended by a volumetric term, e. g., postulated by *Eipper* [66]. For a comprehensive introduction on inelastic material behaviour within a standard continuum-mechanical approach and within the TPM framework, the interested reader is referred to *Simo & Hughes* [170], *Naghdi* [143], *Haupt* [97], *Wieners* [192], *Mahnkopf* [132], and *Ehlers* [59].

A circumstantial introduction into the topic of fracture mechanics can be found in *Hahn* [92], and *Gross & Selig* [88]. From a historical point of view to fracture problems, the interested reader is pointed to the contributions of *Inglis* [108], *Griffith* [86, 87], *Westergaard* [191], *Orowan* [152], *Irwin* [109–111], and *Rice* [159]. Because also pure elastic materials exhibit inelastically though small process zones in the near vicinity of sharp openings, the cohesive fracture theory is generally applied. It is based on the works of *Dugdale* [49],

and *Barenblatt* [7]. Both authors published a similar cohesive zone approach independently of each other. The approach in this thesis is regarded as a split-off of the internal mechanical work. With the conclusion of conservative stresses within the cohesive zone, the existence of a cohesive potential function can be assumed. The consequent use of the potential function herein was postulated by *Gasser & Holzapfel* [83]. It also hosts transverse isotropy within the cohesive zone. The cohesive potential is limited with a scalar-valued damage function. Thus, isotropic damage behaviour is implied. This is a common approach in the context of biomaterials to include softening material behaviour. Its irreversible characteristic is ensured by the inclusion of the magnitude of the maximum displacement jump. Sophisticated numerical implementations of the cohesive zone approach in conjunction with discrete fracture models have been presented in *de Borst et al.* [22–24]. Fundamental details on the continuum-mechanical aspects of fracture mechanics can be gained by regarding the works of, e. g., *Simo et al.* [172], and *Oliver et al.* [150, 151]. The work of *Gürses* [89] furthermore respects microstructures at material points. In this thesis, a virtual discontinuity surface, motivated by the work of *Wells et al.* [189, 190], is heuristically introduced. The virtual discontinuity surface overcomes the problem of the singular characteristic of the deformation gradient. An alternative solution to this is the regularisation of the sharp discontinuity surface by the introduction of a discontinuity band, see *Armero & Garikipati* [5], and *Steinmann & Betsch* [176]. This kind of regularisation, with a "smearing" of the discontinuity, can also be found for frictional, i. e., granular materials in *de Borst* [21]. The same author also contributed to a comprehensive comparison of discrete versus smeared crack models in *de Borst et al.* [25]. The variational formulation of the discontinuous boundary-value problem (BVP) is derived with respect to global master balances. The derivation process is based on the works of *Mahnkopf* [132], and *Blome* [14]. Other common approaches for the motivation of the set of discontinuous variational formulations can be found in, e. g., *Hettich* [103], and *Jäger* [112]. Therein, the first work evaluates the material derivation of the discontinuous displacement field. The latter work uses a direct integration of the corresponding quantities over the surface of a discontinuity. This direct integration is motivated by interface considerations. It can be shown that, under certain simplifying assumptions, material instability, the appearance of a discontinuous bifurcation, and the so-called loss of ellipticity are coherent, see e. g. *Linder et. al* [128], and citations therein. The loss of ellipticity is based on the investigation of the so-called acoustic tensor which reveals the common *Rankine*-criterion for the numerical computation of the crack propagation direction.

In engineering practise, the Finite-Element Method (FEM) has become a common approach for numerical simulations. It is a numerical technique for the finding of approximate solutions to partial differential equations (PDE). Multiple authors contributed to its fundamental introduction, e. g., *Bathe* [8], *Schwarz* [169], *Braess* [29], and *Zienkiewicz & Taylor* [198], to name only a few. Herein, the PDE under study arise from weak formulations of the governing equations to the developed biphasic continuum-mechanical model. For an introduction into the application of the FEM to TPM problems, the interested reader is referred to, e. g., *Ehlers et al.* [62], *Ellsiepen* [67], and *Ammann* [2]. In order to numerically simulate jump quantities in the discretised field equations, the FEM needs to be extended, or enriched, respectively. Probably the most popular enrichment of the FEM

is the so-called extended Finite-Element Method (XFEM), see *Belytschko & Black* [10], *Moës et al.* [139], *Dolbow* [48], and *Sukumar et al.* [179], for the – as far as the author of this monograph is aware – original works on this topic. Note that it was shown by *Areias & Belytschko* [4] that the so-called *Hansbo* method, cf. *Hansbo & Hansbo* [93, 94], leads to identical results as the XFEM enrichment. The FEM and the XFEM, respectively, presuppose a feasible discretisation in space and time of the governing field equations. For the spatial discretisation of multi-phasic materials, cf. *Taylor & Hood* [180]. For a summery of special stabilisation techniques in the context of finite-element discretisation of multi-phasic materials, the interested reader is referred *Huang et al.* [106]. The temporal discretisation with single-step *Runge-Kutta* methods is following *Ellsiepen* [67, 68]. In this thesis, 3-d problems are discretised with 8-node hexahedron elements. These type of elements are generally accepted to be superior over tetrahedron elements. For the numerical integration over discontinuities, the corresponding elements need to be divided into two parts along the crossing discontinuity. The so-called Marching Cubes Algorithm (MCA), see *Lorensen & Cline* [129], is a very efficient method for this task. As a side-product, it also results in a proper triangulation of the crossing discontinuity surface. Thus, the numerical implementation of the cohesive zone model is straightforward. As far as the author is aware, this thesis is the first contribution to use the MCA in the context of computational fracture mechanics. A crucial point in the numerical simulation of failure mechanics is the modelling of the appearance and the propagation of discontinuities. Classical level-set functions are nowadays a common chosen tracking method for 2-d simulations of strong discontinuities, see *Stolarska* [177], and *Osher & Fedkiw* [153]. Vectorially discretised level-set functions have been generally introduced and transferred to the XFEM framework by *Ventura et al.* [186, 187]. But, because vector level-set functions are numerically to costly for 3-d problems, the Global Tracking Algorithm (GTA) should be preferred. The method – as far as the author is aware – originates for its application to computational failure mechanics from *Oliver et al.* [150, 151] and *Samaniego* [163]. Since then, the GTA has been adopted successfully to simulate discrete fracture by, e. g., *Dumstorff & Meschke* [51], *Cervera & Chiumenti* [35], and *Feist & Hofstetter* [73]. The reader who is interested in a comprehensive comparison of crack path strategies is referred to *Jäger et al.* [112–114].

1.3 Outline of this Thesis

This thesis is structured into four main chapters. Additionally, this first **Chapter 1**, and the last Chapter 6, frame the thesis. Three appendices accompany the more interested reader.

The fundamentals of continuum mechanics are briefly discussed in **Chapter 2**. Basic continuum-mechanical principles are presented within the framework of the Theory of Porous Media (TPM). A thermodynamically consistent biphasic material model is developed. Constitutive settings describe a fully fluid-saturated, porous solid skeleton. The discussion on boundary-value problems (BVP) closes the considerations on regular continuum mechanics.

A brief introduction into the theoretical fundamentals of fracture mechanics is given in the first part of **Chapter 3**. The second part focuses on the correlation of these fundamentals to a continuum-fracture-mechanical framework. This framework is the basis of the subsequent discussion on the numerical methodology. Furthermore, the investigation of the localisation of discontinuities reveals a crack propagation criterion for the solid skeleton.

Chapter 4 presents the numerical implementation of damage processes within the previously developed biphasic continuum-mechanical model. The numerical implementation focuses on the extension of the well-known Finite-Element Method (FEM). The basic principle of the extended Finite-Element Method (XFEM) is first introduced using an example from the field of elasto-inelastic material behaviour. This example yields to an augmented FEM (AugFEM). Sophisticated tracking techniques are presented for the successful numerical simulation of discontinuities.

The last main chapter, **Chapter 5**, presents numerical examples that are computed on the basis of the theoretical aspects of the preceding chapters. Numerical studies on the AugFEM are presented first. Subsequent, a discontinuous 2-d numerical example simulates the fluid exchange within a tear opening of a hydrated tissue cross section. Finally, 3-d numerical examples address the problem of fracture of the human femur. The latter simulations are computed on a real live geometry and validate the numerical methodology that was proposed in this monograph.

The thesis is summarised in **Chapter 6**. The advantages – and limitations – of the presented numerical methodology are reflected. An outlook is given for sound extensions and future applications.

Some of the mathematical aspects of this thesis are embraced in selected rules of tensor calculus within **Appendix A**. Furthermore, **Appendix B** hosts mechanical details that would have gone beyond the scope of the main chapters. Nevertheless, these details are of interest for a fundamental understanding of the discussed topics. **Appendix C** presents numerical recipes for a practical implementation of the proposed numerical methodology.

Chapter 2:
Continuum Mechanics

The fundamentals of continuum mechanics are briefly discussed in this chapter. Basic continuum-mechanical principles are presented within the framework of the Theory of Porous Media (TPM). After a short overview of the foundations of the TPM, the underlying governing kinematic and balance relations are derived. These relations cover the constitutive settings which provide a continuum-mechanical description of the discussed problem in this monograph. The constitutive settings consist of a rather simple biphasic model because the emphasis of this work will focus on the numerical methodology. This biphasic model implies an always fully saturated, immiscible porous medium. A more sophisticated, e. g., triphasic model, could be a reasonable extension for further studies on damage processes in porous media under partially saturated conditions.

The reader who is interested in a more detailed description of continuum theories is referred to, e. g., *Chadwick* [36], *Gurtin* [91], *Haupt* [99], *Kahn & Huang* [115], *Lemaitre & Chaboche* [126], *Malvern* [133], *Maugin* [135] and *Ehlers* [53, 55, 58–60].

2.1 Foundations of the Theory of Porous Media

Classical, well-known solid or fluid continuum-mechanical theories consider only one, in general homogeneously distributed material or phase, respectively. But in many branches of engineering, one often has to deal with continuum-mechanical problems that cannot be described satisfyingly by only one phase. For example, porous solid materials as shown in Figure 2.1, need additional considerations to the single phase continuum-mechanical theories. In biomechanics, see Figure 2.1_3, it has become a convenient approach to describe biological tissue as immiscible multi-phasic aggregates, see, e. g., *Mow et al.* [140, 141], *Lai et al.* [125], *Frijns et al.* [77], *Ehlers et al.* [65], and *Karajan* [116].
From a historical point of view, the consideration of multi-phasic continua originates from geomechanical consolidation problems, see *Biot* [12]. This first phenomenological approach has been expanded by taking general thermodynamical considerations into account to result into the Theory of Mixtures (TM), cf. the works of *Bowen* [26], *Truesdell & Toupin* [185], and quotations therein. In lack of any microscopic information, the TM was then extended by the concept of volume fractions to basically define the TPM, see *Bowen* [27, 28], until its current understanding, cf. *de Boer* [16, 17], *de Boer & Ehlers* [18], and *Ehlers* [53, 55, 58–60]. Through this extension, the TPM is capable of a macroscopic description of multi-phasic continua, where the information about the underlying microstructure is obtained by the concept of volume fractions. The volume fractions are a measurement of local portions of the individual constituents of the overall medium.

Sand

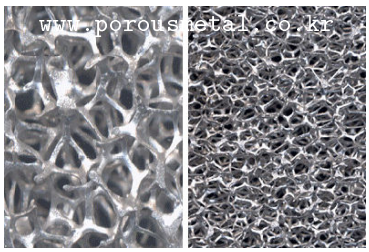

Metal foam

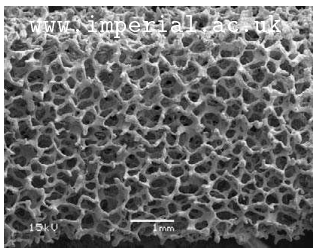

Biocompatible material (45S5 Bioglass®)[1]

Figure 2.1: Porous solid materials.

The basic principle of the TPM comprises a homogenisation process on the porous material, i. e., the real microstructure is statistically averaged (smeared out) through the considered domain, see Figure 2.2. Following this, the prescription of a real or a virtual averaging process over a representative elementary volume (REV) leads to a model φ of superimposed and interacting continua φ^α. Within the REV, the constituents, i. e., the porous solid phase $\alpha = S$ and the interstitial pore fluid $\alpha = F$, are assumed to be immiscible but in a state of ideal disarrangement. Thus, all geometrical and physical quantities are defined as field functions or as statistical mean values over the microstructure, respectively. Through this statistical representation, the real microstructure of porous solid materials can remain unknown. This dispensability of the knowledge of the discrete internal geometry is one of the biggest advantages of the TPM over micromechanical methods. Because, in general, apart from some very few industrial products, the knowledge of any geometry information on a microscopic scale is absence or can only be obtained by very complex measuring methods. This applies, in particular, for grown, biological materials.

2.2 Concept of Volume Fractions

Let V^α be the partial volumes of each constituent φ^α inside the overall biphasic aggregate $\mathcal{B}$. The overall volume V of the aggregate results from the sum of the partial volumes of its constituent bodies $\mathcal{B}^\alpha$ with

$$V = \int_{\mathcal{B}} \mathrm{d}v = \sum_{\alpha} V^\alpha, \quad \text{where } V^\alpha = \int_{\mathcal{B}^\alpha} \mathrm{d}v = \int_{\mathcal{B}} \mathrm{d}v^\alpha \,. \tag{2.1}$$

[1] Bioactive glasses are a group of surface-reactive glass ceramics and include the original bioactive glass, *Bioglass*. The biocompatibility of these glasses has led them to be investigated extensively for use as implant materials in the human body to repair and replace diseased or damaged bone. [WIKIPEDIA]

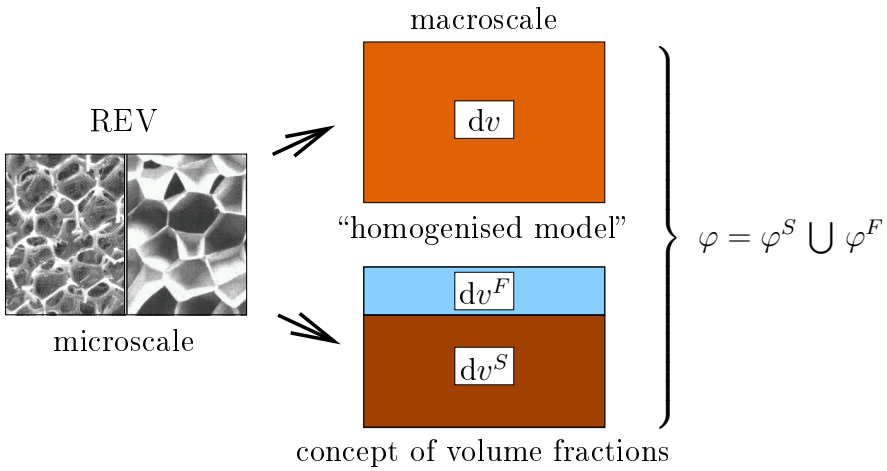

Figure 2.2: Homogenisation: micro-to-macro transition.

In order to relate the volume element $\mathrm{d}v^\alpha$ of each constituent φ^α to the overall volume element $\mathrm{d}v$, a local ratio, in the following denoted by n^α, needs to be defined as

$$\int_{\mathcal{B}} n^\alpha \, \mathrm{d}v := V^\alpha \quad \text{with} \quad n^\alpha = \frac{\mathrm{d}v^\alpha}{\mathrm{d}v} \,. \tag{2.2}$$

The above formulations, (2.1) and (2.2), represent the concept of volume fractions, wherein the quantity $n^\alpha = n^\alpha(\mathbf{x}, t)$ is referred to as the volume fraction itself. In general, one assumes that there is no vacant space in the overall medium, which leads directly to the necessary saturation condition via

$$n^S + n^F = 1 \,, \quad \text{where} \quad \begin{cases} n^S : & \text{solidity}, \\ n^F : & \text{porosity}. \end{cases} \tag{2.3}$$

In analogy to (2.2), the relation between the area element $\mathrm{d}a$ of the overall aggregate $\mathcal{B}$ and the partial area element $\mathrm{d}a^\alpha$ is defined as

$$\mathrm{d}a^\alpha = n^\alpha \, \mathrm{d}a \quad \text{and} \quad \begin{cases} \mathrm{d}\mathbf{a} & = \mathbf{n} \, \mathrm{d}a \,, \\ \mathrm{d}\mathbf{a}^\alpha & = \mathbf{n} \, \mathrm{d}a^\alpha \,, \end{cases} \tag{2.4}$$

where $\mathbf{n}$ is the outward-oriented unit normal vector of the surface. Relation (2.4) is based on early investigations by *Delesse* [42]. *Delesse*[2] was interested in the question on how to determine the proportions of the different constituents of a rock. He showed that the area proportions of individual minerals in a representative crosssectional area of the rock is identical to its volumetric proportions. This is a prerequisite in order to consider porous

[2] *Achille Ernest Oscar Joseph Delesse* (1817–1881): French geologist and mineralogist. His observations on the lithology of the deposits accumulated beneath the sea were of special interest and importance. [Wikipedia]

media on basis of idealised continua, cf. *Fillunger* [74] and *Ehlers* [53]. Continuing the assumption of immiscible phases and taking the saturation condition (2.3) as a basis, two different densities can be introduced for each constituent, viz.

$$\begin{aligned} \rho^{\alpha R} &:= \frac{\mathrm{d}m^\alpha}{\mathrm{d}v^\alpha} && : \text{material density}\,, \\ \rho^{\alpha} &:= \frac{\mathrm{d}m^\alpha}{\mathrm{d}v} && : \text{partial density}\,. \end{aligned} \tag{2.5}$$

Therein, the local mass element $\mathrm{d}m^\alpha$ of each constituent is related to its local volume element $\mathrm{d}v^\alpha$ and to the bulk volume element $\mathrm{d}v$, respectively. Again, in analogy to (2.2) and (2.4), a relation between the material (realistic or effective) density $\rho^{\alpha R}$ and the partial (global or bulk) density ρ^α can be established as

$$\rho^\alpha = n^\alpha \rho^{\alpha R}\,. \tag{2.6}$$

Moreover, the mixture (overall) density ρ results from the sum of the partial densities ρ^α over all constituents φ^α, i. e.,

$$\rho = \sum_\alpha \rho^\alpha = \sum_\alpha n^\alpha \rho^{\alpha R}\,. \tag{2.7}$$

Based on this, it is obvious that material incompressibility of a constituent ($\rho^{\alpha R} = \text{const.}$) does not necessarily lead to the property of bulk incompressibility since the partial density functions ρ^α can still change through changes in the volume fractions n^α.

2.3 Kinematic Relations

Proceeding from the homogenisation process as a basic principle of the TPM, the concept of superimposed and interacting continua arises from the averaging procedure of all geometrical quantities over the REV. Thus, each spatial point $\mathbf{x}$ of the current configuration is, at any time t, simultaneously occupied by particles (or material points) P^α of both constituents φ^α. In the framework of mixture theories, it is assumed that all particles proceed from different reference positions $\mathbf{X}_\alpha$ at time t_0, cf. Figure 2.3. Consequently, each constituent is assigned to its own motion function

$$\mathbf{x} = \boldsymbol{\chi}_\alpha(\mathbf{X}_\alpha, t)\,. \tag{2.8}$$

Therein and in the following, kinematical quantities are identified via a subscript, whereas all other quantities are identified via a superscript. By the assignment of a unique reference position and a unique motion function for each material point P^α, only one single material point of each constituent φ^α can reside at a spatial point $\mathbf{x}$ (together with the material point of the other constituent $\rightsquigarrow$ superimposed continua). Furthermore, the **motion**

functions $\boldsymbol{\chi}_\alpha$ are postulated to be unique and uniquely invertible at any time t. As a result, each material point can also be identified by its reference position $\mathbf{X}_\alpha$ at time t_0:

$$\mathbf{X}_\alpha = \boldsymbol{\chi}_\alpha^{-1}(\mathbf{x}, t) \quad \text{if} \quad J_\alpha := \det \frac{\partial \boldsymbol{\chi}_\alpha(\mathbf{X}_\alpha, t)}{\partial \mathbf{X}_\alpha} \neq 0. \tag{2.9}$$

The existence of unique inverse motion functions $\boldsymbol{\chi}_\alpha^{-1}$ is based on non-singular *Jacobi*an[3] determinants J_α. With (2.8) and (2.9), there are two possible representations of geometrical and physical quantities within a continuum-mechanical model, either with regard to material coordinates $\mathbf{X}_\alpha$ (reference configuration), or with regard to spatial coordinates $\mathbf{x}$ (actual configuration). The former one is referred to as the *Lagrange*an[4] (or material) description, whereas the latter one is referred to as the *Euler*ian[5] (or spatial) description.

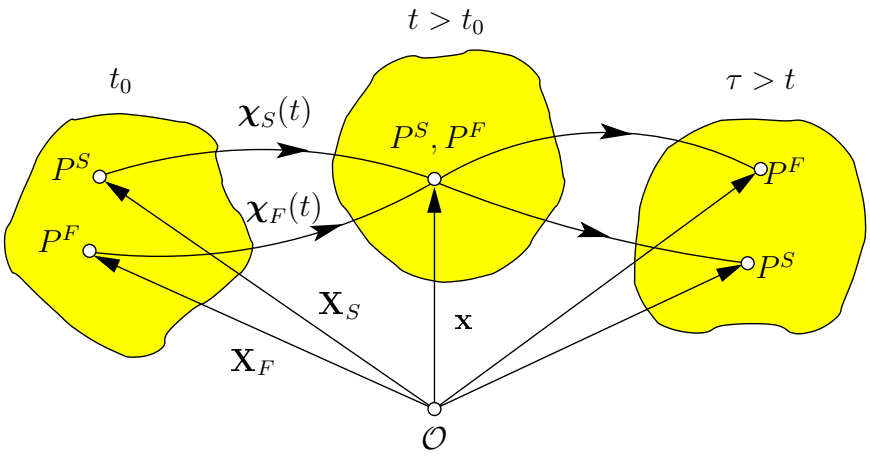

Figure 2.3: Motion of a biphasic mixture.

It follows from (2.8) that both constituents have their own velocity $\overset{\prime}{\mathbf{x}}_\alpha$ and acceleration $\overset{\prime\prime}{\mathbf{x}}_\alpha$ fields, which, in a *Lagrange*an description, are given as follows

$$\overset{\prime}{\mathbf{x}}_\alpha = \frac{\mathrm{d}}{\mathrm{d}t}\boldsymbol{\chi}_\alpha(\mathbf{X}_\alpha, t)\,, \quad \overset{\prime\prime}{\mathbf{x}}_\alpha = \frac{\mathrm{d}^2}{\mathrm{d}^2 t}\boldsymbol{\chi}_\alpha(\mathbf{X}_\alpha, t)\,. \tag{2.10}$$

For coupled solid-fluid problems, this description is generally used for the motion functions of the solid matrix φ^S. Therein, the solid displacement vector $\mathbf{u}_S$ becomes the primary

[3] *Carl Gustav Jacob Jacobi* (1804–1851): German mathematician who, with *Niels Henrik Abel*, founded the theory of elliptic functions. He carried out important research in partial differential equations of the first order and applied them to the differential equations of dynamics. [Encyclopædia Britannica]

[4] *Joseph-Louis Lagrange*, born *Giuseppe Lodovico Lagrangia* (1736–1813): Italian mathematician and astronomer who made significant contributions to all fields of analysis, to number theory, and to classical and celestial mechanics. But above all he impressed on mechanics, having transformed "*Newton*ian mechanics" into a branch of analysis, and exhibited the so-called mechanical "principles" as simple results of the variational calculus. [WIKIPEDIA]

[5] *Leonhard Euler* (1707–1783): Swiss mathematician and physicist who is considered to be the preeminent mathematician of the 18th century. *Euler* made important discoveries in multiple fields of mathematics as well as in mechanics, fluid dynamics, optics, and astronomy. [WIKIPEDIA]

kinematic variable, with $\mathbf{u}_S = \mathbf{u}_S(\mathbf{X}_S, t) := \mathbf{x} - \mathbf{X}_S$. Inserting the inverse motion function $(2.9)_1$ into above field function (2.10) results in an alternative formulation, i. e., in an *Euler*ian description, which reads

$$\begin{aligned} \overset{\prime}{\mathbf{x}}_\alpha &= \overset{\prime}{\mathbf{x}}_\alpha \left[\boldsymbol{\chi}_\alpha^{-1}(\mathbf{x}, t), t\right] = \overset{\prime}{\mathbf{x}}_\alpha (\mathbf{x}, t)\,, \\ \overset{\prime\prime}{\mathbf{x}}_\alpha &= \frac{\mathrm{d}}{\mathrm{d}t}\, \overset{\prime}{\mathbf{x}}_\alpha (\mathbf{x}, t) = \overset{\prime\prime}{\mathbf{x}}_\alpha \left[\boldsymbol{\chi}_\alpha^{-1}(\mathbf{x}, t), t\right] = \overset{\prime\prime}{\mathbf{x}}_\alpha (\mathbf{x}, t). \end{aligned} \tag{2.11}$$

In contrast to solid matrix motion, the pore fluid flow is better expressed in a modified *Euler*ian setting by use of the seepage velocity $\mathbf{w}_F = \overset{\prime}{\mathbf{x}}_F - \overset{\prime}{\mathbf{x}}_S$ with respect to the deforming solid matrix. This arises from the simple fact that the reference position of fluid particles can hardly be monitored. Thus, describing fluid particle motion with respect to spatial coordinates is more reasonable and practicable, respectively. After separate velocity fields have been stated for each constituent, the velocity of the overall medium remains to be defined. This so-called mixture velocity indicates the local barycentric velocity of the overall medium with

$$\dot{\mathbf{x}} = \frac{1}{\rho} \sum_\alpha \rho^\alpha \overset{\prime}{\mathbf{x}}_\alpha \ . \tag{2.12}$$

Following this, the relative velocity of a constituent $\overset{\prime}{\mathbf{x}}_\alpha$ to the barycentric velocity $\dot{\mathbf{x}}$ is defined as the diffusion velocity by

$$\mathbf{d}_\alpha = \overset{\prime}{\mathbf{x}}_\alpha - \dot{\mathbf{x}} \quad \text{with} \quad \sum_\alpha \rho^\alpha \mathbf{d}_\alpha = \mathbf{0}\,. \tag{2.13}$$

One can instantly see, regarding (2.7), (2.12) and $(2.13)_1$, that the diffusion mass flows $(2.13)_2$ of the constituents are summing up to zero. By defining the two velocities $\overset{\prime}{\mathbf{x}}_\alpha$ and $\dot{\mathbf{x}}$, one implicitly assumes differing material (total) derivatives. The material derivatives, denoted by $(\,\cdot\,)'_\alpha$, follow the motions of the constituents φ^α, whereas the so-called mixture derivative $(\,\cdot\,)^\bullet$ follows the barycentric motion of the overall medium φ, see Figure 2.4.

Let $\Gamma = \Gamma(\mathbf{x}, t)$ be a differentiable, scalar-valued field function and let $\boldsymbol{\Gamma}$ be its vectorial counterpart. Then, their material time derivatives read:

$$\begin{aligned} (\Gamma)'_\alpha &= \frac{\mathrm{d}_\alpha}{\mathrm{d}t}\Gamma = \frac{\partial \Gamma}{\partial t} + \operatorname{grad}\Gamma \cdot \overset{\prime}{\mathbf{x}}_\alpha\,, & \dot{\Gamma} &= \frac{\mathrm{d}}{\mathrm{d}t}\Gamma = \frac{\partial \Gamma}{\partial t} + \operatorname{grad}\Gamma \cdot \dot{\mathbf{x}}\,, \\ (\boldsymbol{\Gamma})'_\alpha &= \frac{\mathrm{d}_\alpha}{\mathrm{d}t}\boldsymbol{\Gamma} = \frac{\partial \boldsymbol{\Gamma}}{\partial t} + (\operatorname{grad}\boldsymbol{\Gamma})\, \overset{\prime}{\mathbf{x}}_\alpha\,, & \dot{\boldsymbol{\Gamma}} &= \frac{\mathrm{d}}{\mathrm{d}t}\boldsymbol{\Gamma} = \frac{\partial \boldsymbol{\Gamma}}{\partial t} + (\operatorname{grad}\boldsymbol{\Gamma})\, \dot{\mathbf{x}}\ . \end{aligned} \tag{2.14}$$

Therein, the differential operator $\operatorname{grad}(\,\cdot\,)$ denotes the partial derivative with respect to the actual position $\mathbf{x}$. Analogue to this, a partial derivative with respect to the reference position $\mathbf{X}_\alpha$ of φ^α is denoted by $\operatorname{Grad}_\alpha(\,\cdot\,)$. As a result, the **material deformation**

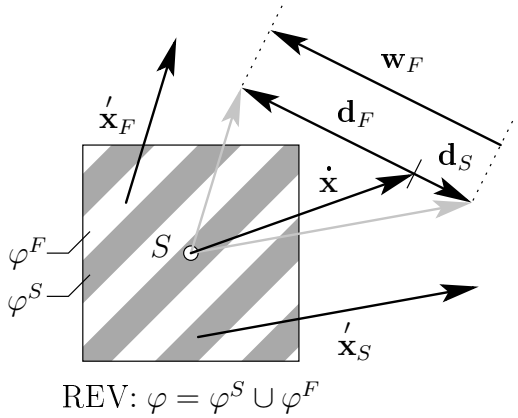

Figure 2.4: Illustration of biphasic mixture velocities.

gradient $\mathbf{F}_\alpha$ is formally introduced by

$$\mathbf{F}_\alpha = \frac{\partial \boldsymbol{\chi}_\alpha(\mathbf{X}_\alpha, t)}{\partial \mathbf{X}_\alpha} = \operatorname{Grad}_\alpha \mathbf{x} \quad \text{or} \quad \mathbf{F}_\alpha = \frac{\partial(\mathbf{X}_\alpha + \mathbf{u}_\alpha)}{\partial \mathbf{X}_\alpha} = \mathbf{I} + \operatorname{Grad}_\alpha \mathbf{u}_\alpha \,, \tag{2.15}$$

if the description of the deformation processes proceeds from the displacement gradient. Herein, $\mathbf{I}$ is the fundamental tensor of second order (second order identity). Note, as a consequence of the preceding framework, only the material deformation gradient of the solid matrix $\mathbf{F}_S$ is used in the following. Taking the seepage velocity $\mathbf{w}_F$ as the primary kinematic variable for the pore fluid, i.e., the fluid motion is described relatively to the deforming skeleton material, it follows that the material deformation gradient $\mathbf{F}_F$ is obsolete. Furthermore, within the TPM, there is no overall material deformation gradient $\mathbf{F}$ for the mixture φ, due to the lack of an overall motion function. Even though, the following relations are denoted only for the solid matrix. Their statements are, in the context of the TPM, also generally valid for the physical description of multiple constituents φ^α with $\mathbf{F}_\alpha$. Proceeding from (2.15), the inverse of the solid material deformation gradient $\mathbf{F}_S^{-1}$ reads

$$\mathbf{F}_S^{-1} = \frac{\partial \boldsymbol{\chi}_S^{-1}(\mathbf{x}, t)}{\partial \mathbf{x}} = \operatorname{grad} \mathbf{X}_S \quad \text{or} \quad \mathbf{F}_S^{-1} = \frac{\partial(\mathbf{x} - \mathbf{u}_S)}{\partial \mathbf{x}} = \mathbf{I} - \operatorname{grad} \mathbf{u}_S \,, \tag{2.16}$$

respectively. Now, with reference to $(2.9)_2$, the *Jacobi*an determinant of the solid matrix can also be written as

$$J_S = \det \mathbf{F}_S > 0 \quad \text{if} \quad \det \mathbf{F}_S(t_0) = 1 \,. \tag{2.17}$$

Since all motion functions $\boldsymbol{\chi}_\alpha$ are assumed to be unique and uniquely invertible, the domain of $\det \mathbf{F}_S$ is restricted to positive values.

The main attribute of the solid material deformation gradient is the transport of line elements $\mathrm{d}\mathbf{X}_S$ from the reference configuration towards line elements $\mathrm{d}\mathbf{x}$ in the actual

configuration (push-forward operation) with

$$\mathrm{d}\mathbf{x} = \mathbf{F}_S \, \mathrm{d}\mathbf{X}_S \,. \tag{2.18}$$

This transport attribute, in terms of a linear mapping, is based on the so-called two-field tensor characteristic of the deformation gradient. The two-field characteristic of $\mathbf{F}_S$ arises from the context that its first basis system $\mathbf{a}_{S\ell}$ (actual, covariant) "lives" in the actual configuration, whereas its second basis system $\mathbf{h}_S^\ell$ (history, contravariant) resides in the reference configuration. This can be recognised by rewriting the deformation gradient with respect to a natural, curvilinear coordinate system θ_S^i $(i = 1, 2, 3)$ via

$$\begin{aligned} \mathrm{d}\mathbf{x} = \mathbf{F}_S \, \mathrm{d}\mathbf{X}_S = \frac{\partial \mathbf{x}}{\partial \mathbf{X}_S} \, \mathrm{d}\mathbf{X}_S \quad &= \left(\underbrace{\frac{\partial \mathbf{x}}{\partial \theta_S^i}}_{} \otimes \underbrace{\frac{\partial \theta_S^i}{\partial \mathbf{X}_S}}_{} \right) \mathrm{d}\mathbf{X}_S \\ &\Rightarrow \Big(\underset{\downarrow}{\mathbf{a}_{S\ell}} \otimes \underbrace{\mathbf{h}_S^\ell}_{\delta_k^\ell} \Big) \, \mathbf{h}_{Sk} \quad = \mathbf{a}_{Sk} \,. \end{aligned} \tag{2.19}$$

Therein, the *Kronecker*[6] delta δ_k^ℓ is equal to unity for $\ell = k$, and equal to zero for all other cases. For details on the co- and contravariational framework see Appendix B.1. In analogy to (2.18), the mapping of area elements $\mathrm{d}\mathbf{A}_S$ and volume elements $\mathrm{d}V_S$ from the reference configuration to their respective counterparts in the actual configuration can be deduced as

$$\mathrm{d}\mathbf{a} = \operatorname{cof} \mathbf{F}_S \, \mathrm{d}\mathbf{A}_S \quad \text{and} \quad \mathrm{d}v = \det \mathbf{F}_S \, \mathrm{d}V_S \,. \tag{2.20}$$

The cofactor cof $(\cdot)$ is defined as $\operatorname{cof} \mathbf{F}_S = (\det \mathbf{F}_S) \, \mathbf{F}_S^{T-1}$. A representative overview of transport theorems for multi-order tensors can be found in Appendix A.2.1.

Based on the preceding transport attribute of the deformation gradient, the linear mapping of the squares of line elements and their difference, respectively, is utilised to introduce **deformation measures** as

$$\begin{aligned} \|\mathrm{d}\mathbf{x}\|^2 = \quad \mathrm{d}\mathbf{x} \cdot \mathrm{d}\mathbf{x} \quad &= (\mathbf{F}_S \, \mathrm{d}\mathbf{X}_S) \cdot (\mathbf{F}_S \, \mathrm{d}\mathbf{X}_S) = \mathrm{d}\mathbf{X}_S \cdot \mathbf{F}_S^T \, \mathbf{F}_S \, \mathrm{d}\mathbf{X}_S \;\rightsquigarrow \mathbf{C}_S := \mathbf{F}_S^T \, \mathbf{F}_S \,, \\ \|\mathrm{d}\mathbf{X}_S\|^2 = \mathrm{d}\mathbf{X}_S \cdot \mathrm{d}\mathbf{X}_S = \quad (\mathbf{F}_S^{-1} \, \mathrm{d}\mathbf{x}) \cdot (\mathbf{F}_S^{-1} \, \mathrm{d}\mathbf{x}) \quad &= \mathrm{d}\mathbf{x} \cdot \underbrace{\mathbf{F}_S^{T-1} \, \mathbf{F}_S^{-1}}_{(\mathbf{F}_S \, \mathbf{F}_S^T)^{-1}} \mathrm{d}\mathbf{x} \;\rightsquigarrow \mathbf{B}_S := \mathbf{F}_S \, \mathbf{F}_S^T \,, \end{aligned} \tag{2.21}$$

[6] *Leopold Kronecker* (1823 – 1891): German mathematician who argued that arithmetic and analysis must be founded on "whole numbers". [WIKIPEDIA]

and **strain measures** as

$$\begin{aligned} \|\mathrm{d}\mathbf{x}\|^2 - \|\mathrm{d}\mathbf{X}_S\|^2 &= \mathrm{d}\mathbf{X}_S \cdot \mathbf{C}_S\,\mathrm{d}\mathbf{X}_S - \mathrm{d}\mathbf{X}_S \cdot \mathrm{d}\mathbf{X}_S \\ &= \mathrm{d}\mathbf{X}_S \cdot (\mathbf{C}_S - \mathbf{I})\,\mathrm{d}\mathbf{X}_S \qquad \rightsquigarrow \mathbf{E}_S = \tfrac{1}{2}(\mathbf{C}_S - \mathbf{I})\,, \\ &= \mathrm{d}\mathbf{x} \cdot \mathrm{d}\mathbf{x} - \mathrm{d}\mathbf{x} \cdot \mathbf{B}_S^{-1}\,\mathrm{d}\mathbf{x} \\ &= \mathrm{d}\mathbf{x} \cdot (\mathbf{I} - \mathbf{B}_S^{-1})\,\mathrm{d}\mathbf{x} \qquad \rightsquigarrow \mathbf{A}_S = \tfrac{1}{2}(\mathbf{I} - \mathbf{B}_S^{-1})\,. \end{aligned} \tag{2.22}$$

Therein, $\mathbf{C}_S$ is the right, and $\mathbf{B}_S$ the left, *Cauchy*[7]*-Green*[8] deformation tensor of the solid matrix. Furthermore, $\mathbf{E}_S$ is the corresponding *Green-Lagrange*an, and $\mathbf{A}_S$ the *Almansi*an[9] strain tensor. Note in passing that the factor $\frac{1}{2}$ in (2.22) results from the fact that a strain tensor linearisation around the natural state ($t = t_0$) should result in the well-known 1-d *Hooke*an[10] elasticity law. Regarding the two-field characteristic of $\mathbf{F}_S$, cf. (2.19), the contravariant basis system, residing in the reference configuration, of $\mathbf{C}_S$ and the covariant basis system, "living" in the actual configuration, of $\mathbf{B}_S$ becomes clear. Both deformation tensors are positive definite, symmetric and can be converted into each other by an orthogonal, two-field rotation tensor $\mathbf{R}_S$, which implies the properties $\mathbf{R}_S^T = \mathbf{R}_S^{-1}$, and $\det \mathbf{R}_S = 1$, via

$$\mathbf{B}_S = \mathbf{R}_S\,\mathbf{C}_S\,\mathbf{R}_S^T\,. \tag{2.23}$$

With regard to the deformation tensors, it is obvious that $\mathbf{E}_S$ is a strain measure referring to the reference configuration, whereas $\mathbf{A}_S$ acts in the actual configuration. For the transport mechanism which converts these two strain tensors one into each other, see Appendix A.2.1. Note that there are several other possible representations of strain tensors which are not discussed here because they are of no relevance to this monograph. For a detailed discussion of deformation and strain measures, the interested reader is referred to, e. g., *Truesdell & Noll* [184], and *Ogden* [149].

Remark: For the occurrence of only **small deformations** and, therefore, only small strains of the solid matrix, the finite deformation approach can be reduced to a geometrically linear one. According to this, the difference between the reference and the current

[7] *Augustin Louis Cauchy* (1789 – 1857): French mathematician who was an early pioneer of analysis. *Cauchy* was a prolific writer; he wrote approximately eight hundred research articles and five complete textbooks. [Wikipedia]

[8] *George Green* (1793 – 1841): British miller and self-taught mathematician who initially published privately at his own expense, because he thought it would be presumptuous for a person like himself, with no formal education in mathematics, to submit scientific contributions to journals. [Wikipedia]

[9] *Emilio Almansi* (1869 – 1948): Italian physicist and mathematician known for his research in the theory of elasticity and nonlinear problems. [Wikipedia]

[10] *Robert Hooke* (1635 – 1703): English natural philosopher, architect and polymath – author's note: a polymath is a person whose expertise spans a significant number of different subject areas – who played an important role in the scientific revolution. *Hooke* is known for his law of elasticity, his book, *Micrographia*, and for first applying the word "cell" to describe the basic unit of life. He's also referred to as "Englands *Leonardo*". [Wikipedia]

configuration is small enough to lead to the following approximations

$$\mathrm{Grad}_S\,(\,\cdot\,) \approx \mathrm{grad}\,(\,\cdot\,) \quad \text{and} \quad \mathrm{Div}_S\,(\,\cdot\,) \approx \mathrm{div}\,(\,\cdot\,)\,. \tag{2.24}$$

Therein, $\mathrm{Div}_\alpha\,(\,\cdot\,)$, $\mathrm{div}\,(\,\cdot\,)$ denote the divergence operators corresponding to $\mathrm{Grad}_\alpha\,(\,\cdot\,)$, $\mathrm{grad}\,(\,\cdot\,)$, respectively, see Appendix A.2.2. Furthermore, in context of the geometrical linear theory, the linearisation of the strain tensors $\mathbf{E}_S$ and $\mathbf{A}_S$ around the natural state yields the same result, i. e., $\mathrm{lin}\,\mathbf{E}_S = \mathrm{lin}\,\mathbf{A}_S$. The linearised strain tensors then read

$$\mathrm{lin}\,\mathbf{A}_S = \mathrm{lin}\,\mathbf{E}_S =: \boldsymbol{\varepsilon}_S = \tfrac{1}{2}\left[\mathrm{grad}\,\mathbf{u}_S + (\mathrm{grad}\,\mathbf{u}_S)^T\right]\,. \tag{2.25}$$

□

In order to postulate a finite material law that is capable of representing material behaviour at large deformations, a foregoing **spectral decomposition of the solid matrix deformation** is convenient. This procedure implies that the solid deformation tensor is decomposed into its eigenvalues and principal directions. Regarding (2.23), one can see that a conversion of the two solid deformation tensors, $\mathbf{C}_S$ and $\mathbf{B}_S$, into each other can be done by a proper orthogonal rotation. Accordingly, both tensors share the same eigenvalues $\lambda_{S(i)}$ and the same three principal invariants $I_{S(i)}$ $(i = 1, 2, 3)$. For the definition of these principal invariants see Appendix A.1.2. In this monograph, for the sake of clarity, the subscript $(\,\cdot\,)_S$, denoting quantities related to the solid phase φ^S, will be omitted for the notation of eigenvalues $(\lambda_{(i)} \equiv \lambda_{S(i)})$, eigenvectors $(\mathbf{m}_i, \mathbf{n}_i \equiv \mathbf{m}_{S(i)}, \mathbf{n}_{S(i)})$, eigentensors $(\mathbf{M}_i, \mathbf{N}_i \equiv \mathbf{M}_{S(i)}, \mathbf{N}_{S(i)})$ and principal invariants $(I_i \equiv I_{S(i)})$. Following this, the corresponding well-known eigenvalue problem can be postulated for both deformation tensors as

$$\mathbf{C}_S\,\mathbf{m} = \lambda\,\mathbf{m} \Leftrightarrow (\mathbf{C}_S - \lambda\,\mathbf{I})\,\mathbf{m} = \mathbf{0} \quad \text{and} \quad \mathbf{B}_S\,\mathbf{n} = \lambda\,\mathbf{n} \Leftrightarrow (\mathbf{B}_S - \lambda\,\mathbf{I})\,\mathbf{n} = \mathbf{0}\,. \tag{2.26}$$

This eigenvalue problem can be solved regarding the characteristic polynomial following the *Cayley*[11]*-Hamilton*[12] theorem, viz.

$$\det(\mathbf{C}_S - \lambda\,\mathbf{I}) = \det(\mathbf{B}_S - \lambda\,\mathbf{I}) = \lambda^3 - I_1\lambda^2 + I_2\lambda - I_3 = 0\,. \tag{2.27}$$

The closed, analytical solution for this characteristic polynomial, i. e., the three real-valued eigenvalues λ_i, can be found with, e. g., *Cardano*'s[13] method, see Appendix A.1.4. Note, the eigenvalues λ_i of $\mathbf{C}_S$, $\mathbf{B}_S$, respectively, correspond to the squares of the principal

[11] *Arthur Cayley* (1821 – 1895): British mathematician who helped to found the modern British school of pure mathematics. He proved that every square matrix is a root of its own characteristic polynomial and was also the first to define the concept of a group in the modern way (as a set with a binary operation satisfying certain laws). [Wikipedia]

[12] *Sir William Rowan Hamilton* (1805 – 1865): Irish physicist, astronomer, and mathematician. His greatest contribution is perhaps the reformulation of "*Newton*ian mechanics", now called "*Hamilton*ian mechanics". [Wikipedia]

[13] *Gerolamo Cardano* (1501 – 1576): Italian Renaissance mathematician, physician, astrologer and gambler who, besides his achievements in algebra, invented the concept of imaginary numbers. [Wikipedia]

stretches (which are incidental to the eigenvalues Λ_i of $\mathbf{F}_S$, viz. $\lambda_i = \Lambda_i^2$). With this, a spectral representation of the deformation tensors in eigenvalues λ_i and its corresponding eigentensors $\mathbf{M}_i$ (reference configuration) and $\mathbf{N}_i$ (actual configuration) yields

$$\mathbf{C}_S = \sum_{i=1}^{3} \lambda_i \, \mathbf{M}_i \quad \text{and} \quad \mathbf{B}_S = \sum_{i=1}^{3} \lambda_i \, \mathbf{N}_i \quad \text{with} \quad \left\{ \begin{array}{rcl} \mathbf{M}_i & = & \mathbf{m}_i \otimes \mathbf{m}_i \,, \\ \mathbf{N}_i & = & \mathbf{n}_i \otimes \mathbf{n}_i \,. \end{array} \right. \tag{2.28}$$

As a direct conclusion from the above, the spectral decomposition of the solid deformation gradient reads $\mathbf{F}_S = \sum_{i=1}^{3} \sqrt{\lambda_i} \, \mathbf{n}_i \otimes \mathbf{m}_i$. Note, because of the orthogonality of the eigenvectors, there is no need of a distinction between co- and contravariant bases.

Remark: The numerical computation of eigenvalues, eigenvectors and eigentensors of second-order tensors (with 3×3 coefficients) is a common challenge in computational mechanics. Unfortunately, the solution of the characteristic polynomial (2.27) with the before mentioned explicit formulae of *Cardano* is, from a computational point of view, quite problematic. In case of similar squares of principal stretches, as they can occur in volumetrically deformable materials, the numerical implementation of the *Cardano*ean method can completely destroy the originally well-conditioned problem, cf. *Markert* [134], and citations therein. Volumetrically deformable materials, including porous media, typically involve deformation tensors with multiple eigenvalues. The differences between these values can be so small that the last significant digits of the coefficients of the polynomial can reach the numerical precision. Even small errors can then lead to the computation of completely different eigenvalues. So, for this type of materials, a high numerical accuracy is fundamental for the spectral decomposition of the deformation tensors. Therefore, iterative solvers for the computation of the spectral decomposition are more sophisticated. Within this class of iterative solvers, solvers based on the so-called transformation methods are the most powerful, e. g., the *Householder*[14] *-QL* algorithm, cf. Appendix C.1.

□

On the basis of the previously introduced deformation and strain measures, **deformation and strain rates** need to be specified. With the definition of the material velocity $\overset{\prime}{\mathbf{x}}_\alpha$, cf. (2.10), the material solid velocity gradient $(\mathbf{F}_S)'_S$ and it's alternative formulated counterpart, the spatial solid velocity gradient $\mathbf{L}_S$, can be expressed as

$$(\mathbf{F}_S)'_S = \operatorname{Grad}_S \overset{\prime}{\mathbf{x}}_S \quad \text{and} \quad \mathbf{L}_S = \operatorname{grad} \overset{\prime}{\mathbf{x}}_S = (\mathbf{F}_S)'_S \, \mathbf{F}_S^{-1} \,. \tag{2.29}$$

The emphasis of the latter, spatial formulation of the velocity gradient and deformation rate, respectively, is the description of fluid particles in motion, since the previously introduced deformation measures are only applicable for solid mechanics. The spatial fluid velocity gradient is denoted as $\mathbf{L}_F$. The spatial velocity gradient can be, like any

[14] *Alston Scott Householder* (1904−1993): American mathematician who was specialised in mathematical biology and numerical analysis, inventor of the "*Householder* transformation" and of "*Householder*'s method". [WIKIPEDIA]

other tensor, additively decomposed into a symmetric and a skew-symmetric part, viz.

$$\mathbf{L}_\alpha = \mathbf{D}_\alpha + \mathbf{W}_\alpha \quad \text{with} \quad \left\{ \begin{array}{lcl} \mathbf{D}_\alpha & := & \mathbf{L}_\alpha^{\mathrm{sym}} = \frac{1}{2}\left(\mathbf{L}_\alpha + \mathbf{L}_\alpha^T\right), \\ \mathbf{W}_\alpha & := & \mathbf{L}_\alpha^{\mathrm{skw}} = \frac{1}{2}\left(\mathbf{L}_\alpha - \mathbf{L}_\alpha^T\right). \end{array} \right. \tag{2.30}$$

2.4 Stress Measures

In general, a body can be subjected to external volume forces and to contact forces. These forces act either from a distance on the overall body $\mathcal{B}$, or from the near vicinity on the surface of the body $\partial\mathcal{B}$. Commonly, the external volume forces are only interpreted as the gravitational forces. In the continuum-mechanical context considered in this monograph, the near vicinity contact forces are of more interest than the external distance forces. This motivates the introduction of **stress measures** that connect near vicinity forces to the body surface. Since stress is defined as "force per unit area", some corresponding area elements need to be defined. In the following, $\mathrm{d}\mathbf{a}$ will denote an area element in the actual configuration and $\mathrm{d}\mathbf{A}_\alpha$ an area element in the reference configuration of the body surface; note the vectorial status of the area element. This follows from a definite surface orientation, represented by a normal vector $\mathbf{n}$, i. e., $\mathrm{d}\mathbf{a} = \mathbf{n}\,\mathrm{d}a$. On basis of *Cauchy*'s theorem, a stress tensor for the overall mixture can be formally introduced as

$$\mathbf{t}(\mathbf{x}, t, \mathbf{n}) = \mathbf{T}(\mathbf{x}, t)\mathbf{n}\,. \tag{2.31}$$

The stress measure $\mathbf{T}$ is in general known as the *Cauchy* or true stress tensor. It represents a tensorial field function, which is independent of the considered surface. Relation (2.31) must also hold for each constituent, viz. $\mathbf{t}^\alpha(\mathbf{x}, t, \mathbf{n}) = \mathbf{T}^\alpha(\mathbf{x}, t)\mathbf{n}$. Therein, $\mathbf{t}$ or $\mathbf{t}^\alpha$, respectively, denote the surface traction vectors of the overall aggregate φ or the mixture, respectively, or of the constituent φ^α. The traction vectors include all effects that result from near vicinity contact forces $\mathrm{d}\mathbf{k}$ of φ or $\mathrm{d}\mathbf{k}^\alpha$ of φ^α. This yields to

$$\mathrm{d}\mathbf{k} = \mathbf{t}\,\mathrm{d}a = (\mathbf{T}\mathbf{n})\,\mathrm{d}a = \mathbf{T}\,\mathrm{d}\mathbf{a} \quad \text{and} \quad \mathrm{d}\mathbf{k}^\alpha = \mathbf{t}^\alpha\,\mathrm{d}a = (\mathbf{T}^\alpha\mathbf{n})\,\mathrm{d}a = \mathbf{T}^\alpha\mathrm{d}\mathbf{a}\,. \tag{2.32}$$

As one can see, the until now discussed stress measures are only related to the area element $\mathrm{d}\mathbf{a}$ in the actual configuration. Consequently, alternative stress measures in the referential configuration need to be identified additionally. The referential configuration stress measures can be introduced by corresponding pull-back transports. Multiple pull-back transports, for each quantity separately, yield to multiple intermediate stress measures, viz.

$$\begin{array}{rcl|rcl} \mathrm{d}\mathbf{k}^\alpha & = & \mathbf{T}^\alpha\mathrm{d}\mathbf{a} = (\det\mathbf{F}_\alpha)\,\mathbf{T}^\alpha\mathrm{d}\bar{\mathbf{a}}\,, & =: & \boldsymbol{\tau}^\alpha\mathrm{d}\bar{\mathbf{a}} \quad \text{with} \quad \mathrm{d}\bar{\mathbf{a}} = (\det\mathbf{F}_\alpha)^{-1}\mathrm{d}\mathbf{a}\,, \\ & = & (\det\mathbf{F}_\alpha)\,\mathbf{T}^\alpha\,\mathbf{F}_\alpha^{T-1}\mathrm{d}\mathbf{A}_\alpha\,, & =: & \mathbf{P}^\alpha\mathrm{d}\mathbf{A}_\alpha \quad \text{with} \quad \mathrm{d}\mathbf{A}_\alpha = (\mathrm{cof}\,\mathbf{F}_\alpha)^{-1}\mathrm{d}\mathbf{a}\,, \\ & = & (\det\mathbf{F}_\alpha)\,\mathbf{F}_\alpha^{-1}\,\mathbf{T}^\alpha\,\mathbf{F}_\alpha^{T-1}\mathrm{d}\mathbf{A}_\alpha\,, & =: & \mathbf{S}^\alpha\mathrm{d}\mathbf{A}_\alpha \quad \text{with} \quad \mathrm{d}\mathbf{A}_\alpha = \mathbf{m}_\alpha\,\mathrm{d}A_\alpha\,. \end{array} \tag{2.33}$$

Therein, $\boldsymbol{\tau}^\alpha$ is known as the *Kirchhoff*[15] or weighted *Cauchy* stress tensor, $\mathbf{P}^\alpha$ as the first and $\mathbf{S}^\alpha$ as the second *Piola*[16]*-Kirchhoff* stress tensor. The first *Piola-Kirchhoff* stress tensor $\mathbf{P}^\alpha$, as a two-field tensor, relates forces denoted in the actual configuration to geometrical quantities of the referential configuration. It is also known as the nominal stress and engineering stress, respectively. Note that $\mathbf{P}^\alpha$ is a non-symmetrical tensor. The second *Piola-Kirchhoff* stress tensor $\mathbf{S}^\alpha$ is fully located in the reference configuration. It describes both, forces and geometrical quantities in the referential configuration after an additional pull-back of the first *Piola-Kirchhoff* stress tensor. With this preliminaries, the two stress vectors $\mathbf{t}^\alpha$ and $\mathbf{p}^\alpha$ can be directly related to each other by a scalar-valued factor, viz.

$$\left.\begin{aligned} \mathrm{d}\mathbf{k}^\alpha &= \mathbf{t}^\alpha \mathrm{d}a &&= (\mathbf{T}^\alpha \mathbf{n})\,\mathrm{d}a &&= \mathbf{T}^\alpha\,\mathrm{d}\mathbf{a} \\ &= \mathbf{p}^\alpha\,\mathrm{d}A_\alpha &&= (\mathbf{P}^\alpha \mathbf{m}_\alpha)\,\mathrm{d}A_\alpha &&= \mathbf{P}^\alpha\,\mathrm{d}\mathbf{A}_\alpha \end{aligned}\right\} \rightsquigarrow \mathbf{t}^\alpha = \mathbf{p}^\alpha \frac{\mathrm{d}A_\alpha}{\mathrm{d}a}\,. \tag{2.34}$$

2.5 Balance Relations

Balance relations are one of the most fundamental concepts in continuum mechanics. All balance relations in continuum mechanics express the idea that the material time rate of a volume-specific mechanical quantity over a body $\mathcal{B}$ must arise from three basic causes, namely,

- a flow (efflux) of the mechanical quantity through the body surface $\partial\mathcal{B}$ and/or
- an external source (supply) of the mechanical quantity and/or
- a production of the mechanical quantity inside the body.

These three causes can be merged together into a balance relation of a general structure. This general structure is also known as the master balance representation. It exhibits the frame of all balance relations in continuum mechanics. Therein, the single balance relations are introduced axiomatically. As this monograph's discussion is based on multi-phasic continua, the fundamental balance relations are considered with respect

[15] *Gustav Robert Kirchhoff* (1824−1887): German physicist who contributed to the fundamental understanding of electrical circuits, spectroscopy, and the emission of black-body radiation by heated objects. Multiple concepts in different scientific fields are named after him, the so-called "*Kirchhoff*'s laws". [Wikipedia]

[16] *Gabrio Piola* (1794−1850): Italian mathematician and physicist whose contributions in the field of analytical mechanics are of fundamental importance for the modern continuum mechanics; descendant of the noble family of Giussano. [Wikipedia]

to *Truesdell*'s[17] metaphysical principles, cf. *Truesdell* [183], namely,

Truesdell's metaphysical principles

1. All properties of the mixture must be mathematical consequences of properties of the constituents.
2. So as to describe the motion of a constituent, we may in imagination isolate it from the rest of the mixture, provided we allow properly for the actions of the other constituents upon it.
3. The motion of the mixture is governed by the same equations as is a single body.

(2.35)

These principles state that the sum of the respective balance relations of the constituents φ^α must result in the corresponding balance relations of the overall mixture φ. Furthermore, the balance relations of the constituents and of the mixture must both inherit the same structure as the balance relations known from classical continuum mechanics. Generally, there are volume-specific scalar and vectorial mechanical quantities to be balanced. With these preliminaries, the **global master balance for the mixture**, see *Ehlers* [58], yields

$$\begin{aligned} \frac{\mathrm{d}}{\mathrm{d}t}\int\limits_{\mathcal{B}} \Psi \,\mathrm{d}v &= \int\limits_{\mathcal{S}} (\boldsymbol{\phi}\cdot\mathbf{n})\,\mathrm{d}a + \int\limits_{\mathcal{B}} \sigma \,\mathrm{d}v + \int\limits_{\mathcal{B}} \hat{\Psi} \,\mathrm{d}v \quad \text{(scalar-valued)}\,, \\ \frac{\mathrm{d}}{\mathrm{d}t}\int\limits_{\mathcal{B}} \boldsymbol{\Psi} \,\mathrm{d}v &= \int\limits_{\mathcal{S}} (\boldsymbol{\Phi}\,\mathbf{n})\,\mathrm{d}a + \int\limits_{\mathcal{B}} \boldsymbol{\sigma} \,\mathrm{d}v + \int\limits_{\mathcal{B}} \hat{\boldsymbol{\Psi}} \,\mathrm{d}v \quad \text{(vector-valued)}\,. \end{aligned} \tag{2.36}$$

The therein introduced mechanical quantities representing variables are listed in Table 2.1. The global representation of the master balance is valid for the overall body $\mathcal{B}$, which is containing all material points P^α. If the integrands of (2.36) are steady and sufficiently often steadily differentiable, the global representation can be transferred into a local representation, which is then valid for each material point itself. The transfer from global to local balances follows from the material time differentiation of the left-hand sides and the application of the *Gauss*ian integral theorem on the surface parts of (2.36). This yields to the **local master balance for the mixture**:

$$\begin{aligned} \dot{\Psi} + \Psi \operatorname{div} \dot{\mathbf{x}} &= \operatorname{div} \boldsymbol{\phi} + \sigma + \hat{\Psi} \quad \text{(scalar-valued)}\,, \\ \dot{\boldsymbol{\Psi}} + \boldsymbol{\Psi} \operatorname{div} \dot{\mathbf{x}} &= \operatorname{div} \boldsymbol{\Phi} + \boldsymbol{\sigma} + \hat{\boldsymbol{\Psi}} \quad \text{(vector-valued)}\,. \end{aligned} \tag{2.37}$$

[17] *Clifford Ambrose Truesdell III* (1919 – 2000): American mathematician, natural philosopher, historian of science, and polemicist. Truesdell was considered a leading authority on the history of mechanics. He, together with his student Noll, contributed to rational mechanics in the most fundamental and shaping way within the last century. [WIKIPEDIA]

Ψ, $\boldsymbol{\Psi}$	: volume-specific densities of the mechanical quantities.
$\boldsymbol{\phi}\cdot\mathbf{n}$, $\boldsymbol{\Phi}\,\mathbf{n}$	: effluxes of the mechanical quantities (external velocity).
σ, $\boldsymbol{\sigma}$	: supply terms of the mechanical quantities (external distance).
$\hat{\Psi}$, $\hat{\boldsymbol{\Psi}}$	: production terms of the mechanical quantities.

Table 2.1: Mechanical quantities representing variables of master balances.

Proceeding from *Truesdell*'s second metaphysical principle, the structure of the **global master balance for the constituents** φ^α can be, analogue to (2.36), introduced as

$$\begin{aligned}
\frac{\mathrm{d}_\alpha}{\mathrm{d}t}\int_{\mathcal{B}} \Psi^\alpha \,\mathrm{d}v &= \int_{\mathcal{S}} (\boldsymbol{\phi}^\alpha\cdot\mathbf{n})\,\mathrm{d}a + \int_{\mathcal{B}} \sigma^\alpha \,\mathrm{d}v + \int_{\mathcal{B}} \hat{\Psi}^\alpha \,\mathrm{d}v \quad \text{(scalar-valued)}\,,\\
\frac{\mathrm{d}_\alpha}{\mathrm{d}t}\int_{\mathcal{B}} \boldsymbol{\Psi}^\alpha \,\mathrm{d}v &= \int_{\mathcal{S}} (\boldsymbol{\Phi}^\alpha\,\mathbf{n})\,\mathrm{d}a + \int_{\mathcal{B}} \boldsymbol{\sigma}^\alpha \,\mathrm{d}v + \int_{\mathcal{B}} \hat{\boldsymbol{\Psi}}^\alpha \,\mathrm{d}v \quad \text{(vector-valued)}\,.
\end{aligned} \tag{2.38}$$

Note that therein and in the following, the constituent variables $(\,\cdot\,)^\alpha$ have the same physical meaning as those denoted in Table 2.1 for the mixture. Following the previous insights, the **local master balance for the constituents** φ^α can be obtained as

$$\begin{aligned}
(\Psi^\alpha)'_\alpha + \Psi^\alpha \operatorname{div}\overset{\prime}{\mathbf{x}}_\alpha &= \operatorname{div}\boldsymbol{\phi}^\alpha + \sigma^\alpha + \hat{\Psi}^\alpha \quad \text{(scalar-valued)}\,,\\
(\boldsymbol{\Psi}^\alpha)'_\alpha + \boldsymbol{\Psi}^\alpha \operatorname{div}\overset{\prime}{\mathbf{x}}_\alpha &= \operatorname{div}\boldsymbol{\Phi}^\alpha + \boldsymbol{\sigma}^\alpha + \hat{\boldsymbol{\Psi}}^\alpha \quad \text{(vector-valued)}\,.
\end{aligned} \tag{2.39}$$

As mentioned before, a consequence to *Truesdell*'s first metaphysical principle is that each balance relation of the constituents (2.39) must summarise up to the according balance of the the overall mixture (2.37). The concluding fields of the multi-phasic continuum φ can be found as

$$\begin{aligned}
\Psi &= \sum_\alpha \Psi^\alpha\,, \quad \boldsymbol{\phi}\cdot\mathbf{n} = \sum_\alpha (\,\boldsymbol{\phi}^\alpha - \Psi^\alpha\,\mathbf{d}_\alpha\,)\cdot\mathbf{n}\,, \quad \sigma = \sum_\alpha \sigma^\alpha\,, \quad \hat{\Psi} = \sum_\alpha \hat{\Psi}^\alpha,\\
\boldsymbol{\Psi} &= \sum_\alpha \boldsymbol{\Psi}^\alpha\,, \quad \boldsymbol{\Phi}\,\mathbf{n} = \sum_\alpha (\,\boldsymbol{\Phi}^\alpha - \boldsymbol{\Psi}^\alpha\otimes\mathbf{d}_\alpha\,)\,\mathbf{n}\,, \quad \boldsymbol{\sigma} = \sum_\alpha \boldsymbol{\sigma}^\alpha\,, \quad \hat{\boldsymbol{\Psi}} = \sum_\alpha \hat{\boldsymbol{\Psi}}^\alpha.
\end{aligned} \tag{2.40}$$

This master balance framework now allows the postulation of the specific mechanical and thermodynamical balance equations for mass, momentum, moment of momentum (m. o. m.), energy and entropy by the insertion of the mechanical quantities given in Table 2.2 and Table 2.3 into the corresponding local master balances (2.37) and (2.39). For the sake of simplicity, as it is a often discussed standard procedure, the derivation process of the balance equations in Table 2.2 and Table 2.3 will be omitted in this monograph. For

	$\Psi,\ \boldsymbol{\Psi}$	$\boldsymbol{\phi},\ \boldsymbol{\Phi}$	$\sigma,\ \boldsymbol{\sigma}$	$\hat{\Psi},\ \hat{\boldsymbol{\Psi}}$
mass	ρ	$\mathbf{0}$	0	0
momentum	$\rho\,\dot{\mathbf{x}}$	$\mathbf{T}$	$\rho\,\mathbf{b}$	$\mathbf{0}$
m. o. m.	$\mathbf{x}\times(\rho\,\dot{\mathbf{x}})$	$\mathbf{x}\times\mathbf{T}$	$\mathbf{x}\times(\rho\,\mathbf{b})$	$\mathbf{0}$
energy	$\rho\,\varepsilon+\frac{1}{2}\,\dot{\mathbf{x}}\cdot(\rho\,\dot{\mathbf{x}})$	$\mathbf{T}^T\,\dot{\mathbf{x}}-\mathbf{q}$	$\dot{\mathbf{x}}\cdot(\rho\,\mathbf{b})+\rho\,r$	0
entropy	$\rho\,\eta$	$\boldsymbol{\phi}_\eta$	σ_η	$\hat{\eta}\geq 0$

Table 2.2: Mechanical quantities for the balance equations of the mixture φ.

more details on this topic, the interested reader is referred to, e. g., *Ehlers* [54, 55, 58], *Ammann* [2] or *Graf* [85].

Regarding the mechanical balance relations for the mixture in Table 2.2, $\rho\,\dot{\mathbf{x}}$ is the momentum of the mixture and $\mathbf{x}\times(\rho\,\dot{\mathbf{x}})$ the corresponding m. o. m.; the external mass-specific volume force is represented by $\mathbf{b}$. Concerning the first thermodynamical balance relation, i. e., the energy balance, ε is the internal energy, $\mathbf{q}$ is the heat influx vector (opposing the surface normal vector $\mathbf{n}$) and r is the external heat supply. Furthermore, for the quantities given in the second thermodynamical balance relation, i. e., the entropy balance, η denotes the entropy, $\boldsymbol{\phi}_\eta$ the entropy efflux and σ_η the external entropy supply. Note that the second thermodynamical balance relation is, in contrast to all other balances, an inequality. The inequality arises from the entropy production $\hat{\eta}\geq 0$, which can never be negative. This considers the irreversibility of the overall thermodynamical process, also known as the second law of thermodynamics. The corresponding insertion process then recovers the well-known local form of the specific **balance equations for** single-phase materials φ and – in the sense of *Truesdell*'s third metaphysical principle – **the mixture** as stated in (2.41). Applying the same insertion process again for the constituents φ^α,

	$\Psi^\alpha,\ \boldsymbol{\Psi}^\alpha$	$\boldsymbol{\phi}^\alpha,\ \boldsymbol{\Phi}^\alpha$	$\sigma^\alpha,\ \boldsymbol{\sigma}^\alpha$	$\hat{\Psi}^\alpha,\ \hat{\boldsymbol{\Psi}}^\alpha$
mass	ρ^α	$\mathbf{0}$	0	$\hat{\rho}^\alpha$
momentum	$\rho^\alpha\,\overset{\prime}{\mathbf{x}}_\alpha$	$\mathbf{T}^\alpha$	$\rho^\alpha\,\mathbf{b}^\alpha$	$\hat{\mathbf{s}}^\alpha$
m. o. m.	$\mathbf{x}\times(\rho^\alpha\,\overset{\prime}{\mathbf{x}}_\alpha)$	$\mathbf{x}\times\mathbf{T}^\alpha$	$\mathbf{x}\times(\rho^\alpha\,\mathbf{b}^\alpha)$	$\hat{\mathbf{h}}^\alpha$
energy	$\rho^\alpha\,\varepsilon^\alpha+\frac{1}{2}\,\overset{\prime}{\mathbf{x}}_\alpha\cdot(\rho^\alpha\,\overset{\prime}{\mathbf{x}}_\alpha)$	$(\mathbf{T}^\alpha)^T\,\overset{\prime}{\mathbf{x}}_\alpha-\mathbf{q}^\alpha$	$\overset{\prime}{\mathbf{x}}_\alpha\cdot(\rho^\alpha\,\mathbf{b}^\alpha)+\rho^\alpha\,r^\alpha$	$\hat{e}^\alpha$
entropy	$\rho^\alpha\,\eta^\alpha$	$\boldsymbol{\phi}^\alpha_\eta$	σ^α_η	$\hat{\eta}^\alpha$

Table 2.3: Mechanical quantities for the balance equations of a constituent φ^α.

the **specific balance equations for the constituents** can be found as stated in (2.43).

mixture $\varphi = \cup_\alpha \varphi^\alpha$ balance equations

$$
\begin{aligned}
\text{mass}: \quad & \dot{\rho} + \rho \operatorname{div} \dot{\mathbf{x}} = 0 \\
\text{momentum}: \quad & \rho\, \ddot{\mathbf{x}} = \operatorname{div} \mathbf{T} + \rho\, \mathbf{b} \\
\text{m.o.m.}^{[18]}: \quad & \mathbf{0} = \mathbf{I} \times \mathbf{T} \quad \rightarrow \quad \mathbf{T} = \mathbf{T}^T \\
\text{energy}: \quad & \rho\, \dot{\varepsilon} = \mathbf{T} \cdot \mathbf{L} - \operatorname{div} \mathbf{q} + \rho\, r \\
\text{entropy}: \quad & \rho\, \dot{\eta} \geq \operatorname{div} \boldsymbol{\phi}_\eta + \sigma_\eta
\end{aligned}
\tag{2.41}
$$

Therein, the newly introduced quantities $\hat{\mathbf{p}}^\alpha$, $\hat{\mathbf{m}}^\alpha$, $\hat{\varepsilon}^\alpha$ and $\hat{\zeta}^\alpha$ need to be considered more detailed; Section 2.6 will discuss these details. These $(\hat{\cdot})$ denoted quantities represent the direct production of the constituents. For a better understanding of these quantities one can think of, as an example for the direct mass production $\hat{\rho}^\alpha$, ice becoming water due to a phase transition. Additionally, in order to allow proper interaction in-between the constituents, see *Truesdell*'s second metaphysical principle $(2.35)_2$, indirect production terms need to be introduced. The relations of the direct, the indirect and the total production quantities (terms) are given on the right side of Table 2.42.

$$
\begin{aligned}
\text{mass}: \quad & \sum_\alpha \hat{\rho}^\alpha = 0 \qquad \big| \quad \text{see } (2.43)_1 \\
\text{momentum}: \quad & \sum_\alpha \hat{\mathbf{s}}^\alpha = \mathbf{0} \qquad \big| \quad \hat{\mathbf{s}}^\alpha = \hat{\mathbf{p}}^\alpha + \hat{\rho}^\alpha\, \overset{\prime}{\mathbf{x}}_\alpha , \\
\text{m.o.m.}: \quad & \sum_\alpha \hat{\mathbf{h}}^\alpha = \mathbf{0} \qquad \big| \quad \hat{\mathbf{h}}^\alpha = \hat{\mathbf{m}}^\alpha + \mathbf{x} \times \hat{\mathbf{s}}^\alpha , \\
\text{energy}: \quad & \sum_\alpha \hat{e}^\alpha = 0 \qquad \big| \quad \hat{e}^\alpha = \hat{\varepsilon}^\alpha + \hat{\mathbf{p}}^\alpha \cdot \overset{\prime}{\mathbf{x}}_\alpha + \hat{\rho}^\alpha \left(\varepsilon^\alpha + \tfrac{1}{2}\, \overset{\prime}{\mathbf{x}}_\alpha \cdot \overset{\prime}{\mathbf{x}}_\alpha\right) , \\
\text{entropy}: \quad & \sum_\alpha \hat{\eta}^\alpha \geq 0 \qquad \big| \quad \hat{\eta}^\alpha = \hat{\zeta}^\alpha + \hat{\rho}^\alpha\, \eta^\alpha .
\end{aligned}
\tag{2.42}
$$

[18] The only insight from the m.o.m. balance equation is the symmetry condition of the *Cauchy* stress tensor. Therefore, this balance equation is no longer needed as an independent balance equation. Note that this is solely valid for the non-polar theory, also known as *Cauchy* or *Boltzmann*[19] continua. The polar theory counterpart is known as *Cosserat*[20] continua, and additionally takes rotational degrees of freedom for the particles into account. For details on this topic, the reader is referred to *Scholz* [165], *Diebels* [43, 44], and *Ehlers* [59].

[19] *Ludwig Boltzmann* (1844–1906): Austrian physicist famous for his founding contributions in the fields of statistical mechanics and statistical thermodynamics. He was one of the most important advocates for atomic theory at a time when that scientific model was still highly controversial. On his grave stone in Vienna, *Max Planck* had engraved the fundamental *Boltzmann* equation: $S = k \log W$. [Wikipedia]

[20] *Francois & Eugene Cosserat* (1866–1931 & 1852–1914): French researchers with a background in the field of astronomy, mathematics and civil engineering. The *Cosserat* model has emerged from the seminal work of the brothers at the turn of the last century (*Theorie des corps deformables*, 1909). Their main aim was to produce the correct general form of the energy for the variational problem. [*Neff* [144]]

As one can see, the summation of the direct and the indirect production results in the constituents total production, i. e., the right column of Table 2.3. In accordance to (2.40), the total production of the respective mechanical quantity must sum up to zero, see the left side of Table 2.42. One exception therein is the constituent's entropy production. Its sum – and only its sum – is assumed to be always positive. In the sixties of the last century this assumption was vividly discussed, as some researchers postulated that the second law of thermodynamics must also hold for each constituent of multi-phasic materials separately. This interpretation has lately been found to be too restrictive, cf. *Ehlers* [53], and *Truesdell* [183], for a historical overview on this.

constituent φ^α balance equations

$$
\begin{aligned}
\text{mass}: \quad & (\rho^\alpha)'_\alpha + \rho^\alpha \operatorname{div} \mathbf{x}'_\alpha &&= \hat{\rho}^\alpha \\
\text{momentum}: \quad & \rho^\alpha \mathbf{x}''_\alpha &&= \operatorname{div}\mathbf{T}^\alpha + \rho^\alpha \mathbf{b}^\alpha + \hat{\mathbf{p}}^\alpha \\
\text{m. o. m.}^{21}: \quad & \mathbf{0} &&= \mathbf{I} \times \mathbf{T}^\alpha + \hat{\mathbf{m}}^\alpha \\
\text{energy}: \quad & \rho^\alpha (\varepsilon^\alpha)'_\alpha &&= \mathbf{T}^\alpha \cdot \mathbf{L}_\alpha - \operatorname{div} \mathbf{q}^\alpha + \rho^\alpha r^\alpha + \hat{\varepsilon}^\alpha \\
\text{entropy}: \quad & \rho^\alpha (\eta^\alpha)'_\alpha &&= \operatorname{div}\left(-\frac{1}{\Theta^\alpha}\,\mathbf{q}^\alpha\right) + \frac{1}{\Theta^\alpha}\,\rho^\alpha r^\alpha + \hat{\zeta}^\alpha
\end{aligned}
\tag{2.43}
$$

Moreover, in anticipation to Section 2.6, two common *a priori* constitutive assumptions in the thermodynamical framework of single-phase materials are adopted, cf. *Ehlers* [58], viz.

$$
\boldsymbol{\phi}^\alpha_\eta = -\frac{1}{\Theta^\alpha}\,\mathbf{q}^\alpha \quad \text{and} \quad \sigma^\alpha_\eta = \frac{1}{\Theta^\alpha}\,\rho^\alpha r^\alpha \,. \tag{2.44}
$$

Herein, $\Theta^\alpha > 0$ denote the absolute *Kelvin*[22] temperatures of the constituents φ^α, which results in individual temperature fields for each constituent. This constitutive assumption has already been inserted into $(2.43)_5$. With the aim of developing constitutive relations which are capable of describing multi-phasic materials, one has to evaluate restrictions from the balance equations "top-down". This means that the subsequent discussion will base on the "highest" balance equation, i. e., the entropy inequality. This procedure assures a thermodynamical consistent formulation that frames the inherent first and second thermodynamical law. First, the total **entropy production of the mixture** follows

[21] Note that in contrast to the *Cauchy* stress tensor of the mixture $\mathbf{T}$, the constituent stress tensor $\mathbf{T}^\alpha$ is – because of the direct m. o. m. production $\hat{\mathbf{m}}^\alpha$ – even for a *Cauchy* or *Boltzmann* continuum not *a priori* symmetric. The direct m. o. m. production needs to be discussed separately.

[22] *Sir William Thomson, 1st Baron Kelvin* (1824–1907): Irish physicist and engineer. He is widely known for realising that there was a lower limit to temperature, absolute zero; absolute temperatures are stated in units of kelvin in his honour. He worked in a broad field of physics and engineering, including the laying of transatlantic telegraph cables. His versatility in almost all fields of physics led him to have been granted over 70 patents. [WIKIPEDIA]

directly the preceding considerations, viz.

$$\hat{\eta} = \sum_{\alpha} \hat{\eta}^{\alpha} = \sum_{\alpha} \left[\rho^{\alpha} (\eta^{\alpha})'_{\alpha} + \hat{\rho}^{\alpha} \eta^{\alpha} + \operatorname{div} \left(\frac{1}{\Theta^{\alpha}} \mathbf{q}^{\alpha} \right) - \frac{1}{\Theta^{\alpha}} \rho^{\alpha} r^{\alpha} \right] \geq 0 \,. \tag{2.45}$$

Because the included entropy therein is very difficult to measure, a mass-specific constituent energy function

$$\psi^{\alpha} = \varepsilon^{\alpha} - \Theta^{\alpha} \eta^{\alpha} \,, \tag{2.46}$$

the so-called *Helmholtz*[23] free energy, is introduced to substitute the entropy. With this substitution and an accompanying *Legendre*[24] transformation, the dependency of the internal energy ε^{α} on the caloric process variable η^{α} can be transferred to the caloric process variable Θ^{α}. Moreover, with the additional aid of the local energy balance equation $(2.43)_4$, the entropy production for the mixture (2.45) can be reformulated to yield the most common *Clausius*[25] *-Duhem*[26] inequality, viz.

$$\begin{aligned} \sum_{\alpha} \frac{1}{\Theta^{\alpha}} \Big\{ \, & \mathbf{T}^{\alpha} \cdot \mathbf{L}_{\alpha} - \rho^{\alpha} \left[(\psi^{\alpha})'_{\alpha} + (\Theta^{\alpha})'_{\alpha} \, \eta^{\alpha} \right] - \hat{\mathbf{p}}^{\alpha} \cdot \overset{\prime}{\mathbf{x}}_{\alpha} - \\ & - \hat{\rho}^{\alpha} \left(\psi^{\alpha} + \tfrac{1}{2} \overset{\prime}{\mathbf{x}}_{\alpha} \cdot \overset{\prime}{\mathbf{x}}_{\alpha} \right) - \frac{1}{\Theta^{\alpha}} \mathbf{q}^{\alpha} \cdot \operatorname{grad} \Theta^{\alpha} + \hat{e}^{\alpha} \Big\} \geq 0 \,. \end{aligned} \tag{2.47}$$

In order to reduce the extend of the constitutive settings discussion, a further anticipation to Section 2.6 is introduced at this point: this monograph only considers isothermal processes, i. e., $\Theta^{\alpha} = \Theta = \text{const}$. Consequently, the *Clausius-Duhem* inequality (2.47) reduces[27] to the so-called *Clausius-Planck*[28] inequality for heterogeneous materials:

$$\sum_{\alpha} \left[\, \mathbf{T}^{\alpha} \cdot \mathbf{L}_{\alpha} - \rho^{\alpha} \, (\psi^{\alpha})'_{\alpha} - \hat{\mathbf{p}}^{\alpha} \cdot \overset{\prime}{\mathbf{x}}_{\alpha} \, - \hat{\rho}^{\alpha} \left(\psi^{\alpha} + \frac{1}{2} \overset{\prime}{\mathbf{x}}_{\alpha} \cdot \overset{\prime}{\mathbf{x}}_{\alpha} \right) \right] \geq 0 \,. \tag{2.48}$$

[23] *Hermann Ludwig Ferdinand von Helmholtz* (1821 – 1894): German physician and physicist who made significant contributions to several widely varied areas of modern science. He is known for too many contributions to list here. The largest German association of research institutions, the "*Helmholtz* Association", is named after him. [WIKIPEDIA]

[24] *Adrien-Marie Legendre* (1752 – 1833): French mathematician who was at his time best known for his influential textbook on geometry. *Legendre*'s work correlated often with that from *Carl Friedrich Gauß*. [WIKIPEDIA]

[25] *Rudolf Julius Emanuel Clausius* (1822 – 1888): German physicist and mathematician. He is considered one of the central founders of the science of thermodynamics. *Clausius* was the first to state the basic ideas of the second law of thermodynamics. In 1865, he introduced the concept of entropy. [WIKIPEDIA]

[26] *Pierre Maurice Marie Duhem* (1861 – 1916): French physicist, mathematician, and philosopher of science, best known for his writings on the indeterminacy of experimental criteria, and on scientific development in the Middle Ages. Duhem also made major contributions to the science of his day, particularly in the fields of hydrodynamics, elasticity, and thermodynamics. [WIKIPEDIA]

[27] The *Clausius-Duhem* inequality is primary a dissipation inequality. Thus, an additive split of it, into an internal – purely mechanical – and a thermal part, would result in the same inequality as given in (2.48).

[28] *Max Karl Ernst Ludwig Planck* (1858 – 1947): German physicist who is regarded as the founder of the quantum theory for which he received the Nobel Price in Physics in 1918. Because of his dean position at the Berlin University, it was possible for him to establish a new professorship especially for *Albert Einstein*. [WIKIPEDIA]

2.6 Constitutive Settings

The purpose of this section is the development of constitutive settings that are capable of describing damage in multi-phasic materials. Regarding the wider scope of this monograph – the application of the numerical methodology also to bio-mechanical damage problems – the basic morphology of biological tissue is briefly considered. The tissue cells of every multi-cellular organism are embedded in a natural extracellular matrix (ECM). Through a variety of different proteins such as collagen and fibronectin, the ECM is primarily a supportive structure. As the ECM is composed of entangled collagen fibres, it can exhibit anisotropic material behaviour, depending on the arrangement of the collagen fibres. Furthermore, it is known from the literature that biological tissue also exhibits viscoelastic behaviour, if it is subjected to large deformations. For a comprehensive discussion on anisotropy, the composition of biological tissue in general and its continuum-mechanical modelling, the interested reader is referred to *Hayes & Bodine* [100], *Fung* [79], *Boehler* [15], *Schröder* [166], *Schröder et. al* [168], *Cowin* [40], *Holzapfel et al.* [104, 105], *Ehlers & Markert* [64], *Gasser & Holzapfel* [83], *Apel* [3], *Markert* [134], *Karajan* [116], and citation therein.

It is obvious that the evolution of a circumferential continuum-mechanical model for biological tissue requires quite complex material modelling. However, as the main focus of this monograph lies in the development of a general discontinuous numerical framework for multi-phasic materials, the constitutive settings will aim towards a fundamental biphasic TPM model. Therefore, only – at least for the continuous part – isotropic and hyperelastic material properties of the solid matrix are considered in the range of finite deformations. The discussion on boundary-value problems (BVP) closes the continuum-mechanical framework for the numerical implementation of the constitutive settings. Further constitutive settings to this section will be introduced in Section 3.2, and the discussion following therein.

2.6.1 Biphasic TPM Model

For a biphasic TPM model of a fully fluid-saturated, materially incompressible solid, i. e., $\alpha = \{S, F\} \rightsquigarrow \varphi = \varphi^S \cup \varphi^F$, following **initial assumptions** are evident and reasonable:

$$\begin{array}{lll|ll}
\rho^{SR} = \text{const.} & : \text{mat. incomp. solid } \varphi^S\,, & & \text{mat. incomp. fluid } \varphi^F & : \quad \rho^{FR} = \text{const.}\,, \\
\overset{''}{\mathbf{x}}_\alpha = \ddot{\mathbf{x}} = \mathbf{0} & : \text{quasi-static conditions}\,, & & \text{uniform gravitation } \mathbf{g}\ \forall\ \varphi^\alpha & : \quad \mathbf{b}^\alpha = \mathbf{g}\,, \\
\hat{\mathbf{m}}^\alpha = \mathbf{0} & : \quad \text{micro. non-polar}\,, & & \text{isothermal processes} & : \Theta^\alpha = \Theta = \text{const.}\,, \\
\hat{\rho}^\alpha = 0 & : \quad \text{no mass exchange}\,, & & \text{fully saturated} & : \quad n^S + n^F = 1\,.
\end{array} \tag{2.49}$$

With the postulation of material incompressibility, the associated real densities are constant over time, i. e., for initial homogeneity: $\rho^{SR}_{0S} = \rho^{SR} = \text{const.} \rightarrow (\rho^{\alpha R})'_\alpha = 0$ and $\operatorname{grad} \rho^{SR} = \mathbf{0}$. In this context, the restriction of no mass exchange between the phases

allows a reduction of the mass balance of the constituents to a volume balance, yielding to

$$(n^\alpha)'_\alpha + n^\alpha \operatorname{div} \overset{\prime}{\mathbf{x}}_\alpha = 0\,. \tag{2.50}$$

For the solid skeleton, the analytical integration of (2.50) yields to a transport relation for the solid porosity, viz. $n^S = n^S_{0S} \det \mathbf{F}_S^{-1}$; n^S_{0S} denotes the initial solidity. As a consequence, this reveals the dependence of the partial solid density on the deformation gradient as $\rho^S = \rho^S_{0S} \det \mathbf{F}_S^{-1}$. Therein, $\rho^S_{0S} = n^S_{0S}\, \rho^{SR}$ states the initial partial solid density at $t = 0$.

Furthermore, taking the material (total) time derivative of a mechanical quantity, recall (2.14), into account for (2.50), together with the saturation condition $n^S + n^F = 1 \rightarrow (n^S + n^F)'_S = 0$, the volume balance of the overall aggregate can be found as

$$\operatorname{div}\left[(\mathbf{u}_S)'_S + n^F \mathbf{w}_F\right] = 0 \tag{2.51}$$

The lack of mass production simplifies the total momentum production to $\hat{\mathbf{s}}^\alpha = \hat{\mathbf{p}}^\alpha$. According to Table 2.42_2, this yields to the analogy $\hat{\mathbf{p}}^S = -\hat{\mathbf{p}}^F$. For quasi-static conditions and the assumption of uniform gravitation, the momentum balance for the overall aggregate,

$$\operatorname{div} \mathbf{T} + \rho\, \mathbf{g} = \mathbf{0}\,, \tag{2.52}$$

arises from the summation of the constituents momentum balances

$$\operatorname{div} \mathbf{T}^\alpha + \rho^\alpha\, \mathbf{g} + \hat{\mathbf{p}}^\alpha = \mathbf{0}\,. \tag{2.53}$$

Therein, the total *Cauchy* stress tensor is the sum[29] of the partial stress tensors, viz. $\mathbf{T} = \mathbf{T}^S + \mathbf{T}^F$.

Even though the partial *Cauchy* stress tensor can not be *a priori* considered as symmetrical, recall $(2.43)_3$, it can be shown that – as a result of the homogenisation process – the constituent's direct m.o.m. production $\hat{\mathbf{m}}^\alpha$ is equal to zero, thus $\mathbf{T}^\alpha = (\mathbf{T}^\alpha)^T$, cf. *Hassanizadeh & Gray* [95], *Ehlers* [59]. Consequently, the presented partial stress tensors $\mathbf{T}^\alpha$, $\boldsymbol{\mathcal{T}}^\alpha$ and $\mathbf{S}^\alpha$ are symmetric; the first *Piola-Kirchhoff* stress tensor $\mathbf{P}^\alpha$ is, because of its two-field characteristic, generally non-symmetric. Thus, together with the previous insights, **the entropy inequality** (2.48) **of the mixture** reduces **for purely mechanical processes** to

$$\mathbf{T}^S \cdot \mathbf{D}_S - \rho^S (\psi^S)'_S + \mathbf{T}^F \cdot \mathbf{D}_F - \rho^F (\psi^F)'_F - \hat{\mathbf{p}}^F \cdot \mathbf{w}_F \geq 0 \tag{2.54}$$

[29] Note in passing that this – at first sight – contradiction to (2.40), i. e., $\mathbf{T} = \sum_\alpha (\mathbf{T}^\alpha - \rho^\alpha\, \mathbf{d}_\alpha \otimes \mathbf{d}_\alpha)$, is intrinsically dissolved with the assumptions stated in (2.49), viz.

$$\rho\, \ddot{\mathbf{x}} = \sum_\alpha \left[\, \rho^\alpha\, \overset{\prime\prime}{\mathbf{x}}_\alpha - \operatorname{div}(\rho^\alpha\, \mathbf{d}_\alpha \otimes \mathbf{d}_\alpha) + \hat{\rho}^\alpha\, \overset{\prime}{\mathbf{x}}_\alpha \,\right] = \mathbf{0} \quad \rightarrow \quad \operatorname{div}\Big(\sum_\alpha \rho^\alpha \mathbf{d}_\alpha \otimes \mathbf{d}_\alpha\Big) = \mathbf{0}\,.$$

For details on this topic, the reader is referred to *de Boer & Ehlers* [18].

Note that the energy balance is in this context obsolete, because of the assumption of isothermal processes. However, its fundamental context for the derivation of (2.54) can't be neglected.

To close the biphasic model under consideration, constitutive equations are required for the partial *Cauchy* stress tensor $\mathbf{T}^\alpha$, as well as for the momentum production of the fluid constituent $\hat{\mathbf{p}}^F$. The entropy inequality (2.54) imposes the necessary thermodynamical restrictions for the finding of the missing constitutive equations. Furthermore, the finding process is constrained by the saturation condition (2.3). Thus, the saturation condition has to be considered while evaluating the entropy inequality. Therefore, a *Lagrange*an multiplier $\mathcal{P}$ is – in the sense of an incompressibility constraint – introduced to the material time derivative of the saturation, viz.

$$\mathcal{P}(n^S + n^F)'_S = 0\,. \tag{2.55}$$

Combining (2.55) with (2.54) transfers the entropy inequality to

$$\begin{aligned}\mathbf{T}^S \cdot \mathbf{D}_S - \rho^S(\psi^S)'_S + \mathbf{T}^F \cdot \mathbf{D}_F - \rho^F(\psi^F)'_F - \hat{\mathbf{p}}^F \cdot \mathbf{w}_F - \\ -\mathcal{P}\underbrace{(n^S \operatorname{div} \overset{\prime}{\mathbf{x}}_S + n^F \operatorname{div} \overset{\prime}{\mathbf{x}}_F + \operatorname{grad} n^F \cdot \mathbf{w}_F)}_{-(n^S + n^F)'_S = -\operatorname{div}\left[(\mathbf{u}_S)'_S + n^F \mathbf{w}_F\right]} \geq 0\,.\end{aligned} \tag{2.56}$$

With the aid of the relation $\operatorname{div} \overset{\prime}{\mathbf{x}}_\alpha = \mathbf{L}_\alpha \cdot \mathbf{I} = \mathbf{D}_\alpha \cdot \mathbf{I}$, the entropy inequality can be rewritten to introduce the classical **concept of effective stresses**. First, so-called extra quantities are introduced, denoted by $(\,\cdot\,)_E$, to act as substitutes for the braced terms in (2.57).

$$\begin{aligned}\overbrace{(\mathbf{T}^S + n^S \mathcal{P}\,\mathbf{I})}^{=:\,\mathbf{T}^S_E} \cdot \mathbf{D}_S - \rho^S(\psi^S)'_S + \overbrace{(\mathbf{T}^F + n^F \mathcal{P}\,\mathbf{I})}^{=:\,\mathbf{T}^F_E} \cdot \mathbf{D}_F - \rho^F(\psi^F)'_F - \\ - \underbrace{(\hat{\mathbf{p}}^F - \mathcal{P} \operatorname{grad} n^F)}_{=:\,\hat{\mathbf{p}}^F_E} \cdot \mathbf{w}_F \geq 0\,.\end{aligned} \tag{2.57}$$

The necessity of the extra quantities is evident through the demand of material incompressibility. Due to this demand, the partial stress $\mathbf{T}^S$, $\mathbf{T}^F$ and the momentum production $\hat{\mathbf{p}}^F$ can only be determined to a certain percentage, cf. *de Boer & Ehlers* [19]. Thus, the extra quantities allow a modular treatment of the specific solid skeleton, the pore fluid and their interaction, see

$$\left.\begin{aligned}\mathbf{T}^S &= \mathbf{T}^S_E - n^S \mathcal{P}\,\mathbf{I}\,,\\ \mathbf{T}^F &= \mathbf{T}^F_E - n^F \mathcal{P}\,\mathbf{I}\,,\end{aligned}\right| \quad \hat{\mathbf{p}}^F = \hat{\mathbf{p}}^F_E + \mathcal{P} \operatorname{grad} n^F\,. \tag{2.58}$$

The extra quantities need to be determined by appropriate constitutive equations. However, in soil mechanics, the extra stresses $\mathbf{T}^S_E$ are usually known as the effective stresses.

Hence, $\mathcal{P}$ can be be identified as the unspecific effective pore pressure $\mathcal{P} := p^{FR}$. According to (2.57), one can see that the effective stress concept is a direct consequence of the entropy inequality, and not a separate constitutive equation. The basis of this concept has already been formulated by *Terzaghi* [181] in 1925. It has been extended in detail – including its application within the TPM – by *Bishop* [13], *Skempton* [175], and *de Boer & Ehlers* [18]. The overall *Cauchy* stress is obtained by a summation of the partial stresses, such that

$$\mathbf{T} = \mathbf{T}_E - \mathcal{P}\,\mathbf{I} \quad \text{with} \quad \mathbf{T}_E = \mathbf{T}_E^S + \mathbf{T}_E^F . \tag{2.59}$$

An order-of-magnitude analysis of the friction force $\operatorname{div}\mathbf{T}_E^F$ incorporated in the momentum balance of φ^F, in comparison to the extra momentum production $\hat{\mathbf{p}}_E^F$, results in the negligibility of the fluid extra stress, i. e., $\mathbf{T}_E^F \approx \mathbf{0}$, see *Hassanizadeh* [96], *Ehlers et. al* [62, 63], and *Diebels et al.* [46]. This is a common assumption in hydraulics. Note in passing that, although the fluid extra stress $\mathbf{T}_E^F$ has been neclected, the fluid viscosity is included via $\hat{\mathbf{p}}_E^F$ also known as the effective drag force. Furthermore, concerning the incompressible fluid constituent, it can be shown that the fluid free energy function is constant, i. e., it lacks any process variables: $\psi^F = \psi^F(-) = \text{const.} \rightsquigarrow (\psi^F)'_F = 0$, cf. *Ehlers* [59]. Consequently, the internal friction in-between the porous solid skeleton and the viscous pore fluid is only covered by the momentum production $\hat{\mathbf{p}}_E^F$. The preceding insights then reduce the entropy inequality to its final representation for this monograph, viz.

$$\mathbf{T}_E^S \cdot \mathbf{D}_S - \rho^S (\psi^S)'_S - \hat{\mathbf{p}}_E^F \cdot \mathbf{w}_F \geq 0 . \tag{2.60}$$

The development of constitutive equations in the framework of the TPM is based on fundamental principles given by *Noll* [145], *Truesdell* [182], and *Coleman & Noll* [38]. Namely, these principles are determinism, equipresence, local action, material frame indifference (objectivity) and dissipation. Regarding (2.60), one can identify a set of undefined response functions $\mathcal{R} = \{\psi^S, \mathbf{T}_E^S, \hat{\mathbf{p}}_F^E\}$. The undefined response functions need constitutive equations (principle of determinism) that fit the thermodynamical principles. The principle of equipresence states that the set of independent equations must be interpreted as functions of a common set of, also independent, process variables: $\mathcal{R} = \mathcal{R}(\mathcal{V})$. For the model under consideration – an isothermal immiscible aggregate consisting of a solid skeleton which is fully saturated by a single viscous pore fluid – the following basic set of independent process variables is postulated: $\mathcal{V} = \{\mathbf{C}_S, \mathbf{w}_F\}$; thus,

$$\{\psi^S, \mathbf{T}_E^S, \hat{\mathbf{p}}_E^F\} = \mathcal{R}\,\{\mathbf{C}_S, \mathbf{w}_F\} . \tag{2.61}$$

The finding of the process variables will not be shown in this monograph. The reader who is interested in more information on this topic is referred to the comprehensive works of *de Boer et. al* [20], *Ehlers* [53], and *Karajan* [116]. However, concerning continuum fracture mechanics, the fundamental principles for the development of corresponding constitutive equations will be revisited in Section 3.2.

By citing the principle of phase separation from *Ehlers* [52], constitutive assumptions are made for the free energy function ψ^S: the free energy function of the solid only depends on

the solid deformation, viz. $\psi^S = \psi^S(\mathbf{C}_S)$. As a consequence, the material time derivation of ψ^S reads

$$(\psi^S)'_S = \frac{\partial \psi^S}{\partial \mathbf{C}_S} \cdot (\mathbf{C}_S)'_S \,. \tag{2.62}$$

Coupling (2.62) with (2.60) yields[30] the effective solid *Cauchy* stress tensor[31] as

$$\mathbf{T}^S_E = \mathbf{F}_S \, (2\rho^S \frac{\partial \psi^S}{\partial \mathbf{C}_S}) \, \mathbf{F}^T_S = 2\rho^S \, \frac{\partial \psi^S}{\partial \mathbf{B}_S} \, \mathbf{B}_S \,. \tag{2.64}$$

The remainder of (2.60) represents the dissipative (irreversible) part of the entropy inequality. It reveals a proportionality condition of the fluid momentum production to the seepage velocity, viz.

$$-\,\hat{\mathbf{p}}^F_E \cdot \mathbf{w}_F \geq 0 \quad \rightsquigarrow \quad \hat{\mathbf{p}}^F_E \propto -\mathbf{w}_F \,. \tag{2.65}$$

2.6.2 Solid Skeleton

In the following, an isotropic, hyperelastic (*Green* elastic) type material model will be assumed for the constitutive modelling process of the solid skeleton. The concept of hyperelasticity implies that the effective stress tensor is derivable from a strain-energy density function, cf. *Ogden* [149]. Thus, the strain-energy function must exhibit a potential characteristic. Such a potential strain-energy function is only capable to describe reversible processes. This is a direct analogy to the remainder in $(2.65)_1$, because, in this context, the remainder is solely responsible for irreversible effects. The strain-energy function is introduced as

$$\mathcal{W}^S := \rho^S_{0S} \, \psi^S \,. \tag{2.66}$$

Therein, $\mathcal{W}^S$ represents the stored elastic energy per unit reference volume rather then per unit mass (as ψ^S does). As a consequence from (2.62), the strain-energy function inherits the dependency of the right *Cauchy*-*Green* deformation tensor, ergo, $\mathcal{W}^S = \mathcal{W}^S(\mathbf{C}_S)$. In order to find a suitable energy function that fulfils previously claimed restrictions (material frame indifference and isotropy), it is necessary to formulate the function with respect to the principal invariants I_i and eigenvalues λ_i, respectively, of $\mathbf{C}_S$:

$$\mathcal{W}^S = \hat{\mathcal{W}}^S(I_i) = \tilde{\mathcal{W}}^S(\lambda_i) \quad \text{with} \quad i = 1,2,3 \,. \tag{2.67}$$

[30] Note $(\mathbf{C}_S)'_S = 2\mathbf{F}^T_S \mathbf{D}_S \mathbf{F}_S \rightsquigarrow (\mathbf{T}^S_E - 2\rho^S \mathbf{F}_S \frac{\partial \psi^S}{\partial \mathbf{C}_S} \mathbf{F}^T_S) = \mathbf{0}$ for arbitrary values of the free variable $\mathbf{D}_S$.

[31] For the sake of completeness, the stress tensors equivalent to $\mathbf{T}^S_E$, cf. (2.33), read for isotropic materials

$$\boldsymbol{\tau}^S_E = 2\rho^S_{0S} \frac{\partial \psi^S}{\partial \mathbf{B}_S} \mathbf{B}_S \longleftrightarrow \mathbf{P}^S_E = (2\rho^S_{0S} \frac{\partial \psi^S}{\partial \mathbf{B}_S} \mathbf{B}_S)\mathbf{F}^{T-1}_S \longleftrightarrow \mathbf{P}^S_E = \mathbf{F}_S(2\rho^S_{0S} \frac{\partial \psi^S}{\partial \mathbf{C}_S}) \longleftrightarrow \mathbf{S}^S_E = 2\rho^S_{0S} \frac{\partial \psi^S}{\partial \mathbf{C}_S} \,. \tag{2.63}$$

Recall that the principal invariants and eigenvalues of $\mathbf{C}_S$ are identical to those of the left solid deformation tensor $\mathbf{B}_S$, see (2.27).

For a sophisticated description of the porous solid skeleton within the framework of the TPM, a hyperelastic *Ogden*-type strain energy function will be used. However, the original *Ogden*-type strain-energy function is not capable to account a compaction point, see *Odgen* [148]. Thus, it is not directly applicable to porous media. Therefore, the **strain-energy function** $\mathcal{W}^S_{Ogden}$ is extended by a volumetric term $\mathcal{U}^S_{Eipper}$ postulated by *Eipper* [66] yielding to

$$\begin{aligned} \mathcal{W}^S_{Ogden} &= \mu^S \sum_{j=1}^{3} \left[\sum_{i=1}^{3} \frac{\mu_j^*}{\alpha_j} \left(\lambda_i^{(\alpha_j/2)} - 1 \right) - \mu_j^* \ln(J_S) \right] + \mathcal{U}^S_{Eipper}(J_S) \quad \text{with} \\ \mathcal{U}^S_{Eipper} &= \frac{\lambda^S}{\gamma\,[\gamma - 1 + (1 - n^S_{0S})^{-2}]} \left((J_S)^\gamma - 1 - \gamma \ln(\frac{J_S - n^S_{0S}}{1 - n^S_{0S}}) + \gamma\, n^S_{0S}\, \frac{J_S - 1}{1 - n^S_{0S}} \right) . \end{aligned} \tag{2.68}$$

Herein, the solid matrix parameter μ^S and λ^S represent the first and second *Lamé*[32] constants, and J_S the *Jacobi*an determinant; μ_j^*, α_j, and γ represent dimensionless, real-valued parameters that determine the nonlinearity of the function. The following restrictions for the parameters ensure the mandatory polyconvexity of (2.68):

$$\mu^S, \lambda^S > 0\,, \quad \sum_{j=1}^{3} \mu_j^* \geq 0\,, \quad \mu_j^*\, \alpha_j^* > 0\,, \quad \gamma \geq 1\,. \tag{2.69}$$

For further details on the derivation of (2.68) and its parameters (2.69), the interested reader is referred to *Eipper* [66]. With (2.68) and (2.64), the corresponding *Cauchy* stress tensor yields

***Cauchy* stress tensor**

$$\begin{aligned} \mathbf{T}^S_E &= 2\,\frac{1}{J_S}\frac{\partial \mathcal{W}^S}{\partial \mathbf{B}_S}\,\mathbf{B}_S \\ &= \frac{\mu^S}{J_S} \sum_{j=1}^{3} \sum_{i=1}^{3} \mu_j^* \left(\lambda_i^{(\alpha_j/2)} - 1 \right) \mathbf{N}_i + \\ &\quad + \frac{\lambda^S}{\gamma - 1 + (1 - n^S_{0S})^{-2}} \left((J_S)^{(\gamma-1)} - \frac{1}{J_S - n^S_{0S}} + \frac{n^S_{0S}}{1 - n^S_{0S}} \right) \mathbf{I}\,. \end{aligned} \tag{2.70}$$

[32] *Gabriel Léon Jean Baptiste Lamé* (1795 – 1870): French mathematician who worked on engineering mathematics and elasticity where two elastic constants are named after him. His own opinion was that his general theory of curvilinear coordinates were his most important contribution. *Lamé* was considered the leading French mathematician of his time by many, in particular by *Carl Friedrich Gauß*. [*O'Connor & Robertson* [147]]

2.6.3 Interstitial Fluid

Next, the second constituent of the mixture, the interstitial fluid is regarded. It is assumed that the interstitial fluid is incompressible and viscous. Since there is no energy potential for the fluid constituent to be determined, only the proportionality condition (2.65) needs to be evaluated. By following a common TPM ansatz for biphasic materials, a *Darcy*[33]-like approach is postulated for the proportionality relation between the momentum production $\hat{\mathbf{p}}_E^F$ and the seepage velocity $\mathbf{w}_F$, viz.

$$\hat{\mathbf{p}}_E^F = -\frac{(n^F)^2\,\gamma^{FR}}{k^F}\,\mathbf{w}_F \quad \text{with} \quad \begin{cases} \textit{Darcy}\text{-like permeability} \\ \qquad k^F = k^F(n^S) = \dfrac{\gamma^{FR}}{\mu^{FR}}\,K^S_{Eipper}\,, \\ \text{and intrinsic permeability, cf. } \textit{Eipper}\ [66], \\ \qquad K^S_{Eipper} = \left(\dfrac{1-n^S}{1-n^S_{0S}}\right)^{\kappa} K^S_{0S}\,. \end{cases} \tag{2.71}$$

Therein, the parameter $\gamma^{FR} = \rho^{FR}\,|\mathbf{g}|$ represents the fluid specific weight, and $\mu^{FR} > 0$ the dynamic fluid viscosity. Furthermore, isotropic permeability is assumed. Note that, due to the introduction of the intrinsic permeability K^S_{Eipper} in (2.71), **deformation-dependent permeability** has been introduced implicitly. This is crucial for the discussion on porous media fluid flow within the range of finite deformations. The postulated intrinsic permeability K^S_{Eipper} takes the initial permeability K^S_{0S} of the undeformed reference configuration into account. The nonlinearity of the deformation is governed by κ. Obviously, the deformation-dependent permeability is deactivated for $\kappa = 0$. In this case, the *Darcy*-like permeability becomes the original *Darcy* permeability coefficient. Insertion of (2.71) into $(2.58)_3$, and afterwards into the quasi-static fluid momentum balance (2.53) yields the well-known *Darcy*(-like) equation for the description of interstitial fluid flow in a porous medium

$$\boxed{\begin{array}{c}\textbf{interstitial fluid flow}\\ \boxed{n^F\mathbf{w}_F = -\dfrac{k^F}{\gamma^{FR}}\left(\operatorname{grad}\mathcal{P} - \rho^{FR}\mathbf{g}\right).}\end{array}} \tag{2.72}$$

2.6.4 Boundary-value Problem (BVP)

The purpose of this subsection is to motivate a set of equations that govern the prescribed continuum-mechanical model with focus on a numerical implementation. Therefore, the until now "strong" formulated balance equations of the mixture need to be transferred to a so-called "weak" formulation. The strong (local) formulated balance equations are valid in an absolute sense per material point $\mathbf{x}$, whereas their correspondent weak (integral) formulations transfer the balances to the body $\mathcal{B}$ in the sense of a distribution. This is a

[33] *Henry Philibert Gaspard Darcy* (1803–1858): French engineer who built an impressive pressurised (only by gravity) water distribution system in Dijon following the failure of attempts. Therefore, he developed a theory/law to describe flow through sands; it has since been generalised to a variety of situations and is in widespread use today. [WIKIPEDIA]

crucial step for the investigation of arbitrary problems with numerical methods, because the strong formulation is too strict for a numerical approximation.

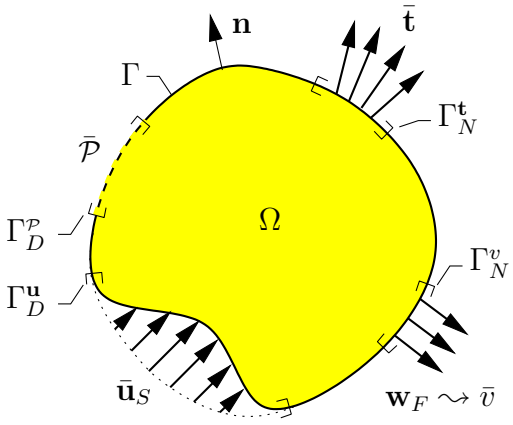

Figure 2.5: Illustration of BVP.

The governing equations of the biphasic model under consideration, namely the overall momentum and the overall volume balance, incorporate three variable field functions: the solid displacement vector $\mathbf{u}_S$, the seepage velocity vector $\mathbf{w}_F$, and the scalar-valued pore fluid pressure $\mathcal{P}$. By the substitution of the seepage velocity in the overall volume balance (2.51) with a suitable filter equation, like that given in (2.72), the number of variable field functions reduces to two. Note that this is only valid for quasi-static processes. The set of primary variables then reads $\{\mathbf{u}_S, \mathcal{P}\}$. Thus, the overall momentum balance (2.52) responds to $\mathbf{u}_S$, and the overall volume balance (2.51) directly responds to $\mathcal{P}$. The BVP is illustrated in Figure 2.5. In a mathematical sense, Ω is the spatial domain of the body $\mathcal{B}$. The surface of the body $\partial\mathcal{B}$ is represented by the boundary of the domain Γ. The boundary Γ is split into

- the *Dirichlet*[34] boundary Γ_D, corresponding directly to the primary variables $\mathbf{u}_S$ and $\mathcal{P}$, with essential boundary conditions (BC), and into
- the *Neumann*[35] boundary Γ_N with natural BC.

For both governing equations, *Dirichlet* and *Neumann* BC must be defined. Thereby, following restrictions apply:

$$\begin{aligned} \Gamma &= \Gamma_D \cup \Gamma_N \,, \\ \Gamma_D &= \{\Gamma_D^{\mathbf{u}}, \Gamma_D^{\mathcal{P}}\} \,, \quad \left| \quad \emptyset = \Gamma_D^{\mathbf{u}} \cap \Gamma_N^{\mathbf{t}} \,, \right. \\ \Gamma_N &= \{\Gamma_N^{\mathbf{t}}, \Gamma_N^{v}\} \,, \quad \left| \quad \emptyset = \Gamma_D^{\mathcal{P}} \cap \Gamma_N^{v} \,. \right. \end{aligned} \tag{2.73}$$

These restrictions state that boundary parts are not permitted on which both, *Dirichlet* and *Neumann* BC, for one respective primary variable are defined. In contrast, overlapping BC between the two primary variables are valid. Thus, the strong form of the BVP

[34] *Peter Gustav Lejeune Dirichlet* (1805–1859): German mathematician credited with the modern formal definition of a function. He was appointed to fill the vacant chair of *Gauß* upon the latter's death. *Dirichlet*'s brain is preserved in the department of physiology at the University of Göttingen, along with the brain of *Carl Friedrich Gauß*. [WIKIPEDIA]

[35] *Carl Gottfried Neumann* (1832–1925): German mathematician and physicist who made contributions in thermodynamics. He worked on a wide range of topics in applied mathematics such as mathematical physics, potential theory, and electrodynamics. [*Cheng & Cheng* [37]]

can be formulated as follows: find suitable functions for $\mathbf{u}_S(\mathbf{x},t)$ and $\mathcal{P}(\mathbf{x},t)$ such that the problem defining equations

$$\begin{aligned} \operatorname{div}\big[(\mathbf{u}_S)'_S \overbrace{- \frac{k^F}{\gamma^{FR}}\left(\operatorname{grad}\mathcal{P} - \rho^{FR}\mathbf{g}\right)}^{n^F\mathbf{w}_F}\big] &= 0\,, \\ \operatorname{div}(\mathbf{T}^S_E - \mathcal{P}\mathbf{I}) + \rho\,\mathbf{g} &= \mathbf{0}\,, \end{aligned} \tag{2.74}$$

satisfy the BC with

$$\begin{aligned} \mathbf{u}_S &= \bar{\mathbf{u}}_S\,, \quad \text{on } \Gamma^{\mathbf{u}}_D\,, \\ \mathbf{t} &= \bar{\mathbf{t}}\,, \quad \text{on } \Gamma^{\mathbf{t}}_N\,, \end{aligned} \qquad \left| \qquad \begin{aligned} \mathcal{P} &= \bar{\mathcal{P}}\,, \quad \text{on } \Gamma^{\mathcal{P}}_D\,, \\ v &= \bar{v}\,, \quad \text{on } \Gamma^{v}_N\,. \end{aligned} \right. \tag{2.75}$$

In a first step for the derivation of the weak forms of (2.74), each equation is multiplied with corresponding test functions and integrated over the domain Ω; the test functions $\{\delta\mathcal{P},\, \delta\mathbf{u}_S\}$ weight the equations as

$$\begin{aligned} \int_\Omega \Big\{ \Big[\operatorname{div}\big[(\mathbf{u}_S)'_S - \frac{k^F}{\gamma^{FR}}\left(\operatorname{grad}\mathcal{P} - \rho^{FR}\mathbf{g}\right)\big] \Big]\, \delta\mathcal{P} \Big\}\, \mathrm{d}v = 0\,, \quad \forall \quad \delta\mathcal{P} \in \mathcal{T}^{\mathcal{P}}\,, \\ \int_\Omega \Big\{ \Big[\operatorname{div}(\mathbf{T}^S_E - \mathcal{P}\mathbf{I}) + \rho\,\mathbf{g} \Big] \cdot \delta\mathbf{u}_S \Big\}\, \mathrm{d}v = 0\,, \quad \forall \quad \delta\mathbf{u}_S \in \mathcal{T}^{\mathbf{u}}\,. \end{aligned} \tag{2.76}$$

The application of the product rule and the *Gauss*ian divergence theorem, see Section A.1, on (2.76) yields to the weak formulation of the BVP, viz.

weak formulation of the BVP

$$\begin{aligned} \int_\Omega \operatorname{div}(\mathbf{u}_S)'_S\, \delta\mathcal{P}\, \mathrm{d}v + \int_\Omega \frac{k^F}{\gamma^{FR}}\left(\operatorname{grad}\,\mathcal{P} - \rho^{FR}\,\mathbf{g}\right)\cdot \operatorname{grad}\,\delta\mathcal{P}\, \mathrm{d}v = -\int_{\Gamma^v_N} \underbrace{n^F\mathbf{w}_F\cdot\mathbf{n}}_{=:\,\bar{v}}\, \delta\mathcal{P}\, \mathrm{d}a\,, \\ \int_\Omega (\mathbf{T}^S_E - \mathcal{P}\,\mathbf{I})\cdot \operatorname{grad}\,\delta\mathbf{u}_S\, \mathrm{d}v - \int_\Omega \rho\,\mathbf{g}\cdot\delta\mathbf{u}_S\, \mathrm{d}v = \int_{\Gamma^{\mathbf{t}}_N} \underbrace{\left[(\mathbf{T}^S_E - \mathcal{P}\,\mathbf{I})\,\mathbf{n}\right]}_{=:\,\bar{\mathbf{t}}}\cdot\delta\mathbf{u}_S\, \mathrm{d}a\,. \end{aligned} \tag{2.77}$$

[37] *Ivan Grigoryevich Bubnov* (1872−1919): Russian structural engineer specialised in the construction of ships, in particular submarines. A main contribution of *Bubnov* to the development of the FEM is that he realised (1913) that "...extremely simple solutions can also be obtained [...] [by] substitute the expansion [...] in the general differential expression for equilibrium, multiply the expression [...] and integrate over the entire volume of the body...". [*Gander & Wanner* [80]]

[38] *Boris Galerkin* (1871−1945): Russian/Soviet mathematician and engineer. *Galerkin* himself calls the method which carries today his name the "*Ritz*[36]method". The main contribution of *Galerkin* is to realise that one does not need a minimisation principle in order to construct a finite dimensional system following the recipe given by *Ivan Grigoryevich Bubnov*. [*Gander & Wanner* [80]]

[39] *Walther Ritz* (1878−1909): Swiss theoretical physicist who introduced the theoretical basis for the FEM by formulating a variational principle on plate problems. This variational principle is also known

The weak formulation (2.77) is in general also known as the "method of weighted residua" or the *Bubnov*[37]*-Galerkin*[38] method, respectively, if $\{\mathbf{u}_S, \mathcal{P}\}$ and $\{\delta\mathbf{u}_S, \delta\mathcal{P}\}$ proceed from the same basis functions, see Section 4.1.

In (2.77), $\bar{v}$ represents the volume efflux of φ^F over the boundary $\Gamma_N^v(\mathbf{n})$, and $\bar{\mathbf{t}}$ represents the external load vector on the boundary $\Gamma_N^{\mathbf{t}}(\mathbf{n})$ of the aggregate φ. Note that the external load vector acts on both constituents. This is an important property for the direct application of physical meaningful BC, as no differentiation of the constituents BC is necessary. The previous considerations need a mathematical framework. Therefore, ansatz spaces containing the ansatz functions for $\{\mathbf{u}_S, \mathcal{P}\}$, and test spaces containing the test (weighting) functions $\{\delta\mathbf{u}_S, \delta\mathcal{P}\}$ need to be defined; the test functions are designed to vanish on $\Gamma_D^{\mathbf{u}}$, $\Gamma_D^{\mathcal{P}}$, respectively. The ansatz and test spaces are defined as follows:

$$\begin{aligned}
\mathcal{A}^{\mathbf{u}}(t) &= \{ \quad \mathbf{u}_S \in \mathcal{H}^1(\Omega)^d : \quad \mathbf{u}_S(\mathbf{x}) = \bar{\mathbf{u}}_S(\mathbf{x},t) \text{ on } \Gamma_D^{\mathbf{u}} \}, \\
\mathcal{A}^{\mathcal{P}}(t) &= \{ \quad \mathcal{P} \in \mathcal{H}^1(\Omega) \quad : \quad \mathcal{P}(\mathbf{x}) = \bar{\mathcal{P}}(\mathbf{x},t) \text{ on } \Gamma_D^{\mathcal{P}} \}, \\
\mathcal{T}^{\mathbf{u}} &= \{ \delta\mathbf{u}_S \in \mathcal{H}^1(\Omega)^d : \delta\mathbf{u}_S(\mathbf{x}) = \mathbf{0} \text{ on } \Gamma_D^{\mathbf{u}} \}, \\
\mathcal{T}^{\mathcal{P}} &= \{ \quad \delta\mathcal{P} \in \mathcal{H}^1(\Omega) \quad : \quad \delta\mathcal{P}(\mathbf{x}) = 0 \text{ on } \Gamma_D^{\mathcal{P}} \}.
\end{aligned} \tag{2.78}$$

Therein, $d \in \{1,2,3\}$ indicates the dimension of the problem, and $\mathcal{H}^1(\Omega)$ indicates the *Sobolev*[39] space.

Remark: Note in passing that for some problems it can be necessary to set the seepage velocity $\mathbf{w}_F$ explicitly as a boundary condition. Therefore, one would not eliminate the seepage velocity by the substitution with a filter law. Consequently, an additional balance equation arising from (2.72) is

$$\frac{n^F\gamma^{FR}}{k^F}\mathbf{w}_F + \operatorname{grad}\mathcal{P} - \rho^{FR}\mathbf{g} = \mathbf{0} \rightsquigarrow \int_\Omega \Big\{\Big[\frac{n^F\gamma^{FR}}{k^F}\mathbf{w}_F + \operatorname{grad}\mathcal{P} - \rho^{FR}\mathbf{g}\Big]\cdot\delta\mathbf{w}_F\Big\}\,\mathrm{d}v = 0\,,$$

$$\Longrightarrow \int_\Omega (\frac{n^F\gamma^{FR}}{k^F}\mathbf{w}_F - \rho^{FR}\mathbf{g})\cdot\delta\mathbf{w}_F\,\mathrm{d}v - \int_\Omega \mathcal{P}\operatorname{div}(\delta\mathbf{w}_F)\,\mathrm{d}v = -\int_{\Gamma_N^{\mathbf{w}}} \underbrace{\mathcal{P}\,\mathbf{n}}_{=:\,\bar{\mathbf{w}}_F}\cdot\delta\mathbf{w}_F\,\mathrm{d}a\,, \tag{2.79}$$

would expand the set of weakly imposed governing equations. In (2.79), $\delta\mathbf{w}_F$ denotes the test function for the primary variable $\mathbf{w}_F$, and $\bar{\mathbf{w}}_F$ represents the fluid efflux over the boundary $\Gamma_N^{\mathbf{w}}$; these three quantities are introduced analogue to their vectorial counterparts in the preceding paragraph. Note that this would result in the numerical disadvantage of additional nodal degrees of freedom for $\mathbf{w}_F$. In general, it is sufficient to compute the seepage velocity in a post-processing step. Obviously, as a direct consequence to

as "*Ritz*' method". [WIKIPEDIA]

[39] *Sergei Lvovich Sobolev* (1908 – 1989): Soviet mathematician, working in mathematical analysis and partial differential equations. He introduced the notions that are now fundamental for several different areas of mathematics. [WIKIPEDIA]

(2.79), the weak formulation of the overall volume balance $(2.77)_1$ would yield to

$$\int_{\Omega} \operatorname{div}(\mathbf{u}_S)'_S \, \delta\mathcal{P} \, \mathrm{d}v - \int_{\Omega} n^F \mathbf{w}_F \cdot \operatorname{grad} \, \delta\mathcal{P} \, \mathrm{d}v = - \int_{\Gamma_N^v} \bar{v} \, \delta\mathcal{P} \, \mathrm{d}a \,. \tag{2.80}$$

□

Chapter 3:
Fracture Mechanics

The goal of the first part of this chapter is to give a brief introduction into the theoretical aspects of fracture. The second part focuses on the correlation of these fundamentals to a continuum fracture-mechanical framework. Note that the field of fracture mechanics is of course much broader than the fundamental basic aspects discussed herein. Anyway, all the fracture contexts applied later in this monograph base on the fundamentals that are presented in following first section. For the sake of simplicity, Section 3.1 restricts itself to linear elastic material behaviour for a single-phase solid body. Therein, the theory of strong discontinuities is initially discussed by considering 2-d examples. This results in foundations necessary for more general aspects in continuum fracture mechanics. For a circumstantial introduction into the topic of fracture mechanics, the interested reader is referred to *Hahn* [92] and *Groß & Selig* [88]. The following continuum fracture-mechanical framework also allows to discuss fracture mechanics compatible with the TPM. Section 3.2 is the basis of the subsequent discussion on the numerical methodology. For more details on continuum-mechanical aspects of fracture mechanics, the interested reader is referred to, e. g., *Simo et al.* [172], and *Oliver et al.* [150, 151].

3.1 Fundamental Fracture Mechanics

Within this section, material behaviour is limited to linear elasticity within a 2-d environment. Furthermore, the 2-d environment is simplified by regarding only plain strain assumptions. Consequently, all the examples regarded in this section are shells of unit thickness. In order to illustrate the fundamentals of fracture mechanics straightforward, only single-phase materials are considered in this section, i. e., the notation of quantities with a super- $(\cdot)^\alpha$ or subscript $(\cdot)_\alpha$, respectively, is redundant. Only with these limitations, it is possible to obtain analytical solutions for fracture-mechanical problems in closed form. The analysis of more complex circumstances is reliant to numerical methods, see Section 4.3. So, the reduced formula framework used in this section can be summarised as

$$\begin{aligned}
&\boldsymbol{\varepsilon} = \tfrac{1}{2}\left[\operatorname{grad}\mathbf{u} + (\operatorname{grad}\mathbf{u})^T\right] && : \text{small strain tensor}\,,\\
&\varepsilon_{33} = 0\,,\sigma_{33} \neq 0 && : \text{plane strain}\,,\\
&\boldsymbol{\sigma} = 2\mu\boldsymbol{\varepsilon} + \lambda(\boldsymbol{\varepsilon}\cdot\mathbf{I})\mathbf{I} && : \textit{Hooke}\text{an law (linear stress-strain relation)}\,.
\end{aligned} \tag{3.1}$$

In the literature, this methodology is referred to as Linear Elastic Fracture Mechanics (LEFM).

3.1.1 Stress Concentration

Stress concentrations occur inevitably in the presence of macroscopic cracks, defects or other material flaws. Here, these macroscopic defects are discussed as sharp geometrical openings or macroscopic notches, respectively. In order to prepare a plausible description of stress concentration in solids, one can visualise **stress trajectories** (lines of force). Consider an infinite rectangular shell subjected to an uniform tensile stress σ_2^0; at first materially homogeneous, and at second with a central elliptical void in it. The conjunctional visualisation of the stress trajectories shows the difference between the spacing of the lines, see Figure 3.1. The local decrease in the spacing between the lines indicates a local increase in stress as more lines of force are flowing through the same area. The elliptical

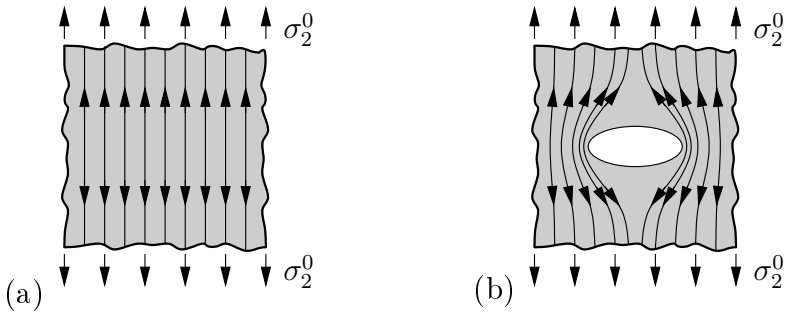

Figure 3.1: (a), (b) stress trajectories (lines of force).

void of the depicted shell in Figure 3.1(b) is now assumed to have the major axis $2s$ and the minor axis $2b$, see Figure 3.2(a). As far as the author of this monograph is aware, this problem was first treated in *Inglis* [108]. The following discussion is meant to outline the derivation of a formulation that is capable to describe such stress concentrations. For a circumstantial reflection on this topic the interested reader is referred to, e. g., *Hahn* [92], *Groß & Selig* [88], and *Gürses* [89]. *Inglis* used a specific curvilinear, elliptical coordinate

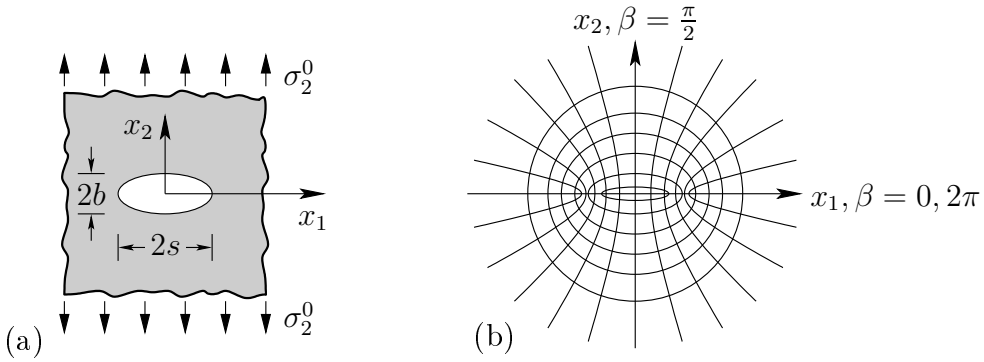

Figure 3.2: (a) infinite shell of unit thickness, (b) elliptical coordinate system.

system, see Figure 3.2(b), to transfer cartesian stress coefficients σ_{ij} $(i, j = \{1, 2\})$ into elliptical stress coefficients $\sigma_{\alpha\beta}$. Following relations hold between the cartesian and the

elliptical coordinate system:

$$x_1 = c\cosh\alpha\cos\beta \quad \text{and} \quad x_2 = c\sinh\alpha\sin\beta \quad \text{with} \quad c^2 = \frac{x_1^2}{\cosh^2\alpha} + \frac{x_2^2}{\sinh^2\alpha}\,. \tag{3.2}$$

The elliptical coordinate system represents an ellipse for each value of α. By an eligible choice of the constant c, it is possible to describe very sharp ellipses. These sharp, slit-like ellipses can be utilised to represent macroscopic notches. With this, the stress component $\sigma_{\beta\beta}$ at the surface of such a sharp elliptical void, where $\sigma_{\alpha\alpha} = 0$, can be obtained as

$$\sigma_{\beta\beta} = \sigma_2^0\,\frac{\sinh 2\alpha - 1 + e^{2\alpha}\cos 2\beta}{\cosh 2\alpha - \cos 2\beta}\,. \tag{3.3}$$

Note that this formula is the final result of the application of a series of special complex potentials suggested by *Inglis*. For $\beta = \{0, \pi\}$, $\sigma_{\beta\beta}$ gets maximal. As a geometric consequence, this stress component then equals the cartesian stress component in x_2 direction, i.e., $\sigma_{\beta\beta} = \sigma_{22}$. Regarding the relations $c^2 = s^2 - b^2$, $\sinh 2\alpha = 2\,\frac{sb}{c^2}$, $e^{2\alpha} = \cosh 2\alpha + \sinh 2\alpha$, and $\cosh 2\alpha = \frac{(s+b)^2}{c^2}$ from the transition of the coordinate system (3.2), the conclusion of the stress concentration at the tip $(x_1 = a, x_2 = 0)$ of the elliptical void reads

$$\sigma_{22}(x_1 = s, x_2 = 0) = \sigma_2^0\left(1 + 2\,\frac{s}{b}\right)\,. \tag{3.4}$$

One can see that the stress concentration becomes unbounded, i.e., $\sigma_{22} \to \infty$, for an elongation of the ellipse in x_2 direction $\frac{s}{b} \to \infty$. An alternative representation of (3.4), in terms of the radius of curvature[1] r' at the direct tip of the ellipse, yields

$$\sigma_{22}(x_1 = s, x_2 = 0) = \sigma_2^0\left(1 + 2\sqrt{\frac{s}{r'}}\right) \quad \text{with} \quad r'(x_1 = s, x_2 = 0) = \frac{b^2}{s}\,. \tag{3.5}$$

These last two representations of the stress concentration at the tip, (3.4) and (3.5), finally allow for sharp, slit-like ellipses $(\frac{s}{b} \gg 1)$ an approximation, viz.

$$\sigma_{22} \approx 2\,\sigma_2^0\,\frac{s}{b} \approx 2\,\sigma_2^0\sqrt{\frac{s}{r'}}\,. \tag{3.6}$$

The most important insight of (3.6) is the fact that, within the given context, the stress concentration depends on the shape of the void rather than on its size. Note that herein the character of the stress intensity factor relation can already be identified, see Section 3.1.2.

[1] For a 2-d curve, given parametrically in cartesian coordinates $x_2(\ell) = (x_1(\ell), x_2(\ell))$, the curvature is

$$r' = \frac{\left|\frac{\partial x_1}{\partial \ell}\frac{\partial^2 x_2}{\partial \ell^2} - \frac{\partial x_2}{\partial \ell}\frac{\partial^2 x_1}{\partial \ell^2}\right|}{\sqrt[3]{(\frac{\partial x_1}{\partial \ell})^2 + (\frac{\partial x_2}{\partial \ell})^2}}\,.$$

3.1.2 Singular Stress Fields

With the aim of an elastic analysis, a macroscopic crack is viewed as a plane separation located inside the material. The form of its two ends (crack tips) are regarded, in analogy to Section 3.1.1, as elliptical curves. *Irwin* [111] classified cracks according to the kinematically independent motions of the upper and lower surfaces of the crack relatively to each other, see Figure 3.3(a). At present, this classification is generally accepted and denoted as modes I, II, III. In Figure 3.3(a), the jump bracket $[\![u_i]\!]$ has been employed

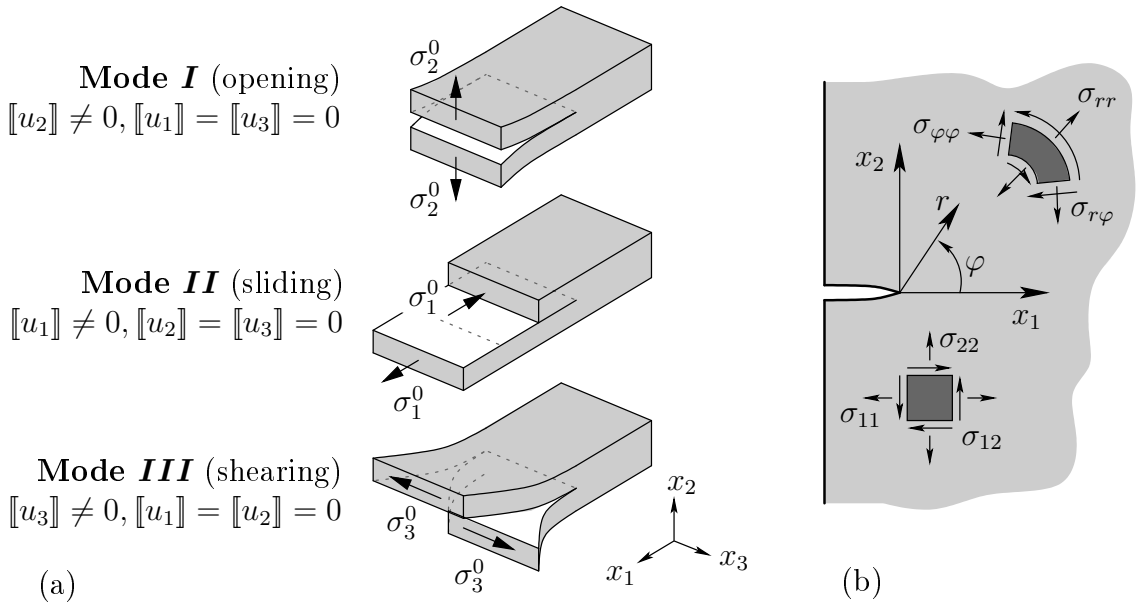

Figure 3.3: (a) displacement/crack modes, (b) polar coordinate system.

to denote the difference of the displacement components evaluated at both faces of the crack. This jump bracket notation will be continuously applied on all jump quantities that occur on this monograph, see (3.37). Each motion of the crack surfaces relatively to each other can be associated with corresponding stress and strain fields in the near vicinity of the edges. Stress and strain fields at the vicinity of edges of elliptical voids have been investigated early by *Westergaard* [191]. However, as far as the author of this monograph is aware, the general applicability of singular stress fields in the presence of cracks was first recognised by *Irwin* [110]; a nice complementary overview of his contribution to the field of fracture mechanics can be found in *Yarema* [195]. Continuing from the insight of (3.6), *Irwin* introduced the concept of **stress intensity factors**[2] (SIF). SIF are parameters that amplify the magnitude of the applied stress. Quantities assigned to the three crack modes are denoted by the corresponding sub- or superscript, respectively, I, II, and III. With respect to SIF, the stress fields around the vicinity of a crack tip are

[2]Initially, working on hot stretching of Polymethylmethacrylat (PMMA) led *Kies* [118], a collaborator of *Irwin*, to observe that the critical stress for a given crack size depended only on the PMMA fracture energy and on the PMMA elastic modulus, ergo, two material parameters. *Irwin* then, working on stress fields at the crack tip, introduced the stress intensity factor K which he named in honour of Kies, cf. *Cotterell* [39].

given as

$$\boldsymbol{\sigma}^{I}(r,\varphi) = \frac{K_I}{\sqrt{2\pi r}}\,\mathbf{f}^{I}(\varphi)\,, \quad \boldsymbol{\sigma}^{II}(r,\varphi) = \frac{K_{II}}{\sqrt{2\pi r}}\,\mathbf{f}^{II}(\varphi) \quad \text{and} \quad \boldsymbol{\sigma}^{III}(r,\varphi) = \frac{K_{III}}{\sqrt{2\pi r}}\,\mathbf{f}^{III}(\varphi)\,. \tag{3.7}$$

Therein, the stress field is expressed in terms of a polar coordinate system around the crack tip, see Figure 3.3(b). The dimension of K_i $(i = I, II, III)$ is that of the product of stress times the square root of length. The dimensionless functions $\mathbf{f}^i$ only depends on spatial coordinates. They determine the distribution of the stress field. Due to the restriction of this section to linear elasticity, the stress field of a general case of loading can be computed additively as $\boldsymbol{\sigma} = \boldsymbol{\sigma}^{I} + \boldsymbol{\sigma}^{II} + \boldsymbol{\sigma}^{III}$. The SIF do not only depend on the applied load but also on the problem geometry. They can be found as a result of the following limit transitions:

$$K_I = \sqrt{2\pi}\lim_{r\to 0}\sqrt{r}\,\sigma_2^0\,, \quad K_{II} = \sqrt{2\pi}\lim_{r\to 0}\sqrt{r}\,\sigma_1^0 \quad \text{and} \quad K_{III} = \sqrt{2\pi}\lim_{r\to 0}\sqrt{r}\,\sigma_3^0\,. \tag{3.8}$$

Numerous publications committed solutions of SIF, each solution depending on especially defined boundary conditions, e. g., *Rooke* [161], and *Wu* [194]. As an example, the SIF – in reference to Figure 3.2(a) – of an infinite shell with a sharp crack of length $2s$, subjected to remote tensile stress σ_2^0, see Figure 3.4(a), is given in (3.9). The corresponding stress field in polar coordinates for the given SIF follows in (3.10). As it is necessary for subsequent applications, the associated principle stress and displacement fields are given in (3.11) and (3.12), respectively. In the latter, κ represents a material parameter which is for plain strain problems $\kappa = 3 - 4\,\nu$. It is a common challenge to compute SIF numerically for arbitrary boundary conditions. This problem will be addressed in Section 4.3.

3.1.3 Energetic Approach to Fracture Mechanics

Alternatively to the previously discussed stress concentrations and the therefrom originated singular stress fields, one can also apply an energetic approach to address singular problems in fracture mechanics. In this context, the ***Griffith***[3] **theory** has proven its general applicability for elastic[4] brittle materials. *Griffith*'s theory is in general acknowledged as the origin of continuum fracture mechanics. The theory is based on a variation of energy during crack propagation. *Griffith* [86] stated that solids have a surface energy which must be compensated for a given crack to propagate. Furthermore, the surface energy of a solid is stated to exhibit a potential characteristic, analogue to, e. g., the surface

[3] *Alan Arnold Griffith* (1893–1963): English engineer who is best known for his work on stress and fracture in metals that is now known as metal fatigue. He was also one of the first to develop, in 1926, a strong theoretical basis for the jet engine. [WIKIPEDIA]

[4] Note in passing that *Griffith*'s theory, see $(3.20)_3$ and (3.21), has also been extended to account for limited plastic material behaviour encountered around the crack tip, viz. $G = 2(\gamma + \gamma_p)$. Therein, γ_p represents the plastic dissipation per unit area of surface created. This extension has been independently proposed by *Irwin* [109] and *Orowan* [152] at about the same time, cf. *Gürses* [89].

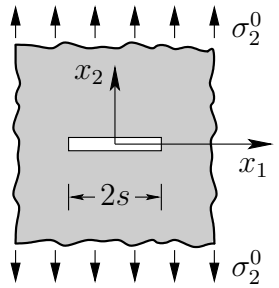

(a)

$$K_I = \sigma_2^0 \sqrt{\pi s} \tag{3.9}$$

$$\left\{ \begin{array}{c} \sigma_{rr} \\ \sigma_{\varphi\varphi} \\ \sigma_{r\varphi} \end{array} \right\} = \frac{K_I}{\sqrt{2\pi r}} \left\{ \begin{array}{c} \cos\frac{\varphi}{2}\left(1+\sin^2\frac{\varphi}{2}\right) \\ \cos^3\frac{\varphi}{2} \\ \sin\frac{\varphi}{2}\cos^2\frac{\varphi}{2} \end{array} \right\} \tag{3.10}$$

$$\left\{ \begin{array}{c} \sigma_1 \\ \sigma_2 \end{array} \right\} = \frac{K_I}{\sqrt{2\pi r}} \cos\frac{\varphi}{2} \left\{ \begin{array}{c} 1+\sin\frac{\varphi}{2} \\ 1-\sin\frac{\varphi}{2} \end{array} \right\} \tag{3.11}$$

$$\left\{ \begin{array}{c} u_1 \\ u_2 \end{array} \right\} = \frac{K_I}{2\mu} \sqrt{\frac{r}{2\pi}} \left\{ \begin{array}{c} \cos\frac{\varphi}{2}\left[\kappa - 1 + 2\sin^2\left(\frac{\varphi}{2}\right)\right] \\ \sin\frac{\varphi}{2}\left[\kappa + 1 - 2\cos^2\left(\frac{\varphi}{2}\right)\right] \end{array} \right\} \tag{3.12}$$

(b)

Figure 3.4: (a) infinite shell with a sharp crack of length $2s$ subjected to remote stress σ_2^0 and (b) the corresponding SIF, stress fields, principal stress fields and displacement fields.

tension of fluids. Therefore, the first law of thermodynamics (here, conservation of only mechanical energy) is extended by a crack surface energy contribution U_Γ as

$$\mathsf{U} = \underbrace{\mathsf{U}_{int} + \mathsf{U}_{ext}}_{\mathsf{U}_{pot}} + \mathsf{U}_\Gamma \quad \text{with} \quad \left\{ \begin{array}{lcl} \mathsf{U} & : & \text{total system energy}, \\ \mathsf{U}_{int} & : & \text{total elastic strain energy (internal)}, \\ \mathsf{U}_{ext} & : & \text{external load energy potential}, \\ \mathsf{U}_\Gamma & : & \text{surface energy of crack propagation}, \\ \mathsf{U}_{pot} & : & \text{total potential energy of the system}. \end{array} \right. \tag{3.13}$$

Therein, the basic idea is that during crack propagation elastic strain energy is "unleashed" and the solid surface energy increases. The latter energy increase results from the surface energy of additional crack surfaces. As a consequence, the total potential energy U_{pot} of a cracked solid is always less than that of an uncracked solid. The energy approach can be presented best by recalling the foregoing example of an infinite shell of unit thickness, see Figure 3.4(a). Therefore, the derivation of the total system energy (3.13) with respect to the crack propagation length $\mathrm{d}s$ is proposed[5] as

$$\frac{\mathrm{d}\mathsf{U}}{\mathrm{d}s} = \frac{\mathrm{d}\mathsf{U}_{int}}{\mathrm{d}s} + \frac{\mathrm{d}\mathsf{U}_{ext}}{\mathrm{d}s} + \frac{\mathrm{d}\mathsf{U}_\Gamma}{\mathrm{d}s} = 0\,. \tag{3.14}$$

[5] Actually, *Griffith* examined energetic instability criteria of crack growth, i. e., he considered $\frac{\mathrm{d}\mathsf{U}}{\mathrm{d}s} \leq 0$. However, for the following discussion on continuum fracture mechanics, the consideration of only the critical condition $\frac{\mathrm{d}\mathsf{U}}{\mathrm{d}s} = 0$ is sufficient.

Griffith [87] used the stress analysis that was developed by *Inglis* [108], recall Section 3.1.1, to show that the change of the strain energy due to a sharp crack is for the given example

$$\triangle \mathsf{U}_{int}(s) = \frac{\pi(\sigma_2^0\, s)^2}{E'} \quad \text{with} \quad E' = \frac{E}{1-\nu^2} \quad \text{(plane strain)}\,. \tag{3.15}$$

For (3.15), E and ν denote well-known material parameters, *Young*'s[6] modulus and *Poisson*'s[7] ratio. The total elastic strain energy U_{int} is the sum of the initial strain energy of the uncracked shell U_{int}^0, and the change of the strain energy $\triangle \mathsf{U}_{int}$, viz. $\mathsf{U}_{int}(s) = \mathsf{U}_{int}^0 + \triangle \mathsf{U}_{int}(s)$. Note that the initial strain energy of the uncracked shell is obviously independent of the crack length $2s$. For linear elastic materials, it is possible to express the work done by the external load as

$$\mathsf{U}_{ext}(s) = -2\mathsf{U}_{int}(s)\,. \tag{3.16}$$

This relation is based on *Clapeyron*'s[8] theorem, cf. *Fosdick & Truskinovsky* [75]. The elastic surface area U_Γ can be obtained by the introduction of the surface energy per unit area γ, viz.

$$\mathsf{U}_\Gamma(s) = 2(2s\gamma)\,. \tag{3.17}$$

Note that γ is a measurable material parameter, representing the surface energy per unit area. The factor 2 in (3.17) comes from the two faces of the crack. Consequently, the total system energy reads

$$\mathsf{U}(s) = -\mathsf{U}_{int}^0 - \triangle \mathsf{U}_{int}(s) + 4s\gamma \quad \rightsquigarrow \quad \frac{\mathrm{d}\mathsf{U}}{\mathrm{d}s} = -\frac{2\pi(\sigma_2^0)^2 s}{E'} + 4\gamma = 0\,. \tag{3.18}$$

With this, a critical value for the remote tensile stress σ_2^{crit}, or for the half flaw size s^{crit} (note that the total critical crack length is $2s^{crit}$), respectively, can be defined for which the crack propagates:

$$\sigma_2^{crit} = \sqrt{\frac{2E'\gamma}{\pi s}} \quad \text{or} \quad s^{crit} = \frac{2E'\gamma}{\pi(\sigma_2^0)^2}\,. \tag{3.19}$$

These results are of significant importance: critical values can now be determined experimentally because they only depend on material parameters. This leads to a new argument

[6] *Thomas Young* (1773–1829): English polymath who made notable contributions to the fields of vision, light, solid mechanics, energy, physiology, language, musical harmony and Egyptology. In *Young*'s own judgement, his most important achievement was to establish the wave theory of light. [WIKIPEDIA]

[7] *Siméon Denis Poisson* (1781–1840): French mathematician, geometer, and physicist. Several mathematical concepts are named after him, e. g., the well-known "*Poisson* equation". He published over 300 scientific contributions. [WIKIPEDIA]

[8] *Benoît Paul Émile Clapeyron* (1799–1864): French engineer and physicist, one of the founders of thermodynamics. He further developed the idea of a reversible process and made substantive extensions of *Rudolf Julius Emanuel Clausius*' work, known as the *Clausius-Clapeyron* relation. In civil engineering and structural analysis, *Clapeyron*'s theorem of three moments is very well known. [WIKIPEDIA]

that crack propagation can occur when the energy supplied to the solid exceeds a critical value. This is a crucial advantage over the approach of crack propagation for critical stress values related to single points, because, in a mathematical sense, singular stress fields at the tip of a sharp crack always occur, no matter how small the applied external stress is. Hence, it is possible to say that the SIF are local parameters while the energy release rate describes a global relation.

In 1957, *Irwin* [110] reformulated the energetic approach of the *Griffith* theory into a more suitable form for engineering applications. Recalling (3.13), (3.14), and (3.18), the difference of the total system energy between the state of a fixed crack (length $2s$) and the state of an elongated (on both ends by $\mathrm{d}s$) crack yields

$$\begin{aligned} \big[\mathsf{U}_{int}(2s) + \mathsf{U}_{ext}(2s)\big] - \big[\mathsf{U}_{int}(2s + 2\mathrm{d}s) + \mathsf{U}_{ext}(2a + 2\mathrm{d}s)\big] &= 4\gamma \mathrm{d}s\,, \\ -\big[\,\frac{\mathrm{d}\mathsf{U}_{int} + \mathrm{d}\mathsf{U}_{ext}}{\mathrm{d}s}\,\big] &= 4\gamma\,, \\ -\frac{2\pi(\sigma_2^0)^2 s}{E'} &= 4\gamma\,. \end{aligned} \tag{3.20}$$

The left hand side of (3.20) is designated to yield to the **energy release rate**. It represents the elastic energy per unit crack surface area that is available for infinitesimal crack propagation. The right hand side of (3.20) represents the material resistance to crack propagation. The original definition[9] of the energy release rate reads

$$G := -\tfrac{1}{2}\big[\,\frac{\mathrm{d}\mathsf{U}_{int} + \mathrm{d}\mathsf{U}_{ext}}{\mathrm{d}s}\,\big] = \frac{\pi(\sigma_2^0)^2 s}{E'}\,. \tag{3.21}$$

The factor $\frac{1}{2}$ in (3.21) arises from the symmetry of the particular example, see Figure 3.4(a), where the crack extension takes place at both ends of the crack. With (3.21)

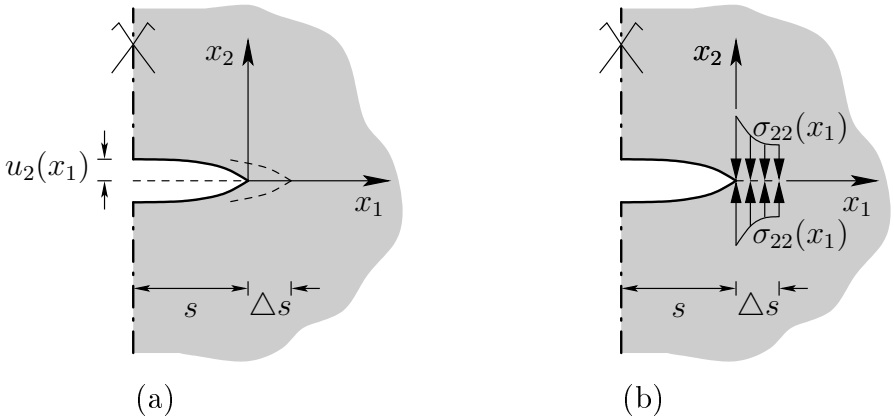

Figure 3.5: Crack closure problem: (a) virtual crack propagation $\mathrm{d}s$, (b) virtual traction forces.

[9] Note in passing that *Irwin* used the term "crack extension force" in analogy to a force on a dislocation and chosed the letter $\mathcal{G}$ in honour of *Griffith*; nowadays a Roman letter G is acceptable, cf. *Cotterell* [39].

it is possible to show that the energetic approach to fracture mechanics is essentially equivalent to the approach with singular stress field parameters (SIF) for linear elastic material behaviour. This relation will be derived regarding a pure Mode I example, again, analogue to the foregoing example depicted in Figure 3.4(a). Although the relation will be derived with respect to a specific example, it is a general relationship that applies also to other configurations. In the given example, virtual traction forces $\sigma_{22} = \sigma_{22}(x_1)$ are applied to a small virtual crack extension $\triangle s$ in x_1-direction such that the crack $u_2 = u_2(x_1)$ is closed in that region, see Figure 3.5. The corresponding[10] work $\triangle W$ of the crack closure problem in the near distance of the crack tip reads

$$\triangle W = \int_0^{\triangle s} \sigma_{22}\, u_2 \,\mathrm{d}x_1 \quad \rightsquigarrow \quad \underbrace{\lim_{\triangle s \to 0} \left(\frac{\triangle W}{\triangle s}\right)}_{= G} = \lim_{\triangle s \to 0} \Big[\frac{1}{\triangle s} \int_0^{\triangle s} \sigma_{22}\, u_2 \,\mathrm{d}x_1\Big] \,. \tag{3.22}$$

Therein, *Irwin*'s[11] crack closure integral $(3.22)_2$ relates the global energy release rate G to the local crack tip stress and displacement fields for a small crack extension $\triangle s$, cf. *Irwin* [110]. This is directly related to (3.21). The displacement u_2 and the stress function σ_{22} for the crack closure problem (3.22) follow from (3.11) and (3.12), respectively, by setting φ and r according to Figure 3.5:

$$\begin{aligned} u_2(r = \triangle s - x_1, \varphi = \pi) &= \frac{\kappa + 1}{2\mu} K_I(s + \triangle s) \sqrt{\frac{\triangle s - x_1}{2\pi}} \,, \\ \sigma_{22}(r = x_1, \varphi = 0) &= \frac{K_I(s)}{\sqrt{2\pi x_1}} \,. \end{aligned} \tag{3.23}$$

In $(3.23)_1$, $K_I(s + \triangle s)$ represents the SIF of the original crack tip with the crack length $s + \triangle s$ before the closing, whereas in $(3.23)_2$, $K_I(s)$ represents the SIF after the closing. Insertion of (3.23) in $(3.22)_2$ yields to the **equivalence of the energy release rate and SIF**, viz.

$$\begin{aligned} G_I &= \frac{\kappa + 1}{4\,\mu\,\pi} K_I^2 \lim_{\triangle s \to 0} \Big[\frac{1}{\triangle s} \overbrace{\int_0^{\triangle s} \sqrt{\frac{\triangle s - x_1}{x_1}} \,\mathrm{d}x_1}^{= \triangle s \, \frac{\pi}{2}} \Big] \,, \\ \rightsquigarrow \quad G_I &= \frac{\kappa + 1}{8\mu} K_I^2 = \frac{K_I^2}{E'} \quad (\text{Mode } I) \,. \end{aligned} \tag{3.24}$$

[10] It is crucial to note that here only one side of the crack extension is included into the work integral. Other contributions may include both sides of the crack extension into the work integral but then have to add the factor $\frac{1}{2}$, corresponding to the original definition of the energy release rate (3.21).

[11] *George Rankin Irwin* (1907–1998): American scientist in the field of fracture mechanics and strength of materials. He defined the fundamental concept of a stress intensity factor and the critical stress intensity factor which is a material property. [WIKIPEDIA]

The subscript $(\cdot)_I$ of the energy release rate denotes its Mode I relation. The equivalence of the energy release rate and the SIF for Mode II and Mode III cracks follows analogously to the preceding derivation, viz.

$$G_{II} = \frac{K_{II}^2}{E'} \quad (\text{Mode } II) \quad \text{and} \quad G_{III} = \frac{K_{III}^2}{2\mu} \quad (\text{Mode } III)\,. \tag{3.25}$$

For a general mixed mode crack extension, the energy release rates of the corresponding modes can be superposed, yielding

$$G = \frac{K_I^2}{E'} + \frac{K_{II}^2}{E'} + \frac{K_{III}^2}{2\mu}\,. \tag{3.26}$$

3.1.4 J-integral

Until know, only elastic material behaviour has been considered. Obviously, this does not represent real material behaviour. Therefore, especially with focus on the development of a continuum fracture-mechanical framework, inelastic material behaviour needs to be considered. A further step towards the development of such a framework is the introduction of the *Rice* integral, also well known as the ***J*-integral**, cf. *Rice* [159]. Initially, the concept of the J-integral has been already introduced in 1951 by *Eshelby* [72] before it was applied to 2-d notch problems by *Rice*. The J-integral exhibits the advantage of its applicability to inelastic fracture mechanics. With it, the validity of the previously introduced SIF and the energy release rate can be extended towards materials with moderate inelastic process zones. A crucial attribute of the J-integral is that it is in general path independent. It will be introduced while considering a linear elastic homogeneous solid body $\mathcal{B}$, see Figure 3.6. Note that here, in contrast to the other sections in this fundamental fracture mechanics chapter, a 3-d setting will be used. The difference between a 2-d and a 3-d setting is for this particular discussion negligible. However, the later following application of the J-integral will benefit from the setting chosen here.

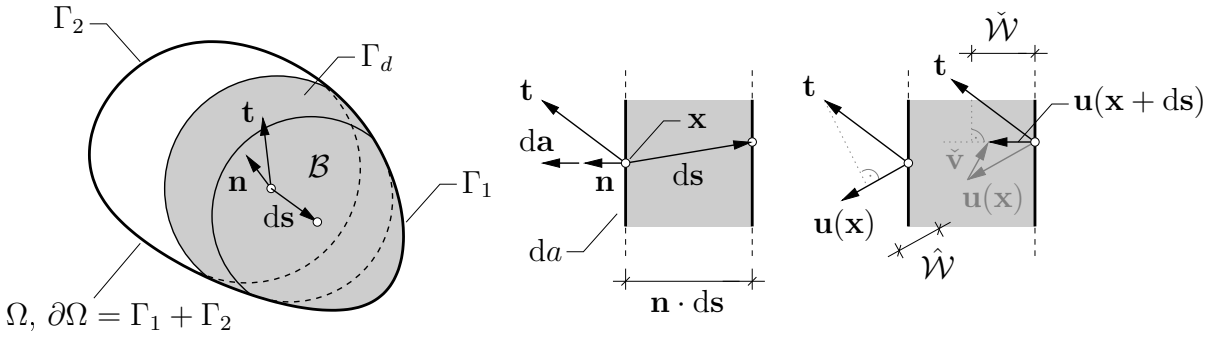

Figure 3.6: Shift of boundary surface by withdrawing of material.

Let the body $\mathcal{B}$ partially occupy the domain Ω. The surface $\partial\Omega$ of the domain consists of two parts, Γ_1 and Γ_2. The body itself ends inside the domain at the discontinuity surface

$\Gamma_d(\mathbf{n})$; the corresponding surface normal vector is represented by $\mathbf{n}$. Consequently, there is no material inside the opposing part of the domain. Furthermore, let the surface tension vector $\mathbf{t} = \boldsymbol{\sigma}\,\mathbf{n}$ act on the surface Γ_d. By applying a shift (constant translation) $\mathrm{d}\mathbf{s}$ of the surface Γ_d, the system energy changes by $\mathrm{d}\mathsf{U}$. The shift is considered as a "withdrawing" or "adding", respectively, of material. As a result, the system energy change consists of the strain (internal) energy density $\mathcal{W}(\boldsymbol{\sigma}, \boldsymbol{\varepsilon})$, stored in the strip $\mathrm{d}\mathbf{s}$, and the external load energy $\mathrm{d}\mathsf{U}_{ext}$, viz.

$$
\begin{aligned}
\mathrm{d}\mathsf{U}_{int} &= \int_{\Gamma_d} (\mathcal{W}\,\mathbf{n}\cdot\mathrm{d}\mathbf{s})\,\mathrm{d}a \qquad \text{with} \quad \mathcal{W} = \int_0^{\boldsymbol{\varepsilon}} \boldsymbol{\sigma}\cdot\mathrm{d}\boldsymbol{\varepsilon} = \frac{1}{2}\,\boldsymbol{\sigma}\cdot\boldsymbol{\varepsilon}\,, \\
\mathrm{d}\mathsf{U}_{ext} &= -\int_{\Gamma_d} \big[\,\check{\mathcal{W}} - \hat{\mathcal{W}}\,\big]\,\mathrm{d}a \qquad \text{with} \quad \begin{cases} \check{\mathcal{W}} = \mathbf{t}\cdot\mathbf{u}(\mathbf{x}+\mathrm{d}\mathbf{s})\,, \\ \qquad\;\; = \mathbf{t}\cdot\big[\mathbf{u}(\mathbf{x}) + \underbrace{\mathbf{H}\,\mathrm{d}\mathbf{s}}_{=:\,\check{\mathbf{v}}}\big]\,, \\ \mathbf{H} = \operatorname{grad}\mathbf{u}(\mathbf{x})\,, \\ \hat{\mathcal{W}} = \mathbf{t}\cdot\mathbf{u}(\mathbf{x})\,, \end{cases} \\
&= -\int_{\Gamma_d} (\mathbf{H}^T\boldsymbol{\sigma}\,\mathbf{n}\cdot\mathrm{d}\mathbf{s})\,\mathrm{d}a\,, \\
&\rightsquigarrow \mathrm{d}\mathsf{U} = \mathrm{d}\mathsf{U}_{int} + \mathrm{d}\mathsf{U}_{ext} = \int_{\Gamma_d} \big[\,\underbrace{(\mathcal{W}\,\mathbf{I} - \mathbf{H}^T\boldsymbol{\sigma})}_{=:\,\boldsymbol{\mathcal{E}}}\,\mathbf{n}\cdot\mathrm{d}\mathbf{s}\big]\,\mathrm{d}a\,. \qquad (3.27)
\end{aligned}
$$

This derivation of the – based on a material shift – system energy change reveals the direct relation to the *Eshelby*[12] stress tensor $\boldsymbol{\mathcal{E}}$. The *Eshelby* stress tensor is a crucial quantity within the theory of configurational (material) forces. *Eshelby* [72] proposed the concept of configurational forces in 1951, which correlates with the concept of the J-integral. Configurational forces represent forces that act on imperfections or singularities, respectively. The basis of the theory of configurational forces is the evaluation of the balance equation $\operatorname{div}\boldsymbol{\mathcal{E}} + \mathbf{f} = \mathbf{0}$; see Section B.3 for a detailed derivation of this balance equation. Based on this, the surface integral in (3.27) can be rewritten into a volume integral, thus yielding to

$$
\int_{\Gamma_D} (\boldsymbol{\mathcal{E}}\,\mathbf{n}\cdot\mathrm{d}\mathbf{s})\,\mathrm{d}a = \Big(\int_{\Gamma_D} \boldsymbol{\mathcal{E}}\,\mathrm{d}\mathbf{a}\Big)\cdot\mathrm{d}\mathbf{s} \rightsquigarrow \int_{\Omega^*} \operatorname{div}\boldsymbol{\mathcal{E}}\,\mathrm{d}v \quad \text{with} \quad \partial\Omega^* : \text{closed surface}\,. \qquad (3.28)
$$

Note in passing that this only holds if $\boldsymbol{\mathcal{E}} = \boldsymbol{\mathcal{E}}^T$. It can be shown that the divergence of $\boldsymbol{\mathcal{E}}$ vanishes independently of the domain Ω^*, under the assumptions of a homogeneous (no

[12] *John Douglas Eshelby* (1916–1981): English physicist who gained most of his knowledge through self-study. His work on defect mechanics and micromechanics of inhomogeneous solids has provided the basis of the theory of configurational (material) forces. He had a broad scientific interest with an encyclopædic general knowledge, inter alia, through his passionate interest in secondhand books. [*Bilby* [11]]

singularities, nor discontinuities), elastic material with the strain energy density ($\mathcal{W} = \mathcal{W}(\boldsymbol{\varepsilon})$) and the absence of body forces ($\operatorname{div}\boldsymbol{\sigma} = \mathbf{0}$), viz.

$$\begin{aligned}
\operatorname{div}\boldsymbol{\mathcal{E}} &= \operatorname{div}\left[\mathcal{W}\,\mathbf{I} - \mathbf{H}^T\boldsymbol{\sigma}\right] = \nabla(\tfrac{1}{2}\,\boldsymbol{\sigma}\cdot\boldsymbol{\varepsilon}) - \operatorname{div}(\mathbf{H}^T\boldsymbol{\sigma}) \quad \text{with} \quad \nabla(\,\cdot\,) = \operatorname{grad}(\,\cdot\,)\,, \\
&= \underbrace{(\nabla\tfrac{1}{2}\,\boldsymbol{\sigma})^{\overset{13}{T}}}_{=\,\mathbf{0}}\boldsymbol{\varepsilon}^T + (\nabla\boldsymbol{\varepsilon})^{\overset{13}{T}}(\tfrac{1}{2}\,\boldsymbol{\sigma}^T) - \big[(\nabla\mathbf{H}^T)\,\boldsymbol{\sigma} + \mathbf{H}^T\,\underbrace{\operatorname{div}\boldsymbol{\sigma}}_{=\,\mathbf{0}}\big]\,, \\
&\quad \text{with } \boldsymbol{\sigma} = \boldsymbol{\sigma}^T\,, \text{ and } \nabla\boldsymbol{\varepsilon} = (\nabla\boldsymbol{\varepsilon})^{\overset{23}{T}}\,, \text{ follows } (\nabla\boldsymbol{\varepsilon})^{\overset{13}{T}}(\tfrac{1}{2}\,\boldsymbol{\sigma}^T) = (\nabla\mathbf{H}^T)\,\boldsymbol{\sigma}\,, \\
&= \mathbf{0}
\end{aligned} \tag{3.29}$$

For an index-based notation of the derivation (3.29), the interested reader is referred to *Eriksson* [71], and *Huber et al.* [107]. Consequently, the integral $(3.28)_3$ is domain independent. This property allows the construction of other forms of domain or path independent integrals by using transformations of (3.29). Let $\int_{\Omega^*}(\,\cdot\,)\,\mathrm{d}v = \int_{\Gamma_1}(\,\cdot\,)\mathrm{d}\mathbf{a} + \int_{\Gamma_D}(\,\cdot\,)\mathrm{d}\mathbf{a}$ be the integral over the closed surface of the body $\mathcal{B}$. Because the integral of the *Eshelby* stress tensor vanishes, the identity $\int_{\Gamma_1}(\,\cdot\,)\mathrm{d}\mathbf{a} = -\int_{\Gamma_D}(\,\cdot\,)\mathrm{d}\mathbf{a}$ holds. Further, let $\int_{\partial\Omega}(\,\cdot\,)\,\mathrm{d}v = \int_{\Gamma_1}(\,\cdot\,)\mathrm{d}\mathbf{a} + \int_{\Gamma_2}(\,\cdot\,)\mathrm{d}\mathbf{a}$ be the integral over the overall domain Ω. Because the surface Γ_2 surrounds a void, the previous insights yield to the formal introduction of the J-integral in a vectorial notation, namely $\mathbf{j}$, viz.

$$\mathrm{d}\mathsf{U} = \int_{\Gamma_D}\boldsymbol{\mathcal{E}}\,\mathrm{d}\mathbf{a}\cdot\mathrm{d}\mathbf{s} = -\int_{\partial\Omega}\boldsymbol{\mathcal{E}}\,\mathrm{d}\mathbf{a}\cdot\mathrm{d}\mathbf{s} = -\mathbf{j}\cdot\mathrm{d}\mathbf{s} \quad \text{with} \quad \mathbf{j} := \int_{\partial\Omega}\boldsymbol{\mathcal{E}}\,\mathrm{d}\mathbf{a}\,. \tag{3.30}$$

In order to transfer the vectorial notation of the J-integral into the previously used 2-d example framework, the surface Γ_2 is considered as to be "fold up" around a notch, see Figure 3.7. Let the shift $\mathrm{d}\mathbf{s}$ only take place in $\mathbf{e}_1$-direction. Thus, the J-integral vector can be reduced to:

$$\begin{aligned}
J = \int_{\partial\Omega}\boldsymbol{\mathcal{E}}\,\mathrm{d}\mathbf{a}\cdot\mathbf{e}_1\,, &= \int_{\mathcal{C}}\left[\mathcal{W}\,\mathbf{n}\cdot\mathbf{e}_1 - \mathbf{H}^T\boldsymbol{\sigma}\,\mathbf{n}\cdot\mathbf{e}_1\right]\mathrm{d}c\,, \\
&= \int_{\mathcal{C}}\left[\mathcal{W}\,n_1 - \frac{\partial\mathbf{u}}{\partial x_1}\cdot\mathbf{t}\right]\mathrm{d}c\,.
\end{aligned} \tag{3.31}$$

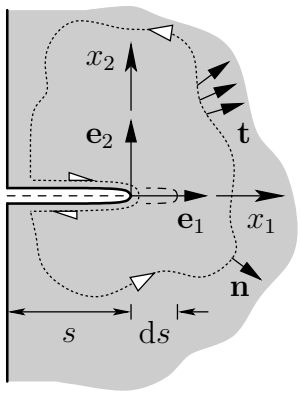

Figure 3.7: J-integral path.

Note in passing that this is also the original definition of the J-integral by *Rice* [159]. Therein, the surface integration over $\partial\Omega$ corresponds, for a 2-d setting, to a line integral

$\int_c (\,\cdot\,)\mathrm{d}c$. The orientation of the line integral is counterclockwise. With (3.31), the relation of the J-integral to the preceding energy release (3.21) rate becomes obvious, viz.

$$-\frac{\mathrm{d}\mathsf{U}}{\mathrm{d}s} = \int_{\mathcal{C}} \left[\mathcal{W}\, n_1 - \frac{\partial u_i}{\partial x_1}\,\sigma_{i\ell} n_\ell\right] \mathrm{d}c \quad \text{with} \quad \mathrm{d}s = \mathrm{d}\mathbf{s}\cdot\mathbf{e}_1 \quad \rightsquigarrow J = G_{(I)} = \frac{K_I^2}{E'} \quad (\text{Mode } I)\,. \tag{3.32}$$

It is also possible to apply the concept of the J-integral to mixed mode cracks, e. g., $J = \frac{1}{E'}(K_I^2 + K_{II}^2) + \frac{1}{2\mu}K_{III}^2$. Furthermore, it is of practical significance that this approach can be also applied to elastic-plastic crack problems. This is possible due to the aforementioned integration path independency of (3.31), cf. *Rice* [159].

3.1.5 Cohesive Fracture Theory

In Section 3.1.1, the discussion on sharp openings in linear elastic materials revealed stress singularities near the tip ($r \to 0 \rightsquigarrow \sigma \to \infty$). This of course does not represent real material behaviour. Instead, even elastic materials exhibit inelastic, even though small, process zones in the near vicinity of sharp openings. These zones limit the stress response and prevent it from being infinite. Only on this basis of finite stresses, the differential equations of equilibrium and boundary conditions postulated in Section 2.5 can be satisfied. In the framework of the LEFM, the size of the inelastic zone in front of an opening is assumed to be small compared to the sizes of both, the length of the opening $2s$, and the K-dominant region r_K. These preliminaries are referred to as **small scale yielding**. Note that because the material is assumed to be elastic, except in the small inelastic region around the fracture tip, the propagation of the opening can still be treated as non-ductile fracture. A first approximation for the estimation of the size of the process zone goes back to *Irwin* [111]. His approximation is based on the substitution of a pure elastic stress distribution by an elasto-plastic stress distribution, see Figure 3.8(a). For the computation of the pure elastic stress distribution recall (3.11). The elasto-plastic stress distribution is assumed to be constant inside the plastic zone. Its elastic remain is given by a shift of the pure elastic stress distribution with ℓ_a. The length $r_p^{\mathcal{I}}$ of the plastic zone follows the constraint that both resulting forces must be identical inside the plastic zone, viz.

$$\int_0^{\ell_a+\ell_b} \frac{K_I}{\sqrt{2\pi r}}\,\mathrm{d}r = \sigma_2^y \underbrace{(\ell_a + \ell_b)}_{2r_p^{\mathcal{I}}} \quad \rightsquigarrow \quad 2r_p^{\mathcal{I}} = \frac{1}{\pi}\left(\frac{K_I}{\sigma_2^y}\right)^2. \tag{3.33}$$

Note that the length of the plastic zone is denoted as $2r_p^{\mathcal{I}}$; this is a common notation. This follows the assumption of a circular plastic zone around the crack tip, see *Wells* [188]. The estimation of the **shape of the plastic process zone** is in general non-trivial. For a rough impression of the shape of the plastic process zone it is possible to visualise the contour of the area for which the elastic stress distribution field satisfies a yield function. Inserting the principle stress field (3.11) into the circular *von Mises* yield function, see

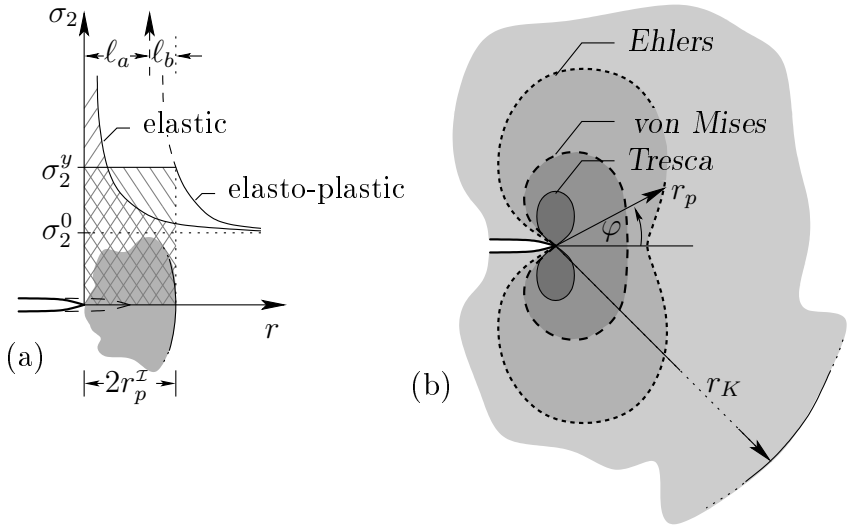

Figure 3.8: (a) elastic and elasto-plastic stress distribution after *Irwin*, (b) shapes of plastic zones (contour of the area for which the elastic stress-distribution field satisfies the corresponding yield function).

(B.10), yields to the contour function of the plastic zone by

$$r_p = \frac{K_I^2}{2\pi\sigma_2^y}\cos^2\frac{\varphi}{2}\left(3\sin^2\frac{\varphi}{2}+1\right). \tag{3.34}$$

The material character in this zone is assumed to be ideally plastic. In order to visualise a qualitative comparison, the two plastic zones of the yield functions of *Tresca*[13] , see (3.35), and of *Ehlers*, see (B.16), are added to Figure 3.8(b). Recall, this visualisation of the plastic zones is limited to the framework of small scale yielding.

For increasing plastic zones the LEFM cannot be applied any more. Instead, alternative approaches need to be specified to take the plastic material behaviour into account. In slim shells of ductile materials, tongue-like plastic zones in front of crack tips can be observed, see Figure 3.9(a). On this basis, *Dugdale*[14] [49] proposed an elastic-plastic model, known as the **yield strip model**. Therein, ideal elasto-plastic material behaviour is assumed to concentrate in a line in front of the crack. The physical crack length s_0 is then virtually

[13] *Henri Édouard Tresca* (1814–1885): French engineer who is probably best known for the *Tresca* criterion of material failure which, in terms of the deviatoric principal stresses $\sigma^D_{\{1,2,3\}}$, reads

$$F = [(\sigma_1^D-\sigma_2^D)^2-4\kappa^2]\,[(\sigma_2^D-\sigma_3^D)^2-4\kappa^2]\,[(\sigma_3^D-\sigma_1^D)^2-4\kappa^2] = 0\,. \tag{3.35}$$

His reputation as an engineer was so good that *Gustave Eiffel* put his name on number 3 in his list of 72 people making the Eiffel tower in Paris possible. *Tresca* was also involved in the design process of the standard metre etalon. [WIKIPEDIA]

[14] *Donald Stephen Dugdale* (1930–2005): Professor of the Department of Mechanical and Process Engineering (University of Sheffield, U. K.) who dedicated his scientific field of work to fracture mechanics.

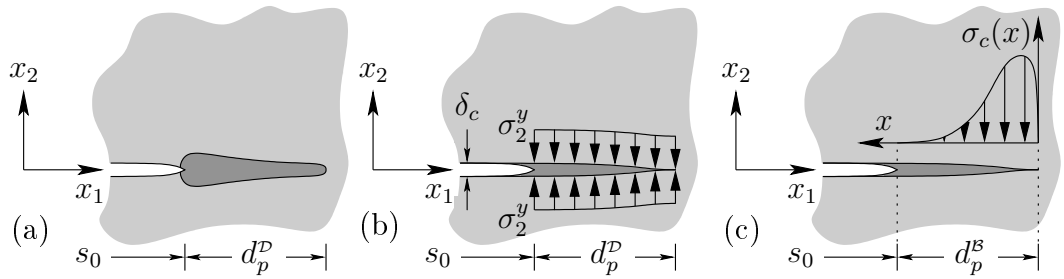

Figure 3.9: (a) tongue-like plastic zone in front of a crack tip, (b) elastic-plastic model after *Dugdale*, (c) non-linear cohesive stress function after *Barenblatt*.

extended on this line by $d_p^{\mathcal{D}} = 2r_p^{\mathcal{D}}$, resulting in a new crack length $s = s_0 + 2r_p^{\mathcal{D}}$. On both sides of this virtual extension of the crack surface, the yield stress σ_2^y is applied, see Figure 3.9(b). The solution for this method can be found by a superposition of two elastic sub-problems, see Figure 3.10. Consequently, the stress singularity and the SIF vanish at the crack tip of the virtual extension, i. e., the end of the plastic zone. With this, the LEFM regains its validity for each of the elastic sub-problems and the former discussed SIF can be applied again. The length of the plastic zone can be found as

$$2r_p^{\mathcal{D}} = \frac{\pi}{8}\left(\frac{K_I}{\sigma_2^y}\right)^2 . \tag{3.36}$$

The separation of the upper and lower side of the virtually extended crack line is denoted as $\delta_c = \delta_c(x_1)$, with $\delta_c(x_1 = s) = 0$, see Figure 3.9(b). It is a measure of the state of deformation and a common fracture parameter for the crack tip $\delta_c(x_1 = s_0) = \delta_c^{\text{crit}}$. It has been proposed as the **crack tip opening displacement** (CTOD) parameter by *Wells* [188].

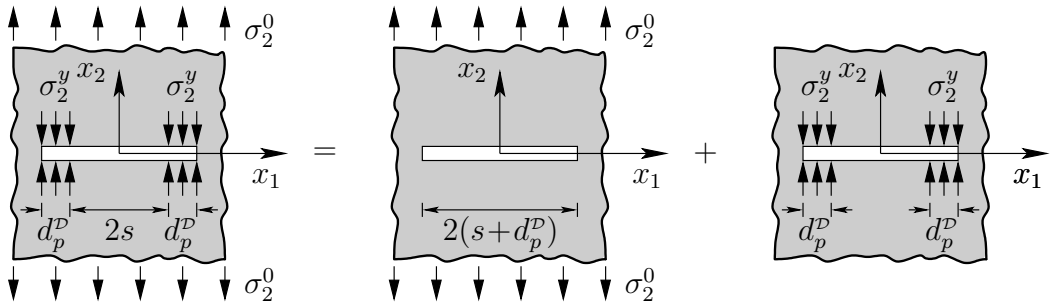

Figure 3.10: Superposition of two pure elastic sub-problems to gain an elasto-plastic model after *Dugdale*.

Alternatively to the elasto-plastic model from *Dugdale*, *Barenblatt* [7] proposed an apparently similar model. It is often referred to as the **cohesive fracture theory**. The basis of the cohesive fracture theory is the same as for the yield strip model. The only difference between these contributions lies in the yield stress distribution over the virtual

elongation of the crack surface. In *Barenblatt*'s proposal, the fracture process at the crack tip is specified by a non-linear cohesive stress function $\sigma_c(x)$, see Figure 3.9(c). This non-linear cohesive stress function constitutes the interatomic forces in the cohesive zone. The solution of this model is highly dependent on the choice of the cohesive stress function. The problem is usually approached numerically, as a general analytical solution is not available.

3.2 Continuum Fracture Mechanics

In order to formulate fracture mechanics within a continuum-mechanical framework, some kinematical aspects, analogue to Section 2.3, need to be discussed. The following section adopts the pioneering work of *Simo et al.* [172], on strong discontinuities in continuum mechanics, and later contributions to this topic by *Oliver et al.* [150, 151]. These fundamentals are herein extended towards the TPM. This monograph assumes that strong discontinuities (jumps) only occur in the displacement field of the solid phase φ^S.

3.2.1 Strong Discontinuity Kinematics

For the fundamentals of **strong discontinuity kinematics**, let $\mathcal{S}_0(\mathbf{X}_S, t_0)$ be the material (fixed) surface of a discontinuity through the solid phase φ^S at time t_0. Furthermore, let $\mathcal{S}_0$ intersect the body $\mathcal{B}_0$ in the reference configuration as pictured in Figure 3.11. The body $\mathcal{B}$ and the body parts $\{\mathcal{B}^+, \mathcal{B}^-\}$ are assumed to be, at any time t, encased in a fluid; this surrounding fluid is assumed to be identical to the interstitial fluid phase φ^F. Note that in the following all jump[15]-related values on the discontinuity surface are denoted as $[\![\,\cdot\,]\!]$, and consist of a "left" $(\,\cdot\,)^+$ and a "right" side $(\,\cdot\,)^-$. The two body parts $\mathcal{B}_0^+$ and $\mathcal{B}_0^-$ are assumed to be perfectly connected to each other in the reference configuration as

$$\mathcal{B}_0 = \mathcal{B}_0^+ \cup \mathcal{B}_0^- \quad \text{with} \quad \left\{ \begin{array}{lcll} \mathcal{S}(\mathcal{B}_0) & = & \partial\mathcal{B}_0^+ \cup \partial\mathcal{B}_0^- & : \text{overall body surface,} \\ \mathcal{S}(\mathcal{B}_0^+) & = & \partial\mathcal{B}_0^+ \cup \mathcal{S}_0^+ & : \text{“left” body surface,} \\ \mathcal{S}(\mathcal{B}_0^-) & = & \partial\mathcal{B}_0^- \cup \mathcal{S}_0^- & : \text{“right” body surface.} \end{array} \right. \tag{3.38}$$

Therein, $\mathcal{S}_0^+$ and $\mathcal{S}_0^-$ denote the two sides of the material surface $\mathcal{S}_0$. The corresponding surface normal vector $\mathbf{m}_S^s$ and the surface increment $\mathrm{d}A_S^s$ are implied by

$$\mathcal{S}_0 \mid \mathrm{d}\mathbf{A}_S^s = \mathbf{m}_S^s \, \mathrm{d}A_S^s \quad \text{with} \quad \left\{ \begin{array}{lcl} \mathcal{S}_0^+ & \mid & \mathrm{d}\mathbf{A}_S^{s,+} \equiv \mathrm{d}\mathbf{A}_S^s \,, \\ \mathcal{S}_0^- & \mid & \mathrm{d}\mathbf{A}_S^{s,-} := -\mathbf{m}_S^s \, \mathrm{d}A_S^s \,. \end{array} \right. \tag{3.39}$$

[15] In this monograph, the general definition for jump quantities over a singular surface $\mathcal{S}(\mathbf{n}^{\mathcal{S}} \, \mathrm{d}a^{\mathcal{S}})$ reads:

$$[\![(\,\cdot\,)(\mathbf{x}, t)]\!] := (\,\cdot\,)^+ - (\,\cdot\,)^- = \lim_{\varepsilon \to 0} \left\{ (\,\cdot\,)(\mathbf{x}_0 + \varepsilon \, \mathbf{n}^{\mathcal{S}}) - (\,\cdot\,)(\mathbf{x}_0 - \varepsilon \, \mathbf{n}^{\mathcal{S}}) \right\} . \tag{3.37}$$

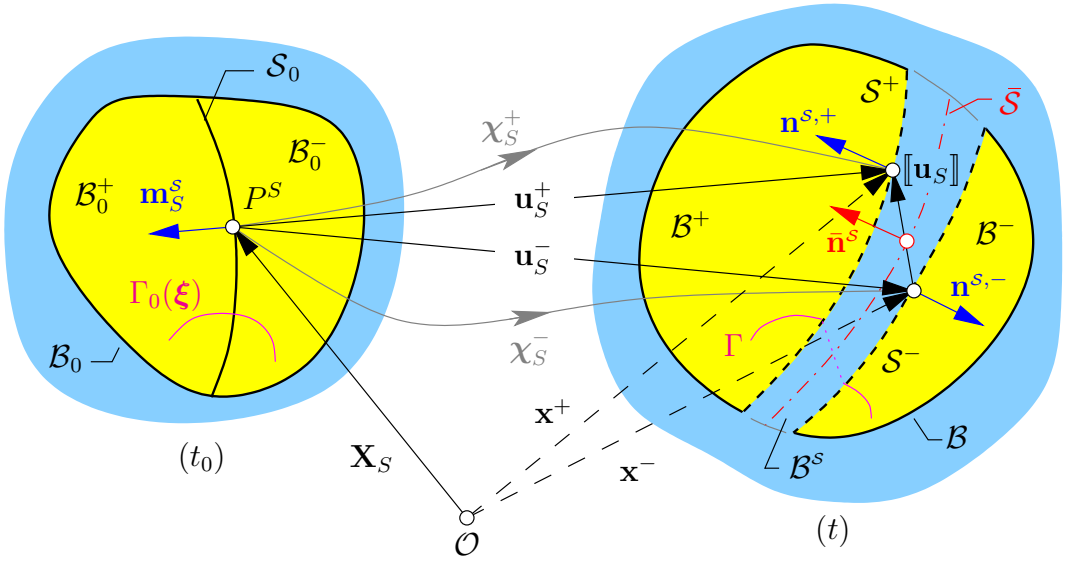

Figure 3.11: Kinematic relations in continuum fracture mechanics in extension to Figure 2.3.

Thus, let the solid motion function $\boldsymbol{\chi}_S$ consists of two parts, each of it continuous for all related material points $\mathbf{X}_S$, viz.

$$\boldsymbol{\chi}_S = \begin{cases} \boldsymbol{\chi}_S^+(\mathbf{X}_S, t) & : \mathcal{B}_0^+ \to \mathcal{B}^+(t) \quad \forall\, \mathbf{X}_S \in \mathcal{B}_0^+ \,, \\ \boldsymbol{\chi}_S^-(\mathbf{X}_S, t) & : \mathcal{B}_0^- \to \mathcal{B}^-(t) \quad \forall\, \mathbf{X}_S \in \mathcal{B}_0^- \,. \end{cases} \tag{3.40}$$

Remark: Due to the limitation of strong discontinuities only occurring in the displacement field of the solid phase, the fluid motion function $\boldsymbol{\chi}_F : \mathcal{B}_0 \to \mathcal{B}(t)\ \forall\ \mathbf{X}_F \in \mathcal{B}_0$ is virtually unaffected if the surfaces of the discontinuity, $\mathcal{S}^+$ and $\mathcal{S}^-$, are fully permeable. Nevertheless, the opening or change, respectively, of the body $\mathcal{B}_0 \to \mathcal{B}(t) = \mathcal{B}_0 + \mathcal{B}^s(t)$ must not be neglected. This will be taken into account in the successive discussion on balance relations for the fractured body. □

The two field characteristic of (3.40) leads to a weak discontinuity, i. e., a kink, in the solid motion function $\boldsymbol{\chi}_S$. As a consequence, the deformation gradient, its determinant, the displacement field, and all related strain and stress measures can be strongly discontinuous over $\mathcal{S}_0$. Hence, the deformation quantities

$$\mathbf{F}_S = \begin{cases} \mathbf{F}_S^+ \ \forall\ \mathbf{X}_S \in \mathcal{B}_0^+ \,, \\ \mathbf{F}_S^- \ \forall\ \mathbf{X}_S \in \mathcal{B}_0^- \,, \end{cases} \quad \Big| \quad J_S = \begin{cases} J_S^+ \ \forall\ \mathbf{X}_S \in \mathcal{B}_0^+ \,, \\ J_S^- \ \forall\ \mathbf{X}_S \in \mathcal{B}_0^- \,, \end{cases} \tag{3.41}$$

are defined separately for both parts of the body. Regarding the solid displacement field on the discontinuity surface $\mathcal{S}_0$, see Figure 3.11, the corresponding jump can be identified as

$$[\![\mathbf{u}_S]\!] = [\![\mathbf{u}_S]\!](\mathbf{X}_S, t) := \mathbf{u}_S^+ - \mathbf{u}_S^- \quad \forall\ \mathbf{X}_S \in \mathcal{S}_0 \,. \tag{3.42}$$

By introducing an enrichment factor $\psi(\mathbf{X}_S)$ as a step function, the displacement field function $\mathbf{u}_S$ can be composed by a continuous and a discontinuous part; the latter one implying the displacement jump:

$$\mathbf{u}_S = \mathbf{u}_S(\mathbf{X}_S, t) = \underbrace{\tilde{\mathbf{u}}_S(\mathbf{X}_S, t)}_{\text{continuous}} + \underbrace{\psi(\mathbf{X}_S)[\![\mathbf{u}_S]\!]}_{\text{discontinuous}} . \tag{3.43}$$

Note in passing that this is also the very basic principle of the extended Finite-Element Method (XFEM), see Section 4.3. In this context, the following two step functions are legitimate enrichments for strong discontinuities[16]:

$$\psi_1(\mathbf{X}_S) = \mathscr{H}(\mathbf{X}_S) = \left\{ \begin{array}{l} 1 \;\forall\; \mathbf{X}_S \in \mathcal{B}_0^+ , \\ 0 \;\forall\; \mathbf{X}_S \in \mathcal{S}_0 , \\ 0 \;\forall\; \mathbf{X}_S \in \mathcal{B}_0^- ; \end{array} \middle| \begin{array}{r} 1 \;\forall\; \mathbf{X}_S \in \mathcal{B}_0^+ , \\ 0 \;\forall\; \mathbf{X}_S \in \mathcal{S}_0 , \\ -1 \;\forall\; \mathbf{X}_S \in \mathcal{B}_0^- . \end{array} \right\} = \operatorname{sign}(\mathbf{X}_S) = \psi_2(\mathbf{X}_S) \tag{3.44}$$

Within this monograph, the first variant $\psi_1(\mathbf{X}_S)$ containing the unmodified *Heaviside*-function $\mathscr{H}(\mathbf{X}_S)$ is chosen as the enrichment for the displacement field, see Figure 3.12(a). With it, the material derivative of the displacement field arises as

$$\operatorname{Grad}_S \mathbf{u}_S = \frac{\partial \mathbf{u}_S}{\partial \mathbf{X}_S} = \underbrace{\operatorname{Grad}_S \tilde{\mathbf{u}}_S + \mathscr{H} \frac{\partial [\![\mathbf{u}_S]\!]}{\partial \mathbf{X}_S}}_{\text{regular} := \bigtriangledown_S \bar{\mathbf{u}}_S} + \underbrace{\delta_\mathcal{S}([\![\mathbf{u}_S]\!] \otimes \mathbf{m}_S^\mathcal{S})}_{\text{singular} := \bigtriangledown_S \bar{\bar{\mathbf{u}}}_S} . \tag{3.45}$$

Consequently, the solid deformation gradient $\mathbf{F}_S = \mathbf{I} + \operatorname{Grad}_S \mathbf{u}_S$ inherits the singular character of (3.45). The derivation of $\mathscr{H}(\mathbf{X}_S)$ results in the singular *Dirac*[17] -Delta $\delta_\mathcal{S}$ with the properties

$$\delta_\mathcal{S} = \delta_\mathcal{S}(\mathbf{X}_S) = \left\{ \begin{array}{rl} +\infty & \forall\; \mathbf{X}_S \in \mathcal{S}_0 , \\ 0 & \forall\; \mathbf{X}_S \in \mathcal{B}_0^+ \cup \mathcal{B}_0^- \end{array} \right. \quad \text{with} \int_{\mathcal{B}_0^+ \cup \mathcal{B}_0^-} \delta_\mathcal{S} f(\mathbf{X}_S) \, \mathrm{d}V_S = \int_{\mathcal{S}_0} f(\mathbf{X}_S^\mathcal{S}) \, \mathrm{d}A_S^\mathcal{S} . \tag{3.46}$$

The singular part of (3.45) does not contribute for material points located beside the discontinuity surface, but adds unbounded values for points located on the surface itself, see Figure 3.12(b). Obviously, the surface of the discontinuity changes together with the surrounding body over time; so does the reflection of the normal vector $\mathbf{m}_S^\mathcal{S}$ in the actual

[16] Weak discontinuities (kinks) in continuum field functions can be represented by, e. g., the abs-function as an enrichment: $\psi_\mathcal{A}(\mathbf{X}_S) = \operatorname{abs}(\phi(\mathbf{X}_S)) = |\phi(\mathbf{X}_S)|$.

[17] *Paul Adrien Maurice Dirac* (1902 – 1984): English theoretical physicist who made fundamental contributions to the early development of both quantum mechanics and quantum electrodynamics. Among other discoveries, he formulated the Dirac equation and predicted the existence of antimatter. Dirac shared the Nobel Price in physics for 1933 with *Erwin Schrödinger*. [WIKIPEDIA]

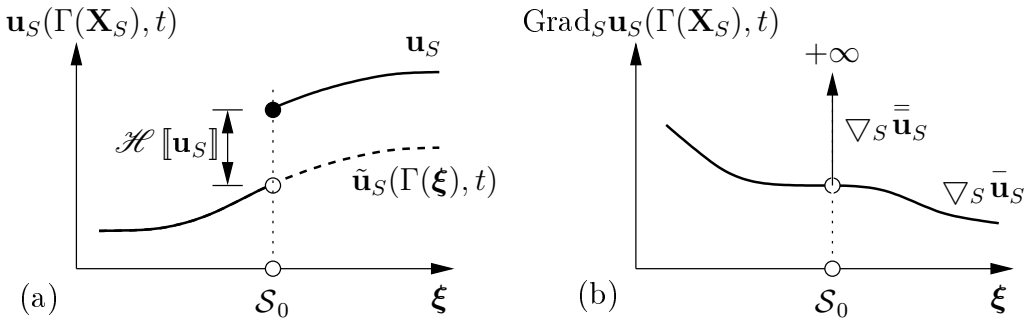

Figure 3.12: (a) jump in displacement field function, (b) its material derivation.

configuration. Applying a push-forward transport $(2.20)_1$ to the surface increment of the discontinuity yields

$$\mathrm{d}\mathbf{a}^* = \det\mathbf{F}_S\,\mathbf{F}_S^{T-1}\mathrm{d}\mathbf{A}_S^{\mathcal{S}} \rightsquigarrow \mathbf{n}^* = J_S\,\mathbf{F}_S^{T-1}\mathbf{m}_S^{\mathcal{S}}\,\frac{\mathrm{d}A_S^{\mathcal{S}}}{\mathrm{d}a^*} \quad \text{with} \quad \mathrm{d}\mathbf{a}^* = \mathbf{n}^*\,\mathrm{d}a^*\,. \tag{3.47}$$

This represents the transport mechanism of the discontinuity surface normal vector into the actual configuration, $\mathbf{m}_S^{\mathcal{S}} \rightarrow \mathbf{n}^*(t)$. Because of the singular characteristic of the deformation gradient $(3.41)_1$, the normal vector $\mathbf{n}^*$ is not well-defined and can be either $\mathbf{n}^{\mathcal{S},+}$ or $\mathbf{n}^{\mathcal{S},-}$, see Figure 3.11. One possible solution for this problem is the regularisation of $\nabla_S\,\bar{\bar{\mathbf{u}}}_S$ by introducing a discontinuity band instead of a sharp discontinuity surface. Another ansatz to avoid singular deformation functions has been discussed in *Armero & Garikipati* [5], and *Steinmann & Betsch* [176]. Therein, the jump in the deformation map is restricted to be spatially constant, which inherently leads to parallel discontinuity surfaces in the actual configuration; thus, to an incompatibility. Alternatively to these approaches, a virtual surface $\bar{\mathcal{S}}$, which is centred in-between the two sides of the discontinuity, will be introduced in the subsequent Section 3.2.2. The introduction of the virtual surface is motivated through the application of the **cohesive zone model**, see also, e. g., *Wells et al.* [190].

Remark: In anticipation of the following Section 3.2.3, it is noted that the evaluation of (3.45), together with $(3.46)_2$, results in the same weak, variational formulation of the BVP as it does after the considerations about discontinuous global master balances. The latter is accompanied by an extension of the *Reynolds*[18] transport theorem. The evaluation process with respect to (3.45) is a common approach in the literature to motivate the set of discontinuous variational formulations, see e. g., *Hettich* [103]. In detail, the evaluation on the basis of $(2.77)_2$ yields for an arbitrary vector-valued functional $\mathbf{a} = \mathbf{b} + \mathbf{c}$ with

[18] *Osborne Reynolds* (1842 – 1912): British physicist who was a prominent innovator in the understanding of fluid dynamics. In fluid mechanics, the "*Reynolds* number" Re is a dimensionless number that gives a measure of the ratio of inertial forces to viscous forces. The concept was introduced by *George Gabriel Stokes* in 1851, but *Reynolds* popularised its use in 1883. [WIKIPEDIA]

$\mathbf{c} = \mathscr{H}\mathbf{d}$ the following relation:

$$\begin{aligned} & \int_\Omega \mathbf{A} \cdot \nabla \mathbf{a} \, \mathrm{d}v \quad \text{with} \quad \nabla \mathbf{c} = \mathscr{H} \nabla \mathbf{d} + \mathbf{d} \otimes \nabla \mathscr{H} \quad \text{and} \quad \nabla \mathscr{H} = \delta \mathbf{n} \,, \\ \rightsquigarrow \quad & \cdots + \int_\Omega \mathbf{A} \cdot \mathbf{d} \otimes \delta \mathbf{n} \, \mathrm{d}v = \cdots + \int_\Omega \delta(\mathbf{e} \cdot \mathbf{d}) \, \mathrm{d}v \quad \text{with} \quad \mathbf{e} = \mathbf{A}\mathbf{n} \,, \\ \Rightarrow \quad & \int_\Omega \mathbf{A} \cdot \nabla \mathbf{b} \, \mathrm{d}v + \int_\Omega \mathbf{A} \cdot \mathscr{H} \nabla \mathbf{d} \, \mathrm{d}v + \int_\Gamma \mathbf{e} \cdot \mathbf{d} \, \mathrm{d}a \,. \end{aligned} \tag{3.48}$$

Anyway, discontinuous global master balances and the accompanied extension of the *Reynolds* transport theorem is the favoured methodology in this monograph. It is applied to model the cohesive zone in the framework of the classical continuum-mechanical field theories. The sustaining of the general applicability of the global master balances is one of the reasons – if not the main reason – for the elegance of the TPM. The derivation of (3.48) in this context will be the subject of subsequent sections. Note in passing that it is also a common approach to obtain cohesive XFEM balance equations by the direct integration of corresponding quantities over the surface of a discontinuity. This direct integration is motivated by interface considerations. The integrative contributions are then included into the principle of virtual work and subsequent into the balance of mechanical energy, see, e. g., *Jäger* [112]. □

3.2.2 Cohesive Zone Model

This monograph will apply the **cohesive zone model**, originated from *Dugdale* [49], and *Barenblatt* [7]. The cohesive zone model implies that tractions can be transmitted through both sides of the discontinuity, i. e., through the surfaces $\mathcal{S}^+$ and $\mathcal{S}^-$, see Section 3.1.5. To avoid a possible incompatibility, a virtual surface $\bar{\mathcal{S}}$, together with its surface normal vector $\bar{\mathbf{n}}^{\mathcal{S}}$, is heuristically introduced in the actual configuration. This surface is designed to be centred in between $\mathcal{S}^+$ and $\mathcal{S}^-$, see Figure 3.11. As far as the author is aware, this idea originates from *Wells* [189]. With this preliminaries, the corresponding, also virtual, motion function

$$\bar{\boldsymbol{\chi}}_S^{\mathcal{S}} = \tfrac{1}{2} \left[\boldsymbol{\chi}_S^+ + \boldsymbol{\chi}_S^- \right] \quad : \mathcal{S}_0 \rightarrow \bar{\mathcal{S}}(t) \quad \forall \, \mathbf{X}_S \in \mathcal{S}_0 \tag{3.49}$$

and deformation gradient

$$\bar{\mathbf{F}}_S^{\mathcal{S}} = \tfrac{1}{2} \left[\mathbf{F}_S^+ + \mathbf{F}_S^- \right] \quad \forall \, \mathbf{X}_S \in \mathcal{S}_0 \quad \text{with} \quad \det\left(\bar{\mathbf{F}}_S^{\mathcal{S}}\right) := \bar{J}_S^{\mathcal{S}} \tag{3.50}$$

provide a framework for the definition of unique discontinuity surface traction. As a consequence, the deformation gradient for material points at $\mathbf{X}_S$ on the virtual discontinuity

surface $\bar{\mathcal{S}}$ reads

$$\boxed{\begin{array}{l}\textbf{virtual deformation gradient on } \bar{\mathcal{S}} \\ \boxed{\bar{\mathbf{F}}_S^{\mathcal{S}}(\mathbf{X}_S) = \mathbf{I} + \mathrm{Grad}_S \tilde{\mathbf{u}}_S + \tfrac{1}{2}\dfrac{\partial [\![\mathbf{u}_S]\!]}{\partial \mathbf{X}_S}}\end{array}} \tag{3.51}$$

The factor $\frac{1}{2}$ places the virtual surface in the middle of $\mathcal{S}^+$ and $\mathcal{S}^-$. With this, an associated pull-back and push-forward transport mechanisms can be introduced. In particular, the surface normal vector on the virtual discontinuity surface can be identified by

$$\bar{\mathbf{n}}^{\mathcal{S}} = \bar{J}_S^{\mathcal{S}}\, \bar{\mathbf{F}}_S^{\mathcal{S},T-1} \mathbf{m}_S^{\mathcal{S}}\, \frac{\mathrm{d}A_S^{\mathcal{S}}}{\mathrm{d}\bar{a}^{\mathcal{S}}} \quad \text{with} \quad \mathrm{d}\bar{\mathbf{a}}^{\mathcal{S}} = \bar{\mathbf{n}}^{\mathcal{S}}\, \mathrm{d}\bar{a}^{\mathcal{S}}\,. \tag{3.52}$$

Further kinematical details need to be regarded for the subsequent discussion on the cohesive zone model. Thus, the actual configuration traction force vector that can be transmitted through both sides of the discontinuity surface, $\mathcal{S}^+$ and $\mathcal{S}^-$, is postulated as $\bar{\mathbf{t}}^{S,\mathcal{S}}$, see Figure 3.13. The traction force vector is shifted in order to act on the virtual

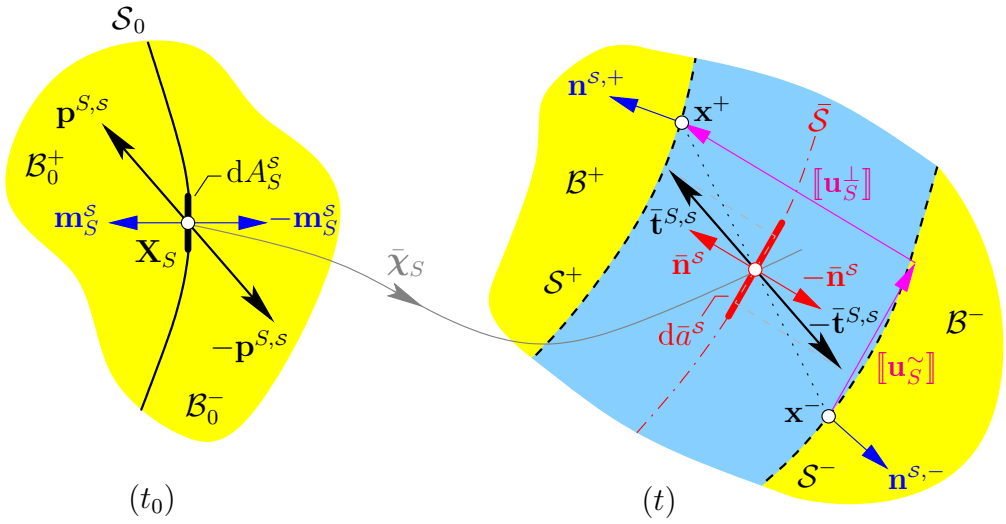

Figure 3.13: Kinematic relations in continuum fracture mechanics in detail.

representation of the discontinuity surface $\bar{\mathcal{S}}$. With (3.52) and (2.34) the traction force vector can be related again to its counterpart $\mathbf{p}^{S,\mathcal{S}}$ in the reference configuration, viz.

$$\bar{\mathbf{t}}^{S,\mathcal{S}} = \frac{\mathrm{d}A_S^{\mathcal{S}}}{\mathrm{d}\bar{a}^{\mathcal{S}}}\, \mathbf{p}^{S,\mathcal{S}}\,. \tag{3.53}$$

Note that these traction quantities are herein solely related to the solid constituent φ^S of the overall aggregate. Furthermore, the normal $[\![\mathbf{u}_S^{\perp}]\!]$ associated to the displacement

jump $[\![\mathbf{u}_S]\!]$ and its tangential $[\![\mathbf{u}_S^{\sim}]\!]$ gaps are introduced as depicted in Figure 3.13. They are computed as

$$[\![\mathbf{u}_S^{\perp}]\!] = ([\![\mathbf{u}_S]\!] \cdot \bar{\mathbf{n}}^{\mathcal{S}})\, \bar{\mathbf{n}}^{\mathcal{S}} \quad \text{and} \quad [\![\mathbf{u}_S^{\sim}]\!] = [\![\mathbf{u}_S]\!] - [\![\mathbf{u}_S^{\perp}]\!]\,. \tag{3.54}$$

3.2.3 Strong Discontinuities in Continuum Mechanics

For the application of the cohesive zone model and by that the inclusion of strong discontinuities into the classical continuum-mechanical field theories, the global representation of the master balances (2.38) needs to be modified. In the following, only vector-valued mechanical quantities need to be considered. The modified global master balance is congruent for scalar-valued mechanical quantities. The former global master balance remains still valid for the sub-parts $\mathcal{B}^+$ and $\mathcal{B}^-$ but their flow contingent $\boldsymbol{\Phi}^\alpha$ over the surface $\mathcal{S}$ must include the additional surface(s) $\mathcal{S}^{+/-}$ or $\bar{\mathcal{S}}$, respectively. This is attended by the superposition principle for cohesive zones from Section 3.1.5, see Figure 3.14. Hence, the

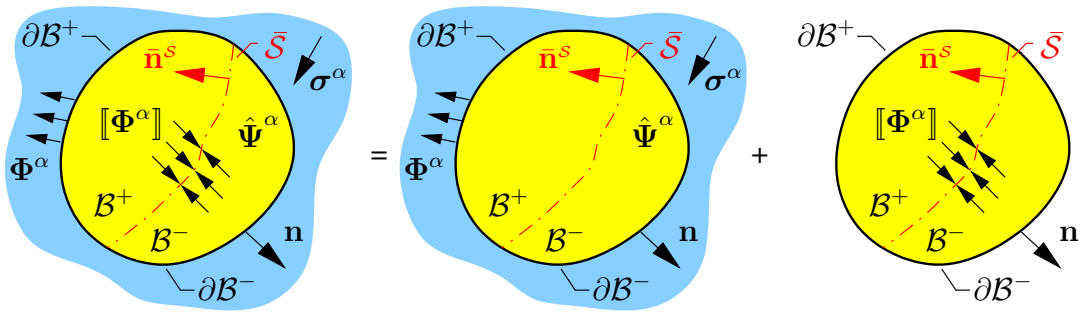

Figure 3.14: Superposition principle for cohesive zones on continuum mechanics.

surfaces of the sub-parts read $\partial\mathcal{B}^+ \cup \mathcal{S}^+$ and $\partial\mathcal{B}^- \cup \mathcal{S}^-$. The global master balance for the single sub-parts results

$$\begin{aligned}
\text{for } \mathcal{B}^+ : \quad \frac{\mathrm{d}_\alpha}{\mathrm{d}t} \int\limits_{\mathcal{B}^+} \boldsymbol{\Psi}^\alpha \,\mathrm{d}v \;&=\; \int\limits_{\partial\mathcal{B}^+} (\boldsymbol{\Phi}^\alpha\, \mathbf{n})\,\mathrm{d}a + \int\limits_{\mathcal{B}^+} \boldsymbol{\sigma}^\alpha \,\mathrm{d}v + \int\limits_{\mathcal{B}^+} \hat{\boldsymbol{\Psi}}^\alpha \,\mathrm{d}v \\
&\quad + \int\limits_{\mathcal{S}^+} \left[(\boldsymbol{\Phi}^\alpha)^+ \,(-\mathbf{n}^{\mathcal{S},+})\right] \mathrm{d}a^{\mathcal{S}}\,, \\
\text{for } \mathcal{B}^- : \quad \frac{\mathrm{d}_\alpha}{\mathrm{d}t} \int\limits_{\mathcal{B}^-} \boldsymbol{\Psi}^\alpha \,\mathrm{d}v \;&=\; \int\limits_{\partial\mathcal{B}^-} (\boldsymbol{\Phi}^\alpha\, \mathbf{n})\,\mathrm{d}a + \int\limits_{\mathcal{B}^-} \boldsymbol{\sigma}^\alpha \,\mathrm{d}v + \int\limits_{\mathcal{B}^-} \hat{\boldsymbol{\Psi}}^\alpha \,\mathrm{d}v \\
&\quad + \int\limits_{\mathcal{S}^-} \left[(\boldsymbol{\Phi}^\alpha)^- \,(-\mathbf{n}^{\mathcal{S},-})\right] \mathrm{d}a^{\mathcal{S}}\,.
\end{aligned} \tag{3.55}$$

Note the negative sign of the normal vectors $\mathbf{n}^{\mathcal{S},+/-}$, which is due to their reciprocal orientation to the "regular" normal vectors of $\partial\mathcal{B}^{+/-}$. Recall the definition (3.39); thus,

$\bar{\mathbf{n}}^{\mathcal{S}} := \mathbf{n}^{\mathcal{S},+} = -\mathbf{n}^{\mathcal{S},-}$. From the sum of (3.55) over the overall body $\mathcal{B} = \mathcal{B}^{+} \cup \mathcal{B}^{-}$ follows the final form of the modified global master balance of vector-valued mechanical quantities for a mixture constituent, viz.

modified global master balance with $\bar{\mathcal{S}}$

$$\frac{\mathrm{d}_{\alpha}}{\mathrm{d}t} \int_{\mathcal{B}} \boldsymbol{\Psi}^{\alpha} = \int_{\partial\mathcal{B}} (\boldsymbol{\Phi}^{\alpha}\,\mathbf{n})\,\mathrm{d}a + \int_{\mathcal{B}} \boldsymbol{\sigma}^{\alpha}\,\mathrm{d}v + \int_{\mathcal{B}} \hat{\boldsymbol{\Psi}}^{\alpha}\,\mathrm{d}v - \int_{\bar{\mathcal{S}}} [\![\boldsymbol{\Phi}^{\alpha}]\!]\,\bar{\mathbf{n}}^{\mathcal{S}}\,\mathrm{d}a^{\mathcal{S}} \tag{3.56}$$

Therein, the general notation of jump quantities (3.37) is used. To find the local form of (3.56), the – in the left part of the equation – underlying *Reynold*s transport theorem needs to be extended, too. This extension must incorporate singular surfaces that intersect the continua. For details on this extension see Section B.4. With this, the volume integral of the extended global master balance can be, analogously to Section 2.5, found as

$$\int_{\mathcal{B}} \Big[\underbrace{\frac{\partial \boldsymbol{\Psi}^{\alpha}}{\partial t} + \operatorname{div}(\boldsymbol{\Psi}^{\alpha} \otimes \overset{\prime}{\mathbf{x}}_{\alpha})}_{(\boldsymbol{\Psi}^{\alpha})'_{\alpha} + \boldsymbol{\Psi}^{\alpha} \operatorname{div} \overset{\prime}{\mathbf{x}}_{\alpha}} - \operatorname{div} \boldsymbol{\Phi}^{\alpha} - \boldsymbol{\sigma}^{\alpha} - \hat{\boldsymbol{\Psi}}^{\alpha} \Big]\,\mathrm{d}v = \int_{\bar{\mathcal{S}}} [\![\boldsymbol{\Psi}^{\alpha} \otimes (\overset{\prime}{\mathbf{x}}_{\alpha} - \overset{\prime}{\mathbf{x}}_{\bar{\mathcal{S}}}) - \boldsymbol{\Phi}^{\alpha}]\!]\,\bar{\mathbf{n}}^{\mathcal{S}}\,\mathrm{d}a^{\mathcal{S}}\,. \tag{3.57}$$

The left part of this equation is continuous over the volume integral. As a consequence, its local form for all material points P^{α} in $\mathcal{B}$ is identical to $(2.39)_2$. The local balance relation for material points on $\bar{\mathcal{S}}$ results from the surface integral over it, i. e., the right part of (3.57):

local balance on $\bar{\mathcal{S}}$

$$[\![\boldsymbol{\Psi}^{\alpha} \otimes (\overset{\prime}{\mathbf{x}}_{\alpha} - \overset{\prime}{\mathbf{x}}_{\bar{\mathcal{S}}}) - \boldsymbol{\Phi}^{\alpha}]\!]\,\bar{\mathbf{n}}^{\mathcal{S}} = \mathbf{0} \tag{3.58}$$

Therein, the requirement for continuity over the surface $\bar{\mathcal{S}}$ is presumed. Obviously, one has to consider two sets of material points, $\{P^{\alpha} \in \{\mathcal{B}\}\}$ and $\{P^{\alpha} \in \{\mathcal{B}, \bar{\mathcal{S}}\}\}$; the first set following only the balance relations (2.39) and the latter set additionally following (3.58). As a consequence, balance relations of mechanical quantities for both sets of material points can only be interpreted in an integral (weak) sense. For the sake of completeness, the general local constituent balance equations over the surface $\bar{\mathcal{S}}$ are given at a glance in (3.59). Note that these relations lack the production quantities $(\hat{\cdot})$. Furthermore, for scalar-valued quantities of (3.58), it has been assumed that $[\![\Psi^{\alpha}(\overset{\prime}{\mathbf{x}}_{\alpha} - \overset{\prime}{\mathbf{x}}_{\bar{\mathcal{S}}}) - \Phi^{\alpha}]\!] \cdot \bar{\mathbf{n}}^{\mathcal{S}} = 0$ without any further derivation. With the previous restriction of a material (fixed) discontinuity surface through – only – the solid phase φ^{S}, i. e., $\overset{\prime}{\mathbf{x}}_{\bar{\mathcal{S}}} = \overset{\prime}{\mathbf{x}}_{S}$, the relative velocity part of (3.58) vanishes for balance relations over the solid constituent. In this case, for balance relations concerning the fluid constituent φ^{F} the relative velocity part is identified as the seepage velocity $\mathbf{w}_F = \overset{\prime}{\mathbf{x}}_{F} - \overset{\prime}{\mathbf{x}}_{S}$. This yields an additional fluid flow over the surface $\bar{\mathcal{S}}$. Recall, due to the assumption of constant material densities $(\rho^{\alpha R})'_{\alpha} = 0$

and the lack of mass exchange between the constituents $\hat{\rho}^\alpha = 0$, the mass balance was reduced to a volume balance.

constituent balance equations over $\bar{\mathcal{S}}$

$$
\begin{aligned}
\text{mass}: \quad 0 &= [\![\rho^\alpha (\overset{\prime}{\mathbf{x}}_\alpha - \overset{\prime}{\mathbf{x}}_{\bar{s}})]\!] \cdot \bar{\mathbf{n}}^{\mathcal{S}} \\
\text{momentum}: \quad \mathbf{0} &= [\![\rho^\alpha \overset{\prime}{\mathbf{x}}_\alpha \otimes (\overset{\prime}{\mathbf{x}}_\alpha - \overset{\prime}{\mathbf{x}}_{\bar{s}}) - \mathbf{T}^\alpha]\!]\, \bar{\mathbf{n}}^{\mathcal{S}} \\
\text{m.o.m.}: \quad \mathbf{0} &= [\![[\mathbf{x} \times (\rho^\alpha \overset{\prime}{\mathbf{x}}_\alpha)] \otimes (\overset{\prime}{\mathbf{x}}_\alpha - \overset{\prime}{\mathbf{x}}_{\bar{s}}) - \mathbf{x} \times \mathbf{T}^\alpha]\!]\, \bar{\mathbf{n}}^{\mathcal{S}} \\
\text{energy}: \quad 0 &= [\![[\rho^\alpha \varepsilon^\alpha + \tfrac{1}{2}\, \overset{\prime}{\mathbf{x}}_\alpha \cdot (\rho^\alpha \overset{\prime}{\mathbf{x}}_\alpha)](\overset{\prime}{\mathbf{x}}_\alpha - \overset{\prime}{\mathbf{x}}_{\bar{s}}) - [(\mathbf{T}^\alpha)^T \overset{\prime}{\mathbf{x}}_\alpha - \mathbf{q}^\alpha]]\!] \cdot \bar{\mathbf{n}}^{\mathcal{S}} \\
\text{entropy}: \quad 0 &= [\![\rho^\alpha \eta^\alpha (\overset{\prime}{\mathbf{x}}_\alpha - \overset{\prime}{\mathbf{x}}_{\bar{s}}) - \boldsymbol{\phi}_\eta^\alpha]\!] \cdot \bar{\mathbf{n}}^{\mathcal{S}}
\end{aligned}
\tag{3.59}
$$

The additional surface integral over $\bar{\mathcal{S}}$ must be taken into account while discussing the weak formulation of the BVP from Section 2.6.4. Starting with the "lowest" balance relation, the **modified volume balance** equation from $(2.77)_1$ then yields

modified volume balance with $\bar{\mathcal{S}}$

$$
\begin{aligned}
\int_{\mathcal{B}} \operatorname{div}(\mathbf{u}_S)'_S\, \delta\mathcal{P}\, \mathrm{d}v + \int_{\mathcal{B}} \frac{k^F}{\gamma^{FR}} (\operatorname{grad}\mathcal{P} - \rho^{FR}\mathbf{g}) \cdot \operatorname{grad}\, \delta\mathcal{P}\, \mathrm{d}v = &- \int_{\partial\mathcal{B}} v\, \delta\mathcal{P}\, \mathrm{d}a + \\
&+ \int_{\bar{\mathcal{S}}} \underbrace{[\![(n^F \mathbf{w}_F)]\!] \cdot \bar{\mathbf{n}}^{\mathcal{S}}}_{=:\, \bar{v}^{\mathcal{S}}}\, \delta\mathcal{P}\, \mathrm{d}a^{\mathcal{S}}
\end{aligned}
\tag{3.60}
$$

One can see that, in contrast to the external efflux v, the volume balance addition over $\bar{\mathcal{S}}$ is positive definite. Thus, the consequently resulting internal fluid flow $\bar{v}$ is inward oriented. Therefore, it is defined as an internal fluid influx. Furthermore, the volume balance addition is postulated to be an additional internal body volume $\mathcal{B}^{\mathcal{S}}$. This additional body volume must also fulfil the saturation condition $n^S + n^F = 1$. Because of the strong discontinuity in the solid displacement field, $\mathcal{B}^{\mathcal{S}}$ needs to be filled with the interstitial fluid exclusively, i.e., $n^S(\mathcal{B}^{\mathcal{S}}) = 0, n^F(\mathcal{B}^{\mathcal{S}}) = 1$. The filling is assumed to be instantaneous. Thus, the additional volume can be directly connected to the influx $\bar{v}^{\mathcal{S}}$, see (3.61). These circumstances are visualised in Figure 3.15. Regarding the next "higher" balance relation, the **momentum balance** equation, one has to differentiate the designated right side of $(2.77)_2$ first. Summing up $(2.77)_2$ over both constituents yields

$$
\int_{\bar{\mathcal{S}}} [\![\underbrace{\rho^F (\overset{\prime}{\mathbf{x}}_F \otimes \mathbf{w}_F)}_{=\, \mathbf{T}^F} - \mathbf{T}^F - (\mathbf{T}_E^S - \mathcal{P}\,\mathbf{I})]\!]\, \bar{\mathbf{n}}^{\mathcal{S}}\, \mathrm{d}a^{\mathcal{S}} = \int_{\bar{\mathcal{S}}} - \underbrace{[\![\mathbf{T}_E^S]\!]\, \bar{\mathbf{n}}^{\mathcal{S}}}_{=:\, \bar{\mathbf{t}}^{S,\mathcal{S}}} + \underbrace{[\![\mathcal{P}\,\mathbf{I}]\!]}_{=\, \mathbf{0}}\, \bar{\mathbf{n}}^{\mathcal{S}}\, \mathrm{d}a^{\mathcal{S}}\,. \tag{3.62}
$$

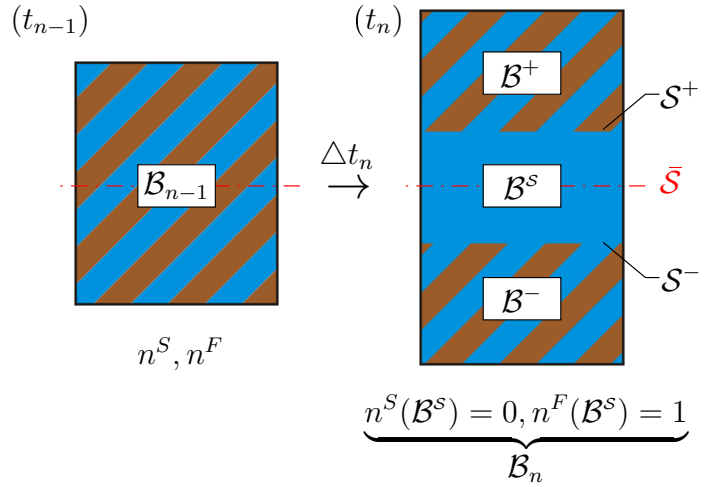

$$\begin{aligned} \mathcal{B}_{n-1} &= \mathcal{B}^+ + \mathcal{B}^- \\ \mathcal{B}_n &= \mathcal{B}_{n-1} + \mathcal{B}^{\mathcal{S}} \\ \mathcal{S}^+, \mathcal{S}^- &\rightsquigarrow \bar{\mathcal{S}} \end{aligned}$$

$$\boxed{\int_{\bar{\mathcal{S}}} \bar{v}^{\mathcal{S}} \, \mathrm{d}a^{\mathcal{S}} = \frac{\mathcal{B}_n - \mathcal{B}_{n-1}}{\triangle t_n}} \tag{3.61}$$

Figure 3.15: Additional fluid volume as internal fluid flow.

Therein, the interstitial fluid pressure jump $[\![\mathcal{P}]\!]$ is non existent, because the previous assumptions state a discontinuity free fluid pressure field function, i. e., $\mathcal{P}^+ = \mathcal{P}^-$. With this, the weak formulation of the modified momentum balance for the constituents reads

modified momentum balance with $\bar{\mathcal{S}}$

$$\int_{\mathcal{B}} (\mathbf{T}_E^S - p\,\mathbf{I}) \cdot \operatorname{grad} \delta\mathbf{u}_S \, \mathrm{d}v + \int_{\bar{\mathcal{S}}} \bar{\mathbf{t}}^{S,\mathcal{S}} \cdot \delta\mathbf{u}_S \, \mathrm{d}a^{\mathcal{S}} = \int_{\mathcal{B}} \rho\,\mathbf{b} \cdot \delta\mathbf{u}_S + \int_{\partial\mathcal{B}} \mathbf{t} \cdot \delta\mathbf{u}_S \, \mathrm{d}a \,. \tag{3.63}$$

As one can see, the discontinuous stress quantity $[\![\mathbf{T}_E^S]\!]$ on $\bar{\mathcal{S}}$ or $\bar{\mathbf{t}}^{S,\mathcal{S}}$, respectively, turns out to be an additional internal stress support. Thus, it is added on the left side of (3.63). Substituting the test function $\delta\mathbf{u}_S$ with a virtual displacement, the discontinuous stress quantity can be interpreted as an interface, or cohesive, virtual work.

In the following, the **cohesive virtual work** will be regarded as a split-off of the internal mechanical – also virtual – work, denoted as δW_{coh}. This split-off stands in contrast to the externally on $\partial\mathcal{B}$ acting stress vector $\mathbf{t}$. Consequently, the internal work over the body $\mathcal{B}$ consists of two internal parts, a bulk part, and a cohesive zone. With this, the overall virtual work δW yields

$$\delta W(\mathbf{T}) = \delta W_{bulk}(\mathbf{T}_E^S, \mathcal{P}) + \delta W_{coh}(\bar{\mathbf{t}}^{S,\mathcal{S}}) - \delta W_{ext}(\mathbf{b}, \mathbf{t}) \,. \tag{3.64}$$

In the following, conservative stresses will be concluded for the cohesive zone. Thus, a potential must exist for the derivation of the cohesive zone stress $\bar{\mathbf{t}}^{S,\mathcal{S}}$. Therefore, the *Ogden*-type strain-energy function for the solid skeleton (2.68) discussed in Section 2.6 needs to be extended in order to also reflect the cohesive zone. Analogously to (3.64), the

strain-energy function will be additively split into two parts, viz.

$$\mathcal{W}^S = \mathcal{W}^S_{Ogden} + \tilde{\mathcal{W}}^S_{coh} \,. \tag{3.65}$$

The dependency of the cohesive potential $\tilde{\mathcal{W}}^S_{coh}$ on the opening of the discontinuity, represented by the discontinuity jump vector $[\![\mathbf{u}_S]\!]$, is self-evident. However, for the consistent modelling of large deformations, non-isotropic material behaviour will be presumed – only – for the cohesive zone. For the subsequent introduction of the cohesive potential function, the non-isotropic material behaviour is restricted to transverse isotropy.

Remark: The transverse isotropy is a special case of anisotropy. Identical to orthotropic materials, transverse isotropic materials have no coupling between stretching and shear distortion. But additionally, for transverse isotropic materials, there is a preferred direction that can be rotated without changing its elastic properties. Thus, in planes perpendicular to this preferred direction, the material elasticity properties are independent of the preferred direction. Note that in different oriented planes, the properties are again direction dependent. □

Consequently, it is necessary to include directional information into the formulation of the potential. Thus, besides the discontinuity jump vector, the surface normal vector $\bar{\mathbf{n}}^S$ needs to be incorporated into $\tilde{\mathcal{W}}^S_{coh}$. The surface normal vector represents the preferred direction of the transverse isotropy. Furthermore, it is assumed that softening material behaviour, comparable to (B.12), may occur in the cohesive zone. Thus, postulating isotropic[19] damage, a scalar-valued damage function $d = d(\mathbf{X}_S, t) \in [0, 1]$ is introduced as a limiting factor for the cohesive potential, viz.

$$\tilde{\mathcal{W}}^S_{coh} := (1 - d)\, \mathcal{W}^S_{coh} \,. \tag{3.66}$$

The isotropic damage function is constitutively chosen as

$$d = 1 - e^{-a\, u^b} \quad \text{with} \quad u = u(\mathbf{X}_S, t) = \max\Big[\, \| [\![\mathbf{u}_S(\mathbf{X}_S, s)]\!] \| \,\Big]^t_{s=0} \,. \tag{3.67}$$

The magnitude of the maximum displacement jump u ensures the irreversible characteristic of the damage process, since (3.67) is monotonically increasing. The time variable $s \in [0, t]$ specifies the irreversible damage path. Note in passing that u is designed as a so-called history variable. For its numerical computation, its previous value needs to be stored at every relevant point on the surface $\mathcal{S}_0$. In (3.67), the material response to the damage process is reflected by the material parameters a and b.

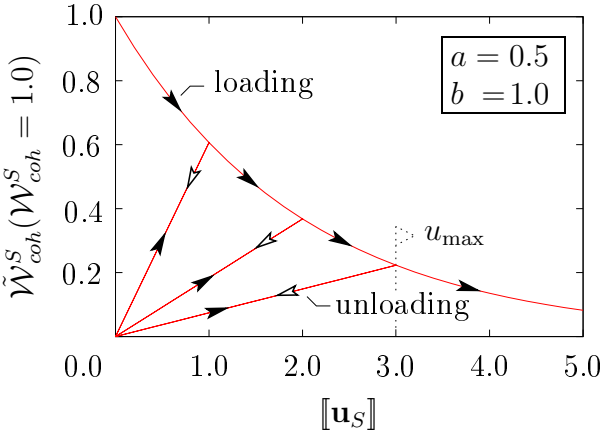

Figure 3.16: Cohesive potential function.

This type of damage function is often chosen in the context of biomaterials, see e. g., *Gasser & Holzapfel* [83]. A visualisation of a corresponding cohesive potential function is given in Figure 3.16. Therein, the maximum displacement jump $u_{\max}$ is – per surface point $\mathbf{X}_S \in \mathcal{S}_0$ – irreversible during unloading phases.

Analogously to Section 2.6.1, the combination of $\mathcal{W}^S_{Ogden}$ and $\tilde{\mathcal{W}}^S_{coh}$ must still satisfy the fundamental principles determinism, equipresence, local action, material frame indifference, and dissipation. For the cohesive potential, the sets of process variables and response functions are postulated as

$$\{\tilde{\mathcal{W}}^S_{coh}, \bar{\mathbf{t}}^{S,\mathcal{S}}\} = \mathcal{R}\{\boldsymbol{\mathcal{U}}^S, \boldsymbol{\mathcal{N}}^S, d\} \quad \text{with} \quad \left\{ \begin{array}{rcl} \boldsymbol{\mathcal{U}}^S & = & [\![\mathbf{u}_S]\!] \otimes [\![\mathbf{u}_S]\!] \,, \\ \boldsymbol{\mathcal{N}}^S & = & \bar{\mathbf{n}}^{\mathcal{S}} \otimes \bar{\mathbf{n}}^{\mathcal{S}} \,. \end{array} \right. \tag{3.68}$$

These sets correspond to the aforementioned dependencies of the cohesive potential. Therein, two structural tensors, $\boldsymbol{\mathcal{U}}^S$ and $\boldsymbol{\mathcal{N}}^S$, are introduced as the dyadic products of the directional vectors $[\![\mathbf{u}_S]\!]$ and $\bar{\mathbf{n}}^{\mathcal{S}}$. The structural tensors are necessary to characterise the transverse isotropy of $\tilde{\mathcal{W}}^S_{coh}$. The principle of material frame indifference states the independency of the cohesive material behaviour to the position of observer, i. e.,

$$\overset{*}{\tilde{\mathcal{W}}}{}^S_{coh}(\boldsymbol{\mathcal{U}}^S, \boldsymbol{\mathcal{N}}^S, d) = \tilde{\mathcal{W}}^S_{coh}(\overset{*}{\boldsymbol{\mathcal{U}}}{}^S, \overset{*}{\boldsymbol{\mathcal{N}}}{}^S, \overset{*}{d}) \quad \forall\, \mathbf{Q} \in \mathcal{SO}_3 \,. \tag{3.69}$$

$\mathcal{SO}_3$ characterises the special (proper) orthogonal group of $\mathbf{Q}$. The notation $\overset{*}{(\cdot)}$ indicates quantities in the rotated actual configuration. The tensor $\mathbf{Q}$ represents an arbitrary rigid body rotation with the properties $\mathbf{Q}^T = \mathbf{Q}^{-1}$ and $\det \mathbf{Q} = 1$. Hence, the rotation of the actual configuration of the structural tensors yields $\mathbf{Q}\boldsymbol{\mathcal{U}}^S\mathbf{Q}^T$ and $\mathbf{Q}\boldsymbol{\mathcal{N}}^S\mathbf{Q}^T$. Scalar-valued quantities, like $\tilde{\mathcal{W}}^S_{coh}$ and d, are naturally invariant for rigid body rotations. Note in passing that both structural tensors are even tensors, i. e., the sign of the preferred direction vector $\bar{\mathbf{n}}^{\mathcal{S}} = -\bar{\mathbf{n}}^{\mathcal{S}}$ is eliminated; the sign of the displacement jump $[\![\mathbf{u}_S]\!]$ is, due to the restriction of non-penetrating discontinuity surfaces, always positive. However, the principle of material frame indifference cannot be satisfied a priori for the given structural tensors. In this context, the theory of invariants is applied to the cohesive potential function. As a consequence, the principle of objectivity can be satisfied by formulating the cohesive potential with respect to five basic invariants[20] $J_{(\cdot)\,i}$ of the structural tensors, viz.

$$\mathcal{W}^S_{coh}(\boldsymbol{\mathcal{U}}^S, \boldsymbol{\mathcal{N}}^S) = \mathcal{W}^S_{coh}(J_{\{\mathcal{U},\mathcal{N}\}\,i}) \quad \text{with} \quad i = 1, 2, \ldots, 5 \,. \tag{3.70}$$

[19] For the case of non-isotropic damage behaviour, a tensorial damage function $\boldsymbol{\mathcal{D}}$ would be necessary to represent the micro-crack distribution in the cohesive zone, see *Gasser & Holzapfel* [83], and citations therein. For the sake of simplicity, the introduction of such a tensorial function will be waived here.

[20] Alternatively, as the lower basic and the principal invariants are directly related to each other, the cohesive potential could be also given as $\mathcal{W}^S_{coh}(I_{\mathcal{U}\,i}, J_{\{\mathcal{U},\mathcal{N}\}\,j})$, with $i = 1, 2, 3$ and $j = 4, 5$.

The corresponding invariants, cf. Section A.1.2 and Section A.1.3, read

$$\begin{aligned} J_{\mathcal{U}1} &= \operatorname{tr} \boldsymbol{\mathcal{U}}^S\,, \\ J_{\mathcal{U}2} &= \operatorname{tr} (\boldsymbol{\mathcal{U}}^S)^2\,, \\ J_{\mathcal{U}3} &= \operatorname{tr} (\boldsymbol{\mathcal{U}}^S)^3\,, \end{aligned} \quad \left| \quad \begin{aligned} J_{\{\mathcal{U}\mathcal{N}\}4} &= \operatorname{tr} (\boldsymbol{\mathcal{U}}^S \boldsymbol{\mathcal{N}}^S)\,, \\ J_{\{\mathcal{U}\mathcal{N}\}5} &= \operatorname{tr} [(\boldsymbol{\mathcal{U}}^S)^2 \boldsymbol{\mathcal{N}}^S]\,. \end{aligned} \right. \tag{3.71}$$

Therein, the invariant $J_{\{\mathcal{U}\mathcal{N}\}4}$ represents the squared "fibre" stretch (length) in the direction of $\bar{\mathbf{n}}^{\mathcal{S}}$, whereas the mixed invariant $J_{\{\mathcal{U}\mathcal{N}\}5}$ has no physical meaning. For a profound discussion on invariant formulations and non-isotropic material behaviour, the interested reader is referred to *Schröder & Neff* [167] and *Karajan* [116].

The **cohesive potential function** is postulated, following *Gasser & Holzapfel* [83], as

$$\mathcal{W}^S_{coh}(J_{\mathcal{U}1}, J_{\{\mathcal{U}\mathcal{N}\}4}) = \frac{\lambda^S_{\perp}}{2} J_{\{\mathcal{U}\mathcal{N}\}4} + \frac{\mu^S_{\sim}}{2}(J_{\mathcal{U}1} - J_{\{\mathcal{U}\mathcal{N}\}4})\,. \tag{3.72}$$

The material parameters $\lambda^S_{\perp}$ and $\mu^S_{\sim}$ characterise the normal and tangential response. Consequently, the traction vector $\bar{\mathbf{t}}^{S,\mathcal{S}}$ arises from the derivation of the cohesive potential function, viz.

cohesive traction on $\bar{\mathcal{S}}$

$$\bar{\mathbf{t}}^{S,\mathcal{S}} = \frac{\partial \tilde{\mathcal{W}}^S_{coh}}{\partial [\![\mathbf{u}_S]\!]} = (1-d)\big(\bar{\mathbf{t}}^{S,\mathcal{S}}_{\perp} + \bar{\mathbf{t}}^{S,\mathcal{S}}_{\sim}\big)$$
$$\text{with} \quad \bar{\mathbf{t}}^{S,\mathcal{S}}_{\perp} = \lambda^S_{\perp}\,[\![\mathbf{u}^{\perp}_S]\!] \quad \text{and} \quad \bar{\mathbf{t}}^{S,\mathcal{S}}_{\sim} = \mu^S_{\sim}\,[\![\mathbf{u}^{\sim}_S]\!]\,. \tag{3.73}$$

3.2.4 Localisation of Discontinuities

In order to simulate failure mechanics, it is essential to compute the crack propagation direction numerically. The fundamental failure criteria discussed in Section 3.1 are in principal applicable to most fracture problems. But, from a numerical point of view, these fundamental criteria tend to be too "expensive" for 3-d simulations. Thus, an additional criterion is favoured for the prediction of the failure initiation. The failure is in general initiated at the state where the material stability is lost. The loss of material stability can be interpreted as the appearance of a discontinuous bifurcation. It can be shown that, under certain simplifying assumptions, material instability, the appearance of a discontinuous bifurcation and the so-called loss of ellipticity are coherent, see e.g. *Linder et. al* [128], and citations therein. Hence, the failure prediction can be computed with the criteria of loss of ellipticity. The loss of ellipticity is based on the investigation of the so-called (tangent) acoustic tensor $\boldsymbol{\mathcal{Q}}$. Furthermore, it can be shown that the

investigation of $\boldsymbol{\mathcal{Q}}$ results in the common *Rankine*[21]-criterion for failure processes.

In the following, only the basic procedure for the determination of the biphasic finite acoustic tensor will be presented. For a circumstantial overview on this topic, the interested reader is referred to *Mahnkopf* [132]. The determination of the relevant acoustic tensor is based on a localisation analysis. For this analysis, the jump related constituent balance equations, recall (3.59), are evaluated on a first[22]-order singular surface $\mathcal{S}$, in order to localise discontinuities. If a first-order singular surface with respect to the constituents velocity $\overset{\prime}{\mathbf{x}}_\alpha$ is found, a bifurcation process is assumed for further increasing external loads. The localisation analysis is based on the assumptions of homogeneity, quasi-static processes, material singular surfaces ($\overset{\prime}{\mathbf{x}}_S = \overset{\prime}{\mathbf{x}}_\mathcal{S}$), and, compared to the sonic velocity of the fluid phase, a relatively small seepage velocity. These assumptions correlate to those presented by *Blome* [14]. Provided a jump free pressure field $[\![\mathcal{p}]\!]$, recall equation (3.62), the aforementioned evaluation of the constituents – mass and momentum – balance equations yields

$$\left[\left(\mathbf{I}\otimes\boldsymbol{\mathcal{T}}_E^S + \overset{4}{\boldsymbol{\mathcal{C}}}{}^{23}_{T}\right)(\bar{\mathbf{n}}^\mathcal{S}\otimes\bar{\mathbf{n}}^\mathcal{S})\right]\boldsymbol{\beta}_S =: \boldsymbol{\mathcal{Q}}(\bar{\mathbf{n}}^\mathcal{S})\boldsymbol{\beta}_S = \mathbf{0}\,. \tag{3.75}$$

Therein, the acoustic tensor $\boldsymbol{\mathcal{Q}}$ is postulated with respect to *Mahnkopf* [132]. This acoustic tensor is also known as the drained acoustic tensor in the literature, see e. g. *Callari et. al* [33]. Note that $\overset{4}{\boldsymbol{\mathcal{C}}}{}^{23}_{T}$ is the fourth-order material tangent with a transposition of its second basis system with its third one, cf. Appendix A. In (3.75), $\boldsymbol{\beta}_S$ represents the so-called amplitude vector which points in the direction of $\bar{\mathbf{n}}^\mathcal{S}$. Consequently, it is assumed that $\boldsymbol{\beta}_S = \boldsymbol{\beta}_S(\bar{\mathbf{n}}^\mathcal{S})$. Further details on $\boldsymbol{\beta}_S$ are for the following determination of a crack propagation criteria irrelevant. For non-trivial solutions of (3.75), i. e., $\boldsymbol{\beta}_S \neq \mathbf{0}$, the condition $\det\left(\boldsymbol{\mathcal{Q}}\right) = 0$ needs to be fulfilled. Thus, within the given context, the proportionality

$$\boldsymbol{\mathcal{Q}}\,\boldsymbol{\beta}_S \propto \mathbf{T}_E^S\,\mathbf{n}^* \tag{3.76}$$

holds for a vector $\mathbf{n}^* = \mathbf{n}^*(\bar{\mathbf{n}}^\mathcal{S})$. Based on these insights, the crack propagation criterion can be postulated by regarding an eigenvalue λ_i and eigenvector $\mathbf{n}_i^*$ problem, viz.

$$(\mathbf{T}_E^S - \lambda_i\mathbf{I})\,\mathbf{n}_i^* = \mathbf{0} \quad\rightsquigarrow\quad \det(\mathbf{T}_E^S - \lambda_i\mathbf{I}) = 0 \quad\text{with}\quad i = 1,2,3\,. \tag{3.77}$$

This can be interpreted as follows, when the maximum eigenvalue λ_{max}, i. e., the maximum

[21] *William John Macquorn Rankine* (1820–1872): Scottish engineer and physicist who is, together with *Rudolf Clausius* and *Sir William Thomson, 1st Baron Kelvin*, the founding contributor of the science of thermodynamics. He published several hundred papers and notes on science and engineering topics, also including a complete theory of the steam engine. [WIKIPEDIA]

[22] The n-order of a singular surface $\mathcal{S}$ is defined by void jumps of the gradients, with order 0 to $n-1$, of a mechanical quantity Ψ^α, viz.

$$[\![\mathrm{Grad}^k_\alpha\Psi^\alpha]\!] = \mathbf{0} \quad\text{with}\quad k = 0,\dots,n-1\,. \tag{3.74}$$

principle stress, exceeds a critical value f_c, the crack propagation criterion is met with

$$\{\lambda_2, \lambda_3\} < \lambda_{max} > f_c \,. \tag{3.78}$$

Thus, the crack-propagation direction is perpendicular to the correlated maximum principle-stress direction $\mathbf{n}^*_{max}$. This criterion is also known as the normal stress, *Coulomb*[23], or *Rankine* criterion.

[23] *Charles Augustin de Coulomb* (1736 – 1806): French physicist who is best known for developing "*Coulomb*'s law", the definition of the electrostatic force of attraction and repulsion. Also the SI unit of charge, the coulomb, was named after him. [WIKIPEDIA]

Chapter 4:
Numerical Methodology

This chapter presents the numerical implementation of the previously developed biphasic continuum-mechanical model. The numerical implementation focuses on the extension of the well-known Finite-Element Method (FEM) for the numerical simulation of discrete damage processes. The extension or enrichment, respectively, is necessary to numerically cover jump quantities in the discretised field functions. Probably the most popular enrichment of the FEM is the so-called extended Finite-Element Method (XFEM). The basic principle of the XFEM is the rendering of discontinuous field functions with additional global degrees of freedom (DOF). Prior to the discussion on the XFEM, its basic principle is first introduced using an example from the field of elasto-inelastic material behaviour. This example yields an augmented FEM (AugFEM). Finally, sophisticated tracking techniques are presented for the successful numerical simulation of discontinuities.

As the general FEM has become a standard in engineering practise, multiple authors contributed to its fundamental introduction, e. g., *Bathe* [8], *Schwarz* [169], *Braess* [29], and *Zienkiewicz & Taylor* [198], to name only a few. For an introduction into the application of the FEM to TPM problems, the interested reader is referred to, e. g., *Ehlers et al.* [62], *Ellsiepen* [67], and *Ammann* [2]. Concerning the numerical approximation of discontinuous field functions within the framework of the XFEM, see *Belytschko & Black* [10], *Moës et al.* [139], *Dolbow* [48], and *Sukumar et al.* [179], for the – as far as the author of this monograph is aware – original works on this topic. A sophisticated finite-element based computational framework for the 3-d propagation of cracks on basis of a variational formulation and on node doubling has been presented by *Gürses & Miehe* [90]. An initial presentation of the AugFEM can be found in *Rempler et al.* [158].

4.1 Finite-Element Method (FEM)

The FEM is a numerical technique for the finding of approximate solutions to partial differential equations (PDE). These PDE arise in general from weak formulations of governing equations to continuum-mechanical problems. These problems have been discussed in detail in the previous chapters. A feasible discretisation of the quantities, in the ansatz and test spaces (2.78), is crucial for the numerical realisation of the corresponding material behaviour. The following discretisation process proceeds from Section 2.6.4. Given the weak formulation of the BVP (2.77), the discretisation extends to a spatial and a temporal domain. In the following, each spatial discretised quantity, function or space, respectively, is denoted with the superscript $(\cdot)^h$; the discretisation in time is represented with the subscript $(\cdot)_n$.

4.1.1 Spatial Discretisation

The spatial discretisation of the domain Ω requires its partition into E non-overlapping subdomains Ω_e, the so-called finite-elements. Each finite-element consists of N_e nodes, individually referenced to as P^j. Multiple neighbouring elements can partially share nodes. The total sum of N nodes form the spatial discretised domain Ω^h. The discretised domain is also called the finite-element mesh. Furthermore, it is the set of all subdomains Ω_e and is, together with the set of all nodes $\mathcal{N}$, given by

$$\Omega \approx \Omega^h = \bigcup_{e=1}^{E} \Omega_e \quad \text{and} \quad \mathcal{N} = \bigcup_{j=1}^{N} P^j(\Omega_e)\,. \tag{4.1}$$

In analogy to the spatial discretisation of the domain, the until now continuous ansatz and test spaces (2.78) need to be discretised as well. Thus, the space discrete ansatz $\{\mathbf{u}_S^h, \mathcal{P}^h\}$ and test functions $\{\delta\mathbf{u}_S^h, \delta\mathcal{P}^h\}$ approximate the continuous field functions as follows:

$$\begin{aligned}
\mathbf{u}_S(\mathbf{x},t) &\approx \mathbf{u}_S^h(\mathbf{x},t) &&= \bar{\mathbf{u}}_S^h(\mathbf{x},t) &&+ \sum_{j=1}^{N} \boldsymbol{\Upsilon}_{\mathbf{u}}^j(\mathbf{x})\ \mathbf{u}_S^j(t) &&\in \mathcal{A}^{\mathbf{u},h}(t)\,,\\
\mathcal{P}(\mathbf{x},t) &\approx \mathcal{P}^h(\mathbf{x},t) &&= \bar{\mathcal{P}}^h(\mathbf{x},t) &&+ \sum_{j=1}^{N} \boldsymbol{\Upsilon}_{\mathcal{P}}^j(\mathbf{x})\ \mathcal{P}^j(t) &&\in \mathcal{A}^{\mathcal{P},h}(t)\,,\\
\delta\mathbf{u}_S(\mathbf{x}) &\approx \delta\mathbf{u}_S^h(\mathbf{x}) &&= &&\sum_{j=1}^{N} \boldsymbol{\Upsilon}_{\mathbf{u}}^j(\mathbf{x})\,\delta\mathbf{u}_S^j &&\in \mathcal{T}^{\mathbf{u},h}\,,\\
\delta\mathcal{P}(\mathbf{x}) &\approx \delta\mathcal{P}^h(\mathbf{x}) &&= &&\sum_{j=1}^{N} \boldsymbol{\Upsilon}_{\mathcal{P}}^j(\mathbf{x})\,\delta\mathcal{P}^j &&\in \mathcal{T}^{\mathcal{P},h}
\end{aligned}$$

$$\text{with} \quad \begin{cases}
\boldsymbol{\Upsilon}_{(\cdot)}^j(\mathbf{x}) = \left[\operatorname{diag}\left(\Upsilon_{\mathrm{DOF}}^j(\mathbf{x})\right)\right] & : \text{ matrix of global basis functions}\,,\\
\mathrm{DOF} \in \{u_{S1}, \ldots, u_{Sd}, \mathcal{P}\} & : \text{ degrees of freedom (primary variables)}\,,\\
\Upsilon_{\mathrm{DOF}}^j = 0\,, \text{ on } \Gamma_D^h & : \text{ global basis functions}\,,\\
j = 1, \ldots, N & : \text{ node index}\,.
\end{cases} \tag{4.2}$$

Therein, $\{\mathcal{A}^{\mathbf{u},h}, \mathcal{A}^{\mathcal{P},h}\}$ and $\{\mathcal{T}^{\mathbf{u},h}, \mathcal{T}^{\mathcal{P},h}\}$ denote the discretised trial and test spaces. The enclosed global basis functions[1] in $\boldsymbol{\Upsilon}_{(\cdot)}^j$ are linearly independent and fulfil the homogeneous *Dirichlet* boundary conditions on Γ_D^h. The unknown nodal quantities, i. e., the DOF $\{\mathbf{u}_S^j, \mathcal{P}^j\}$, are defined at their respective finite-element node P^j. Note that the global basis functions only depend on the spatial position $\mathbf{x}$, whereas the DOF are only time-dependent. Each scalar-valued DOF-coefficient, namely $\{u_{S1}, \ldots, u_{Sd}, \mathcal{P}\}$, is assigned to

[1] Here, the *Bubnov-Galerkin* method is applied. Thus, $\{\mathbf{u}_S^h, \mathcal{P}^h\}$ proceed from the same basis functions as their test counterparts $\{\delta\mathbf{u}_S^h, \delta\mathcal{P}^h\}$, recall Section 2.6.4.

respective basis functions $\Upsilon^j_{\mathrm{DOF}}$. Thus, the DOF-coefficients can be mapped inside the discrete domain. This mapping allows the computation of physical quantities besides finite-element nodes, e.g., at integration points. With

$$\Upsilon^j_{\mathrm{DOF}}(\mathbf{x}) = 0 \quad \text{if} \quad \mathbf{x} \notin \bigcup_{e \in E^*} \Omega_e \quad \text{and} \quad \Upsilon^j_{\mathrm{DOF}}(\mathbf{x}_i) = \delta^j_i \quad \text{with} \quad \begin{cases} i,j & = & 1,\dots,N\,, \\ i=j & : & \delta^j_i = 1\,, \\ i \neq j & : & \delta^j_i = 0\,, \end{cases} \tag{4.3}$$

the mapping is only supporting finite-elements E^* which are attached to the respective node P^j. Moreover, with (4.3), the basis functions $\Upsilon^j_{\mathrm{DOF}}$ are normalised by the *Kronecker* symbol δ^j_i at every nodal position $\mathbf{x}_i$. These limitations assure that the DOF correspond to the values of the approximated solution at each finite-element node. Furthermore, the discrete test functions $\{\delta\mathbf{u}^h_S(\mathbf{x}), \delta\mathcal{P}^h(\mathbf{x})\}$ must satisfy the Partition-of-Unity (PU) principle. This principle states that the sum of the basis functions is for every point $\mathbf{x} \in \Omega^h$ equal to one. Consequently, this results in a system of $DOF \times N$ linearly independent equations.

A "static" **reference element** Ω^ξ_e is defined for the element-wise numerical evaluation of the system of linearly independent equations. Its local coordinates are represented by $\boldsymbol{\xi}$. The geometry transformation between the reference and a deformed (physical) element is mapped isoparametrically, viz. $\boldsymbol{\Upsilon}^j_{GEO} = \boldsymbol{\Upsilon}^j$. Element integrals can then be substituted by

$$\int_{\Omega_e} f(\mathbf{x})\,\mathrm{d}v \;=\; \int_{\Omega^\xi_e} f(\underbrace{\sum_{j=1}^{N_e} \boldsymbol{\Upsilon}^j_{GEO}(\boldsymbol{\xi})\,\mathbf{x}_j}_{\mathbf{x}(\boldsymbol{\xi})})\,\bar{J}(\boldsymbol{\xi})\,\mathrm{d}v_\xi \qquad \text{with} \quad \begin{cases} \boldsymbol{\Upsilon}^j_{GEO} & = & \boldsymbol{\Upsilon}^j\,, \\ \bar{J}(\boldsymbol{\xi}) & = & \det\left(\dfrac{\mathrm{d}\mathbf{x}(\boldsymbol{\xi})}{\mathrm{d}\boldsymbol{\xi}}\right)\,. \end{cases} \tag{4.4}$$

The volume of the reference element is denoted with v_ξ. The *Jacobi*an determinant $\bar{J}$ of the reference element is computed similarly as its counterpart (2.17). As a result of the geometry transformation, the integration of (nearly) arbitrary shaped finite-elements can be transferred to the reference element. Moreover, a relation of the physical coordinate system $\mathbf{x}$ to the local coordinates $\boldsymbol{\xi}$ can be established as

$$\mathbf{x}(\boldsymbol{\xi}) = \sum_{j=1}^{N_e} \boldsymbol{\Upsilon}^j(\boldsymbol{\xi})\,\mathbf{x}_j\,. \tag{4.5}$$

Therein, the (physical) coordinates of the finite-element nodes are represented by $\mathbf{x}_j$. With (4.5), all physical quantities can be transferred to the local coordinates $\boldsymbol{\xi}$. For the sake of clarity, physical quantities which are regarded in the framework of local coordinates will be denoted as $(\cdot)(\boldsymbol{\xi})$ instead of $(\cdot)(\mathbf{x}(\boldsymbol{\xi}))$.

In this monograph, the **numerical integration** is implemented with the *Gauss*ian[2] quadrature scheme. This quadrature scheme is using K_e integration points at fixed local positions $\boldsymbol{\xi}_k \subset \Omega_e^\xi$, and corresponding quadrature weights w_k, such that

$$\int_{\Omega_e} f(\mathbf{x})\,\mathrm{d}v \;=\; \sum_{k=1}^{K_e} f\left(\mathbf{x}(\boldsymbol{\xi}_k)\right)\, \bar{J}(\boldsymbol{\xi}_k)\, w_k\,. \tag{4.6}$$

Obviously, the level of approximation to $(4.6)_1$ is directly dependent on the number of integration points. The number of integration points is defined by the integration (polynominal) order. The proper choice of the integration order is of fundamental importance for an accurate FEM solution; too few integration points can lead to unphysical results, cf. *Wieners et al.* [193].

Remark: The finite-element discretisation of multi-phasic materials differs from that of single-phase materials. In the framework of the TPM, the governing equations are fully – and strongly – coupled. Therefore, these equations need to be solved simultaneously. This results in multiple primary variables, here, the solid displacement $\mathbf{u}_S$ and the pore fluid pressure $\mathcal{P}$. As a consequence, the finite-element discretisation yields to the mixed finite-element method. Therein, the chosen ansatz functions have to fulfil the so-called inf-sup (*Ladyzhenskaya*[3] *-Babuška-Brezzi* – LBB) condition. In this context, it is possible to fulfil the inf-sub condition by the application of *Taylor-Hood* elements, cf. *Taylor & Hood* [180]. This element type uses quadratic ansatz functions for $\mathbf{u}_S$ and linear ansatz functions for $\mathcal{P}$. The application of *Taylor-Hood* elements will be omitted in this monograph as the geometrical realisation of such discontinuous elements would exceed the scope of this work. Instead, both variables will be discretised with linear ansatz functions. The author of this monograph is aware that linear-linear discretisations of $\mathbf{u}_S$ and $\mathcal{P}$ can lead to strange instabilities causing mesh-dependent solutions. These phenomena are based on so-called spurious pressure modes, see *Braess* [30] and *Brezzi & Fortin* [31]. In particular, when both the permeability and compressibility of the pore fluid tend to zero, the solution will "lock" or oscillate wildly. Such problems can be overcome with special stabilisation techniques. For a summery of this topic, the interested reader is referred *Huang et al.* [106]. □

[2] *Johann Carl Friedrich Gauß* (1777 – 1855): German scientist who contributed significantly to many fields. Sometimes he is referred to as the "greatest mathematician since antiquity". *Gauß* published only a fraction of his discoveries during his lifetime. The impressive profundity and immense scope of his work was only detected after the publication of his diaries in 1898. His brain was preserved and studied. Highly developed convolutions were found, which in the early 20$^{\text{th}}$ century was suggested as the explanation of his genius. [WIKIPEDIA]

[3] *Olga Alexandrovna Ladyzhenskaya* (1922 – 2004): Soviet and Russian mathematician who is known for her work on partial differential equations and fluid dynamics. She overcame great odds of a personal and political nature to become one of the most influential mathematicians of her generation. [*Riddle* [160]]

4.1.2 Temporal Discretisation

For the finding of a proper time discretisation method, the spatially discretised but temporally still continuous governing equations need to be analysed regarding their time dependency. This is also known as a so-called semi-discrete initial-value problem. For the sake of clarity, the temporal analysis will be denoted in an abstract illustration of all involved quantities following *Ellsiepen* [67]. Thus, all DOF from each node of the underlying finite-element mesh are summarised in a vector $\boldsymbol{y}$. The BVP can then be condensed into a clear, abstract form, viz.:

$$\boldsymbol{y} = \left[(\mathbf{u}_S^1, \mathcal{P}^1), \ldots, (\mathbf{u}_S^N, \mathcal{P}^N)\right]^T \,, \quad \Big| \quad \boldsymbol{F}(t, \boldsymbol{y}, \boldsymbol{y}') = [\ \mathsf{M}\ \boldsymbol{y}' + \mathsf{k}\ (\boldsymbol{y}) - \mathsf{f}\ ] \stackrel{!}{=} \mathbf{0}\,. \tag{4.7}$$

Herein, for convenience the abbreviation $(\cdot)' := (\cdot)'_S$ is used. Note in passing that the vector $\boldsymbol{y}$ has again the dimension $DOF \times N$. In $(4.7)_2$, the letter M represents the generalised mass matrix, k the generalised stiffness vector containing the nonlinear dependencies on $\boldsymbol{y}$, and f the generalised force vector of the external forces. The initial conditions $\boldsymbol{y}(t_0) = \boldsymbol{y}_0$ are given with $t_0 \leq t$. Analysing the global system of equations $\boldsymbol{F}(t, \boldsymbol{y}, \boldsymbol{y}')$, one can see that M inherits the singularity[4] property from the volume balance $(2.77)_1$. The singularity property arises from the missing time dependency of the primary variable $\mathcal{P}$ in the volume balance. This yields to the specification of $(4.7)_2$ as an index-1 system of differential-algebraic equations (DAE); such a system consists of ordinary differential equations (ODE) and linear – or nonlinear – algebraic equations. The index-1 indicates the number of operations that are necessary to transform the system of DAE into a system of ordinary algebraic equations. The coupled system of DAE increases the requirements of stability criteria for the numerical time-integration method. So-called higher order ***Runge*[5]*-Kutta*[6] methods** comply with these criteria. *Runge-Kutta* methods are an important family of implicit and explicit iterative methods in the field of numerical analysis. They belong to the so-called single-step methods. Furthermore, they are categorised by their number of order or their s-stages, respectively.

Remark: Even though the following discussion on the temporal discretisation process might seem to be a bit extensive, it is reasonable for a comprehensive understanding of *Runge-Kutta* methods. This understanding is crucial for a successful numerical implementation of the presented numerical methodology. In particular, the substantial implementation into the FEM-program PANDAS is highly dependent on this. □

In the following, the construction of a suitable time-integration method for the problem

[4] A matrix is defined to be singular if it is not invertible, i. e., its determinant is zero, $\boldsymbol{F}^{-1} = (\det \boldsymbol{F})^{-1} \operatorname{adj} \boldsymbol{F} \Leftrightarrow \frac{\partial \boldsymbol{F}}{\partial \mathcal{P}'} = \mathbf{0}$.

[5] *Carl David Tolmé Runge* (1856 – 1927): German mathematician, physicist, and spectroscopist. He was co-developer and co-eponym of the "*Runge-Kutta* methods". [WIKIPEDIA]

[6] *Martin Wilhelm Kutta* (1867 – 1944): German mathematician who co-developed the "*Runge-Kutta* methods". He also submitted and multiple important contributions in aerodynamics. Kutta became professor at the University of Stuttgart in 1912, where he stayed until his retirement in 1935. [WIKIPEDIA]

under study will be based on a discussion on very basic, first order ODE, namely

$$\boldsymbol{y}'(t) = \boldsymbol{f}(t, \boldsymbol{y}(t)), \quad \boldsymbol{y}(t_0) = \boldsymbol{y}_0, \quad \boldsymbol{y} \in \mathbb{R}^m, \quad t \in [t_0, T]\,. \tag{4.8}$$

Note that the bold face letters $\boldsymbol{y}' = [y_i', \ldots, y_M']^T$ and $\boldsymbol{f} = [f_i, \ldots, f_M]^T$ indicate vectorial quantities. Each coefficient $\{y_i', f_i\}$ represents a single ODE. The single ODE can be coupled to each other; either strongly, weakly or also not at all. Therefore, the problem discussed here can be regarded either as a single ODE or as a whole system of ODE. The time interval $[t_0, T]$ is decomposed by the time-step size $h_n = t_{n+1} - t_n > 0$ into $\mathbb{N}$ subintervals $[t_n, t_{n+1}]$, viz. $0 = t_0 < t_1 < \cdots < t_{\mathbb{N}-1} < t_{\mathbb{N}}$, with $n = 0, 1, 2, \ldots, \mathbb{N}-1$. It is assumed that the exact solution of a starting point $(t_0, \boldsymbol{y}(t_0))$ is given and that the solution of $\boldsymbol{y}(t_n + h_n)$ can be found by

$$\begin{aligned} \boldsymbol{y}(t_n + h_n) &= \boldsymbol{y}(t_n) + \int_{t_n}^{t_n+h_n} \boldsymbol{f}(t, \boldsymbol{y}(t))\, \mathrm{d}t = \boldsymbol{y}(t_n) + h_n \int_0^1 \boldsymbol{f}(t_n + \tau\, h_n, \boldsymbol{y}(t_n + \tau\, h_n))\, \mathrm{d}\tau \\ &= \sum_{k=0}^{\infty} \frac{h_n^k}{k!}\, \boldsymbol{y}^{(k)}(t_n) + \boldsymbol{\mathcal{R}}_k(t_n, h_n)\,. \end{aligned} \tag{4.9}$$

For the numerical approximation of the analytical right-hand side integrals $(4.9)_1$, a *Taylor*[7] series expansion[8] $(4.9)_2$ is applied. Therein, $\boldsymbol{\mathcal{R}}_k = \boldsymbol{\mathcal{R}}_k(t_n, h_n)$ denotes the *Lagrange*an remainder.

The numerical approximation $\boldsymbol{y}_{n+1}$ of the unknown values $\boldsymbol{y}(t_n + h_n)$ can be categorised into two different classes of methods, i. e., single-step and multi-step methods. Single-step methods refer to only one previous solution to determine the next unknown values. Multi-step methods attempt to gain efficiency by keeping and using the information from multiple previous steps. With regard to memory costs, particularly in the context of the designated enlarged global system of equations of the XFEM, only single-step methods are discussed in this monograph. The definition of **single-step methods** reads

$$\boldsymbol{y}_{n+1} = \boldsymbol{y}_n + h_n\, \boldsymbol{\phi}^R(t_n, \boldsymbol{y}_n; h_n) \quad \text{with the approximations} \quad \left\{ \begin{array}{rcll} \boldsymbol{y}_{n+1} & \approx & \boldsymbol{y}(t_n + h_n)\,, & \\ \boldsymbol{y}_n & \approx & \boldsymbol{y}(t_n)\,, & \text{and} \\ \boldsymbol{y}_0 & = & \boldsymbol{y}(t_0)\,. & \end{array} \right. \tag{4.10}$$

Therein, $\boldsymbol{\phi}^R = \boldsymbol{\phi}^R(t_n, \boldsymbol{y}_n; h_n)$ is an incremental function. This incremental function is only referring to quantities from one single-step. For *Taylor*-series-based methods, the incremental function implies terms from $(4.9)_2$ that follow $k > 0$. Note that for the sake of clarity, the notation of the implied dependency on $(\ldots; h_n)$ will be omitted in the following

[7] *Brook Taylor* (1685 – 1731): English mathematician who invented his best know work, the "*Taylor* series", at the age of 27. *Herrmann* [102]

[8] Alternatively to the *Taylor* series expansion of the right-hand side integral of $(4.9)_1$, one can also introduce *Runge-Kutta* methods by the application of a numerical quadrature rule like, e. g., a *Gauss*ian quadrature, see *Ellsiepen* [67].

discussion. Because of the approximation principle of $\boldsymbol{y}_{n+1}$, an imprecision error must be expected. This error depends on the amount of increments included in $\boldsymbol{\phi}^R$ and on the accuracy of the preceding solutions $\boldsymbol{y}_n$. Multiple levels of accuracy exist for a numerical approximation of the incremental function $\boldsymbol{\phi}^R$. For the most basic approximation, only the first term of the *Taylor* series expansion $(4.9)_2$ is taken into account. The remaining remainder is neglected. This is called **explicit** (or **forward**) ***Euler*'s method**, and it reads

$$\begin{aligned} \boldsymbol{y}(t_{n+1}) &= \boldsymbol{y}(t_n) + h_n\,\boldsymbol{y}'(t_n) + \overbrace{\frac{h_n^2}{2}\,\boldsymbol{y}''(\tau)}^{\boldsymbol{\mathcal{R}}_{k=2}(\tau,h_n)} \quad \text{with} \quad t_n < \tau < t_{n+1}\,, \\ \approx \boldsymbol{y}_{n+1} &= \boldsymbol{y}_n + h_n\,\boldsymbol{f}(t_n,\boldsymbol{y}_n)\,. \end{aligned} \tag{4.11}$$

This formulation can also be interpreted as a 1^{st} order *Runge-Kutta* method. This low-level method is, because of its poor accuracy, hardly ever used in practise. Nevertheless, it nicely explains the principle of methods based on *Taylor* series. For differential equations resulting from spatially fixed FE discretisations, the system of ODE becomes "stiff". This stiffness inhibits the use of explicit time-integration schemes because the numerical results can become unstable. So, one step forward to common numerical procedures for the solution of stiff ODE is to reformulate the explicit method $(4.11)_2$ implicitly. This is called **implicit** (or **backward**) ***Euler*'s method** and it starts from the *Taylor* series expansion as

$$\boldsymbol{y}(t_n) = \boldsymbol{y}(t_{n+1}-h_n) = \boldsymbol{y}(t_{n+1}) - h_n\,\boldsymbol{y}'(t_{n+1}) + \frac{h_n^2}{2}\,\boldsymbol{y}''(\tau)\,, \tag{4.12}$$

until its implicit dependence of the unknown $\boldsymbol{y}_{n+1}$ reads

$$\begin{aligned} \boldsymbol{y}(t_{n+1}) &= \boldsymbol{y}(t_n) + h_n\,\boldsymbol{y}'(t_{n+1}) + \frac{h_n^2}{2}\,\boldsymbol{y}''(\tau) \quad \text{with} \quad t_n < \tau < t_{n+1}\,, \\ \approx \boldsymbol{y}_{n+1} &= \boldsymbol{y}_n + h_n\,\boldsymbol{f}(t_{n+1},\boldsymbol{y}_{n+1})\,. \end{aligned} \tag{4.13}$$

By the extension of the incremental function $\boldsymbol{\phi}^R$ with additional *Taylor*-series terms, one can directly identify higher order *Runge-Kutta* methods, viz.

$$\boldsymbol{y}(t_{n+1}) = \underbrace{\boldsymbol{y}(t_n) + h_n\,\boldsymbol{y}^{(1)}(t_n)}_{\substack{\textit{Euler's}\\ \text{method}}} + \underbrace{\frac{h_n^2}{2}\,\boldsymbol{y}^{(2)}(t_n)}_{\substack{\textit{Runge-Kutta}\\ 2^{\text{nd}}\text{ order method}}} + \cdots + \underbrace{\frac{h_n^k}{k!}\,\boldsymbol{y}^{(k)}(t_n)}_{\substack{\textit{Runge-Kutta}\\ k^{\text{th}}\text{ order method}}} + \boldsymbol{\mathcal{R}}_k \quad \text{with} \quad k = 0,\ldots,\infty\,. \tag{4.14}$$

It has been proven that higher order implicit *Runge-Kutta* methods provide a suitable numerical integration scheme for general TPM problems. The higher the order of the method is, the higher its accuracy gets. Practically speaking, people stop at the 5^{th} order. The most popular *Runge-Kutta* method is – from a practical viewpoint because of

its symmetrical form and its simple coefficients – the 4^{th} order method, also known as the "classical *Runge-Kutta* method".

The final construction of a suitable *Runge-Kutta*-based numerical time-integration method for the problems under study is based on the previous insights. In order to avoid the necessity of numerically computing high-order derivatives $\boldsymbol{y}^{(k)}(=\boldsymbol{f}^{(k-1)})$ in $\boldsymbol{\phi}^R$, see (4.10) and (4.14), the *Runge-Kutta* methods reformulate the higher-order derivative terms of the *Taylor*-series expansion by

$$\begin{aligned} \boldsymbol{\phi}^R(t_n, \boldsymbol{y}_n; h_n) &= \sum_{i=1}^{s} b_i \, \boldsymbol{Y}'_{ni} \,, \\ (\boldsymbol{k}_{ni} =)\ \boldsymbol{Y}'_{ni} &= \boldsymbol{f}(t_n + c_i \, h_n, \boldsymbol{y}_n + h_n \sum_{j=1}^{s} a_{ij} \, \boldsymbol{Y}'_{nj}) \,, \\ \boldsymbol{y}_{n+1} &= \boldsymbol{y}_n + h_n \, \boldsymbol{\phi}^R(t_n, \boldsymbol{y}_n; h_n) \,. \end{aligned} \tag{4.15}$$

Therein, $\boldsymbol{Y}'_{ni} = \boldsymbol{Y}'_{ni}(t_n, \boldsymbol{y}_n)$ are stage derivatives[9] at the time-step stages $T_{ni} = t_n + c_i \, h_n$. The stage derivatives are approximations for $\boldsymbol{y}'(T_{ni})$. The weighting factors a_{ij}, b_i, c_i are pre-defined and pre-calculated in order to obtain efficient, stable and accurate methods. These factors are usually summarised in a so-called *Butcher* tableau, see *Butcher* [32]. Alternatively to the computation of the stage derivatives $\boldsymbol{Y}'_{ni}$, it is also possible, and quite common in numerical codes, to directly compute the stage solution $\boldsymbol{Y}_{ni} = \boldsymbol{Y}_{ni}(t_n, \boldsymbol{y}_n)$ by

$$\begin{aligned} \boldsymbol{\phi}^R(t_n, \boldsymbol{y}_n; h_n) &= \sum_{i=1}^{s} b_i \, \boldsymbol{f}(t_n + c_i \, h_n, \, \boldsymbol{Y}_{ni}) \,, \\ \boldsymbol{Y}_{ni} &= \boldsymbol{y}_n + h_n \sum_{j=1}^{s} a_{ij} \, \boldsymbol{f}(t_n + c_j \, h_n, \, \boldsymbol{Y}_{nj}) \,, \\ &= \boldsymbol{y}_n + h_n \sum_{j=1}^{s} a_{ij} \, \boldsymbol{Y}'_{nj} \,, \\ \boldsymbol{y}_{n+1} &= \boldsymbol{y}_n + h_n \, \boldsymbol{\phi}^R(t_n, \boldsymbol{y}_n; h_n) \,. \end{aligned} \tag{4.16}$$

A figurative example of an explicit 2^{nd} order *Runge-Kutta* method, the so-called *Heun*'s[10] method, is given in Figure 4.1. This geometrical visualisation is exemplarily denoted for one single coefficient $\{y = y_i, f = f_i\}$ of the vectors $\boldsymbol{y}$ and $\boldsymbol{f}$. As one can see, the difference in constructing an explicit or implicit *Runge-Kutta* method is rooted in the choice of the corresponding weighting factors a_{ij}.

With focus on the applicability to the FEM, the general, fully-implicit *Runge-Kutta* method (IRK), i. e., $a_{ij} \neq 0$ for $j \geq i$, is unmeant. The sparse structure of the linearised

[9] Note in passing that it is quite common in the literature to use the variable $\boldsymbol{k}_{ni}$ instead of the here – for the sake of a concise notation – denoted variable $\boldsymbol{Y}'_{ni}$. These variables are also referred to as slope.

[10] Karl Heun (1859–1929): German mathematician who is known for his improvement of *Carl David Tolmé Runge*'s method for the solution of differential-algebraic solutions. His improvement is called "*Heun*'s method", the "modified *Euler* method", or "the explicit trapezoidal rule". [WIKIPEDIA], [164]

An explicit 2nd order *Runge-Kutta* method: *Heun*'s method ($s = 2$)

Butcher tableau (*Heun*):

$$\begin{array}{c|cc} c_1 & a_{11} & a_{12} \\ 0 & 0 & 0 \\ c_2 & a_{21} & a_{22} \\ 1 & 1 & 0 \\ \hline & b_1 & b_2 \\ & \frac{1}{2} & \frac{1}{2} \end{array}$$

for $j \geq i$:
$a_{ij} = 0$: explicit
$a_{ij} \neq 0$: implicit

2nd order *Runge-Kutta* method (s-derivatives):

$$\begin{aligned} Y'_{n1} &= f\big(t_n + c_1\, h_n,\, y_n + h_n\,(a_{11}\, Y'_{n1} + a_{12}\, Y'_{n2})\big) \\ Y'_{n2} &= f\big(t_n + c_2\, h_n,\, y_n + h_n\,(a_{21}\, Y'_{n1} + a_{22}\, Y'_{n2})\big) \\ \phi^R &= b_1\, Y'_{n1} + b_2\, Y'_{n2} \end{aligned}$$

2nd order *Runge-Kutta* method (s-solutions):

$$\begin{aligned} Y_{n1} &= y_n + h_n\,(a_{11}\, Y'_{n1} + a_{12}\, Y'_{n2}) \\ Y_{n2} &= y_n + h_n\,\big(a_{21}\, Y'_{n1} + a_{22}\, Y'_{n2}\big) \\ \phi^R &= b_1\, f(t_n + c_1\, h_n,\, Y_{n1}) + b_2\, f(t_n + c_2\, h_n,\, Y_{n2}) \end{aligned}$$

$$\rightsquigarrow\; y_{n+1} = y_n + h_n \left[\tfrac{1}{2} \underbrace{f(t_n, \{y_n | Y_{n1}\})}_{Y'_{n1}} + \tfrac{1}{2} \underbrace{f(t_n + h_n, \{y_n + h_n\, Y'_{n1} | Y_{n2}\})}_{Y'_{n2}} \right]$$

Geometrical visualisation:

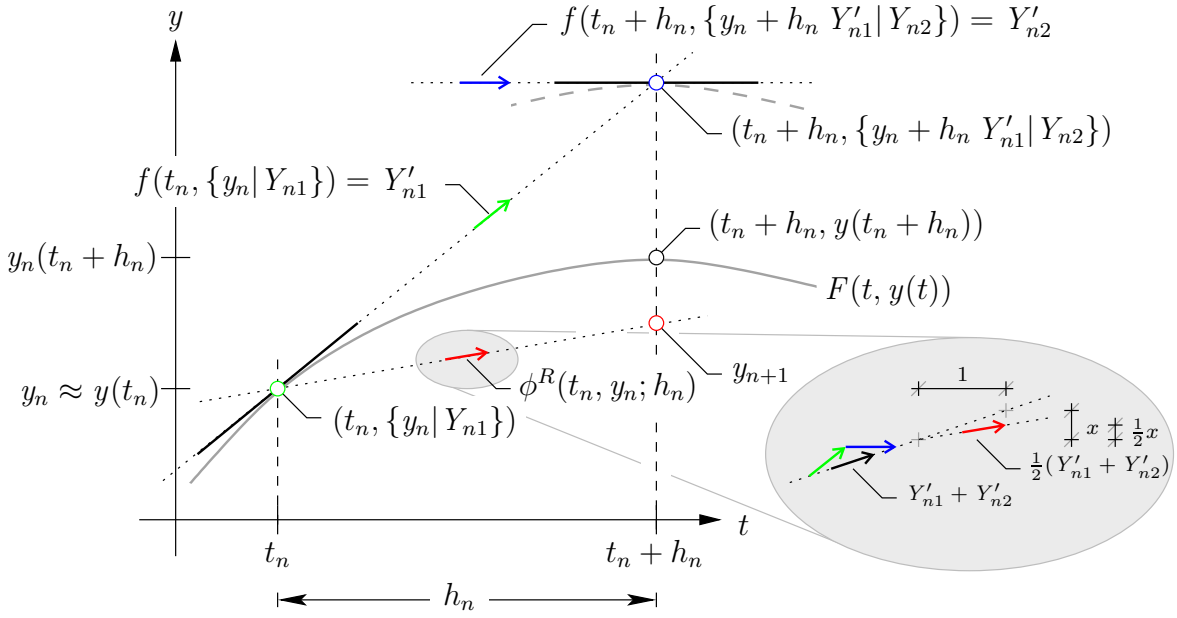

Figure 4.1: Figurative example for the geometrical visualisation of an explicit 2nd order *Runge-Kutta* method; it is represented by stage derivatives Y'_{ni}, or stage solutions Y_{ni}.

FE systems would be destroyed through the IRK-type coupling of the stages. Following this, only the special type of diagonally implicit *Runge-Kutta* method (DIRK) is discussed

in this monograph. For a DIRK method, the relations $a_{si} = b_i$ and $a_{ij} = 0$ for $j > i$ hold. Therein, the condition $a_{si} = b_i$ guarantees a stiffly accurate method. This originates from the fact that the solution of $\boldsymbol{Y}_{ns}$ on the last stage coincides with the new solution $\boldsymbol{y}_{n+1}$. These characteristics allow to reduce the integration steps from $(4.16)_3$ to

$$\boldsymbol{Y}_{ni} = \boldsymbol{y}_n + h_n \sum_{j=1}^{i} a_{ij}\, \boldsymbol{Y}'_{nj} = \underbrace{\boldsymbol{y}_n + h_n \sum_{j=1}^{i-1} a_{ij}\, \boldsymbol{Y}'_{nj}}_{\boldsymbol{S}_{ni}} + h_n\, a_{ii}\, \boldsymbol{Y}'_{ni}\,. \tag{4.17}$$

The per-stage starting values are denoted by $\boldsymbol{S}_{ni}$. The starting values only depend on already calculated stage derivatives from previous stages. The stage tableau in Figure 4.2 visualises the decoupling of the stage-variable solutions. In order to reduce the round-off

$$\begin{array}{rcl}
\boldsymbol{Y}_{n1} &=& \overbrace{\boldsymbol{y}_n}^{\boldsymbol{S}_{n1}} + h_n\, a_{11}\, \boldsymbol{Y}'_{n1} \\
\boldsymbol{Y}_{n2} &=& \overbrace{\boldsymbol{y}_n + h_n\, a_{21}\, \boldsymbol{Y}'_{n1}}^{\boldsymbol{S}_{n2}} + h_n\, a_{22}\, \boldsymbol{Y}'_{n2} \\
\vdots & & \\
\boldsymbol{Y}_{ni} &=& \overbrace{\boldsymbol{y}_n + h_n \sum_{j=1}^{i-1} a_{ij}\, \boldsymbol{Y}'_{nj}}^{\boldsymbol{S}_{ni}} + h_n\, a_{ii}\, \boldsymbol{Y}'_{ni} \\
\vdots & & \\
\boldsymbol{Y}_{ns} &=& \overbrace{\boldsymbol{y}_n + h_n\, a_{s1}\, \boldsymbol{Y}'_{n1} + \cdots + h_n\, a_{s(s-1)}\, \boldsymbol{Y}'_{n(s-1)}}^{\boldsymbol{S}_{ns}} + h_n\, a_{ss}\, \boldsymbol{Y}'_{ns} \\
\Downarrow & & \\
\boldsymbol{y}_{n+1} &=& \boldsymbol{y}_n + h_n\, b_1\, \boldsymbol{Y}'_{n1} + \cdots + h_n\, b_s\, \boldsymbol{Y}'_{ns}
\end{array}$$

Figure 4.2: Stage tableau of a s-stage DIRK.

errors, it is a common procedure in numerical codes to introduce the stage increments $\triangle \boldsymbol{Y}_{ni} := \boldsymbol{Y}_{ni} - \boldsymbol{y}_n$. Stage increments exhibit the advantage of smaller computed values. As a consequence, the numerical error shrinks. The stage increments are then defined as

$$\frac{\triangle \boldsymbol{Y}_{ni}}{h_n\, a_{ii}} = \frac{1}{h_n\, a_{ii}} \Big(\underbrace{\boldsymbol{S}_{ni} - \boldsymbol{y}_n}_{\overline{\boldsymbol{Y}}'_{ni}} \Big) + \boldsymbol{Y}'_{ni} \quad \rightsquigarrow \quad \frac{\triangle \boldsymbol{Y}_{ni} - \overline{\boldsymbol{Y}}'_{ni}}{h_n\, a_{ii}} = \boldsymbol{Y}'_{ni}\,. \tag{4.18}$$

Therein, $\overline{\boldsymbol{Y}}'_{ni}$ denotes the accumulated stage derivative. Finally, the preceding insights

allow the definition of a sound temporal discretisation scheme for (4.7), viz.

$$\rightsquigarrow \boldsymbol{F}(T_{ni}, \underbrace{\boldsymbol{y}_n + \triangle\boldsymbol{Y}_{ni}}_{\boldsymbol{Y}_{ni}}, \underbrace{\frac{\triangle\boldsymbol{Y}_{ni} - \overline{\boldsymbol{Y}}'_{ni}}{h_n\, a_{ii}}}_{\boldsymbol{Y}'_{ni}}) =: \boldsymbol{R}_{ni}(\triangle\boldsymbol{Y}_{ni}) = \boldsymbol{0}\,, \quad i = 1, \ldots, s\,. \tag{4.19}$$

The so-called residual vector $\boldsymbol{R}_{ni}$ now depends solely on the stage increments $\triangle\boldsymbol{Y}_{ni}$. The temporal discretisation scheme (4.19) also allows the direct application of pre-defined weighting factors. The weighting factors are chosen with focus on the numerical problem under study. The numerical examples in this monograph are computed with the following two weighting-factor schemes:

"CASH32" (DIRK)

$$\begin{aligned} \gamma &= 0.4358665215\ldots \\ \delta &= \tfrac{1}{4}\,(6\gamma^2 - 20\gamma + 5) \\ \alpha &= 1 - \delta - \gamma \end{aligned}$$

γ	γ		
$\frac{1+\gamma}{2}$	$\frac{1-\gamma}{2}$	γ	
1	α	δ	γ
	α	δ	γ

"Euler" (IRK)

1	1
	1

(4.20)

The given values from $(4.20)_1$ are taken from *Ellsiepen* [67]; they are based on *Cash* [34], *Alexander* [1], and *Fritzen* [78]. This *Runge-Kutta*-based temporal integration scheme is in the FEM program PANDAS called "CASH32". For convenience, the more basic numerical examples in this monograph are computed with a standard backward (implicit) *Euler* integration scheme. The corresponding *Butcher* tableau is given in $(4.20)_2$. For further details and practical examples on the *Runge-Kutta* method, the interested reader is referred to *Herrmann* [102], *Kreyszig* [123], and *Ellsiepen* [68].

Remark: With the discretisation scheme $(4.20)_1$, the introduction of so-called embedded *Runge-Kutta* methods is straightforward. Embedded *Runge-Kutta* methods allow a numerically cheap calculation of a second approximate solution $\hat{\boldsymbol{y}}_{n+1}$ by the introduction of additional weighting factors. As a consequence, an embedded error estimation can be obtained by the difference between the two solutions $e = \|\boldsymbol{y}_{n+1} - \hat{\boldsymbol{y}}_{n+1}\|$. The substantial topic of this error estimation process will not be discussed here. The interested reader is referred to *Markert* [134], *Diebels et al.* [47] and citations therein. □

4.1.3 Solution of the System of Differential-Algebraic Equations

With the preceding spatial and temporal discretisation, the problem under study (4.19) needs to be solved for every stage of the DIRK method (4.20). In case of the "CASH32"-based Runge-*Kutta* integration scheme, the stage solution needs to be evaluated multiple times. Consequently, multiple solution increments accumulate to the final approximation

of the next time step $\boldsymbol{y}_{n+1}$. Therefore, the underlying fully discretised weak formulations of the BVP are given for every stage i as

$$\begin{aligned} R_{ni}^{V,h} \;=\; & \int_{\Omega^h} \operatorname{div}\Big(\frac{\triangle \boldsymbol{U}_{S,ni}^h - \overline{\boldsymbol{U}}_{S,ni}'^h}{h_n\, a_{ii}}\Big)\, \delta\mathcal{P}^h \,\mathrm{d}v \\ & + \int_{\Omega^h} \frac{k^F(\boldsymbol{U}_{S,ni}^h)}{\gamma^{FR}} \left[\operatorname{grad}\,(\mathcal{P}_n^h + \triangle\mathcal{P}_{ni}^h) - \rho^{FR}\,\mathbf{g}\right] \cdot \operatorname{grad}\,\delta\mathcal{P}^h \,\mathrm{d}v \\ & + \int_{\Gamma_N^{v,h}} \bar{v}^h(T_{ni})\, \delta\mathcal{P}^h \,\mathrm{d}a = 0 \quad \text{with} \quad \boldsymbol{U}_{S,ni}^h = \mathbf{u}_{S,n}^h + \triangle\boldsymbol{U}_{S,ni}^h\,, \end{aligned} \tag{4.21}$$

$$\begin{aligned} R_{ni}^{M,h} \;=\; & \int_{\Omega^h} \Big(\mathbf{T}_E^S(\boldsymbol{U}_{S,ni}^h) - \mathcal{P}_{ni}^h\,\mathbf{I}\Big) \cdot \operatorname{grad}\,\delta\mathbf{u}_S^h \,\mathrm{d}v \\ & - \int_{\Omega^h} \rho\,\mathbf{g}\cdot\delta\mathbf{u}_S^h \,\mathrm{d}v \\ & - \int_{\Gamma_N^{\mathbf{t},h}} \bar{\mathbf{t}}^h(T_{ni}) \cdot\, \delta\mathbf{u}_S^h \,\mathrm{d}a = 0 \quad \text{with} \quad \mathcal{P}_{ni}^h = \mathcal{P}_n^h + \triangle\mathcal{P}_{ni}^h\,. \end{aligned} \tag{4.22}$$

The weak formulations of the BVP of the volume balance are condensed in the vector coefficients $R_{ni}^{V,h}$; the entries from the momentum balance are condensed in $R_{ni}^{M,h}$. Therein, the capital letter variables $\{\boldsymbol{U}_{S,ni}^h, \mathcal{P}_{ni}^h\} \triangleq \boldsymbol{Y}_{ni}$, and $\{\triangle\boldsymbol{U}_{S,ni}^h, \triangle\mathcal{P}_{ni}^h\} \triangleq \triangle\boldsymbol{Y}_{ni}$, denote the stage solutions of the DOF and their stage increments, respectively. The stage solutions solely depend on already known variables. Thus, only the stage increments are unknown. The variable $\overline{\boldsymbol{U}}_{S,ni}'^h \triangleq \overline{\boldsymbol{Y}}_{ni}'$ represents the accumulated stage derivative of the solid displacement DOF. Obviously, the – also spatially discretised – *Neumann* boundary-values $\bar{v}^h$ and $\bar{\mathbf{t}}^h$ have to adopt the respective *Runge-Kutta* time stage T_{ni}, too. Note that the spatial test functions $\{\delta\mathbf{u}_S^h, \delta\mathcal{P}^h\}$ are not time dependent. Furthermore, the quantities $\{k^F,\, \mathbf{T}_E^S\}$ are deformation-dependent. Thus, they also depend on the stage values $\boldsymbol{U}_{S,ni}^h$. With these preliminaries, the solution process for the minimisation problem can be constructed as

$$\begin{aligned} \boldsymbol{R}_{ni} = \begin{bmatrix} [R_{ni}^{V,h,1}, \ldots, R_{ni}^{V,h,N}]^T \\ [R_{ni}^{M,h,1}, \ldots, R_{ni}^{M,h,N}]^T \end{bmatrix} \overset{!}{=} \mathbf{0} \quad \overset{Newton}{\rightsquigarrow} \quad & \overbrace{\frac{\mathrm{d}\boldsymbol{R}_{ni}(\triangle\boldsymbol{Y}_{ni}^m)}{\mathrm{d}\triangle\boldsymbol{Y}_{ni}^m}}^{=:\,\mathrm{D}\boldsymbol{R}_{ni}^m} \boldsymbol{\Delta}^m = \boldsymbol{R}_{ni}(\triangle\boldsymbol{Y}_{ni}^m)\,, \\ & \boldsymbol{\Delta}^m = [\mathrm{D}\boldsymbol{R}_{ni}^m]^{-1}\, \boldsymbol{R}_{ni}(\triangle\boldsymbol{Y}_{ni}^m) \\ & \Rightarrow \triangle\boldsymbol{Y}_{ni}^{m+1} = \triangle\boldsymbol{Y}_{ni}^m - \boldsymbol{\Delta}^m \\ & \big\|\boldsymbol{R}_{ni}(\triangle\boldsymbol{Y}_{ni}^{m+1})\big\| < tol. \end{aligned} \tag{4.23}$$

The minimisation problem $(4.23)_{\text{left}}$ can be solved by the application of a regular *Newton*[11] method. Therein, the presented procedure $(4.23)_{\text{right}}$ is repeated until the norm of the residual vector fulfils a pre-defined tolerance. The *Newton* iteration steps are indexed by the counter m. A crucial point in this procedure is the solution of the *Newton* increment $\boldsymbol{\Delta}^m$. In the framework of the overall numerical environment, the embedded solution of $\boldsymbol{\Delta}^m$ is the numerically most expensive part. The solution of the *Newton* increment is based on the residual tangent $\mathrm{D}\boldsymbol{R}_{ni}^m$. Therefore, a sound derivative of the function $\boldsymbol{R}_{ni}$ with respect to the *Runge-Kutta* stage increments $\triangle\boldsymbol{Y}_{ni}^m$ is needed. This derivative or residual tangent, respectively, is also known as the *Jacobi*an matrix. In this monograph, the residual tangent is computed numerically. Its numerical computation is based on the central difference quotient, viz.

$$\mathrm{D}\boldsymbol{R}_{ni}^m = \frac{\boldsymbol{R}_{ni}(\triangle\boldsymbol{Y}_{ni}^m + \boldsymbol{\epsilon}) - \boldsymbol{R}_{ni}(\triangle\boldsymbol{Y}_{ni}^m - \boldsymbol{\epsilon})}{2\,\boldsymbol{\epsilon}} \quad \text{with} \quad \epsilon = 10^{-6}\,. \tag{4.24}$$

The delta vector $\boldsymbol{\epsilon}$ needs to be assembled individually, such that to every single entry of $\triangle\boldsymbol{Y}_{ni}^m$ the delta value ϵ is added or subtracted, respectively. Even though the numerical computation of $\mathrm{D}\boldsymbol{R}_{ni}^m$ is costly (and in comparison to an analytically computed tangent somewhat inaccurate), its implementation is rather simple. Its simplicity is of great value within the context of multiple enrichment to the standard FEM. With it, the numerical implementation of enrichment is straightforward.

4.2 Augmented Finite-Element Method (AugFEM)

Prior to the following XFEM chapter, this section introduces the basic principle of adding DOF to the global system of DAE. This principle is presented in the context of elastic-inelastic material behaviour. As the scope of this section is to only briefly introduce the basic elastic-inelastic principles, it solely discusses single-phase materials. Therefore, only non-α-indexed equations and physical quantities appear herein. The numerical simulation of elastic-inelastic material behaviour proceeds from Appendix B.2. Thus, the following discussion is, for the sake of simplicity, also limited to small deformations, recall (2.24), and (2.25). The scalar-based yield function is, for the present purpose, set to a *von Mises*-type yield function, cf. (B.10).

The standard FEM is reviewed and an alternative method, i. e., an augmented Finite-Element Method (AugFEM) is presented. For the AugFEM, the history variables, which provide the information of inelastic deformations from previous time steps, are represented as Finite-Element functions. This results in additional DOF. As a consequence, generally

[11] *Sir Isaac Newton* (1643 – 1727): English scientist who is been considered by many to be the greatest and most influential scientist who ever lived. His monograph "Philosophiæ Naturalis Principia Mathematica" lays the foundations for most of classical mechanics. In this work, *Newton* described universal gravitation and the three laws of motion, which dominated the scientific view of the physical universe for the next three centuries. Thus, the field of classical mechanics is also known as "*Newton*ian mechanics". He was also highly religious. As an unorthodox Christian he wrote more on Biblical hermeneutics and occult studies than on science and mathematics, the subjects he is mainly associated with. [WIKIPEDIA]

accepted standard formulations for evaluating inelastic deformations in a numeric substep can now be replaced by a fully coupled *Newton* method, cf. Section 4.1.3.

In order to model the nonlinear material behaviour of elastic-inelastic materials, it is essential to respect the development over time of inelastic deformations occurring in both elasto-plastic and elasto-viscoplastic processes. This time-dependent material behaviour implies the use of an evolution equation for the inelastic contributions to the overall deformations. Proceeding from the standard FEM, the evolution equation, which is determined by a flow rule, see, e. g., (B.15), is generally multi-evaluated at each integration point inside each element. The internal problem of evaluating the evolution equation at every integration point is commonly solved by the closest point projection method, also referred to as return mapping or radial[12] return, see, e. g., *Simo & Hughes* [170]. The closest point projection is derived from an implicit (backward) *Euler* integration scheme, see $(4.20)_2$, by inserting the non-linear stress response into the equilibrium equation. The linearisation of the resulting nonlinear equation yields the consistent tangent approach, see *Simo & Taylor* [174]. Therefore, as was discussed in *Simo et al.* [171], it is necessary to provide internal variables or so-called history variables $\boldsymbol{\varepsilon}_p$, which contain the plastic strain behaviour from previous time steps. This results in a local DAE system for each integration point in order to obtain the actual plastic deformation and thereafter the appropriate stress, see, e. g., *Ehlers* [59]. It is obvious that this leads to an enormous numerical cost for a large number of integration points. In the following, the general possibility of representing the internal variables as FE functions is discussed. The principle of this possibility was mentioned in, e. g., *Ammann* [2], and *Becker & Miehe* [9]. This possibility was examined in *Herres et al.* [101] as an explicit expression of the consistency parameter, and the internal variables were cast into a unified algorithmic framework. Former contributions with similar numerical approaches are often discussed in the context of strain-gradient plasticity. These approaches have been documented elaborately in, e. g., *Liebe & Steinmann* [127]. An alternative solution algorithm is discussed in *Kulkarni et al.* [124].

4.2.1 Standard Small-strain Elasto-viscoplasticity

For the numerical realisation of nonlinear material behaviour of a continuum-mechanical model, all describing quantities (the displacement $\mathbf{u}$ as a primary variable and the plastic strains $\boldsymbol{\varepsilon}_p$ along with the accumulated plastic strain ε_{pv} as secondary internal variables) need to be discretised in the spatial and in the temporal domain. The discretisation in the framework of the standard FEM leads to a global and a local system of DAE. Recall, the following relations are based on a *von Mises*-type yield function, see Appendix B.2.

The displacement $\mathbf{u}$ is approximated in a finite-element space identical to (4.2). The **spatial discretisation** defines the ansatz space $\mathcal{A}^{\mathbf{u},h}(t)$ and the trial space $\mathcal{T}^{\mathbf{u},h}$. Then, the momentum equilibrium equation (B.7) is formulated weakly and spatially discretised,

[12] Note in passing that, the terminology radial originates from a circular shaped yield function, like the here used *von Mises*-type yield function. In general, yield functions are not limited to be circular shaped, see, e. g., Figure B.4.

i. e.,

$$\int_{\Omega^h} \boldsymbol{\sigma}^h \cdot \boldsymbol{\varepsilon}(\delta \mathbf{u}^h)\,\mathrm{d}v \;=\; \int_{\Gamma_N^{\mathbf{t},h}} \bar{\mathbf{t}}^h \cdot \delta \mathbf{u}^h\,\mathrm{d}a \quad \text{with} \quad \boldsymbol{\varepsilon}(\delta \mathbf{u}^h) := \operatorname{grad} \delta \mathbf{u}^h\,. \tag{4.25}$$

In this discrete setting, all integrals are approximated by the aforementioned *Gauss*ian quadrature. Thus, it remains to determine the stress $\boldsymbol{\sigma}^h(\boldsymbol{\xi}_k, t)$ and, therefore, also the internal variables $\boldsymbol{\varepsilon}_p^h = \boldsymbol{\varepsilon}_p^h(\boldsymbol{\xi}_k, t)$, and $\varepsilon_{pv} = \varepsilon_{pv}(\boldsymbol{\xi}_k, t)$, at the integration points $\boldsymbol{\xi}_k$ only. This can be condensed into an abstract system form like (4.7), viz.

$$\begin{aligned} \boldsymbol{u} &= \left[\mathbf{u}^1, \ldots, \mathbf{u}^N\right]^T\,, & \boldsymbol{F}_1(t, \boldsymbol{u}, \boldsymbol{u}', \boldsymbol{q}) &= \left[\;\; \mathsf{M}\;\boldsymbol{u}' + \mathsf{k}\;(\boldsymbol{u}, \boldsymbol{q}) - \mathsf{f} \;\;\right] \stackrel{!}{=} \mathbf{0}\,, \\ \boldsymbol{q} &= \left[(\boldsymbol{\varepsilon}_p^1, \varepsilon_{pv}^1), \ldots, (\boldsymbol{\varepsilon}_p^N, \varepsilon_{pv}^N)\right]^T\,, & \boldsymbol{F}_2(t, \boldsymbol{q}, \boldsymbol{q}', \boldsymbol{u}) &= \left[\;\; \mathsf{A}\;\boldsymbol{q}' - \mathsf{g}\;(\boldsymbol{q}, \boldsymbol{u}) \;\;\right] \stackrel{!}{=} \mathbf{0}\,, \end{aligned} \tag{4.26}$$

$$\rightsquigarrow \boldsymbol{F}(t, \boldsymbol{y}, \boldsymbol{y}') = \begin{bmatrix} \boldsymbol{F}_1 \\ \\ \boldsymbol{F}_2 \end{bmatrix} \stackrel{!}{=} \mathbf{0} \quad \text{with} \quad \boldsymbol{y} = (\boldsymbol{u}^T, \boldsymbol{q}^T)^T\,. \tag{4.27}$$

Therein, $\boldsymbol{u}$ represents the vector containing the primary (nodal) variables, and $\boldsymbol{q}$ is the vector in which the secondary (internal) variables are collected. The primary variables are stored at each node of the finite-element mesh and thus integrated into the global system of DAE. The secondary variables are internally stored at each integration point because they are only evaluated inside the local system of DAE.

The **temporal discretisation** of (4.27) is analogue to Section 4.1.2. For the sake of simplicity, an implicit (backward) *Euler* scheme, cf. $(4.20)_2$, is used for the temporal discretisation. The starting point relates to $\boldsymbol{\varepsilon}_{p,0}^h = \mathbf{0}$ at $t_0 = 0$. For every time step n, the displacement $\mathbf{u}_n^h$ satisfying the *Dirichlet* boundary conditions, the stress $\boldsymbol{\sigma}_n^h$ and the plastic strain $\boldsymbol{\varepsilon}_{p,n}^h$ satisfying the discretised constitutive relation (B.9), viz.

$$\boldsymbol{\sigma}_n^h \;:=\; \boldsymbol{\sigma}(\mathbf{u}_n^h, \boldsymbol{\varepsilon}_{p,n}^h) \;=\; \overset{4}{\boldsymbol{\mathcal{C}}} \left[\, \boldsymbol{\varepsilon}(\mathbf{u}_n^h) - \boldsymbol{\varepsilon}_{p,n}^h \,\right]\,, \tag{4.28}$$

must fulfil the equilibrium equation (4.25) and the incremental flow rule

$$\begin{aligned} \triangle \boldsymbol{\varepsilon}_{p,n}^h \;&:=\; \boldsymbol{\varepsilon}_{p,n}^h - \boldsymbol{\varepsilon}_{p,n-1}^h \\ &=\; \underbrace{\frac{\triangle t_n}{\eta} \left\langle \frac{F(\boldsymbol{\sigma}_n^h; \kappa_n^h)}{\sigma_0} \right\rangle^r}_{\lambda_n^h} \frac{\partial F(\boldsymbol{\sigma}_n^h; \kappa_n^h)}{\partial\, \boldsymbol{\sigma}}\,, \end{aligned} \tag{4.29}$$

with $\kappa_n^h = \overset{*}{\kappa}(\varepsilon_{pv,n}^h)$ and $\varepsilon_{pv,n}^h = \varepsilon_{pv,n-1}^h + \sqrt{\frac{2}{3}}\,|\triangle\boldsymbol{\varepsilon}_{p,n}^h|$. In order to evaluate the incremental flow rule, the so-called trial stress is defined

$$\begin{aligned}\boldsymbol{\sigma}_{\text{trial},n}^h(\mathbf{u}_n^h, \boldsymbol{\varepsilon}_{p,n-1}^h) &:= \overset{4}{\boldsymbol{\mathcal{C}}}\left[\,\boldsymbol{\varepsilon}(\mathbf{u}_n^h) - \boldsymbol{\varepsilon}_{p,n-1}^h\,\right] \\ &= \boldsymbol{\sigma}_n^h + 2\mu\triangle\boldsymbol{\varepsilon}_p^{h,n}\,,\end{aligned} \tag{4.30}$$

which allows to rewrite (4.29) in the form $\triangle\boldsymbol{\varepsilon}_{p,n}^h = \Lambda_n^h\,\boldsymbol{\zeta}_n^h$ with $\Lambda_n^h = |\triangle\boldsymbol{\varepsilon}_{p,n}^h|$ and

$$\boldsymbol{\zeta}_n^h = \frac{\partial F(\boldsymbol{\sigma}_n^h;\kappa_n^h)}{\partial\,\boldsymbol{\sigma}} = \frac{(\boldsymbol{\sigma}_n^h)^D}{|(\boldsymbol{\sigma}_n^h)^D|} = \frac{\triangle\boldsymbol{\varepsilon}_{p,n}^h}{|\triangle\boldsymbol{\varepsilon}_{p,n}^h|} = \frac{(\boldsymbol{\sigma}_{\text{trial},n}^h)^D}{|(\boldsymbol{\sigma}_{\text{trial},n}^h)^D|}\,. \tag{4.31}$$

Now, two cases are considered. If $|(\boldsymbol{\sigma}_{\text{trial},n}^h)^D| \le \sqrt{\frac{2}{3}}\;\overset{*}{\kappa}(\varepsilon_{pv,n-1}^h)$, the plastic multiplier is set to $\Lambda_n^h = 0$. Otherwise, $|(\boldsymbol{\sigma}_n^h)^D| = \left|(\boldsymbol{\sigma}_{\text{trial},n}^h)^D\right| - 2\mu\Lambda_n^h$ is observed. For the latter case, the identity

$$\begin{aligned}F(\boldsymbol{\sigma}_n^h;\kappa_n^h) &= |(\boldsymbol{\sigma}_n^h)^D| - \sqrt{\tfrac{2}{3}}\;\overset{*}{\kappa}(\varepsilon_{pv,n}^h) \\ &= \left|(\boldsymbol{\sigma}_{\text{trial},n}^h)^D\right| - 2\mu\Lambda_n^h - \sqrt{\tfrac{2}{3}}\;\overset{*}{\kappa}\left(\varepsilon_{pv,n-1}^h + \sqrt{\tfrac{2}{3}}\Lambda_n^h\right) \\ &=: f_n^h\left(\left|(\boldsymbol{\sigma}_{\text{trial},n}^h)^D\right|, \Lambda_n^h\right)\end{aligned} \tag{4.32}$$

allows to rewrite the incremental flow function depending on $(\boldsymbol{\sigma}_{\text{trial},n}^h, \Lambda_n^h)$ and the history variable $\varepsilon_{pv,n-1}^h$ from the previous time step. The flow function is inserted in (4.29), which gives

$$\Lambda_n^h = \frac{\triangle t_n}{\eta}\left\langle\frac{f_n^h\left(\left|(\boldsymbol{\sigma}_{\text{trial},n}^h)^D\right|, \Lambda_n^h\right)}{\sigma_0}\right\rangle^r\,. \tag{4.33}$$

Note in passing that, for rate-independent plasticity (elasto-plasticity), above considerations are in general condensed into the so-called *Karush*[13]*-Kuhn-Tucker*[14]conditions. By the application of the *Karush-Kuhn-Tucker* conditions, the plastic multiplier Λ_n^h is computed with the constraints $F \le 0\,, \Lambda_n^h \ge 0\,, \Lambda_n^h F = 0$. For given $\boldsymbol{\sigma}_{\text{trial},n}^h$, let $\Lambda_n^h = \Lambda_n^h\left(\left|(\boldsymbol{\sigma}_{\text{trial},n}^h)^D\right|\right)$ be the solution of the nonlinear problem (4.33). Note that only

[13] *William Karush* (1917 – 1997): American mathematician who is best known for his contribution to the "*Karush–Kuhn–Tucker* conditions". He was the first to publish the necessary conditions for the inequality constrained problem in his Masters thesis. He became only renowned after a seminal conference paper by *Harold William Kuhn* and *Albert William Tucker*. [Wikipedia]

[14] *Albert William Tucker* (1905 – 1995): Canadian-born American mathematician who made important contributions in topology, game theory, and non-linear programming. He is, together with *William Karush* and *Harold William Kuhn*, best known for the "*Karush–Kuhn–Tucker* conditions", a basic result in non-linear programming, which was published in conference proceedings, rather than in a journal. [Wikipedia]

for the special case $h_e = 0$ and $r = 1$ the solution is known in closed form, so that, in general, the return parameter Λ_n^h has to be approximated by a few *Newton* steps. In order to obtain a unique solution in the case of softening, it is required that $\frac{\triangle t_n}{\eta}$ is sufficiently small. The solution of (4.33) defines the radial return $\boldsymbol{\varepsilon}_{p,n}^h = \mathbb{R}_n^h(\boldsymbol{\sigma}_{\text{trial},n}^h)$ by

$$\mathbb{R}_n^h = \boldsymbol{\varepsilon}_{p,n-1}^h + \Lambda_n^h\big(|(\boldsymbol{\sigma}_{\text{trial},n}^h)^D|\big)\frac{(\boldsymbol{\sigma}_{\text{trial},n}^h)^D}{|(\boldsymbol{\sigma}_{\text{trial},n}^h)^D|}\,, \tag{4.34}$$

and the incremental plastic stress response $\boldsymbol{\sigma}_n^h = \mathbb{S}_n^h\big(\boldsymbol{\varepsilon}(\mathbf{u}_n^h), \boldsymbol{\varepsilon}_{p,n-1}^h\big)$ by

$$\mathbb{S}_n^h = \overset{4}{\boldsymbol{C}}\Big[\,\boldsymbol{\varepsilon}(\mathbf{u}_n^h) - \mathbb{R}_n^h\,\Big]\,. \tag{4.35}$$

Together with (4.25), this results in the nonlinear variational problem

$$R_n^{M,h} = \int_{\Omega^h} \mathbb{S}_n^h \cdot \boldsymbol{\varepsilon}(\delta\mathbf{u}^h)\,\mathrm{d}v - \int_{\Gamma_N^{\mathbf{t},h}} \bar{\mathbf{t}}_n^h \cdot \delta\mathbf{u}^h\,\mathrm{d}a = 0\,. \tag{4.36}$$

This problem can be solved directly with a generalised *Newton* method, see Appendix C.2 for a suitable algorithm.

Remark: Recently, several further nonlinear solution algorithms for this problem class were discussed, e. g., interior point methods in *Krabbenhoft et al.* [121], SQP methods in *Wieners* [192], or the *Newton-Schur*[15] method in *Kulkarni et al.* [124]. The latter method is introduced shortly, as its solution algorithm is relatively akin to the subsequent Section 4.2.2. The *Newton-Schur* method introduces two independent variables, displacement and stress. A *Newton* algorithm for the nonlinear system is constructed with two equations, the temporal discretised equation (4.25) and (4.35). Since the second equation is local, the *Schur* complement can be computed. Thus, only one global system, in form of (4.36), needs to be solved in every *Newton* step. Therein, the nonlinear stress response is replaced by the *Schur* complement. Numerically, this method does not change the discretisation, and thus yields the same discrete solution, but the solution is obtained by a different nonlinear solution algorithm. It turns out that this method also can be transferred to applications in finite plasticity, where the performance is superior to the standard closest point algorithms.

First, in terms of a concise residual vector notation, cf. $(4.23)_2$, the problem (4.27) can be rewritten for a single time step n as

$$\boldsymbol{F} = \begin{bmatrix} \boldsymbol{F}_1 \\ \\ \boldsymbol{F}_2 \end{bmatrix} \overset{!}{=} \mathbf{0} \quad \rightsquigarrow \quad n\colon \quad \boldsymbol{R}(\triangle\boldsymbol{y}) = \begin{bmatrix} \boldsymbol{R}^G(\triangle\boldsymbol{u}, \triangle\boldsymbol{q}) \\ \\ \boldsymbol{R}^L(\triangle\boldsymbol{u}, \triangle\boldsymbol{q}) \end{bmatrix} = \mathbf{0} \quad \text{with} \quad \underbrace{\frac{\mathrm{d}\boldsymbol{R}}{\mathrm{d}\triangle\boldsymbol{y}}}_{=:\,\mathrm{D}\boldsymbol{R}}\boldsymbol{\Delta} = \boldsymbol{R}\,. \tag{4.37}$$

[15] *Issai Schur* (1875 – 1941): Israelian mathematician who worked in Germany for most of his life. As a student of *Ferdinand Georg Frobenius*, he is perhaps best known today for his result on the existence of the "*Schur* decomposition". [WIKIPEDIA]

Therein, the *Newton* iteration index m is omitted for convenience. Note in passing that the formerly used *Runge-Kutta* stage index i is obsolete due to the implicit *Euler* time-integration scheme; consequently, the single stage increment is defined by $\triangle(\,\cdot\,) := \triangle(\,\cdot\,)_n - \triangle(\,\cdot\,)_{n-1}$. The split-up system of equations $\{\boldsymbol{F}_1, \boldsymbol{F}_2\}$ leads after their temporal discretisation to the global residual vector $\boldsymbol{R}^G$ and its local counterpart $\boldsymbol{R}^L$. The residual vectors depend on the increments of the global (primary) and local (secondary) variables condensed in $\triangle\boldsymbol{u}$ and $\triangle\boldsymbol{q}$. The *Newton* increments are represented by $\boldsymbol{\Delta}$. The algorithmically consistent tangent then reads

$$\mathrm{D}\boldsymbol{R} = \frac{\partial \boldsymbol{R}^G}{\partial \triangle \boldsymbol{u}} + \frac{\partial \boldsymbol{R}^G}{\partial \triangle \boldsymbol{q}} \frac{\partial \triangle \boldsymbol{q}}{\partial \triangle \boldsymbol{u}} \,. \tag{4.38}$$

Under the assumption that the local system $\boldsymbol{R}^L$ can be solved sufficiently exact, the local increments can be understood as a function of the global increments $\triangle\boldsymbol{q} = \triangle\boldsymbol{q}(\triangle\boldsymbol{u})$, viz.

$$\boldsymbol{R}^L \stackrel{!}{=} \boldsymbol{0} \,, \quad \frac{\mathrm{d}\boldsymbol{R}^L}{\mathrm{d}\triangle \boldsymbol{u}} = \frac{\partial \boldsymbol{R}^L}{\partial \triangle \boldsymbol{u}} + \frac{\partial \boldsymbol{R}^L}{\partial \triangle \boldsymbol{q}} \frac{\partial \triangle \boldsymbol{q}}{\partial \triangle \boldsymbol{u}} = \boldsymbol{0} \quad \rightsquigarrow \quad \frac{\partial \triangle \boldsymbol{q}}{\partial \triangle \boldsymbol{u}} = -\left(\frac{\partial \boldsymbol{R}^L}{\partial \triangle \boldsymbol{q}} \right)^{-1} \frac{\partial \boldsymbol{R}^L}{\partial \triangle \boldsymbol{u}} \,. \tag{4.39}$$

Thus, the small linear system $(4.39)_2$ can be solved in a decoupled way. This yields to the final form of the algorithmically consistent tangent, viz.

$$\mathrm{D}\boldsymbol{R} = \frac{\partial \boldsymbol{R}^G}{\partial \triangle \boldsymbol{u}} - \frac{\partial \boldsymbol{R}^G}{\partial \triangle \boldsymbol{q}} \left(\frac{\partial \boldsymbol{R}^L}{\partial \triangle \boldsymbol{q}} \right)^{-1} \frac{\partial \boldsymbol{R}^L}{\partial \triangle \boldsymbol{u}} \quad \rightsquigarrow \quad \mathrm{D}\boldsymbol{R}\boldsymbol{\Delta} = \boldsymbol{R}^G \quad \Rightarrow \quad \triangle \boldsymbol{u}^{m+1} = \triangle \boldsymbol{u}^m - \boldsymbol{\Delta}^m \,. \tag{4.40}$$

With this, the accumulated *Newton* solution of the primary variables $\triangle\boldsymbol{u}^{m+1}$ can be computed.

Alternatively to (4.37), the *Newton-Schur* method initially states the problem of small-strain elastic-inelastic material behaviour as follows:

$$n\colon \quad \boldsymbol{R}(\triangle\boldsymbol{u}, \triangle\boldsymbol{\sigma}) = \begin{bmatrix} \boldsymbol{R}^E(\triangle\boldsymbol{u}, \triangle\boldsymbol{\sigma}) \\ \boldsymbol{R}^S(\triangle\boldsymbol{u}, \triangle\boldsymbol{\sigma}) \end{bmatrix} = \boldsymbol{0} \quad \rightsquigarrow \quad \begin{bmatrix} \frac{\partial \boldsymbol{R}^E}{\partial \triangle \boldsymbol{u}} & \frac{\partial \boldsymbol{R}^E}{\partial \triangle \boldsymbol{\sigma}} \\ \frac{\partial \boldsymbol{R}^S}{\partial \triangle \boldsymbol{u}} & \frac{\partial \boldsymbol{R}^S}{\partial \triangle \boldsymbol{\sigma}} \end{bmatrix} \begin{bmatrix} \boldsymbol{\Delta}_{\boldsymbol{u}} \\ \boldsymbol{\Delta}_{\boldsymbol{\sigma}} \end{bmatrix} = \begin{bmatrix} \boldsymbol{R}^E \\ \boldsymbol{R}^S \end{bmatrix} . \tag{4.41}$$

Therein, the two independent primary variables, displacement and stress, are introduced, and condensed into $\triangle\boldsymbol{u}$ and $\triangle\boldsymbol{\sigma}$. The complementary residual vectors are $\boldsymbol{R}^E$, for the regular equilibrium equation, and $\boldsymbol{R}^S$, for the state variable evolution equation. Here, the state variable is the stress tensor $\boldsymbol{\sigma}$. The state variable evolution equation for the stress tensor $\boldsymbol{\sigma}$ can be represented by, e. g.,

$$\boldsymbol{R}^S = \boldsymbol{\sigma}_n + \frac{3\mu \overbrace{(\boldsymbol{\sigma}_n - \boldsymbol{\sigma}_{n-1})}^{\triangle \boldsymbol{\sigma}}}{\overset{*}{\kappa}(\boldsymbol{\sigma}_n)} - \sqrt{\frac{3}{2}} \, |\boldsymbol{\sigma}^D_{\mathrm{trial,n}}| \,. \tag{4.42}$$

The softening/hardening of the material under study is represented in $\overset{*}{\kappa}(\boldsymbol{\sigma})$. By the application of a general *Schur* complement technique[16] for matrix calculus to (4.41), the problem yields

$$\begin{aligned}\left[\frac{\partial \boldsymbol{R}^E}{\partial \triangle \boldsymbol{u}} - \frac{\partial \boldsymbol{R}^E}{\partial \triangle \boldsymbol{\sigma}} \left(\frac{\partial \boldsymbol{R}^S}{\partial \triangle \boldsymbol{\sigma}}\right)^{-1} \frac{\partial \boldsymbol{R}^S}{\partial \triangle \boldsymbol{u}}\right] \boldsymbol{\Delta}_{\boldsymbol{u}} &= \boldsymbol{R}^E - \frac{\partial \boldsymbol{R}^E}{\partial \triangle \boldsymbol{\sigma}} \left(\frac{\partial \boldsymbol{R}^S}{\partial \triangle \boldsymbol{\sigma}}\right)^{-1} \boldsymbol{R}^S\,, \\ \frac{\partial \boldsymbol{R}^S}{\partial \triangle \boldsymbol{\sigma}} \boldsymbol{\Delta}_{\boldsymbol{\sigma}} &= \boldsymbol{R}^S - \frac{\partial \boldsymbol{R}^S}{\partial \triangle \boldsymbol{u}} \boldsymbol{\Delta}_{\boldsymbol{u}}\,, \end{aligned} \tag{4.44}$$

$$\Rightarrow \begin{cases} \triangle \boldsymbol{u}^{m+1} = \triangle \boldsymbol{u}^m - \boldsymbol{\Delta}_{\boldsymbol{u}}^m\,, \\ \triangle \boldsymbol{\sigma}^{m+1} = \triangle \boldsymbol{\sigma}^m - \boldsymbol{\Delta}_{\boldsymbol{\sigma}}^m\,. \end{cases}$$

It has been shown in *Kulkarni et al.* [124] that the performance of this alternative ansatz is superior to the standard closest point algorithm. □

4.2.2 Augmented Small-strain Elasto-viscoplasticity

This section continues the preceding setup for small-strain elasto-viscoplasticity. Here, additional finite-element approximations are used for the plastic strain $\boldsymbol{\varepsilon}_p$. Therefore, the standard finite-element spaces are augmented. This augmentation yields to the introduction of the spaces

$$\mathcal{A}^{\boldsymbol{\varepsilon}}(t) = \{\boldsymbol{\varepsilon}_p \in \mathcal{H}^1(\Omega)^d\} \quad \text{(ansatz)} \quad \text{and} \quad \mathcal{T}^{\boldsymbol{\varepsilon}} = \{\delta\boldsymbol{\varepsilon}_p \in \mathcal{H}^1(\Omega)^d\} \quad \text{(test)}\,. \tag{4.45}$$

In the following, quadratic elements $\mathcal{A}^{\mathbf{u},h}(t)$ are used for the spatially discretised displacements, and linear elements $\mathcal{A}^{\boldsymbol{\varepsilon},h}(t)$ for the plastic strains. Note that in this case, $\boldsymbol{\varepsilon}_p^h$ is a non-local variable, so that it is not possible to eliminate the flow rule locally. Thus, the incremental flow rule (4.29) has to be included into the variational system in weak form:

[16] The common *Schur* complement for matrix calculus is defined as:

$$\begin{bmatrix} \mathbf{A} & \mathbf{B} \\ \mathbf{C} & \mathbf{D} \end{bmatrix} \begin{bmatrix} \mathbf{x} \\ \mathbf{y} \end{bmatrix} = \begin{bmatrix} \mathbf{f} \\ \mathbf{g} \end{bmatrix} \quad \rightsquigarrow \quad \begin{aligned} (\mathbf{D} - \mathbf{C}\mathbf{A}^{-1}\mathbf{B})\,\mathbf{y} = \mathbf{g} - \mathbf{C}\mathbf{A}^{-1}\mathbf{f} \quad &\rightarrow \quad \mathbf{A}\mathbf{x} = \mathbf{f} - \mathbf{B}\mathbf{y}\,, \\ (\mathbf{A} - \mathbf{B}\mathbf{D}^{-1}\mathbf{C})\,\mathbf{x} = \mathbf{f} - \mathbf{B}\mathbf{D}^{-1}\mathbf{g} \quad &\rightarrow \quad \mathbf{D}\mathbf{y} = \mathbf{g} - \mathbf{C}\mathbf{x}\,. \end{aligned} \tag{4.43}$$

find $\{\mathbf{u}_n^h, \boldsymbol{\varepsilon}_{p,n}^h\} \in \{\mathcal{A}^{\mathbf{u},h}(t_n), \mathcal{A}^{\boldsymbol{\varepsilon},h}(t_n)\} \times \mathcal{H}^1(\Omega)^d$ satisfying

$$\begin{aligned} R_n^{M,h} &= \int_{\Omega^h} \boldsymbol{\sigma}_n^h \cdot \boldsymbol{\varepsilon}(\delta\mathbf{u}^h)\, \mathrm{d}v - \int_{\Gamma_N^{\mathbf{u},h}} \bar{\mathbf{t}}_n^h \cdot \delta\mathbf{u}^h\, \mathrm{d}a \;=\; 0\,, \\ R_n^{A,h} &= \int_{\Omega^h} \left(\boldsymbol{\varepsilon}_{p,n}^h - \boldsymbol{\varepsilon}_{p,n-1}^h - \frac{\triangle t^n}{\eta} \left\langle \frac{F(\boldsymbol{\sigma}_n^h; \kappa_n^h)}{\sigma_0} \right\rangle^r \frac{(\boldsymbol{\sigma}_n^h)^D}{|(\boldsymbol{\sigma}_n^h)^D|} \right) \cdot \delta\boldsymbol{\varepsilon}_p^h\, \mathrm{d}v \;=\; 0\,, \end{aligned} \tag{4.46}$$

for all test functions $\{\delta\mathbf{u}^h, \delta\boldsymbol{\varepsilon}_p^h\} \in \{\mathcal{T}^{\mathbf{u},h}, \mathcal{T}^{\boldsymbol{\varepsilon},h}\} \times \mathcal{H}^1(\Omega)^d$. Since F depends in the first argument only on the second invariant, the return parameter function

$$\Lambda_n^h\big(|(\boldsymbol{\sigma}_n^h)^D|, \varepsilon_{pv,n}^h\big) \;=\; \frac{\triangle t_n}{\eta} \left\langle \frac{\tilde{F}\big(|(\boldsymbol{\sigma}_n^h)^D|, \varepsilon_{pv,n}^h\big)}{\sigma_0} \right\rangle^r \tag{4.47}$$

with $\tilde{F}\big(|(\boldsymbol{\sigma}_n^h)^D|, \varepsilon_{pv,n}^h\big) = F(\boldsymbol{\sigma}_n^h; \overset{*}{\kappa}(\varepsilon_{pv,n}^h))$ is well defined. Moreover, since Λ_n^h is *Lipschitz*[17] continuous, a generalised derivative exists and again a (generalised) *Newton* method can be directly applied to the coupled system, see Appendix C.3 for a suitable algorithm. Note that the numerical realisation is quite simple if in algorithmic substep `S4)` the linearisation of the system (4.46) is approximated numerically by the central difference quotient (4.24). This can be denoted in *Runge-Kutta* stage increments analogue to (4.23) or (4.41), respectively, as

$$n : \boldsymbol{R}(\triangle\boldsymbol{u}, \triangle\boldsymbol{e}) = \begin{bmatrix} \boldsymbol{R}^M(\triangle\boldsymbol{u}, \triangle\boldsymbol{e}) \\ \boldsymbol{R}^A(\triangle\boldsymbol{u}, \triangle\boldsymbol{e}) \end{bmatrix} = \boldsymbol{0} \;\rightsquigarrow\; \begin{bmatrix} \dfrac{\partial\boldsymbol{R}^M}{\partial\triangle\boldsymbol{u}} & \dfrac{\partial\boldsymbol{R}^M}{\partial\triangle\boldsymbol{e}} \\ \dfrac{\partial\boldsymbol{R}^A}{\partial\triangle\boldsymbol{u}} & \dfrac{\partial\boldsymbol{R}^A}{\partial\triangle\boldsymbol{e}} \end{bmatrix} \begin{bmatrix} \boldsymbol{\Delta}_{\boldsymbol{u}} \\ \boldsymbol{\Delta}_{\boldsymbol{e}} \end{bmatrix} = \begin{bmatrix} \boldsymbol{R}^M \\ \boldsymbol{R}^A \end{bmatrix}. \tag{4.48}$$

Therein, the primary variables are condensed in $\boldsymbol{u} = [\mathbf{u}^1, \ldots, \mathbf{u}^N]^T$, $\boldsymbol{e} = [\boldsymbol{\varepsilon}_p^1, \ldots, \boldsymbol{\varepsilon}_p^N]^T$, and the residual vectors are composed as $\boldsymbol{R}^M = [R^{M,h,1}, \ldots, R^{M,h,N}]^T$, and $\boldsymbol{R}^A = [R^{A,h,1}, \ldots, R^{A,h,N}]^T$. Note that this procedure completely avoids the evaluation of the radial return.

In Section 5.1, both numerical methods – the FEM and the AugFEM – are exemplarily applied to a viscoplastic *Perzyna*-type regularisation of softening material behaviour within a geometrically linear approach in order to simulate the development of shear bands occurring in a tensile bar. The numerical studies prove comparative results, while exhibiting a computational speed-up for the AugFEM.

[17] *Rudolf Otto Sigismund Lipschitz* (1832–1903): German mathematician and doctoral student of *Peter Gustav Lejeune Dirichlet*. While *Lipschitz* gave his name to the "*Lipschitz* continuity condition", he worked in a broad range of areas. He is considered to be a forgotten pioneer. Main parts of his scientific contributions – especially in the field of associative algebra – have fallen into oblivion after 1950. [Wikipedia]

4.3 The Extended Finite-Element Method (XFEM)

After the small excurs to elasto-viscoplastic material behaviour of single-phase materials in Section 4.2 the following chapter resides again in the framework of multi-phasic materials. Nevertheless, the basic principle of the preceding extension of the FEM is taken up here again. In contrast to the AugFEM, the XFEM is an enriched method where the field describing quantities are enriched. The XFEM belongs to the family of enhanced assumed strain methods (EAS), cf. *Simo & Rafai* [173]. It enables local enrichment in subregions of the discretised domains. In general, the XFEM is mainly used in applications that involve discontinuities in field equations. Within this topic, the XFEM has a broad application area, e. g., material interfaces, cracks, or boundary layers, to name only a few. An important advantage of the XFEM is its accuracy in comparison to the standard FEM. As a consequence, the requirement for a suitable finite-element mesh is reduced. Regular meshes can be used in applications which otherwise would require mesh-refinement with element edges aligning with the discontinuities.

The enrichment of the field quantities within the framework of the XFEM are based on the PU principle, cf. Section 4.1.1. These enrichments result in additional DOF. The enrichment carries additional ansatz functions with local supports that are multiplied with global enrichment functions. Hence, the additional ansatz functions yield a local enrichment. Therein, special attention is required for the integration of the locally enriched subdomains due to possible jumps or kinks in the field functions. Based on the spatial discretisation (4.2), the ansatz of the displacement field function $\mathbf{u}_S(\mathbf{x},t)$ is enriched, viz.

$$
\begin{aligned}
\mathbf{u}_S(\mathbf{x},t) \;\approx\; \mathring{\mathbf{u}}^h_S(\mathbf{x},t) \;&=\; \bar{\mathbf{u}}^h_S(\mathbf{x},t) \;+\sum_{j=1}^{N} \boldsymbol{\Upsilon}^j_{\mathbf{u}}(\mathbf{x}) \;\; \mathbf{u}^j_S(t) \;+\; \sum_{\ell=1}^{M}\sum_{j\in I^*_\ell} \boldsymbol{\Pi}^j_{\mathbf{a}\ell}(\mathbf{x}) \;\; \mathbf{a}^j_{S\ell}(t)\,, \\
\delta\mathbf{u}_S(\mathbf{x}) \;\approx\; \delta\mathring{\mathbf{u}}^h_S(\mathbf{x}) \;&=\; \underbrace{\sum_{j=1}^{N} \boldsymbol{\Upsilon}^j_{\mathbf{u}}(\mathbf{x})\,\delta\mathbf{u}^j_S}_{\substack{\text{FEM approximation}\\ \mathbf{u}^h_S,\,\delta\mathbf{u}^h_S}} \;+\; \underbrace{\sum_{\ell=1}^{M}\sum_{j\in I^*_\ell} \boldsymbol{\Pi}^j_{\mathbf{a}\ell}(\mathbf{x})\,\delta\mathbf{a}^j_{S\ell}}_{\substack{\text{XFEM enrichment}\\ \mathbf{a}^h_{S\ell},\,\delta\mathbf{a}^h_{S\ell}}}
\end{aligned}
$$

$$
\text{with}\quad \left\{\begin{array}{lcll}
\{\mathbf{a}^j_{S\ell}(t),\delta\mathbf{a}^j_{S\ell}\} & \in & \{\mathcal{A}^{\mathbf{a},h}(t),\mathcal{T}^{\mathbf{a},h}\} & : \text{ XFEM ansatz (DOF) and test}\,, \\
\mathring{\mathbf{u}}^h_S(\mathbf{x},t) \in \mathring{\mathcal{A}}^{\mathbf{u},h}(t) & = & \mathcal{A}^{\mathbf{u},h}(t)+\mathcal{A}^{\mathbf{a},h}(t) & : \text{ enriched displacement}\,, \\
\delta\mathring{\mathbf{u}}^h_S(\mathbf{x}) \quad \in \mathring{\mathcal{T}}^{\mathbf{u},h} & = & \mathcal{T}^{\mathbf{u},h}+\mathcal{T}^{\mathbf{a},h} & : \text{ enriched test}\,, \\
\boldsymbol{\Pi}^j_{\mathbf{a}\ell}(\mathbf{x}) & = & \boldsymbol{\Upsilon}^j_{\mathbf{a}\ell}(\mathbf{x})\,\psi_\ell(\mathbf{x}) & : \text{ additional ansatz functions}\,.
\end{array}\right. \tag{4.49}
$$

Multiple XFEM enrichment $\ell = 1,\ldots,M$ can be applied to the discontinuous field functions under study. Each of the enrichment must satisfy the PU[18] constraint, see Figure

[18] In fact, $\boldsymbol{\Pi}^j_{\mathbf{a}i}$ builds only a PU in all elements whose nodes are all in the nodal subsets I^*_i. In

4.3. In this monograph, the number of XFEM enrichment will be restricted to a single one. Consequently, only a single discontinuity can be modelled. Enriched quantities will be denoted by a circle superscript $(\mathring{\cdot})$. The enriched displacement field function reads $\mathring{\mathbf{u}}^h_S$, and the enriched test function $\delta\mathring{\mathbf{u}}^h_S$. Both reside in the ansatz and test spaces $\{\mathring{\mathcal{A}}^{\mathbf{u},h}, \mathring{\mathcal{T}}^{\mathbf{u},h}\}$ which contain the enrichment spaces $\{\mathcal{A}^{\mathbf{a},h}, \mathcal{T}^{\mathbf{a},h}\}$. The additional DOF (primary variables) are represented in $\mathbf{a}^j_S$; their test counterparts are denoted $\delta\mathbf{a}^j_S$. Note that these DOF only support finite-elements which are intersected by discontinuities. Thus, they reside in the nodal subset $j \in I^*$. This is a crucial advantage of the XFEM to other enriched methods, because the number of additional DOF is limited. The additional ansatz functions $\mathbf{\Pi}^j_{\mathbf{a}}$ consist of the local support $\mathbf{\Upsilon}^j_{\mathbf{a}}$, and of the global enrichment function ψ. In this monograph, the local support functions will be chosen identical to the standard FEM ansatz functions, i. e., $\mathbf{\Upsilon}^j_{\mathbf{a}} \equiv \mathbf{\Upsilon}^j_{\mathbf{u}}$. Note that this is not a constraint; the enrichment can be defined based on individual functions, e. g., quadratic FEM but linear XFEM ansatz functions. Different global enrichment functions can be applied for weak or strong discontinuities. For the here discussed problem of strong discontinuities in displacement fields, a set of possible enrichment functions is – in direct analogy to (3.44) – given with

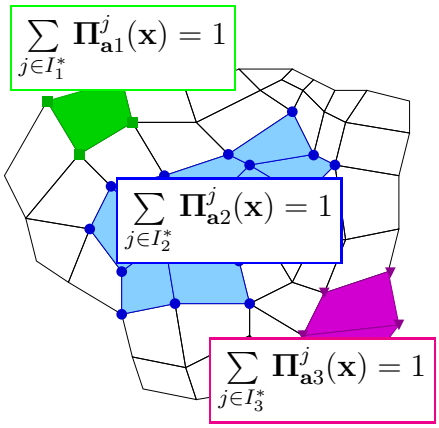

Figure 4.3: PU for multiple XFEM subregion enrichment.

$$\psi_1(\mathbf{x}) = \mathscr{H}\big(\phi(\mathbf{x})\big) = \left\{ \begin{array}{l} 1 \,:\, \phi(\mathbf{x}) > 0 \\ 0 \,:\, \phi(\mathbf{x}) \leq 0 \end{array} \right| \left. \begin{array}{r} 1 \,:\, \phi(\mathbf{x}) > 0 \\ 0 \,:\, \phi(\mathbf{x}) = 0 \\ -1 \,:\, \phi(\mathbf{x}) < 0 \end{array} \right\} = \operatorname{sign}\big(\phi(\mathbf{x})\big) = \psi_2(\mathbf{x})\,. \tag{4.50}$$

Therein, the *Heaviside*- ($\mathscr{H}$) and signum-function (sign) lead to identical results as they span the same approximation space. In (4.50), the scalar-valued global function $\phi(\mathbf{x})$ tracks the discontinuity by its zero-level. This globally represented so-called level-set function is a widely used numerical technique to track – fixed or moving – interfaces implicitly. Examples of proper tracking techniques can be found in Section 4.4.

Remark: One of the reasons for the general success of the XFEM is its capability to consider discontinuities inside finite-elements. In this context, it makes sense to point out an often used alternative. The so-called *Hansbo* method, cf. *Hansbo & Hansbo* [93, 94], was shown identical to the XFEM enrichment in *Areias & Belytschko* [4]. The *Hansbo* method may be interpreted as the superposition of two elements. Therein, the first element is used to define the functions Υ_I and Υ'_{II}, see Figure 4.4 for a 1-d representation; the

elements with only some of their nodes in I^*_i, $\mathbf{\Pi}^j_{\mathbf{a}i}$ does not build a PU, i. e., $\sum_{j\in I^*_i} \mathbf{\Pi}^j_{\mathbf{a}i}(\mathbf{x}) \neq 1$. Theses elements are so-called blending elements. Fortunately, these blending elements do not affect typical – in this monograph discussed – XFEM computations particularly. Thus, the influence of blending elements is in general neglected. Anyway, a possible remedy to this problem has already been proposed by *Fries* [76].

right node is called virtual. The second element is used to define the functions Υ'_I and

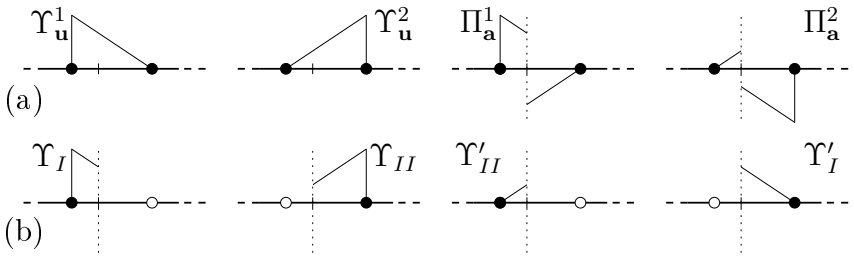

Figure 4.4: Comparison of the (a) classical XFEM $\big(\psi = \mathrm{sign}(\phi)\big)$ with the (b) *Hansbo* method.

Υ_{II}, with the left virtual node. This is – of course – also valid for 2-d and 3-d problems. □

Due to the additional XFEM enrichment, the standard FEM approximations lack the normalisation by the *Kronecker* symbol δ^j_i, cf. (4.3), in general. But this normalisation is crucial for the direct application of *Dirichlet* boundary conditions. One possible remedy for this situation is to find local XFEM enrichment functions $\mathbf{\Pi}^j_{\mathbf{a}}$ that are zero at all nodes. This would immediately yield $\mathring{\mathbf{u}}^h_S = \bar{\mathbf{u}}^h_S$, as usually given in the standard FEM approximation. The remedy is accomplished by a **shifting of the global enrichment functions** ψ, individually for each node as

$$\psi^{\mathrm{shift}}(\mathbf{x}) = \psi(\mathbf{x}) - \psi(\mathbf{x}_j) \quad \rightsquigarrow \quad \mathbf{\Pi}^j_{\mathbf{a}}(\mathbf{x}) = \mathbf{\Upsilon}^j_{\mathbf{u}}(\mathbf{x})\psi^{\mathrm{shift}}(\mathbf{x})\,. \tag{4.51}$$

Consequently, the XFEM enrichment becomes zero at every node k through $k \neq j$: $\mathbf{\Upsilon}^j_{\mathbf{u}}(\mathbf{x}_k) = \mathbf{0}$ and $k = j$: $\psi(\mathbf{x}_k) - \psi(\mathbf{x}_j) = 0$. The final form of the XFEM enriched displacement approximation then reads

$$\mathring{\mathbf{u}}^h_S(\mathbf{x},t) = \underbrace{\bar{\mathbf{u}}^h_S(\mathbf{x},t) + \sum_{j=1}^{N} \mathbf{\Upsilon}^j_{\mathbf{u}}(\mathbf{x})\mathbf{u}^j_S(t)}_{=\,\mathbf{u}^h_S \approx \tilde{\mathbf{u}}_S} + \underbrace{\sum_{j\in I^*} \mathbf{\Upsilon}^j_{\mathbf{u}}(\mathbf{x})\Big[\psi(\mathbf{x}) - \psi(\mathbf{x}_j)\Big]\mathbf{a}^j_S(t)}_{=\,\psi\mathbf{a}^h_S \approx \psi[\![\mathbf{u}_S]\!]}\,. \tag{4.52}$$

Therein, the continuum-mechanical field function for the displacement (3.42) is approximated by the quantities $\mathbf{u}^h_S = \bar{\mathbf{u}}^h_S + \sum_{j=1}^{N} \mathbf{\Upsilon}^j_{\mathbf{u}}\mathbf{u}^j_S$, and $\mathbf{a}^h_S = \sum_{j\in I^*} \mathbf{\Upsilon}^j_{\mathbf{u}}\mathbf{a}^j_S$.

Remark: Discontinuities that end inside the considered domain require a special enrichment. In order to represent such a discontinuity in its proper length, nodes whose support contain the **discontinuity tip** (singularity) should to be enriched, too. For example, the following four discontinuous functions are, in general, used for 2-d simulations:

$$\psi_I = \sqrt{r}\sin\frac{\theta}{2}\,, \quad \psi_{II} = \sqrt{r}\sin\frac{\theta}{2}\sin\theta\,, \quad \psi_{III} = \sqrt{r}\cos\frac{\theta}{2}\,, \quad \psi_{IV} = \sqrt{r}\cos\frac{\theta}{2}\sin\theta\,. \tag{4.53}$$

These functions depend on a local polar coordinate system that is defined at the crack tip. The angle θ is positive definite in counter-clockwise direction, levelled in elongation of the

discontinuity line, and negative definite for the clockwise direction below the elongated discontinuity line. Such functions are provided by the asymptotic modes of displacement at the crack tip. The first function in (4.53) is also discontinuous across the discontinuity line. The singularity surrounding nodes are enriched by (4.53) instead of the regular XFEM functions (4.51), see *Belytschko & Black* [10], and *Strouboulis et al.* [178]. Note that if the solution is not singular at the crack tip, e. g., due to the application of the cohesive zone theory, other functions of enrichment can be selected, see *Moës & Belytschko* [138] and *Zi & Belytschko* [197]. □

4.3.1 Discontinuous Discretisation

Additionally to the spatial discretisation of the FEM in Section 4.1.1, the XFEM discontinuous discretisation remains to be discussed. The discontinuous entries in the balance equations (3.60) and (3.63),

$$\dots \int_{\bar{\mathcal{S}}} \bar{v}^{\mathcal{S}} \delta \mathcal{P} \, \mathrm{d}a^{\mathcal{S}} \dots \quad \text{and} \quad \dots \int_{\bar{\mathcal{S}}} \bar{\mathbf{t}}^{S,\mathcal{S}} \cdot \delta \mathbf{u}_S \, \mathrm{d}a^{\mathcal{S}} \dots \,, \tag{4.54}$$

are considered individually. The balance contribution $(4.54)_1$ can be interpreted as an internal fluid flow. This has been already identified in (3.61). Consequently, a possible ansatz for its overall discretisation can be defined as

$$\int_{\bar{\mathcal{S}}} \bar{v}^{\mathcal{S}} \delta \mathcal{P} \, \mathrm{d}a^{\mathcal{S}} \quad \rightsquigarrow \quad \frac{1}{\varrho_e} \frac{\Omega^h_{e,n} - \Omega^h_{e,n-1}}{\triangle t_n} \, \delta \mathcal{P}^h \,. \tag{4.55}$$

The discretised volume of each finite-element is represented by $\Omega^h_{e,n}$ from the actual time step, and by $\Omega^h_{e,n-1}$ from the previous time step. Efficient algorithms for the computation of the discretised volume or area, for the 2-d case of a finite-element can be found in Appendix C.4 and Appendix C.5. The internal fluid flow $(4.55)_2$ is de facto an additional *Neumann* BC, also known as additional support of the right-hand side. Each node – from a discontinuous element – with a pressure DOF gets a pro-rata value on the right hand side of the residual balance equation. The pro-rata value is scaled by the number of element nodes ϱ_e as a consequence of the transfer of the volume integral to discrete (nodal) values. Note in passing that the sign of the internal fluid flow differs from that of the external fluid flow $\bar{v}^h$, recall (4.21). Furthermore, note that the temporal discretisation from Section 4.1.2 is still valid and applied to the considered discontinuous XFEM problems here. Accordingly, it is crucial to consider any occurring *Runge-Kutta* intermediate steps, i. e., $n \Leftrightarrow ni$, $t_n \Leftrightarrow T_{ni} = t_n + c_i h_n$, and $\triangle t_n \Leftrightarrow c_i h_n$. Alternatively to this approach, it is of course also feasible to apply the subsequent discretisation of the cohesive framework to this balance contribution. Actually, this discretisation is straightforward if the crossing discontinuity surface is numerically identified; as it is presented, albeit only virtual, in the following. Anyway,

the volumetric ansatz $(4.55)_2$ is favoured in this monograph. For the numerical computation of $(4.54)_2$, the surface of the discontinuity itself needs to be spatially discretised. This will be presented with focus on the herein used finite-element types. An intersection of 2-d finite-elements results in simple line segments. Their discretisation and numerical integration follows straightforward. Thus, the following cohesive framework will mainly focus on the 3-d discretisation. 3-d problems are herein discretised with 8-node hexahedron elements because of their superiority over tetrahedron elements. Thus, their intersection planes with the discontinuity surface can result in shapes of triangles, rectangles, pentagons, or hexagons, see Figure 4.5 (a). These shapes need to be triangulated for a sound numerical integration scheme, see Figure 4.5 (b). Again, note that any eventually occurring *Runge-Kutta* intermediate steps must be considered, i. e., $n \Leftrightarrow ni$. The discretisation of $(4.54)_2$ can be defined as

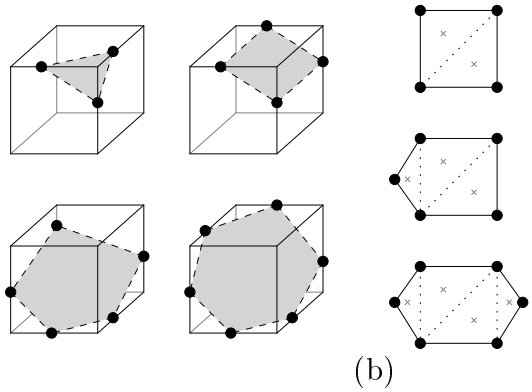

Figure 4.5: (a) Intersection planes of hexahedrons, and (b) their triangulation.

$$\int_{\bar{\mathcal{S}}} \bar{\mathbf{t}}^{S,\mathcal{S}}([\![\mathbf{u}_S]\!], \bar{\mathbf{n}}^{\mathcal{S}}) \cdot \delta\mathbf{u}_S \, \mathrm{d}a^{\mathcal{S}} \quad \rightsquigarrow \quad \int_{\Gamma^{\mathcal{S},h}} \bar{\mathbf{t}}_n^{S,\mathcal{S},h}(\mathbf{a}_{S,n}^h, \bar{\mathbf{n}}_n^{\mathcal{S},h}) \cdot \delta\mathbf{a}_S^h \, \mathrm{d}a^{\mathcal{S}} \,. \tag{4.56}$$

For $(4.56)_2$, the discretisation of the test functional $\delta\mathbf{u}_S$ reduces to the discretised enrichment part $\delta\mathbf{a}_S^h$. This is the result of the activation of cohesive stresses solely by the discontinuous displacement field $\mathbf{a}_{S,n}^h$. Note that $\delta\mathbf{a}_S^h$ lacks the previous enrichment ψ, cf. (4.52); the discontinuity itself is integrated over the discontinuity, in contrast to the overall integration. The discretised values of the cohesive stress vector are computed as follows:

$$\bar{\mathbf{t}}_n^{S,\mathcal{S},h} = (1-d_n^h)\Big(\lambda_\perp^S \underbrace{(\mathbf{a}_{S,n}^h \cdot \bar{\mathbf{n}}_n^{\mathcal{S},h})\bar{\mathbf{n}}_n^{\mathcal{S},h}}_{\mathbf{a}_{S,n}^{h,\perp}} + \mu_\sim^S \underbrace{(\mathbf{a}_{S,n}^h - \mathbf{a}_{S,n}^{h,\perp})}_{\mathbf{a}_{S,n}^{h,\sim}}\Big) \text{ with } \left\{ \begin{array}{rcl} d_n^h &=& 1 - e^{-a\,u_n^b} \,, \\ u_n &=& \max\Big[\|\mathbf{a}_{S,s}^h\|\Big]_{s=0}^{n} \,, \\ && \rightsquigarrow u_{\max},\, d_{\max} \,. \end{array} \right. \tag{4.57}$$

Therein, $\{u_{\max}, d_{\max}\}$ are history variables. They need to be stored or updated, respectively, at each integration point on the surface $\Gamma^{\mathcal{S},h}$. With them, the absolute maximum distance between the two sides of the discontinuity $u_{\max}$, along with the corresponding maximum damage variable $d_{\max}$, can be accessed at each time step. This is necessary for the correct numerical modelling of the assumed linear unloading processes, see Figure 3.16. The irreversibility of the damage is assured through

$$d_n^h = \left\{ \begin{array}{lcl} 1 - e^{-a\,u_n^b} & : & u_n \geq u_{\max} \\ 1 - u_n \dfrac{1-d_{\max}}{u_{\max}} & : & u_n < u_{\max} \end{array} \right\} \quad \text{with} \quad u_n = \|\mathbf{a}_{S,n}^h\| \,. \tag{4.58}$$

The numerical computation and storage of the discretised discontinuity surface will take place in the referential configuration, because of the materially fixed surface $\mathcal{S}_0$. Thus, the element intersection points of the discontinuity are stored per element. These intersection points form the computational basis for the determination of the surface area elements $\Gamma_e^{\mathcal{S},h}$, and the corresponding normal vectors $\mathbf{m}_e^{\mathcal{S},h}$, see Figure 4.6. The transport of the referential intersection points $\mathbf{X}_{S,e}^{\zeta_i}$ to their reflections $\bar{\mathbf{x}}_e^{\zeta_i}$ on the virtual surface $\bar{\mathcal{S}}$ reads

$$\bar{\mathbf{x}}_e^{\zeta_i} = \bar{\mathbf{F}}_S^{\mathcal{S}}\, \mathbf{X}_{S,e}^{\zeta_i} = \mathbf{X}_{S,e}^{\zeta_i} + \tilde{\mathbf{u}}_S^h(\mathbf{X}_{S,e}^{\zeta_i}) + \tfrac{1}{2}\, \mathbf{a}_{S,n}^h(\mathbf{X}_{S,e}^{\zeta_i})\,. \tag{4.59}$$

Therein, the virtual deformation gradient (3.51) has been used. Alternatively, the corresponding balance equations could also be evaluated directly in the referential configuration. However, due to the homogenisation process of the TPM, and the therefrom originating spatial mixture balance equations, this alternative is not considered in this monograph. Within this monograph, the element-wise discontinuity surface is not limited to a plane, see Figure 4.11. Consequently, this results in multiple surface normal vectors $\mathbf{m}_{S,e}^{\mathcal{S},h}$. Their respective images in the actual configuration $\bar{\mathbf{n}}_e^{\mathcal{S},h}$ are computed per triangle element after the transport of the intersection points $\mathbf{X}_{S,e}^{\xi_i} \to \bar{\mathbf{x}}_e^{\xi_i}$. Prior to the identification of the final position of the intersection points in the "static" reference element, the points $\bar{\mathbf{x}}_e^{i}$ are located in the global coordinate system of the actual configuration. As a byproduct, the discontinuity surface area elements – globally and per reference element – are computed for both configurations $\mathrm{d}A_{S,e}^{\xi_j}$, $\mathrm{d}A_{S,e}^{j}$, and $\mathrm{d}a_{S,e}^{\xi_j}$, $\mathrm{d}a_{S,e}^{j}$, respectively. Thus, the *Jacobi*an factor $J_a^j = \mathrm{d}a^j / \mathrm{d}a^{\xi,j}$ for the numerical integration over the reference element is a known quantity. This yields to

$$\int_{\Gamma^{\mathcal{S},h}} \bar{\mathbf{t}}_n^{S,\mathcal{S},h}(\mathbf{x}) \cdot \delta\mathbf{a}_S^h \, \mathrm{d}a^{\mathcal{S}} \quad \approx \quad \sum_j^{\mathrm{J}} \sum_k^{K} \bar{\mathbf{t}}_n^{S,\mathcal{S},h}(\mathbf{x}(\boldsymbol{\xi}_k^j)) \cdot \delta\mathbf{a}_S^h(\boldsymbol{\xi}_k^j) w_k^j J_a^j\,. \tag{4.60}$$

Note in passing that the integration points $\boldsymbol{\xi}_k^j$ on the intersecting surface triangles can be elegantly identified by 3-d tetrahedron subelements; if the respective fourth node of the tetrahedron is positioned on the triangle surface, regular triangle element shape functions can be used.

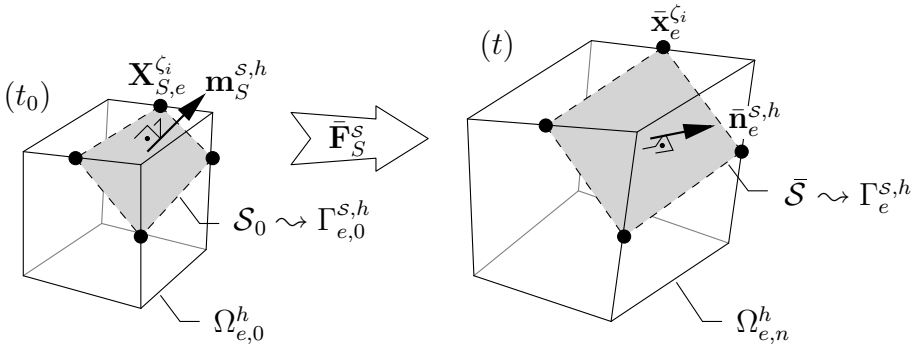

Figure 4.6: Transport of the discontinuity surface.

With these preliminaries, the final form of the fully discretised discontinuous balance equations reads

$$
\begin{aligned}
\mathring{R}^{V,h}_{ni} \;=\; & \int_{\Omega^h} \operatorname{div}\Big(\frac{\triangle \mathring{\boldsymbol{U}}^h_{S,ni}(\dots,\mathbf{a}^h_{S,ni}) - \overset{\circ}{\overline{\boldsymbol{U}}}{}'^h_{S,ni}(\dots,\mathbf{a}^h_{S,ni})}{h_n\, a_{ii}} \Big)\, \delta\mathcal{P}^h \,\mathrm{d}v \\
& + \int_{\Omega^h} \frac{k^F\big(\mathring{\boldsymbol{U}}^h_{S,ni}(\dots,\mathbf{a}^h_{S,ni})\big)}{\gamma^{FR}} \left[\operatorname{grad}\,(\mathcal{P}^h_n + \triangle\mathcal{P}^h_{ni}) - \rho^{FR}\,\mathbf{g}\right] \cdot \operatorname{grad}\,\delta\mathcal{P}^h \,\mathrm{d}v \\
& + \int_{\Gamma^{v,h}_N} \bar{v}^h(T_{ni})\,\delta\mathcal{P}^h \,\mathrm{d}a \;-\; \frac{1}{\varrho_e}\,\frac{\Omega^h_{ni}-\Omega^h_n}{c_i h_n}\,\delta\mathcal{P}^h = 0\,, \\
\mathring{R}^{M,h}_{ni} \;=\; & \int_{\Omega^h} \Big(\mathbf{T}^S_E(\mathring{\boldsymbol{U}}^h_{S,ni}(\dots,\mathbf{a}^h_{S,n})) - \mathcal{P}^h_{ni}\,\mathbf{I}\Big) \cdot \operatorname{grad}\,\delta\mathring{\mathbf{u}}^h_S \,\mathrm{d}v + \int_{\Gamma^{\mathcal{S},h}} \bar{\mathbf{t}}^{S,\mathcal{S},h}_{ni} \cdot \delta\mathbf{a}^h_S \,\mathrm{d}a^{\mathcal{S}} \\
& - \int_{\Omega^h} \rho\,\mathbf{g}\cdot\delta\mathring{\mathbf{u}}^h_S \,\mathrm{d}v - \int_{\Gamma^{\mathbf{t},h}_N} \bar{\mathbf{t}}^h(T_{ni}) \cdot\, \delta\mathring{\mathbf{u}}^h_S \,\mathrm{d}a = 0\,,
\end{aligned}
\tag{4.61}
$$

One can see that – even though the discontinuous enrichment solely contributes to the solid displacement – both equations depend on the additional primary variable $\mathbf{a}^h_{S,n}$. This again reveals the strong coupling of the TPM balance equations. The notation of the balance equations considers possible *Runge-Kutta* intermediate stages, indexed by i. This is crucial for a successful numerical implementation into the FEM-program PANDAS.

discontinuous discretised BVP

$$
\begin{aligned}
\int_{\Omega^h} \operatorname{div}(\mathring{\mathbf{u}}^h_S)'_S\,\delta\mathcal{P}^h \,\mathrm{d}v + \int_{\Omega^h} \frac{k^F}{\gamma^{FR}}\,(\operatorname{grad}\,\mathcal{P}^h - \rho^{FR}\mathbf{g})\cdot\,\operatorname{grad}\delta\mathcal{P}^h \,\mathrm{d}v + \frac{1}{\varrho_e}\,\frac{\Omega^h_n-\Omega^h_0}{t}\,\delta\mathcal{P}^h \;&= \\
= -\int_{\Gamma^{v,h}_N} \bar{v}^h\delta\mathcal{P}^h \,\mathrm{d}a\,, \\
\int_{\Omega^h} (\mathbf{T}^S_E - \mathcal{P}^h\,\mathbf{I}) \,\cdot\, \operatorname{grad}\,\delta\mathbf{u}^h_S \,\mathrm{d}v - \int_{\Omega^h} \rho\,\mathbf{g}\cdot\delta\mathbf{u}^h_S \,\mathrm{d}v = \int_{\Gamma^{\mathbf{t},h}_N} \bar{\mathbf{t}}^h \,\cdot\, \delta\mathbf{u}^h_S \,\mathrm{d}a\,, \\
\int_{\Omega^h} (\mathbf{T}^S_E - \mathcal{P}^h\,\mathbf{I}) \,\cdot\, \mathscr{H}\operatorname{grad}\,\delta\mathbf{a}^h_S \,\mathrm{d}v + \int_{\Gamma^{\mathcal{S},h}} \bar{\mathbf{t}}^{S,\mathcal{S},h}\cdot\delta\mathbf{a}^h_S \,\mathrm{d}a^{\mathcal{S}} - \int_{\Omega^h} \rho\,\mathbf{g}\cdot\mathscr{H}\,\delta\mathbf{a}^h_S \,\mathrm{d}v \;&= \\
= \int_{\Gamma^{\mathbf{t},h}_N} \bar{\mathbf{t}}^h \,\cdot\, \mathscr{H}\,\delta\mathbf{a}^h_S \,\mathrm{d}a\,.
\end{aligned}
\tag{4.62}
$$

The variables $\{\triangle\mathring{\boldsymbol{U}}^h_{S,ni},\ \overset{\circ}{\overline{\boldsymbol{U}}}{}'^h_{S,ni},\ \mathring{\boldsymbol{U}}^h_{S,ni}\}$ represent the enriched counterparts to those presented in (4.21), and (4.22). The application of the variational principle, i. e., $\delta\mathbf{u}^h_S(\delta\mathbf{a}^h_S = \mathbf{0})$,

and $\delta\mathbf{a}_S^h(\delta\mathbf{u}_S^h = \mathbf{0})$, allows a split-up for a clearer representation of the BVP equations. Furthermore, for the sake of clarity, the notation in (4.62) condenses the *Runge-Kutta* intermediate stages to a more common overall representation per time step n.

Remark: Within (4.61), one might wonder about the mixed *Runge-Kutta* quantities $(\cdot)_{ni}$ and $(\cdot)_n$ in the internal fluid flow contribution. This is the result of the application of a single-step temporal integration scheme. For single-step schemes, it is unnecessary to numerically store previous steps (intermediate stages). Thus, the step differences $(\cdot)_{ni-1} - (\cdot)_{ni}$ yield to absolute differences $(\cdot)_{ni} - (\cdot)_n$. This relationship can be nicely visualised with $Z_i := \triangle Y_{ni}$, e.g., for $s = 3$ *Runge-Kutta* stages, viz.

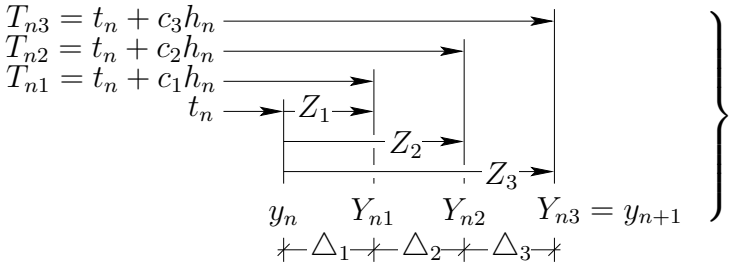

$$\left.\begin{aligned} \triangle_i &= Y_{ni-1} - Y_{ni} = Z_{i-1} - Z_i \\ &\rightsquigarrow \frac{\triangle_i}{(c_{i-1} - c_i)\, h_n} \\ &\Rightarrow \frac{Y_{ni} - y_n}{c_i h_n} \end{aligned}\right\}$$

□

4.3.2 Numerical Integration

Depending on the chosen global enrichment function ψ, jumps, kinks or other discontinuities can be present in the additional ansatz function $\mathbf{\Pi}_\mathbf{a}$. However, the standard *Gauss*ian integration scheme is only suited for element-wise smooth and continuous ansatz functions. Therefore, the numerical integration needs to take element-wise discontinuities into account. In this context, the corresponding elements are divided into two parts along the crossing discontinuity. These parts are then again – due to their unique geometry – divided into subelements. For a sound numerical implementation, these subelements are in general chosen to be of the same element type than their source elements. Thus, the standard *Gauss* quadrature can be applied again to the subelements. Finally, the integral contributions of the subelements are added together to obtain the overall element values, see Figure 4.7. For the most basic element type, linear 2-d triangular elements,

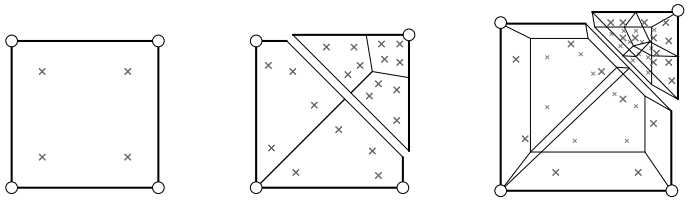

Figure 4.7: Numerical integration points of 2-d/3-d subelements.

the construction of subelements is quite simple. The subdivision process for linear rectangular elements is numerically a bit more costly but also straightforward, see Figure 4.8. Furthermore, the sum of corresponding unique element edge numbers allows the

identification of the crossing position. The 3-d expansion of this procedure can become quite challenging as various cases must be considered. For details on this special – plane intersection surfaces – subdividing process on 3-d hexahedron elements, the interested reader is referred to *Gehrlicher* [84]. However, the usage of 3-d hexahedron subelements bears no relationship to the effort if the general case of non-planar intersection surfaces is considered. Thus, the 3-d subelementation process will be carried out with tetrahedron elements. The previously discussed – per element – intersection points are in general iden-

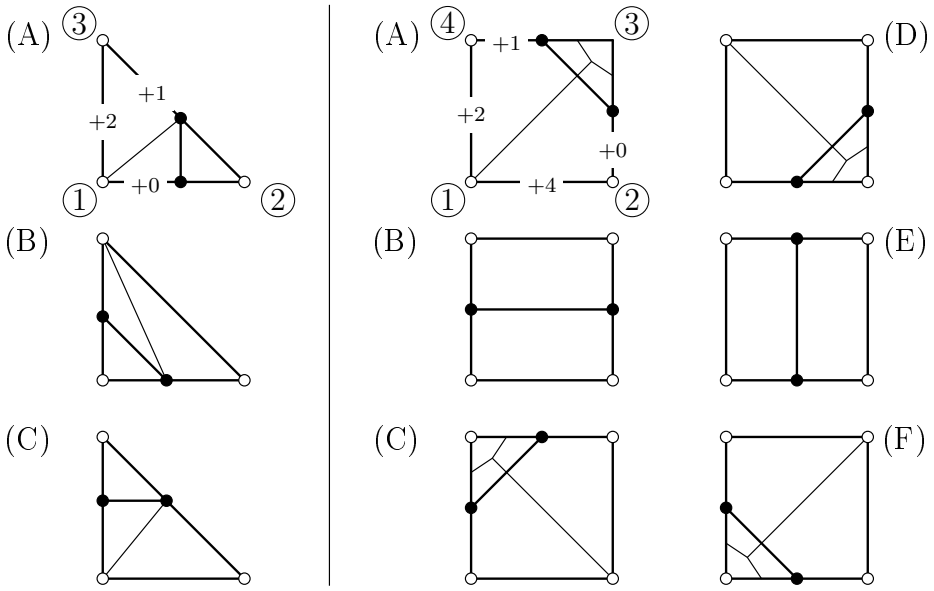

Figure 4.8: Subdividing of 2-d triangular and rectangular elements.

tified by nodal scalar values. They are the result of global tracking strategy techniques. The scalar values are used to linearly interpolate the intersection points. The intersection of the discontinuity surface with a 3-d hexahedron element can result in several different intersection planes. All together, 255 different configurations (plus one "zero-case") are possible. Therein, 130 intersection planes are ambiguous. The remaining 126 intersection planes can be differentiated by seven principal intersection cases, see Figure 4.11. These cases differ in the number of intersection points, and the number of separated element nodes. The element-wise subsurfaces are discretised by up to four triangle elements, recall Figure 4.5. Note that the orientation of these triangle subsurfaces must be also taken into account for the distinction of the intersections. For a correct computation of the numerical integration points and their integration weights, it is crucial to consider – at least in the sequence of node numbering – fixed subelements. The seven principal cases are each subdivided by a fixed tetrahedron scheme. The corresponding configurations are then, depending on their node numbering, turned and squeezed into this subelement scheme. This allows a reduction of complexity of the division procedure.

The element-wise subsurfaces are computed by the so-called **Marching Cubes Algorithm** (MCA), see *Lorensen & Cline* [129]. The MCA[19] originally comes from the field

[19]The Marching Cubes Algorithm is claimed by anti-software patent advocates as a prime example

of computer graphics. Therein, it is used to compute isosurfaces of spatial voxels (scalar field) with polygonal graphic elements. Its application is in general focused on medical visualisations such as CT and MRI scan data images. The algorithm uses an index to a pre-calculated array of 256 possible polygon configurations ($2^8 = 256$) within a cube (hexahedron). In this monograph, the sign of each nodal scalar value of the reference hexahedron finite-element is interpreted as a bit in an 8-bit integer, see Figure 4.9. For positive values, the appropriate bit is set to one; negative values result in a zero bit. The binary sum of all eight element edges indicates the polygon configuration. The polygon configuration is then looked up in the pre-calculated array. A proper implementation of the MCA in the framework of the XFEM can be found in Appendix C.6.

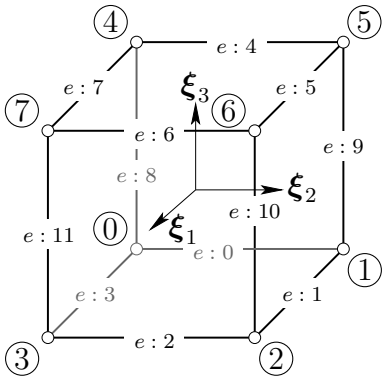

Figure 4.9: MCA hexahedron.

All relevant 126 configurations of the intersection surfaces are presented in Figure 4.11. The intersection points $\mathbf{X}_{S,e}^{\zeta}$, and the triangle normal vectors $\mathbf{m}_S^{s,h}$, indicate the number of subelements $\Omega_{e,\mathrm{sub}}^{h}$ of the possible configurations (configs) per principal case A to G. The numbers in brackets are the indices to the overall 15 possible principal cases, including the ambiguous ones and the "zero-case". The corresponding configuration numbers are based on the aforementioned 8-bit integer, e. g., `[1, 1, -1, 1, -1, 1, -1, -1]` (nodal values) $\rightsquigarrow$ `11010100` (8-bit integer) $\rightsquigarrow$ 212 $\rightsquigarrow$ Case F (11). In Figure 4.11, element nodes with negative values are coloured in red, positive ones in blue. The centre of gravity of each triangle of the intersection surface is depicted by a yellow dot; their corresponding normal vectors are indicated by a red line. The intersection points are visualised with black dots, the subelement tetrahedrons with blue lines. The subelements are indicated by green numbers. Furthermore, the *Gauss*ian integration points are exemplarily depicted for a second order integration; their colouring is inherited from the element nodes. Note that it is necessary to identify[20] the discrete position (side) of the integration points for the correct application of the XFEM enrichment. The integration weights are scaled by the evaluation of a corresponding subelement *Jacobi*an determinant (and the tetrahedron volume correction factor $\frac{1}{6}$).

Remark: The numerical modelling of discontinuities within the XFEM does in general not presume the discretisation of the two sides of a discontinuity. Thus, the trajectory of the discontinuity surfaces can only be revealed vaguely with the introduction of the virtual surface $\bar{\mathcal{S}}$. Alternatively, the position of the **discontinuity surfaces** in the

in the graphics field of the woes of patenting software. An implementation was patented despite being a relatively obvious solution to the surface-generation problem, they claim. Another similar algorithm was developed, called Marching Tetrahedrons, in order to circumvent the patent as well as solve a minor ambiguity problem of marching cubes with some cube configurations. This patent expired in 2005, and it is now legal to use it without royalties since more than 17 years have passed from its issue date [Wikipedia].

[20] Because of the chosen tetrahedron subelements, the identification can be numerically straightforward implemented. One efficient implementation is the computation of five determinants – out of combinations of the tetrahedron nodes with the respective integration point – and the test of their signs.

deformed mesh can be **visualised** by a derivation of the original finite-element mesh. This derivation can be accomplished within a post-processing step. The post-processing step is independent on the regular XFEM computation. Thus, the computation can be solely performed in the visualisation program. Consequently, the topology of the derived mesh can be modified arbitrarily without losing computational efficiency. Therefore, two additional sets of nodes are created for each discontinuous element. Each set of nodes is located on one side of the discontinuity. The displacement of the corresponding nodes is then computed with regular, enriched ansatz functions

$$\mathring{\mathbf{u}}_S^h(\mathbf{X}_S^{\mathcal{S},v}) = \sum_{j=1}^{N_e} \left\{ \boldsymbol{\Upsilon}_{\mathbf{u}}^j(\mathbf{X}_S^{\mathcal{S},v}) \left[\mathbf{u}_S^j + \psi^j \mathbf{a}_S^j \right] \right\} \text{ with } \begin{cases} \mathbf{X}_S^{\mathcal{S},v} & : L \text{ penetration points of } \Gamma_0^{\mathcal{S},h} \\ & \quad (v = 1, \ldots, L)\,, \\ \psi^j & : \text{discrete enrichment}\,. \end{cases} \tag{4.63}$$

The evaluation of the regular ansatz functions $\boldsymbol{\Upsilon}_{\mathbf{u}}^j$ at the penetration points $\mathbf{X}_S^{\mathcal{S},v}$ of the discretised surface $\Gamma_0^{\mathcal{S},h}$ is straightforward. This kind of post-processed visualisation depends on the additional knowledge or storage, respectively, of the variable set $\{\mathbf{X}_S^{\mathcal{S},v}, \psi^j\}$ per discontinuous element. The spatial coordinates of the penetration points read $\mathbf{x}_s^{\mathcal{S},v} = \mathbf{X}_S^{\mathcal{S},v} + \mathring{\mathbf{u}}_S^h$. Other quantities on the additional nodes can be computed analogously, but of course without the additional enrichment. See Figure 4.10 for a 2-d visualisation of

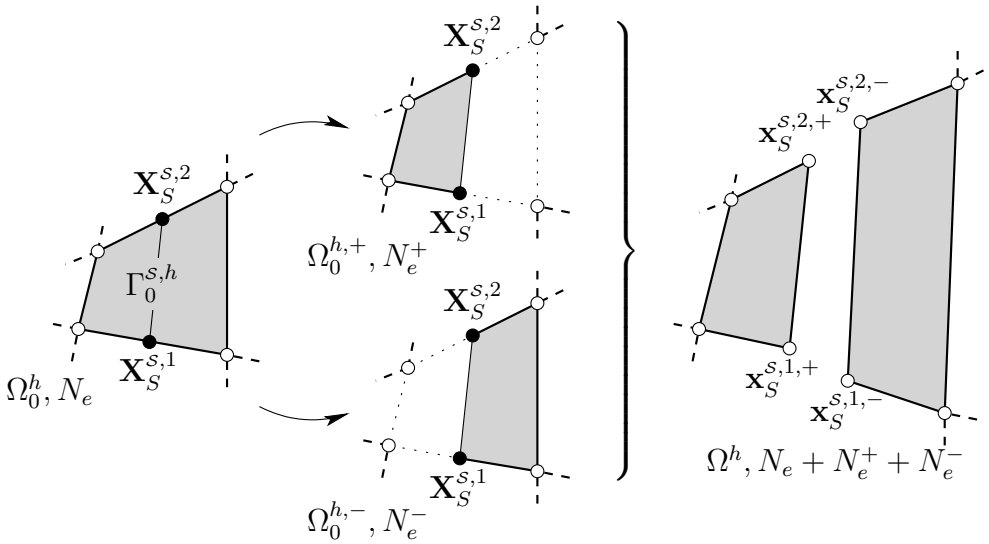

Figure 4.10: Additional node set for the post-processing visualisation of a discontinuity.

this procedure. For more details on this topic, the interested reader is referred to the works of *Remmers* [156] for 2-d triangular elements and *O'Brien & Hodgins* [146] for 3-d tetrahedron elements. Note in passing that because of the self-developed visualisation program PANPOST, cf. *Rempler* [157], mixed element types could be visualised directly. □

$3\times\mathbf{X}^{\zeta}_{S,e}$ | $1\times\mathbf{m}^{\mathcal{S},h}_{S}$ | $11\times\Omega^{h}_{e,\text{sub}}$ | 16× configs

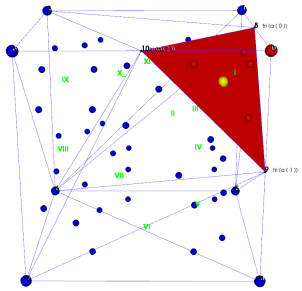

1	254
2	253
4	251
8	247
16	239
32	223
64	191
128	127

Case A (01)

$4\times\mathbf{X}^{\zeta}_{S,e}$ | $2\times\mathbf{m}^{\mathcal{S},h}_{S}$ | $11\times\Omega^{h}_{e,\text{sub}}$ | 24× configs

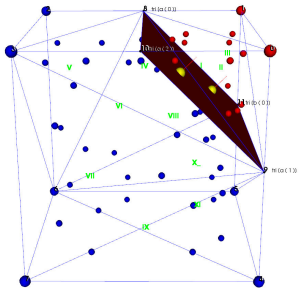

3	48	221
9	144	243
17	96	187
6	192	119
34	252	207
12	246	111
68	238	159
136	249	63

Case B (02)

$5\times\mathbf{X}^{\zeta}_{S,e}$ | $3\times\mathbf{m}^{\mathcal{S},h}_{S}$ | $14\times\Omega^{h}_{e,\text{sub}}$ | 48× configs

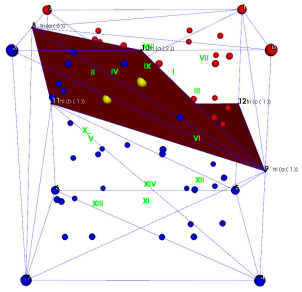

7	38	176	248	217	79
11	208	98	244	47	157
13	49	100	242	206	155
14	50	152	241	205	103
19	200	145	236	55	110
25	196	112	230	59	143
224	70	140	31	185	115
35	76	137	220	179	118

Case C (05)

$4\times\mathbf{X}^{\zeta}_{S,e}$ | $2\times\mathbf{m}^{\mathcal{S},h}_{S}$ | $12\times\Omega^{h}_{e,\text{sub}}$ | 6× configs

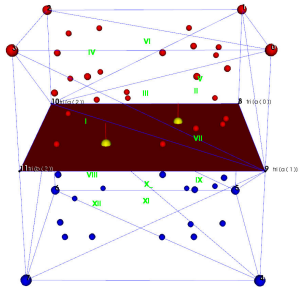

15
51
102
240
204
153

Case D (08)

$6\times\mathbf{X}^{\zeta}_{S,e}$ | $4\times\mathbf{m}^{\mathcal{S},h}_{S}$ | $16\times\Omega^{h}_{e,\text{sub}}$ | 8× configs

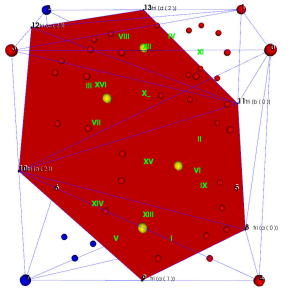

27
39
78
114
228
216
177
141

Case E (09)

$6\times\mathbf{X}^{\zeta}_{S,e}$ | $4\times\mathbf{m}^{\mathcal{S},h}_{S}$ | $16\times\Omega^{h}_{e,\text{sub}}$ | 12× configs

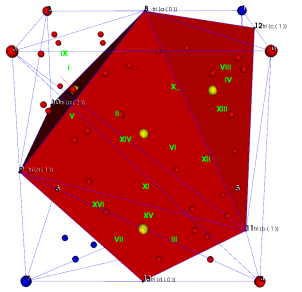

29	201
43	184
54	147
71	142
108	
113	
226	
212	

Case F (11)

$6\times\mathbf{X}^{\zeta}_{S,e}$ | $4\times\mathbf{m}^{\mathcal{S},h}_{S}$ | $16\times\Omega^{h}_{e,\text{sub}}$ | 12× configs

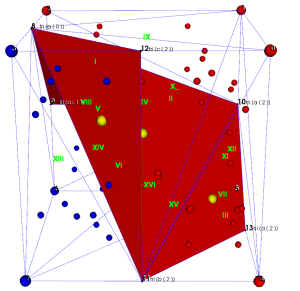

23	198
46	178
57	156
77	139
99	
116	
232	
209	

Case G (14)

Figure 4.11: Subdivision of 3-d hexahedron elements with tetrahedrons.

4.4 Tracking Techniques

A crucial point in the numerical simulation of failure mechanics is the modelling of the appearance and the propagation of discontinuities. The following chapter deals with techniques for a global tracking of displacement jumps in the context of finite-elements. At first, classical level-set functions will be presented. They are nowadays a common chosen tracking method for 2-d simulations of strong discontinuities. In this context, they have been – as far as the author is aware – firstly introduced by *Stolarska* [177]. Besides that, their main application is found in the field of modern computer graphics. For a comprehensive overview on this topic, see *Osher & Fedkiw* [153]. For a sound numerical implementation in the context of the XFEM, level-set functions are vectorially discretised. Vector level-set functions have been generally introduced, and transferred to the XFEM framework, by *Ventura et al.* [186, 187]. During the development of this monograph, vector level-set functions have been the first examined methodology for the numerical tracking of discontinuities. But the application of this methodology turned out to be numerically too costly for 3-d problems. Therefore, the more sophisticated Global Tracking Algorithm (GTA) was chosen to model 3-d discontinuities. The GTA is introduced in Section 4.4.2. It is a robust and yet very elegant strategy to track strong discontinuities in 2-d as well as in 3-d simulations. It has been proposed firstly by *Oliver et al.* [150, 151]. This method has been adopted successfully to simulate discrete fracture by, e. g., *Dumstorff & Meschke* [51], *Cervera & Chiumenti* [35], and *Feist & Hofstetter* [73]. The reader who is interested in a comprehensive comparison of crack path strategies is referred to *Jäger et al.* [112–114]. Note that, although the presented tracking techniques can also be extended to model multiple discontinuity paths, this monograph restricts itself to one single discontinuity path.

4.4.1 2-d Vector Level-Set Functions

Level-set functions identify geometrical areas and/or their movements without parameterising these. The identification process is based on the representation of the border of the geometrical area under study implicitly by a predefined value; this value is most of all chosen to be zero. Thus, the border is defined by $\mathcal{S}_0 = \{\mathbf{X}_S \,|\, \phi(\mathbf{X}_S) = 0\}$. Without going deeper into the field of level-set functions, their principle will be introduced on the basis of a 2-d example. At least in the context of discontinuities, the most useful representation of level-set functions is probably the signed-distance function. It is defined by

$$\phi(\mathbf{X}_S) = \pm \min \|\mathbf{X}_S - \mathbf{X}_S^{\mathcal{S}}\| \quad \forall\, \mathbf{X}_S^{\mathcal{S}} \in \mathcal{S}_0\,, \quad \forall\, \mathbf{X}_S \in \{\mathcal{B}_0^+, \mathcal{B}_0^-\}\,. \tag{4.64}$$

With the *Euklid*ean[21] norm $\|\cdot\|$, the sign differs on the two sides of a closed interface $\mathcal{S}_0$. The function (4.64) allows an implicit description of discontinuities by storing representative values of it at discrete points in the domain $\{\mathcal{B}_0^+, \mathcal{B}_0^-\}$. The signed-distance level-set

[21] *Euclid of Alexandria* (360 BC – 280 BC): Greek mathematician, often referred to as the "Father of Geometry". His book "Elements" is one of the most influential works in the history of mathematics. It is the basis for most geometrical systems, referred to as the "*Euclid*ean geometry" (in contrast to so-called "non-*Euclid*ean geometries that mathematicians discovered in the 19$^{\text{th}}$ century). [WIKIPEDIA]

function is vectorially discretised for a sound implementation into the framework of the XFEM by *Ventura et al.* [186]. The discrete points for the storage of representative values are the nodes $\mathbf{X}_S^j$ of the underlying finite-element mesh. Note that only the discontinuity surrounding nodes $j \in I^*$ are used to store representative values $\tilde{f}^j$. Herein, these nodal values are a data three-tuple $\tilde{f}^j = \{\mathbf{f}(\mathbf{X}_S^j), \mathscr{H}(\mathbf{X}_S^j)\}$. The three-tuple consists of the coefficients of the closest point projection vector $\mathbf{f}^j = \mathbf{f}(\mathbf{X}_S^j)$ of the element node $\mathbf{X}_S^j$ to the discretised discontinuity surface $\mathcal{S}_0 \to \Gamma_0^{s,h}$ or line, respectively, and of a modified *Heaviside* value $\mathscr{H}^j = \mathscr{H}(\mathbf{X}_S^j) = \pm 1$. The latter value identifies the side of the discontinuity. Here, in a 2-d setting, this discretisation results in a polygonal line[22] representation of the discontinuity, see Figure 4.12. Each of the polygonal line segments intersects at least one finite-element. The actual line segment is denoted by $\mathbf{s}_n = \mathbf{X}_{S,n}^{\mathrm{TIP}} - \mathbf{X}_{S,n-1}^{\mathrm{TIP}}$, and the previous one by $\mathbf{s}_{n-1}$. Both line segments end in the discontinuity tip $\mathbf{X}_{S,n}^{\mathrm{TIP}}$ and $\mathbf{X}_{S,n-1}^{\mathrm{TIP}}$, respectively. Let $\mathcal{E}_n \subset \mathbb{R}^2$ be the element domain that contains those finite-elements which are *a*) intersected by $\mathbf{s}_n$, *b*) containing one or both ends of $\mathbf{s}_n$, and *c*) containing nodes whose actual closest point projection vector is shorter than the previous one. The nodes in this element domain – and only these nodes – store the level-set data three-tuple $\tilde{f}^j$. Thus, let $\mathcal{F}_n$ be the set of element nodes at time step n whose level-set data needs to be computed. Consequently, the variable $\mathcal{F}_{n-1}$ represents the analogue node set of the previous time step $n-1$. The complete set of element nodes whose level-set data needs to be computed (updated) is denoted by $\mathcal{F}_a$. Now, there are three different cases to consider for the determination of the nodal set $\mathcal{F}_a$:

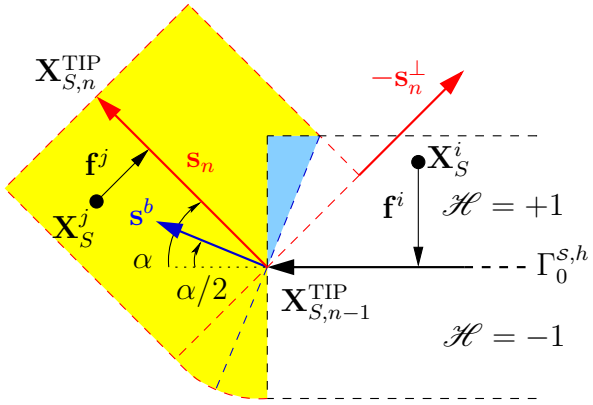

Figure 4.12: Nodal data update area.

- closest distance to the discontinuity is a point projection on $\mathbf{s}_n$,
- change of the closest point projection from $\mathbf{s}_{n-1}$ to $\mathbf{s}_n$,
- closest distance to the discontinuity is a line to the tip $\mathbf{X}_{S,n-1}^{\mathrm{TIP}}$.

In Figure 4.12, the computation area of the nodal level-set data is marked yellow "▭" and the update area is marked blue "▭". With these preliminaries, the set $\mathcal{F}_a$ can be defined

[22] The "only" polygonal line representation of the discontinuity is a consequence of the approximation of the level-set function ϕ^h with linear finite-element ansatz functions, i. e., $\phi^h(\mathbf{X}_S) = \sum_{j=1}^{N_e} \boldsymbol{\Upsilon}^j \phi^j$. This also results in a smoothing of line kinks within an element. Alternative discretisations for the approximation of ϕ^h are discussed in *Ventura et al.* [187].

as:

$$\begin{aligned}\mathcal{F}_a = \big\{\, \mathbf{X}_S^j \in \mathcal{E}_n : \quad & (\mathbf{X}_S^j - \mathbf{X}_{S,n}^{\mathrm{TIP}}) \cdot \mathbf{s}_n \quad \leq \quad 0\,, \\ & (\mathbf{X}_S^j - \mathbf{X}_{S,n-1}^{\mathrm{TIP}}) \cdot \mathbf{s}_{n-1} \;>\; 0 \quad \vee \quad (\mathbf{X}_S^j - \mathbf{X}_{S,n-1}^{\mathrm{TIP}}) \cdot \mathbf{s}^b \;>\; 0 \,\big\} \\ & \text{with} \quad \mathbf{s}^b = \frac{\mathbf{s}_{n-1}}{\|\mathbf{s}_{n-1}\|} + \frac{\mathbf{s}_n}{\|\mathbf{s}_n\|}\,.\end{aligned} \tag{4.65}$$

Note in passing that it may be necessary for 2-d rectangular finite-elements to also implement a correction step after the determination of $\mathcal{F}_a$. The corrector step assures that really all element nodes $\mathbf{X}_{S,e}^j$ of an intersected element "contain" level-set data. The therefore necessary condition reads $(\mathbf{X}_{S,e}^i - \mathbf{X}_{S,n}^{\mathrm{TIP}}) \cdot \mathbf{s}_n > 0$. Finally, the nodal level-set values are determined by

$$\begin{aligned}& \mathscr{H}^j(\mathbf{f}^j) = \mathrm{sign}\big[(\mathbf{X}_S^j - \mathbf{X}_{S,n-1}^{\mathrm{TIP}}) \cdot \mathbf{s}_n^{\perp}\big]\,, \\ & \mathbf{f}^j = \begin{cases} -\hat{\mathbf{s}}_n^{\perp}\big[(\mathbf{X}_S^j - \mathbf{X}_{S,n-1}^{\mathrm{TIP}}) \cdot \hat{\mathbf{s}}_n^{\perp}\big]\,, & \text{if}: \; (\mathbf{X}_S^j - \mathbf{X}_{S,n-1}^{\mathrm{TIP}}) \cdot \mathbf{s}_n \geq 0\,, \\ -(\mathbf{X}_S^j - \mathbf{X}_{S,n-1}^{\mathrm{TIP}})\,, & \text{if}: \; (\mathbf{X}_S^j - \mathbf{X}_{S,n-1}^{\mathrm{TIP}}) \cdot \mathbf{s}_n < 0 \end{cases} \\ & \qquad \text{with} \quad \hat{\mathbf{s}}_n^{\perp} = \frac{\mathbf{s}_n^{\perp}}{\|\mathbf{s}_n^{\perp}\|}\,. \\ \rightsquigarrow \quad & \phi^j = \phi(\mathbf{X}_S^j) = \mathscr{H}^j \|\mathbf{f}^j\| \quad \text{and} \quad \phi^h(\mathbf{X}_S) = \sum_{j=1}^{N_e} \boldsymbol{\Upsilon}^j \phi^j\,.\end{aligned} \tag{4.66}$$

Remark: Besides the previous presentation of level-set functions in the context of damage, their methodology is also a reasonable mechanism for the modelling of material interfaces, e. g., voids in solids. Level-set functions can be used to model arbitrarily shaped voids in finite-element meshes without the necessity of a re-aligning of finite-elements because of the implicit character. Thus, together with the XFEM, arbitrarily shaped solid areas can be modelled, see *Koch* [119]. In principle, any BVP can be generated out of one single, fixed finite-element mesh, see the figure on the right side of this remark. Further possible application areas are, e. g., computational fluid dynamics (CFD) and structure optimisation. □

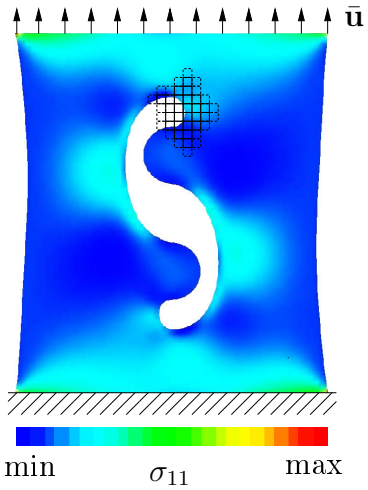

After the combination of vector level-set functions and the XFEM, the numerical implementation of the **propagation mechanism of a discontinuity**, based on SIF, is presented in the following. This is a commonly used approach for 2-d crack problems. Note that this is based on the fundamental concepts of fracture mechanics from Section 3.1. First, the concept of system energy change (3.27) for single-phase materials needs

to be formally extended for its application on multi-phasic materials. Consequently, the external energy $\mathrm{d}\mathsf{U}_{ext}$ contains a fluid pressure contribution on the discontinuity surface $\bar{\mathcal{S}}$ (contour $\mathcal{C}^{\mathcal{S}}$), viz.

$$\begin{aligned} \mathrm{d}\mathsf{U}_{ext} &= \int_{\bar{\mathcal{S}}} \left[(\mathbf{H}^T (\mathbf{T}_E^S - \mathcal{P}\,\mathbf{I}))\,\mathbf{n} \cdot \mathrm{d}\mathbf{s} \right] \mathrm{d}a \\ \rightsquigarrow \quad -\frac{\mathrm{d}\mathsf{U}}{\mathrm{d}s} &= \underbrace{\int_{\mathcal{C}} \left[\mathcal{W}\, n_1 - \frac{\partial u_i}{\partial x_1}\, T^S_{E,i\ell} n_\ell \right] \mathrm{d}c}_{J} - \underbrace{\int_{\mathcal{C}^{\mathcal{S}}} \mathcal{P}\, \frac{\partial u_i}{\partial x_1}\, n_i \,\mathrm{d}c}_{P} \quad \text{with} \quad \bar{\mathcal{S}} \overset{2-d}{\Leftrightarrow} \mathcal{C}^{\mathcal{S}} \,. \end{aligned} \tag{4.67}$$

The shift in $\mathbf{e}_1$-direction reveals a fluid pressure contribution P to the energy release rate, cf. (3.32). Thus, the concept of the J-integral yields for 2-d problems $G_{(I,II)} = J - P = \frac{1}{E'}(K_I^2 + K_{II}^2)$. Recall that E' is connected to the 2-d choice of plain stress or plain strain. In this context, the introduction of two independent equilibrium states of an elastically deformed body is a common procedure. The two equilibrium states are used to numerically compute the SIF. This numerical computation is based on the so-called interaction integral between the two states, cf. *Yau et al.* [196]. The first state with the field variables $u_i^{(1)}$, $\mathcal{P}^{(1)}$, $T_{E,ij}^{S(1)}$, and $E_{S,ij}^{(1)}$ corresponds to the real situation; the latter two quantities denote the coefficients of the stress and strain tensor. The second state with identical variables as the first one but indexed with the superscript $(\,\cdot\,)^{(2)}$ is an auxiliary state. The concept of the J-integral for the sum of the two equilibrium states reads $J^{(1+2)} - P^{(1+2)}$. After this formal extension of the J-integral to multi-phasic materials, it can be straightforward shown that the fluid pressure contribution reveals no interaction contribution between the two states, if the pressure $\mathcal{P}^{(1+2)} \equiv \mathcal{P}$ is constant between the two states. This yields

$$P^{(1+2)} = \int_{\mathcal{C}^{\mathcal{S}}} \mathcal{P}^{(1+2)}\, \frac{\partial u_i^{(1+2)}}{\partial x_1}\, n_i \,\mathrm{d}c = \int_{\mathcal{C}^{\mathcal{S}}} \mathcal{P} \left(\frac{\partial u_i^{(1)}}{\partial x_1} + \frac{\partial u_i^{(2)}}{\partial x_1} \right) n_i \,\mathrm{d}c = P^{(1)} + P^{(2)} \,. \tag{4.68}$$

The assumption of constant pressure is based on a foregoing assumption of the connection of the discontinuity to an unlimited external fluid reservoir. As a consequence, the overall interaction integral yields

$$J^{(1,2)} = \frac{2}{E'}(K_I^{(1)} K_I^{(2)} + K_{II}^{(1)} K_{II}^{(2)}) = -\int_{\Gamma} \left[\mathcal{W}^{(1,2)}\, \delta_1^\ell - \frac{\partial u_i^{(1)}}{\partial x_1}\, T_{E,i\ell}^{S(2)} - \frac{\partial u_i^{(2)}}{\partial x_1}\, T_{E,i\ell}^{S(1)} \right] \frac{\partial q}{\partial x_\ell}\, \mathrm{d}a \,. \tag{4.69}$$

Therein, the contour line integral is converted into a domain integral with the weighting function $q(\mathbf{x})$, see Figure 4.13. The weighting function is defined as $q(\mathbf{x}) = \{1 \;\forall\; \mathbf{x} \in \mathcal{C}_1 \mid 0 \;\forall\; \mathbf{x} \in \mathcal{C}_2 |$ varying monotonically in-between$\}$. $\mathcal{C}_1$ and $\mathcal{C}_2$ are two non-intersecting contours enclosing the tip of the discontinuity. The monotonicity of $q(\mathbf{x})$ is a sufficient

but not necessary requirement. It is discretised with regular FEM ansatz functions, viz. $q(\mathbf{x}) = \sum_{j \in I^{\#}} \boldsymbol{\Upsilon}^j(\mathbf{x})$. The set $I^{\#}$ is defined for all element nodes $\mathbf{x}_j$ with $\|\mathbf{x}_j - \mathbf{x}^{TIP}\| < r$. It is noted that the stress intensity factors are analytically independent of the radius r. However, the choice of numerically larger radii leads to better approximations of the interaction integral. The interaction integral only has to be evaluated over those elements crossed by the circle around the discontinuity tip. In all other elements, the weighting function is constant and does not contribute to the interaction integral, see Figure 4.13(c). Besides, the restriction holds that the discontinuity inside the circle must be straight.

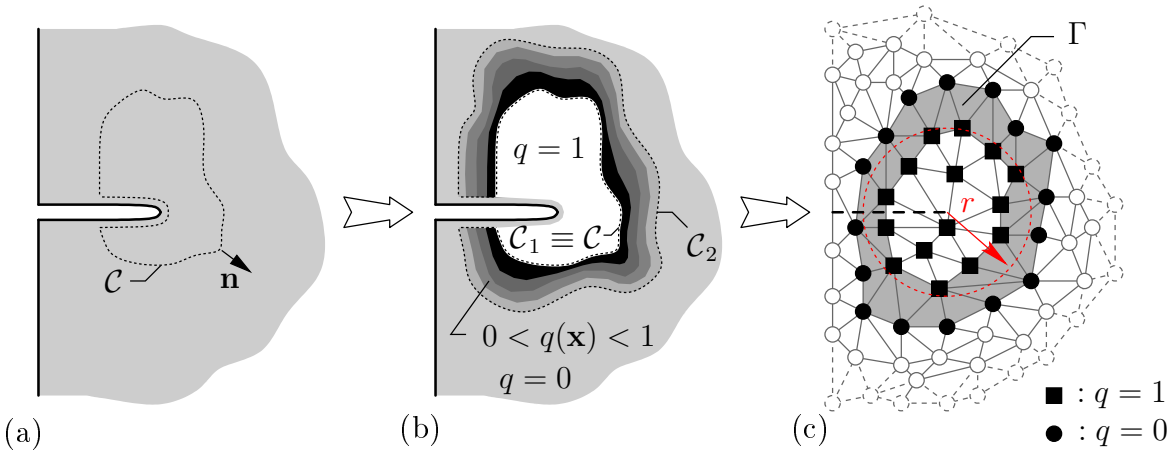

Figure 4.13: Conversion of contour integral (a) into domain integral (b) and discretisation (c).

With these preliminaries, individual stress intensity factors can be computed. The real stress intensity factors are obtained by the choice of the auxiliary mode with $K^{(2)}_{I,II} = 0 \vee 1$. It follows that

$$K_I^{(1:\,\mathrm{real})} = \frac{E'}{2}\, J^{(\mathrm{real},\,\mathrm{aux}\,I)} \quad \text{with} \quad \left\{ \begin{array}{ll} K_I^{(2)} & = 1 \\ K_{II}^{(2)} & = 0 \end{array} \right\} \; : \text{pure Mode } I \text{ auxiliary state}\,,$$

$$K_{II}^{(1:\,\mathrm{real})} = \frac{E'}{2}\, J^{(\mathrm{real},\,\mathrm{aux}\,II)} \quad \text{with} \quad \left\{ \begin{array}{ll} K_I^{(2)} & = 0 \\ K_{II}^{(2)} & = 1 \end{array} \right\} \; : \text{pure Mode } II \text{ auxiliary state}\,. \tag{4.70}$$

This now allows the application of the maximum hoop stress criterion, see *Erdogan & Sih* [70]. For this criterion, the discontinuity growth is assumed to occur in a direction so that the hoop stress $T^S_{E,\theta\theta}$ is maximum. This correlates with the direction in which the shear stress $T^S_{E,r\theta}$ vanishes, i. e.,

$$T^S_{E,r\theta} = \frac{1}{\sqrt{2\pi r}} \cos\frac{\theta}{2} \left[\frac{1}{2} K_I \sin\theta + \frac{1}{2} K_{II} \left(3\cos\theta - 1\right) \right] = 0\,. \tag{4.71}$$

The solution of $\cos\frac{\theta}{2} = 0 \Rightarrow \theta = \pm\pi$ is irrelevant as it points in the backwards direction of the discontinuity. Consequently, (4.71) becomes only zero for $K_I \sin\theta + K_{II}\,(3\,cos\,\theta - 1) =$

0. This yields the solution of the propagation angle θ_S with

$$\theta_S = 2 \arctan \frac{1}{4} \left[\frac{K_I}{K_{II}} \pm \sqrt{\left(\frac{K_I}{K_{II}} \right)^2 + 8} \right] . \tag{4.72}$$

Thus, for the angle θ_S, $T^S_{E,\theta\theta}$ is a principal stress. With this, one can find an equivalent Mode I SIF K_I^{eq}, expressed in relation to the maximum hoop stress, viz.

$$K_I^{\text{eq}} = \sqrt{2\pi r}\, T^S_{E,\theta\theta}(\theta_S) = K_I \cos^3 \frac{\theta_S}{2} - 3K_{II} \cos^2 \frac{\theta_S}{2} \sin \frac{\theta_S}{2} . \tag{4.73}$$

The parameter K_I^{eq} provides a single measure of mixed-mode stress fields. It is used to determine the material-dependent discontinuity growth under mixed-mode loading. For a DIN EN ISO 12737 compatible material strength parameter K_I^c, the growth propagation criterion then follows

$$K_I^{\text{eq}} = K_I^c . \tag{4.74}$$

Remark: It has been shown in *Koch* [120] that the previously discussed crack propagation mechanism cannot be applied straightforward on linear triangle finite-element meshes. The discussed mechanism only converges within a fair discretisation level for – at least – linear rectangular elements. Regarding the benchmark BVP in Figure 4.14 for pure Mode I and pure Mode II loading, one can observe a strong mesh dependency for the numerical computation of θ_S with linear triangular elements, see Figure 4.15. In Figure 4.14, the variable F denotes a force quantity and L a length quantity. Thus, the reference solution of the given BVP (Mode I : $\theta_S = 0°$, Mode II : $\theta_S = -70.5°$, cf. *Erdogan & Sih* [70]) can only be obtained with a rather high discretisation level. Normally, a large radius r could compensate the discretisation level. But the path independency of the J-integral can only be preserved for straight discontinuities within the radius r. This restriction collides with small sized finite-elements where the path of the discontinuity itself is highly discretised. Alternatively, the numerical computation of the crack propagation with linear triangular elements can be replaced by a principal stress criterion, see Section 3.2.4, in particular on (3.77). This criterion shows a very good agreement of the numerical crack propagation results with experiments for even relatively coarse linear triangle element meshes. □

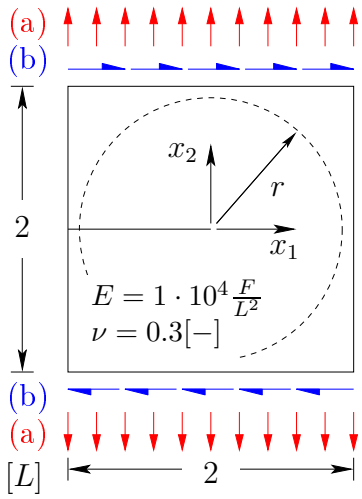

Figure 4.14: Pure (a) Mode I, and (b) Mode II BVP benchmark ($1 \cdot 10^{-4} L$).

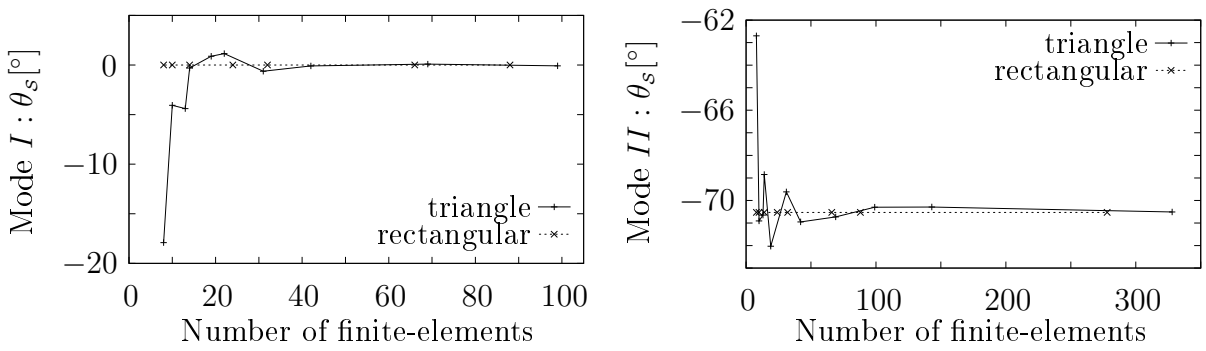

Figure 4.15: Convergence behaviour of triangle and rectangular based finite-element meshes ($r = 0.855\,L$) to pure Mode I, and Mode II benchmark loading, see Figure 4.14.

4.4.2 3-d Global Tracking Algorithm (GTA)

Due to the numerical costs of a 3-d tracking of discontinuities with vector level-set functions, the Global Tracking Algorithm (GTA) is introduced. The GTA is a robust and yet very elegant strategy to globally track strong discontinuities in 2-d as well as in 3-d simulations. The method – as far as the author is aware – originates, for its application to computational failure mechanics, from *Oliver et al.* [150, 151] and *Samaniego* [163]. Since then, it has been applied successfully multiple times in the context of fracture mechanics. The GTA methodology is based on the solution of a constitutive heat-conduction-like problem. Therein, the characterisation of the discontinuity results in an additional field of scalar-valued DOF. The additional DOF are interpreted as global level-set unknowns. As a consequence, arbitrarily shaped discontinuity surfaces can be described $\mathcal{C}^0$-continuously[23]. This is the main reason for the robustness of the method. However, the robustness is achieved at the cost of solving an additional PDE. The additional GTA PDE is only weakly coupled with the regular continuum-mechanically based equations. Thus, it can be solved within a post-processing step after each standard time step. The solution process of the additional PDE has been implemented in the FEM program PANDAS within a so-called staggered algorithm.

The GTA scalar field is denoted $\phi(\mathbf{X}_S)$. For a constant level of ϕ, iso-surfaces can be provided. Thus, the particular iso-surface of level zero $\phi = 0$ is defined to be the geometrical representation of the discontinuity surface $\mathcal{S}_0$. By the application of the principal stress criterion (3.77), it is stated that the discontinuity surface runs perpendicular to the maximum principal stress direction $\mathbf{n}^*_{max} = \mathbf{n}^*_1$. The direction vector $\mathbf{n}^*_{max}$ – as an eigenvector of $\mathbf{T}^S_E$ – is correlated to the maximum eigenvalue λ_{max}. As a consequence, the remaining two eigenvectors $\mathbf{n}^*_i$ $(i = 2, 3)$ are tangential to the propagating disconti-

[23] The continuity class $\mathcal{C}^0$ consists of all continuous functions. Furthermore, the class $\mathcal{C}^1$ consists of all differentiable functions whose derivative is continuous; such functions are called continuously differentiable. Note that a differentiable function might not necessarily be $\mathcal{C}^1$ continuous:

$$\begin{aligned} f(x) &= x^2 \sin(\tfrac{1}{x}) && \text{for } x \neq 0 \text{ and } f(x) = 0 \text{ for } x = 0 && : \text{continuous and differentiable}, \\ f'(x) &= -\cos(\tfrac{1}{x}) + 2x \sin(\tfrac{1}{x}) && \text{for } x \neq 0 \text{ and } f'(x) = 0 \text{ for } x = 0 && : \text{discontinuous at } x = 0\,. \end{aligned}$$

nuity; the two eigenvectors span the discontinuity plane in the spatial configuration. A pull-back transport, along with a normalisation, is applied for their use in the referential configuration, viz.

$$\mathbf{m}_2^* := \frac{\mathbf{F}_S^{-1}\,\mathbf{n}_2^*}{\|\mathbf{F}_S^{-1}\,\mathbf{n}_2^*\|} \quad \text{and} \quad \mathbf{m}_3^* := \frac{\mathbf{F}_S^{-1}\,\mathbf{n}_3^*}{\|\mathbf{F}_S^{-1}\,\mathbf{n}_3^*\|}\,. \tag{4.75}$$

By design, the GTA function ϕ shall provide levels that envelope the vector fields $\mathbf{m}_2^*$ and $\mathbf{m}_3^*$. Those envelopes are perpendicular to the gradient of ϕ. Thus, let ϕ be the solution of the PDE. Thus,

$$\mathbf{m}_2^* \cdot \mathrm{Grad}_S\,\phi = 0 \quad \text{and} \quad \mathbf{m}_3^* \cdot \mathrm{Grad}_S\,\phi = 0\,. \tag{4.76}$$

This motivates the constitutive introduction of a tensor $\mathbf{G}^*$ and a corresponding vector $\mathbf{j}^*$ with

$$\mathbf{G}^* := \mathbf{m}_2^* \otimes \mathbf{m}_2^* + \mathbf{m}_3^* \otimes \mathbf{m}_3^* + \epsilon\,\mathbf{I} \quad \text{and} \quad \mathbf{j}^* := -\mathbf{G}^*\,\mathrm{Grad}_S\,\phi\,. \tag{4.77}$$

Therein, $\mathbf{G}^*$ can be interpreted as an anisotropic "thermal conductivity-like" tensor and the vector $\mathbf{j}^*$ as a "conduction flux". The tensor $\mathbf{G}^*$ has been modified with a small perturbation[24] ϵ in the meaning of fictitious isotropic conductivity. This is a measure to restore the necessary ellipticity of the otherwise rank-one tensor (for the direction $\mathbf{n}_{max}^*$). The ellipticity guarantees that positive eigenvalues exist, a crucial property for the solution of the following weak formulation of the problem; rank-one tensors may have null eigenvalues and consequently inherit a singularity problem. With (4.77), a field equation for the determination of an equilibrium can be postulated as

$$\mathrm{Div}_S\,\mathbf{j}^* = 0 \quad \forall\,\mathbf{X}_S \in \mathcal{B}_0\,. \tag{4.78}$$

This clarifies the terminology "heat-conduction-like problem" as (4.78) is comparable to a heat flow problem of a stationary temperature field. Accordingly, the problem is a classical BVP, cf. Section 2.6.4. Thus, the boundaries of the spatial domain Ω_0 are split into *Dirichlet* Γ_D^ϕ and *Neumann* $\Gamma_N^{\mathbf{j}}$ boundaries with $\phi = \bar{\phi}$ on Γ_D^ϕ, and $\mathbf{j}^* = \bar{\mathbf{j}}^*$ on $\Gamma_N^{\mathbf{j}}$. With the common procedure of transferring a strong equilibrium field equation into its weak formulation, cf. again Section 2.6.4, the referential divergence field (4.78) yields

$$\int_\Omega \mathbf{j}^* \cdot \mathrm{Grad}_S\,\delta\phi\,\mathrm{d}V_S = \int_{\Gamma_N^{\mathbf{j}}} \bar{\mathbf{j}}^* \cdot \mathbf{m}_S\,\delta\phi\,\mathrm{d}A_S\,. \tag{4.79}$$

Note that, in general, a flux-free boundary condition $\bar{\mathbf{j}}^* = \mathbf{0}$ is assumed. One can now see the only weakly coupling of (4.79) with the regular continuum-mechanically based system of DAE (2.77). Furthermore, the linear characteristic of (4.79) is obvious. The spatial

[24] A value of $\epsilon = 10^{-6}$ has been applied for the numerical simulations of this monograph.

discretisation of the field variables reads

$$\begin{aligned} \phi(\mathbf{X}_S) &\approx \phi^h(\mathbf{X}_S) &&= \bar{\phi}^h(\mathbf{X}_S) &&+ \sum_{j=1}^{N} \boldsymbol{\Upsilon}_{\phi}^{j}(\mathbf{X}_S)\ \phi^j &&\in \mathcal{A}^{\phi,h}\,, \\ \delta\phi(\mathbf{X}_S) &\approx \delta\phi^h(\mathbf{X}_S) &&= &&\sum_{j=1}^{N} \boldsymbol{\Upsilon}_{\phi}^{j}(\mathbf{X}_S)\,\delta\phi^j &&\in \mathcal{T}^{\phi,h}\,. \end{aligned} \tag{4.80}$$

The ansatz $\mathcal{A}^{\phi,h}$, the test spaces $\mathcal{T}^{\phi,h}$, the basis functions $\boldsymbol{\Upsilon}_{\phi}^{j}$ and so forth follow analogously to (4.2) and thus, won't be pointed out again. The discretised approximation $\phi^h(\mathbf{X}_S)$ is not time-dependent. Consequently, a temporal discretisation is obsolete; the GTA problem is solely stationary. Thus, the fully discretised weak formulation yields

weak formulation of GTA

$$R^{\phi,h} = \int_{\Omega^h} \mathbf{j}^*(\mathbf{T}_E^S) \cdot \mathrm{Grad}_S\, \delta\phi^h \mathrm{d}V_S = 0\,. \tag{4.81}$$

This linear system is solved after each accepted standard time step in a post-processing step. For the post-processing step, the actual solid *Cauchy* stress tensor $\mathbf{T}_E^S$ needs to be known. Therefore, its decomposed principal stress directions and values are transferred

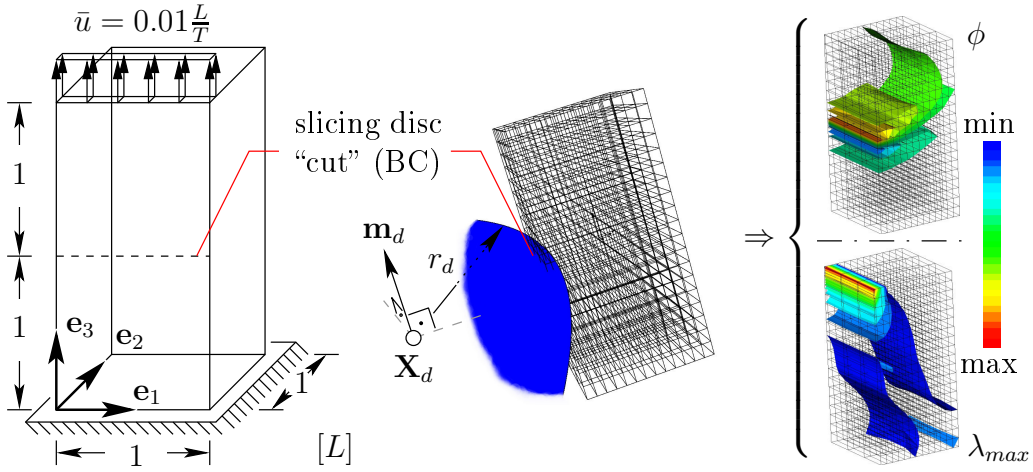

Figure 4.16: Geometry-based initial *Dirichlet* GTA BC.

into the reference configuration, and are then numerically stored at each integration point. The principal stress directions can be adopted efficiently from the preceding evaluation of the *Rankine* **crack propagation criterion**. The decoupled solution mechanism can be implemented within a so-called staggered algorithm. The most crucial part in the solution of (4.81) is the proper choice of initial *Dirichlet* BC. From the multiple possibilities of defining initial BC, e. g., mesh-dependent, per root-element, or geometry-based, only the latter one is implemented in the numerical simulations within this monograph. The

geometry-based initial BC have the advantage of mesh independency. However, a flexible pre-processing step is needed for the determination of the initial values of $\bar{\phi}^h$. Herein, this is done by the computation of the closest point projection to a slicing disc "cut" per element node. The slicing disc is defined by its centre point $\mathbf{X}_d$, its normal vector $\mathbf{m}_d$ and its radius r_d. This pre-processing step is visualised in Figure 4.16. Therein, an exemplary rectangular block under tension is presented to test the GTA implementation. This purely academic BVP has the unit length L and the time unit T. With it, the initial *Dirichlet* BC result in the – depicted on the right hand side – isosurfaces of the scalar field ϕ, and in the thereto perpendicular maximum principle stress field λ_{max}. It can be seen that the zero level of ϕ already characterises the designated discontinuity surface after the initial time step. Regarding the numerical simulation over time, the propagation of the discontinuity (visualised by red dots), and the evaluation of the scalar field ϕ can be nicely seen in Figure 4.17. Although the results of this numerical test BVP should be rather interpreted in a qualitative way, the resulting discontinuity surface $\mathcal{S}_0$ is in good compliance to *Jäger* [112].

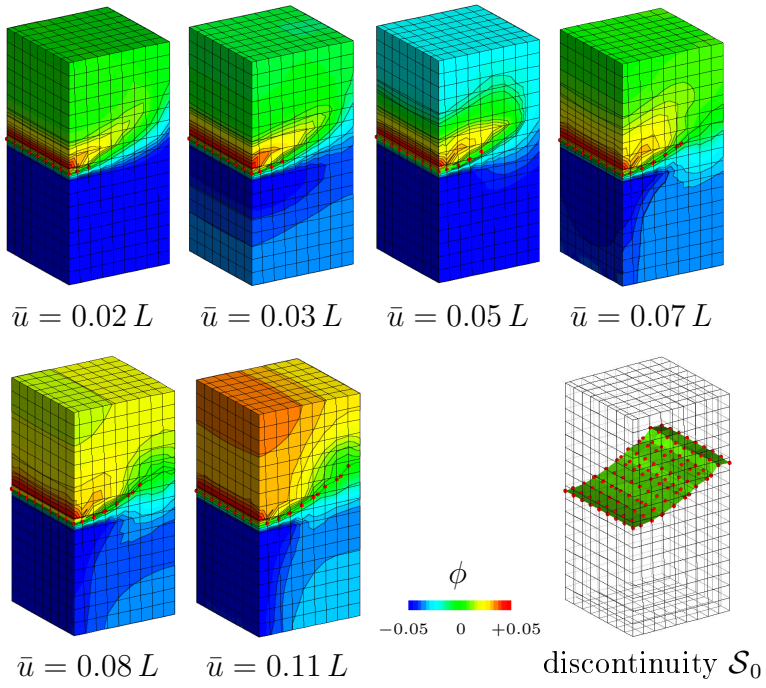

Figure 4.17: Propagation of $\mathcal{S}_0$, and evaluation of ϕ over time.

Chapter 5:
Numerical Examples

The numerical examples are computed on the basis of the theoretical aspects of the preceding chapters. All numerical simulations have been computed with the FEM program PANDAS. During the evaluation of this monograph, PANDAS has been extended to be able to compute 3-d discontinuous problems with the XFEM. By design, this FEM program has no restrictions about the number of coupled balance equations. Its highly sophisticated FEM core code is capable of solving – in principle – arbitrary numbers of strongly coupled balance equations simultaneously. Unfortunately, the core code was not designed to also compute weakly coupled balance equations non-simultaneously. As a consequence of the tracking of discontinuities with the GTA, the solution process had to be extended by a so-called staggered algorithm. The implementation of this algorithm into PANDAS now allows the solution of additional PDE in a post-processing step within each standard time step. Accompanying to this, the post-processing tool PANPOST has been developed to visualise the results of those numerical computations. Furthermore, this visualisation program has also been extended to be capable to visualise strong discontinuities. Note in passing that on top of that several additional software tools had become necessary for the development of the presented numerical methodology. Thus, an extensive numerical toolbox has been developed as a side product.

The implementation of the numerical tracking mechanisms, vector level-set functions and GTA have been already shown in a small test BVP at the end of the corresponding subsections. Before advancing to the more complex numerical examples of the combination TPM and XFEM, numerical studies on the AugFEM are first presented. The subsequent 2-d numerical example simulates the fluid exchange within a tear opening of a hydrated tissue cross section. This BVP is computed within the tracking framework of vector level-set functions. The final 3-d numerical examples address the problem of an avascular necrosis of a human femur fracture. The simulations are computed on a real live geometry and validate the numerical methodology that was proposed in this monograph.

5.1 Numerical Study on the FEM and AugFEM

This numerical example gives a brief overview over the capabilities of the AugFEM. For further details on this topic the interested reader is referred to *Rempler et al.* [158]. The numerical results of the FEM and the AugFEM are compared to each other on two regularly refined meshes, concerning computing time and memory requirement. The following numerical study uses a viscoplastic *Perzyna*-type regularisation within a small-strain approach, cf. Section B.2. For the sake of simplicity, a single-phase material is assumed. The numerical example is considering a 3-d BVP problem based on a 2-d template taken from *Ammann* [2]. The BVP is illustrated in Figure 5.1. Due to symmetry reasons, only a quarter of the tensile bar is discretised. The numerical studies were

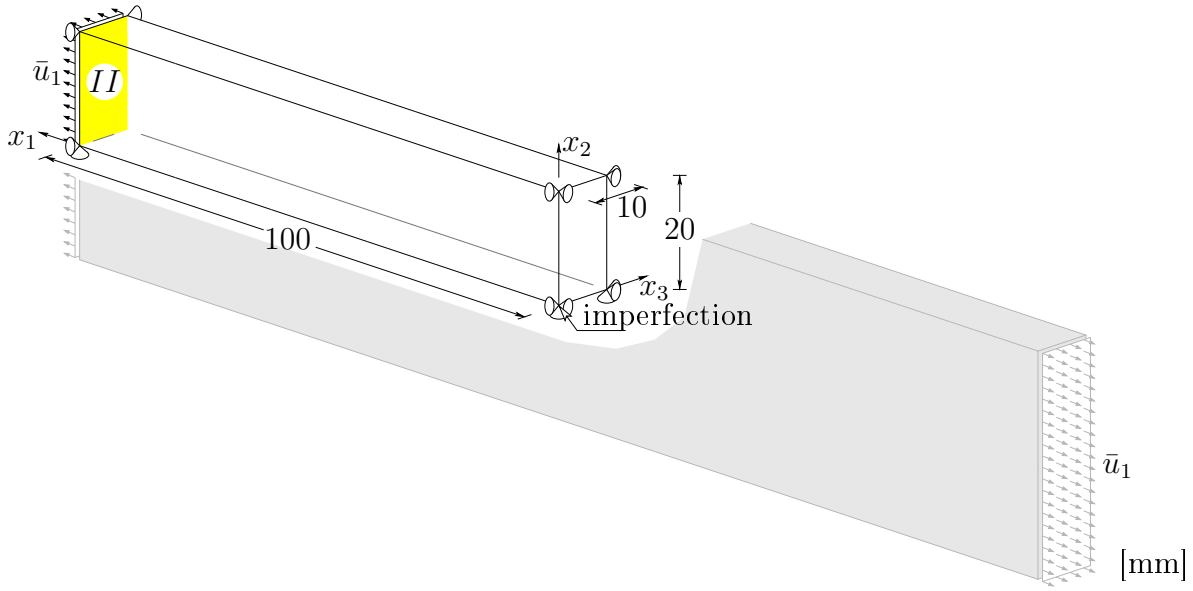

Figure 5.1: BVP: 3-d tensile bar, cf. *Rempler et al.* [158].

computed on meshes consisting of hexahedral elements as shown in Figure 5.4. For a better resolution of the plastic zone, one third of the mesh is meshed finer. In order to initiate a shear band, the *Lamé* constants μ and λ are weakened at the imperfection position $x_1 = 0\,\mathrm{m}, x_2 = 0\,\mathrm{m}$ and $x_3 = 0\,\mathrm{m}$. Commonly for FE computations, this BVP uses a time-step size control within the *Newton* iteration scheme, i. e., the time-step size varies. A *von-Mises*-type yield criterion, cf. (B.10), determines the inelastic material behaviour. The exemplary motivated softening law from (B.12) is assumed. The material parameters are chosen as $\mu = 81\,000\ \mathrm{kN/m^2}, h_{sat} = 0.99, \lambda = 118\,000\ \mathrm{kN/m^2}, \quad h_e = 40, \eta = 0.1\,\mathrm{s}, \kappa_0 = 400\ \mathrm{kN/m^2}, r = 1$. A linearly increasing *Dirichlet* boundary condition $\bar{u}_1$ is applied with $\dot{\bar{u}}_1 = 1\,\mathrm{mm/s}$ at one side of the BVP. The standard FEM solution was computed with quadratic basis functions. The additional degrees of freedom for the augmented FE formulation were discretised using linear basis functions. All numerical results are generated iteratively with a generalised minimum residual (GMRES) scheme, which is preconditioned by a level-3 incomplete LU factorisation (ILU). An identical computation code was used to compare the two methods. The existing FEM source code has just been extended by additional DOF. The numerical integration was implemented with a *Gauss*ian quadrature of order five, resulting in 27 integration points per element. This fully integrated finite-element is highly recommended for the 3-d plasticity problems discussed here.

The resulting surface load on the side II of the tensile bar is compared between the AugFEM and the FEM, see Figure 5.3. The computational results of the AugFEM are close to the standard FEM computations, and the computations finish in a reasonable time, see Table 5.1. For this example, this is due to much larger time-step sizes for the AugFEM. This of course is charged by an increased memory requirement since the additional degrees of freedom result in a larger stiffness matrix. Visualising the necking of the tensile bar, the alternative method shows a sharp localisation of the plastic deformation,

see Figure 5.2. As one can see, the width of the arising shear band is not mesh-dependent. Instead, the shear band width is proportional to the viscosity parameter η, see *Ammann* [2]. This proves that the presented AugFEM leads to comparative results to the standard FEM. Further on, it is shown that the AugFEM results in an advantage in computing time compared to the standard FEM. Thus, by the transfer of internal DAE systems to

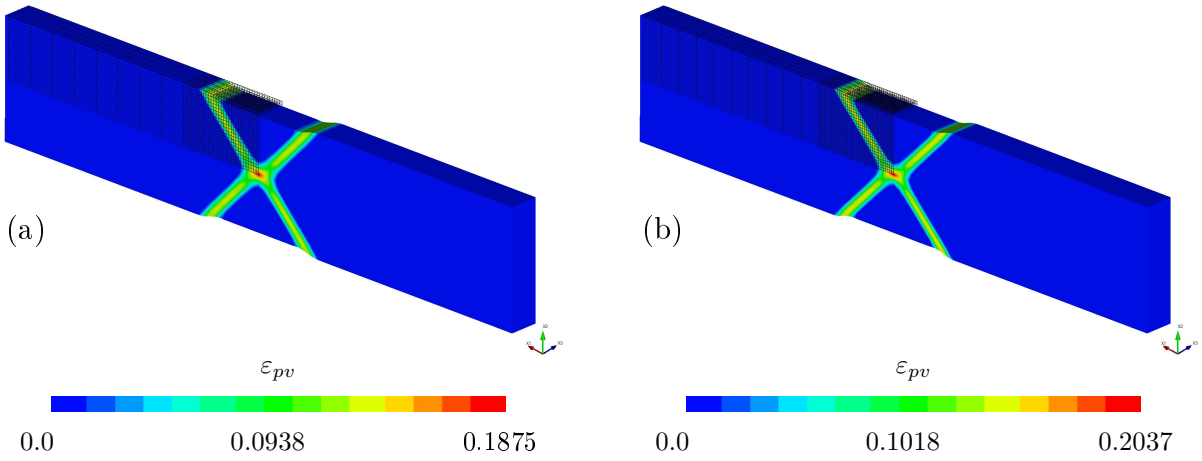

Figure 5.2: 3-d tensile bar: accumulated plastic strains ε_{pv} at deformation $\bar{u}_1 = 0.5\,\text{mm}$ with variable time-step size $\triangle t = 10^{-5}\,\text{s}$ computed with the augmented FE formulation on (a) 3040 and (b) 5520 hexahedral elements (deformation scaled by 3.0), cf. *Rempler et al.* [158].

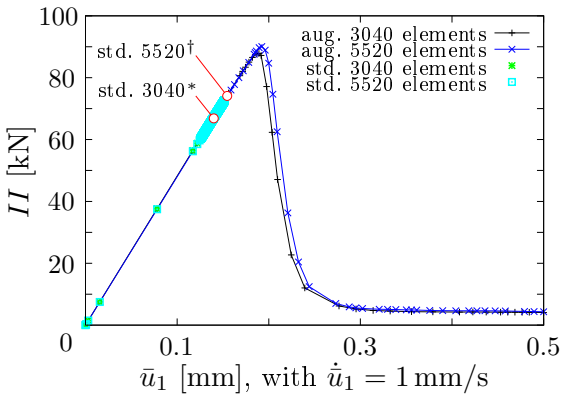

Figure 5.3: 3-d tensile bar: development of the surface load on surface II for successive mesh levels with variable time-step size $\triangle t$, cf. *Rempler et al.* [158]. For details on † and * compare Table 5.1.

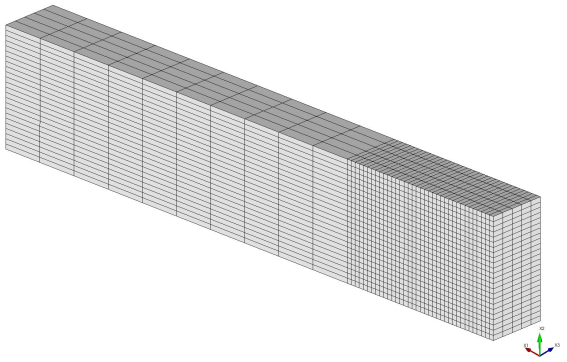

Figure 5.4: 3-d tensile bar: finest mesh with 5520 hexahedral elements, cf. *Rempler et al.* [158].

element nodes, the presented AugFEM is a sound alternative to the standard FEM for the computation of elastic-inelastic material behaviour. Even with this showcase, a drawback of the AugFEM may occur for very localised inelastic zones due to the additional global variables that appear at each node. So there is still a large potential left for optimisa-

tion, e. g., regional limitations of plastic zones and succeeding local enrichment as they are known from the XFEM. The restriction to a local enrichment will result in a reduced global system. Furthermore, there are several techniques on the market to improve the numerical solution of larger systems, e. g., *Krabbenhoft et al.* [121] and *Wieners* [192]. With the advantage in computing time, it is possible to predict the direction of plastic deformation growth earlier. Accompanying this, early statements of designated fracture process zones could be given. For the future, the AugFEM may be the appropriate choice for the fast computation of large plasticity problems due to its implied advantage in feasible parallelisation. Since the actual tendency of multi-core processor systems, the parallel computation of numerical computations is becoming elementary. Further on, the method can be quite directly extended to other regularisation techniques such as, e. g., gradient plasticity, without the necessity of submerging to the integration point level.

Elements		**Computing time** [h:min]		**DOFs / History variables**		**Time steps**		**Newton iterations**		**Memory requirement** (average) [MB]	
Integration points :27 Ansatz for $\mathbf{u}/\boldsymbol{\varepsilon}_p$:quad./lin.	**3-d** *h:Newton*	standard FEM	AugFEM	standard FEM	AugFEM	standard FEM	AugFEM	standard FEM	AugFEM	standard FEM	AugFEM
	3040	≈ 34:03*	34:03	45783 492480	70353 0	1041 7732	40 68	5143	254	586.6 × **3.65**	2143.8
	End of computing ($\bar{u}_1$): 0.14212 mm (FEM) vs. 0.5 mm (AugFEM)										
	5520	≈ 127:02†	127:02	79779 894240	122079 0	1682 3977	51 88	2470	333	1246.0 × **3.61**	4503.8
	End of computing ($\bar{u}_1$): 0.15185 mm (FEM) vs. 0.5 mm (AugFEM)										

Table 5.1: Comparison of the standard FEM and the AugFEM on successive 3-d mesh levels with variable time-step size ($\triangle t$ is chosen depending on the *Newton* convergence). In this test, it can be seen that in the same computing time, where the AugFEM reaches the final displacement $\bar{u}_1 = 0.5$ mm, the standard FEM simulation only arrives at a displacement of approximately 0.15 mm, cf. *Rempler et al.* [158].

5.2 2-d Tear Propagation in Hydrated Biological Tissue

The following 2-d numerical experiment simulates the tear propagation process in an hydrated biological tissue. In particular, the BVP, see Figure 5.5, is designed to model human spleen rupture, see Figure 1.1. The spleen is an organ in the left upper quadrant of the abdomen (also called the belly). It filters blood by removing old or damaged blood cells. Thus, it is one of the most blood-saturated organs in the human body. Consequently, a spleen rupture permits large amounts of blood to leak into the abdominal cavity, it can result in shock and death. It is a situation that requires immediate medical attention. Note that this example is meant to provide first basic insights into discontinuous fluid-saturated porous media. Thus, a rather elementary XFEM framework is used. Consequently, the simulation results should be regarded qualitatively.

The symmetric cross section is loaded under a pure Mode I displacement. Its surrounding edges are assumed to be drained ($\mathcal{P}_0 = 0$). The tissue is modelled using a biphasic TPM model, cf. Section 2.6.1. The model consists of a linear elastic solid skeleton and a viscous interstitial fluid. The XFEM is applied for the numerical treatment of the tearing mechanism. SIF are computed to evaluate the tear extension regarding. A maximum hoop stress criterion, see (4.69) and (4.73), drives the extension process. The computation of the SIF uses the discretised energy configuration scheme. The arising opening in the tissue is considered as to be connected to an external fluid reservoir and is thereby loaded with differing pressures. Furthermore, vector level-set functions are used for the global tracking of the discontinuity. In this framework, only small deformations are considered. With these assumptions, the application of the cohesive zone model is omitted. The material parameters are chosen as given in Figure 5.5. It is a common challenge to find proper material parameters for the simulation of biological tissue. Especially very well blood-saturated tissues, like the here considered spleen, highly differ in its in vivo and ex vivo material properties. Thus, accurate physical experiments, as they are common practise

BVP (material) parameters:

μ^S	=	$32.55 \cdot 10^{+3}$	$\mathrm{N/m^2}$
λ^S	=	$17.09 \cdot 10^{+4}$	$\mathrm{N/m^2}$
n^S_{0S}	=	0.68	
k^F	=	$1.0 \cdot 10^{-4}$	m/s
K_{I_C}	=	$2.0 \cdot 10^{+2}$	$\mathrm{N}\sqrt{\mathrm{m}}$
$\bar{u}_h$	=	$4.0 \cdot 10^{-3}$	m
t_i	=	$3.0 \cdot 10^{+0}$	s
t_h	=	$1.5 \cdot 10^{+1}$	s

loading path:

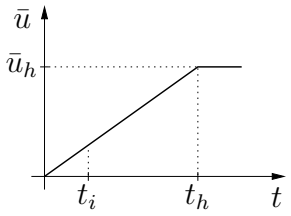

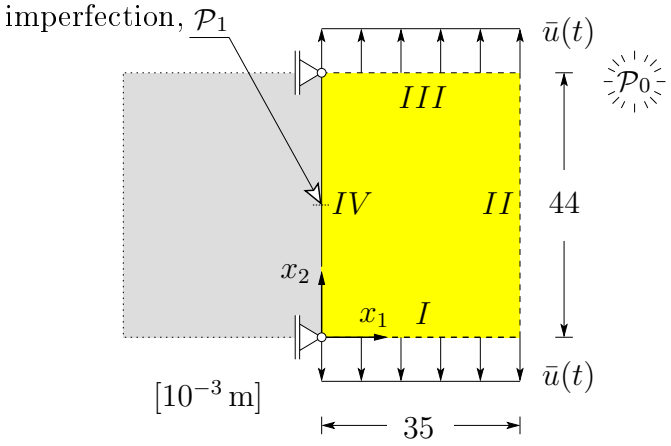

Figure 5.5: BVP: cross section of hydrated tissue.

for non-grown materials, are in general not available. Therefore, the parameters applied here are based on in vivo experiments on pig tissue, cf. *Sailer* [162], and on contributions from *Cutnell & Johnson* [41], and *Baković et al.* [6]. The spleen blood circulation has been assumed to be four times higher than in the overall bulk ($\rightsquigarrow n^S_{0S} = 0.68$).

The displacement loading $\bar{u} = 4.0$ mm is linearly increased in $t = 15$ s, see again Figure 5.5. In order to simulate the interstitial pressure development, three different tear pressure loadings are applied, i. e., $\mathcal{P}_1^{\mathrm{a}} = -10^3\,\mathrm{N/m^2}$, $\mathcal{P}_1^{\mathrm{b}} = 0\,\mathrm{N/m^2}$, and $\mathcal{P}_1^{\mathrm{c}} = 10^3\,\mathrm{N/m^2}$. The pressure loadings are directly applied through *Dirichlet* BC in order to model pressure impacts explicitly. The impact of these three tear pressure loadings to the inside of the tissue is shown in Figure 5.6. Also, the interstitial fluid flow ($\mathbf{w}_F$) – towards or away from the tear opening – is indicated by the pressure distribution $\mathcal{P}$. Note, one can observe that

the tear further expands with increasing $\mathcal{P}_1$.

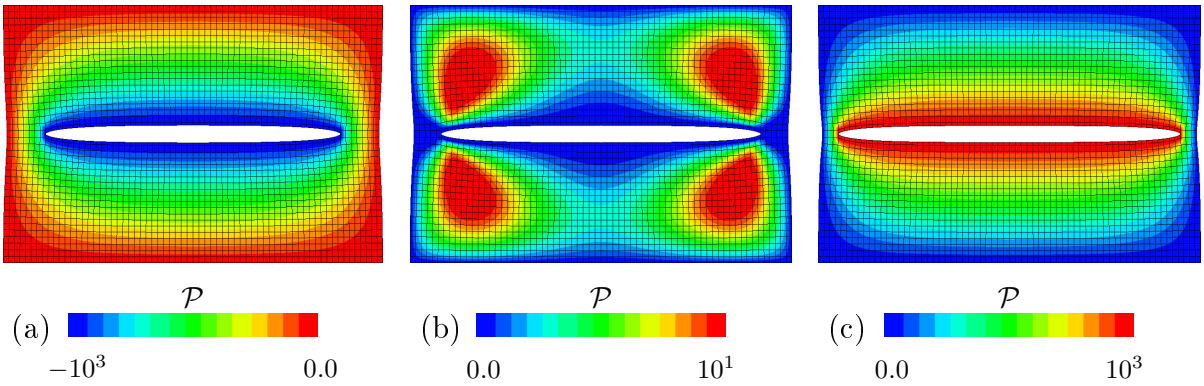

Figure 5.6: 2-d hydrated tissue cross-section: varying interstitial pressure development inside the tissue for three different tear pressure loadings.

5.3 3-d Fracture of the Human Femur

The final 3-d numerical example addresses the problem of femoral neck fracture of the human femur. The femoral neck is located at the proximal end of the femur, near the tip. This type of bone fracture is a common injury that is triggered already by relatively low external forces. Especially older people are affected by such fractures because the natural descaling (osteoporosis) increases the risk of fracture. This type[1] of fracture often disrupts the blood supply to the head of the femur. Depending on the level of restricted blood supply, portions of the femoral neck and femoral head can die (avascular necrosis). This level highly influences the choice of treatment. It is a criterion for joint-preserving measurements, i. e., fixation of the fracture with screws and/or plates or prosthetic implants.

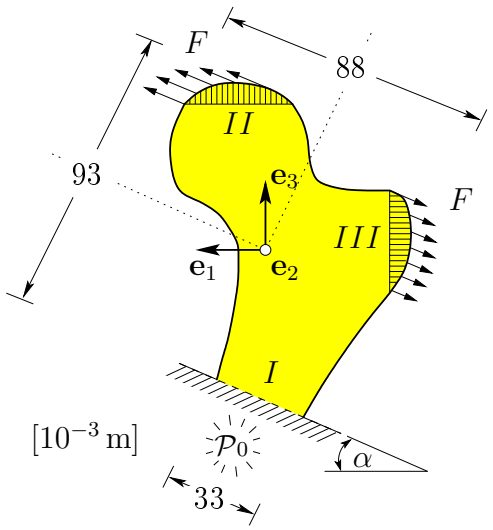

Figure 5.7: BVP: head of the human femur; $\mathbf{e}_2$-depth $= 50 \cdot 10^{-3}$ m.

The geometry of the BVP under study is depicted in Figure 5.7. It is designed to represent the head of a human femur. Three surfaces are discretised to apply BC. Only the lower surface I is drained; this surface is also geometrically fixed. External forces $\pm F$

[1] In clinical practise, two classifications of the femoral neck fracture have proven. The first classification, after *Pauwels* [154], differentiates three types of femoral fractures by the angle between the horizontal and the broken line. The second one, after *Garden* [81], also takes the degree of dislocation of the femoral head and the therefrom resulting restriction of blood supply into account.

are applied opposing on surface II and III. The forces are scaled by the fixed time-step size $\triangle t = 1.0 \cdot 10^{-3}$. The BVP is rotated by the angle α around the $\mathbf{e}_2$-axis to reflect the real life position of the femur. The numerical model is based on the previous developed biphasic continuum-mechanical model. Furthermore, all of the presented numerical methodology is implemented herein. The corresponding parameters are chosen as follows:

$$
\begin{aligned}
\rho^{SR} &= 2.1 \cdot 10^4 \ \mathrm{kg/m^3} & \qquad n^S_{0S} &= 0.6 \\
\rho^{FR} &= 1.0 \cdot 10^4 \ \mathrm{kg/m^3} & \qquad \alpha &= 26^\circ \\
\gamma^{FR} &= 3.24 \cdot 10^4 \ \mathrm{kN/m^3} & \qquad F &= 3.9 \cdot 10^{-3} \ \mathrm{kN} \\
\mu^S_0 &= 2.36 \cdot 10^8 \ \mathrm{kN/m^2} & \qquad \kappa &= 0.0 \\
\lambda^S_0 &= 1.98 \cdot 10^8 \ \mathrm{kN/m^2} & \qquad \mathbf{g} &= 0.0 \ \mathrm{m/s^2} \\
\gamma^S_0 &= 1 & \qquad f_c &= 0.0 \ \mathrm{kN/m^2} \\
\mu^S_\sim &= 1.0 \cdot 10^6 \ \mathrm{kN/m^3} & \qquad a &= 8.0 \cdot 10^{-3} \ \mathrm{1/m} \\
\lambda^S_\perp &= 5.0 \cdot 10^5 \ \mathrm{kN/m^3} & \qquad b &= 0.5
\end{aligned}
$$

The chosen parameters and external loads are inspired by *Krause et al.* [122], and *Gasser & Auer* [82]. Some additional assumptions have been made due to the lack of in vivo material parameters[2]. Consequently, the presented results of physical quantities should be regarded in a qualitative way. In this context, it has been assumed that the fracture extends per computational time step, i.e., the critical value f_c is set to be zero. This extension is limited to one element-row per time step. These simplifications lead to a better comparability of the numerical results. Nevertheless, the simulations are computed on a real life geometry[3]. Initially, the X-ray computed tomography (CT) file has been adapted to meet the requirements of FEM simulations. The mesh generation is based on an initial tetrahedron mesh which was converted into a hexahedron mesh. This has been done by remeshing each tetrahedron element from its centre of gravity with four hexahedron elements. As the consequence, the resulting finite-element mesh consists of randomly positioned and arbitrary shaped hexahedron elements. The final mesh consists of $2,828$ 8-node hexahedron elements and a total number of $28,792$ DOF. So, altogether this kind of mesh requires an efficient and stable numerical methodology.

The numerical experiments are designed to gain insights of external parameters to the internal distribution of pressure, fluid flow, and the shape of the fracture. **Variant A** "cuts" the mesh near the tip of the femur, see Figure 5.8. Recall, this "cut" defines initial *Dirichlet* BC for the GTA. These BC are meant to force a typical femur neck fracture, see Figure 1.2_2. This type of fracture is critical because it often results in the replacement of the femur head with a prosthetic implant. The numerical computation of the shape of the fracture is in good agreement with radiographs. Furthermore, the presented methodology allows insights to the consequent change of the interstitial fluid flow and the internal pressure distribution. **Variant B** "cuts" the mesh on the opposing side to variant A, see Figure 5.9. It is positioned nearer to the body of the femur. These BC are meant to force

[2]Material parameters in the field of biomechanics are typically measured ex vivo. Thus, the material properties of living tissue is in general falsified.

[3]The skeleton data have been obtained by courtesy of S. Van Sint Jan, Laboratory of Anatomy, Biomechanics and Organogenesis, Université Libre de Bruxelles.

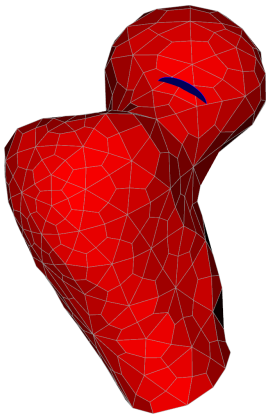

Figure 5.8: Variant A.

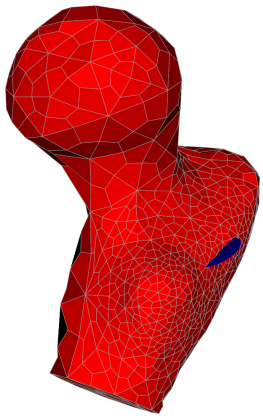

Figure 5.9: Variant B.

Variant A (in 10^{-3} m):

$$\mathbf{X}_d^A = [-7,\, -14,\, 25]^T\, \mathbf{e}_i$$
$$\mathbf{m}_d^A = [1,\, 0,\, 1.5]^T\, \mathbf{e}_i$$
$$r_d^A \;\; = 7$$

Variant B (in n 10^{-3} m):

$$\mathbf{X}_d^B = [-20,\, -18,\, -12]^T\, \mathbf{e}_i$$
$$\mathbf{m}_d^B = [1,\, 0,\, 1.5]^T\, \mathbf{e}_i$$
$$r_d^B \;\; = 7$$

a typical intertrochanteric fracture, see Figure 1.2_3. This type of femur fracture has a good chance of healing. Treatment involves stabilising the fracture with a lag screw and plate device to hold the two fragments in position. The computational result is again in good agreement with radiographs. The shape of the fracture is curved towards the tip of the femur. The results confirm the benefits of the presented numerical simulation method. With it, new coherences can be gained. In this context, the presented numerical methodology can act as a virtual (numerical) lab.

Remark: At this point the author of the monograph would like to point out a general drawback of the GTA. In the context of this BVP, the GTA can fail to predict the correct crack propagation surface. This situation originates from a "switch" of the maximum principal tensile stress direction. Oddly shaped discontinuity surfaces can occur because the GTA is designed to compute perpendicular surfaces to that directions. If the maximum principal tensile stress "switches" its direction, the computed perpendicular surface follows. This is visualised in Figure 5.10. The depicted streamlines are computed from the maximum principal tensile stress direction. The green surface represents the prediction of a designated discontinuity surface for fault initial BC. This limitation must be taken into account in the selection of proper BC. Note in passing that similar effects can also happen within 2-d simulations, see *Dumstorff* [50]. □

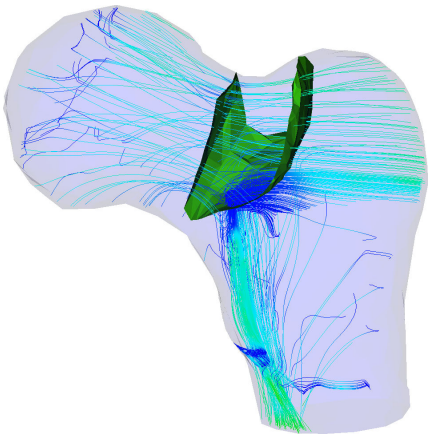

Figure 5.10: Stress direction streamlines and fault GTA discontinuity surface.

Variant A ($F = \pm 3.6 \cdot 10^{-3}\,\mathrm{kN}$) **Variant A** ($F = \pm 18.0 \cdot 10^{-3}\,\mathrm{kN}$)

GTA surface (ϕ), intersection points coloured in red

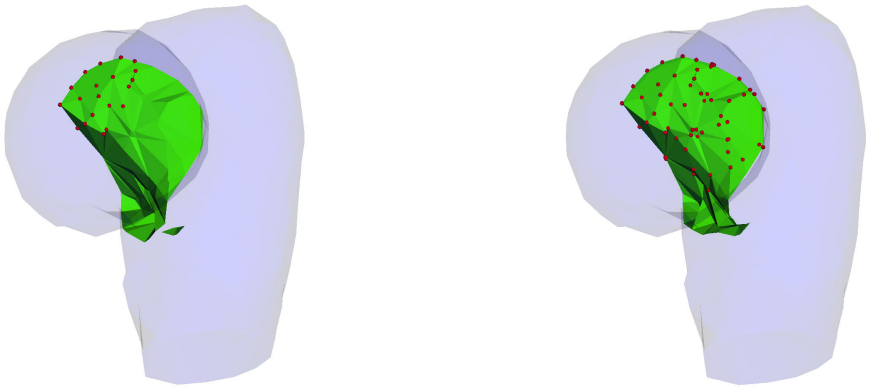

internal pressure distribution ($\mathcal{P}$, $[\mathrm{kN/m^2}]$)

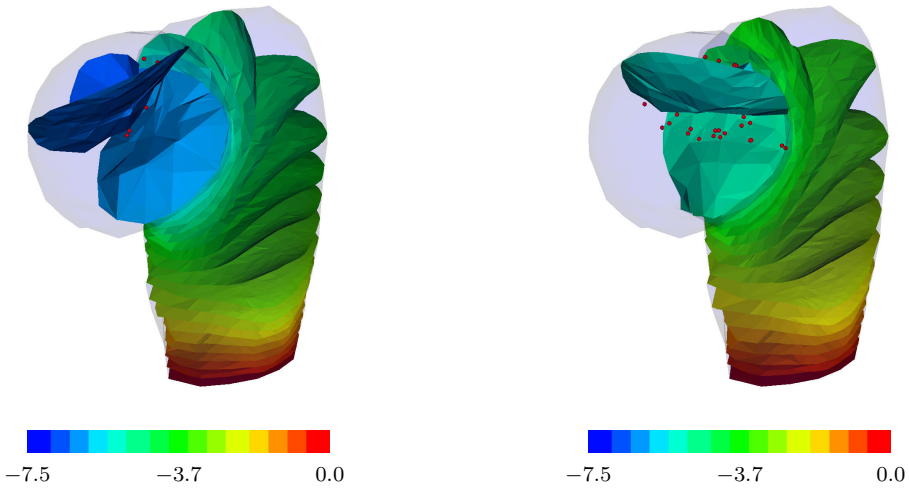

interstitial fluid flow ($\mathbf{w}_F$, $[10^{-3}\,\mathrm{m/s}]$)

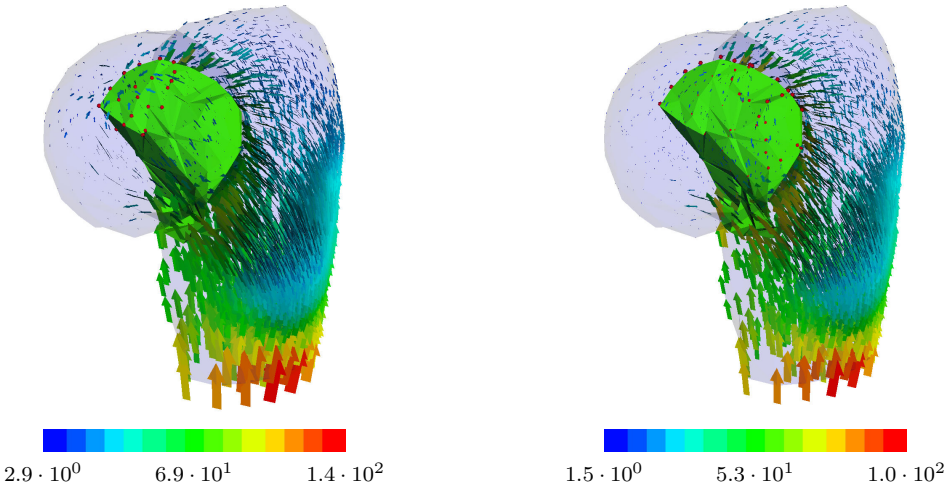

Figure 5.11: Computational results for variant A.

Variant B ($F = \pm 3.6 \cdot 10^{-3}\,\mathrm{kN}$) **Variant B** ($F = \pm 18.0 \cdot 10^{-3}\,\mathrm{kN}$)

GTA surface (ϕ), intersection points colored in red

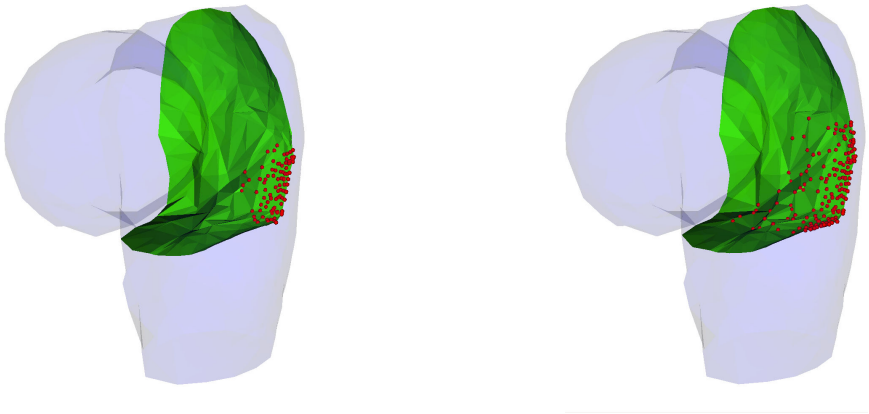

internal pressure distribution ($\mathcal{P}$, [kN/m^2])

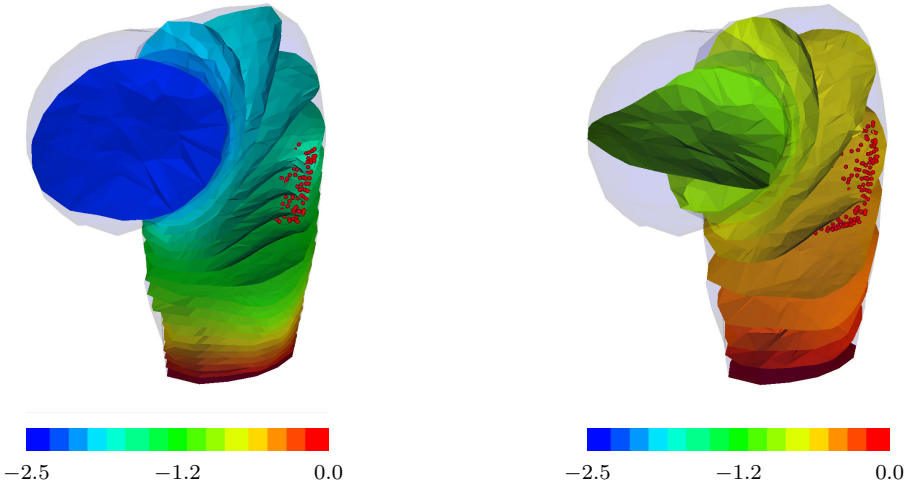

interstitial fluid flow ($\mathbf{w}_F$, [10^{-3} m/s])

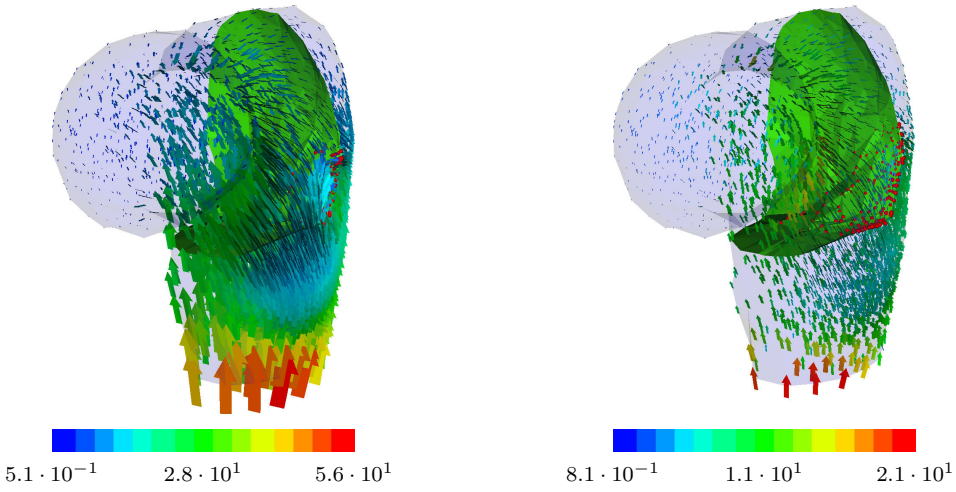

Figure 5.12: Computational results for variant B.

Chapter 6:
Summary and Outlook

The goal of this monograph was the development of a numerical methodology for the simulation of damage processes in multi-phasic materials. Within the wide range of multi-phasic materials, the focus was in particular on the applicability to biomaterials. Therefore, fundamentals of classical continuum-mechanical field theories have been introduced. This introduction was framed within the **TPM**. With the aid of the TPM, it was possible to derive a thermodynamically consistent **multi-phasic material model**. Constitutive settings closed the continuum-mechanical model used in this monograph; it was designed to consist of two phases, in detail, a fully fluid-saturated, materially incompressible solid. The porous solid skeleton has been modelled with a hyperelastic *Ogden*-type strain energy function. In order to take a compaction point of the porous skeleton into account, the strain-energy function has been extended with a volumetric term. The interstitial fluid has been assumed to be viscous. Its interstitial seepage flow through the solid skeleton was modelled with a *Darcy*-like approach. Therein, deformation-dependent permeability has been introduced implicitly. A brief excurs in material plasticity was necessary for the understanding of the later presented extension of the FEM.

In advance to the discussion on continuum fracture mechanics, a brief introduction into the theoretical fundamentals of fracture mechanics has been given. Starting from stress concentration aspects, singular stress fields have motivated **SIF**. An energetic approach, together with the general introduction of the **J-integral**, formulated a framework for the numerical computation of SIF. This framework was interpreted as a first approach towards the numerical simulation of damage processes, albeit only for linear elastic materials. The **cohesive fracture theory** has then been applied to transfer this first approach into a more general framework. Basic strong discontinuity kinematics have been founded on an enriched solid displacement field function. The enriched part of the displacement field function consists of the displacement jump quantity and the ***Heaviside* step function**. As a consequence, the material deformation gradient was identified to inherit a singular character. Thus, a virtual surface, placed in between the two sides of a discontinuity, was introduced in order to avoid possible incompatibilities. The influences of jump quantities over this **virtual surface** have been taken into account for the formulation of the overall BVP. This has been done with respect to global master balance equations. Therefrom, modified weak formulations of the volume and the momentum balances resulted. The additional internal body volume of the opening of the discontinuity has been postulated as an **internal fluid influx**. Furthermore, a transverse isotropic potential function was introduced to derive the cohesive traction forces on the discontinuity. With this, large deformation problems can be addressed. The investigation of the loss of ellipticity, regarding the biphasic finite acoustic tensor, revealed the common ***Rankine* crack propagation criterion** for the solid skeleton.

The spatial and temporal discretisation of the developed biphasic continuum-mechanical model have been presented for the FEM. Therein, the temporal discretisation was based on single-step ***Runge-Kutta* methods**. Prior to the discussion on the XFEM, its basic principle was first introduced using an example from the field of elasto-viscoplastic material behaviour. This yielded to an augmented Finite-Element formulation for inelastic materials, the **AugFEM**. The final **consolidation of** the **XFEM** and the **TPM** used a single enrichment for the numerical discretisation of the discontinuous displacement field. The spatial discretisation applied an additional internal *Neumann* BC as an ansatz for the fully fluid-saturated opening of the discontinuity. The computation of the cohesive traction in the actual configuration was made possible with the transport of the referential intersection points onto the intermediate virtual surface. In order to meet the requirements of the *Gauss*ian integration scheme, a subdivision process was introduced for discontinuous elements. **Hexahedron** finite-elements have been chosen because of their superiority over tetrahedron elements. In this context, the finding of the 3-d sub-elements was based on the **MCA**. Numerous configurations of the MCA have been investigated to pre-compute the fixed sequences of the sub-element node numbering. With these insights, two tracking techniques have been presented. The first, regarding a **vector level-set** function, was used to numerically implement 2-d damage processes. The corresponding propagation criterion based on the numerical computation of the previously introduced fracture fundamentals. The second tracking technique, the **GTA**, was implemented into PANDAS within a staggered algorithm. The GTA made it possible to globally track 3-d discontinuities with an additional discretised, heat-conductivity-like scalar field function.

Three numerical example BVP provide an insight to the practical impact of the theoretical aspects of this monograph. All simulations have been computed with the (X)FEM program PANDAS. The first numerical example proves that the AugFEM is a sound alternative to the standard FEM for the computation of elastic-inelastic material behaviour. The subsequent 2-d numerical example simulates the fluid exchange within a tear opening of a hydrated tissue cross section. The last example shows the 3-d damage capabilities of the presented numerical methodology on the fracture of a human femur. The results confirm the benefits of the presented numerical simulation method. With it, new coherences can be gained.

This monograph successfully proves the proposed combination of the XFEM together with the TPM as a sophisticated numerical methodology for the simulation of damage in multi-phasic materials. With this, it is now possible to simulate 3-d fluid processes in discontinuous porous media. Thus, biomechanical problems can be addressed within the safe frame of a numerical laboratory to help the understanding of coherences. Upon the provided framework, the problems to address are of course not limited to biomechanical materials. Simulations based on this monograph can in general identify leaking processes in rupture, fracture impacts to fluid-saturated media, interstitial fluid flow in cracked materials and more. Anyway, the self-understanding of this monograph is that of a first, basic step towards a more comprehensive numerical framework. The herein presented numerical methodology is far from being complete. There is much room for improvements until the

methodology reflects a universal applicability. It is for example per design not possible to address cavity problems with the herein used biphasic material model. For that kind of problems, it would be necessary to add – at least – a third constituent, i. e., a compressible gas phase. Consequently, phase transition problems would accompany this extension. Every grown, living tissue exhibits several inhomogeneities regarding distribution and alignment of its components. Hence, for a circumferential numerical modelling of damage processes in biological tissue, anisotropy considerations are needed to be taken into account. Furthermore, the used 8-nodal hexahedron finite-elements are a rather elementary discretisation. It is highly recommended to also implement stabilisation techniques, or alternatively, *Taylor-Hood*-elements, to overcome a "locking" or oscillatory behaviour of the solution. Another crucial point is of course the numerical implementation of multiple discontinuities. In this context, several implementation aspects are still open for discussion. However, an extensive numerical toolbox – containing necessary side-products to the main contribution – has been developed that should simplify these future extensions. Concerning the implementation aspects, a transfer of the provided academic code framework into a commercial FEM-program would increase its general usability.

Appendix A: Tensor Calculus

This chapter reflects the tensorial expressions that are used within this monograph. The notation is based on the work of *de Boer* [17]. Furthermore, a comprehensive overview over this topic can also be found in the online available lecture notes, see *Ehlers* [57]. Note in passing that most of the following was taken from those lecture notes. The following relations are – unless otherwise stated – valid for arbitrary basis systems. Greek letters $\{\alpha, \beta\}$ denote scalar values, small boldface letters $\{\mathbf{a}, \mathbf{b}\}$ denote vectors, and bold roman majuscules $\{\mathbf{A}, \mathbf{B}, \mathbf{C}\}$ denote second order tensors; $\mathbf{I}$ is the identity element, and $\mathbf{0}$ the zero element. The adjoint and the cofactor of a tensor are denoted by $\operatorname{adj}(\cdot)$ and $\operatorname{cof}(\cdot)$.

A.1 Tensor Algebra

A.1.1 Collected Rules for Second-order Tensors

Products of tensors with scalars, vectors and tensors:

$$
\begin{aligned}
\alpha\,(\beta\,\mathbf{A}) &= (\alpha\,\beta)\,\mathbf{A} \\
\mathbf{A}\,(\alpha\,\mathbf{a}) &= \alpha(\mathbf{A}\,\mathbf{a}) = (\alpha\,\mathbf{A})\,\mathbf{a} \\
(\alpha+\beta)\,\mathbf{A} &= \alpha\,\mathbf{A} + \beta\,\mathbf{A} \\
\alpha\,(\mathbf{A}+\mathbf{B}) &= \alpha\,\mathbf{A} + \alpha\,\mathbf{B} \\
\mathbf{A}\,(\mathbf{a}+\mathbf{b}) &= \mathbf{A}\,\mathbf{a} + \mathbf{A}\,\mathbf{b} \\
(\mathbf{A}+\mathbf{B})\,\mathbf{a} &= \mathbf{A}\,\mathbf{a} + \mathbf{B}\,\mathbf{a} \\
\alpha\,\mathbf{A} &= \mathbf{A}\,\alpha \\
\mathbf{a} &= \mathbf{A}\,\mathbf{b} \\
\mathbf{I}\,\mathbf{a} &= \mathbf{a} \\
\mathbf{0}\,\mathbf{a} &= \mathbf{0}
\end{aligned}
\qquad
\begin{aligned}
(\alpha\,\mathbf{A})\cdot\mathbf{B} &= \mathbf{A}\cdot(\alpha\,\mathbf{B}) = \alpha\,(\mathbf{A}\cdot\mathbf{B}) \\
\mathbf{A}\cdot(\mathbf{B}+\mathbf{C}) &= \mathbf{A}\cdot\mathbf{B} + \mathbf{A}\cdot\mathbf{C} \\
\mathbf{A}\cdot\mathbf{B} &= \mathbf{B}\cdot\mathbf{A} \\
\mathbf{A}\cdot\mathbf{B} &= 0 \quad \forall\,\mathbf{A}\text{, if } \mathbf{B} \equiv \mathbf{0} \\
\mathbf{A}\cdot\mathbf{A} &> 0 \quad \forall\,\mathbf{A} \neq \mathbf{0} \\
\mathbf{a}\cdot(\mathbf{a}\otimes\mathbf{b}) &= \mathbf{a}\cdot\mathbf{A}\,\mathbf{b}
\end{aligned}
\tag{A.1}
$$

The tensor product of tensors:

$$
\begin{aligned}
\alpha\,(\mathbf{A}\,\mathbf{B}) &= (\alpha\,\mathbf{A})\,\mathbf{B} = \mathbf{A}\,(\alpha\,\mathbf{B}) \\
(\mathbf{A}\,\mathbf{B})\,\mathbf{a} &= \mathbf{A}\,(\mathbf{B}\,\mathbf{a}) \\
(\mathbf{A}\,\mathbf{B})\,\mathbf{C} &= \mathbf{A}\,(\mathbf{B}\,\mathbf{C}) \\
\mathbf{A}\,(\mathbf{B}+\mathbf{C}) &= \mathbf{A}\,\mathbf{B} + \mathbf{A}\,\mathbf{C} \\
(\mathbf{A}+\mathbf{B})\,\mathbf{C} &= \mathbf{A}\,\mathbf{C} + \mathbf{B}\,\mathbf{C}
\end{aligned}
\qquad
\begin{aligned}
\mathbf{A}\,\mathbf{B} &\neq \mathbf{B}\,\mathbf{A} \\
\mathbf{I}\,\mathbf{A} &= \mathbf{A}\,\mathbf{I} = \mathbf{A} \\
\mathbf{0}\,\mathbf{A} &= \mathbf{A}\,\mathbf{0} = \mathbf{0} \\
(\mathbf{a}\otimes\mathbf{b})\,(\mathbf{c}\otimes\mathbf{d}) &= (\mathbf{b}\cdot\mathbf{c})\,\mathbf{a}\otimes\mathbf{d}
\end{aligned}
\tag{A.2}
$$

The transposed and inverse tensor:

$$
\begin{array}{rcl|rcl}
(\mathbf{a}\otimes\mathbf{b})^T &=& (\mathbf{b}\otimes\mathbf{a}) & \mathbf{A}^{-1} &=& (\det\mathbf{A})^{-1}\,\mathrm{adj}\,\mathbf{A} \\
(\alpha\,\mathbf{A})^T &=& \alpha\,\mathbf{A}^T & \mathbf{A}^{-1} &=& (\det\mathbf{A})^{-1}\,\mathrm{cof}\,\mathbf{A}^T \\
(\mathbf{A}\,\mathbf{B})^T &=& \mathbf{B}^T\mathbf{A}^T & \longrightarrow\ \mathbf{A}^{-1} &\text{exists if}& \det\mathbf{A}\neq 0 \\
\mathbf{a}\cdot(\mathbf{B}\,\mathbf{b}) &=& (\mathbf{B}^T\mathbf{a})\cdot\mathbf{b} & \mathbf{A}\,\mathbf{A}^{-1} &=& \mathbf{A}^{-1}\,\mathbf{A}=\mathbf{I} \\
\mathbf{A}\cdot(\mathbf{B}\,\mathbf{C}) &=& (\mathbf{B}^T\mathbf{A})\cdot\mathbf{C} & (\mathbf{A}^{-1})^T &=& (\mathbf{A}^T)^{-1}=:\mathbf{A}^{T-1} \\
(\mathbf{A}+\mathbf{B})^T &=& \mathbf{A}^T+\mathbf{B}^T & (\mathbf{A}\,\mathbf{B})^{-1} &=& \mathbf{B}^{-1}\mathbf{A}^{-1}
\end{array}
\tag{A.3}
$$

The adjoint, cofactor, determinant and inverse of a tensor:

$$
\begin{array}{rcl|rcl}
\mathrm{adj}\,\mathbf{A} &=& (\mathrm{cof}\,\mathbf{A})^T & \det\mathbf{I} &=& 1 \\
(\mathrm{cof}\,\mathbf{A})^T &=& \mathrm{cof}\,\mathbf{A}^T & \det\mathbf{A}^T &=& \det\mathbf{A} \\
\mathrm{adj}\,(\mathbf{A}\,\mathbf{B}) &=& \mathrm{adj}\,\mathbf{A}\,\mathrm{adj}\,\mathbf{B} & \det(\mathrm{adj}\,\mathbf{A}) &=& \det(\mathrm{cof}\,\mathbf{A}) = (\det\mathbf{A})^2 \\
\det(\mathbf{A}\,\mathbf{B}) &=& \det\mathbf{A}\det\mathbf{B} & \det\mathbf{A}^{-1} &=& (\det\mathbf{A})^{-1} \\
\det(\alpha\,\mathbf{A}) &=& \alpha^3\det\mathbf{A} & \det(\mathbf{A}+\mathbf{B}) &=& \det\mathbf{A}+\mathrm{cof}\,\mathbf{A}\cdot\mathbf{B}+ \\
 & & & & & +\mathbf{A}\cdot\mathrm{cof}\,\mathbf{B}+\det\mathbf{B}
\end{array}
\tag{A.4}
$$

The trace operator:

$$
\begin{array}{rcl|rcl}
\mathrm{tr}\,\mathbf{A} &=& \mathbf{A}\cdot\mathbf{I} & \mathrm{tr}\,\mathbf{A}^T &=& \mathrm{tr}\,\mathbf{A} \\
\mathrm{tr}\,(\alpha\,\mathbf{A}) &=& \alpha\,\mathrm{tr}\,\mathbf{A} & \mathrm{tr}\,(\mathbf{A}\,\mathbf{B}) &=& \mathrm{tr}\,(\mathbf{B}\,\mathbf{A}) = \mathbf{A}\cdot\mathbf{B}^T=\mathbf{A}^T\cdot\mathbf{B} \\
\mathrm{tr}\,(\mathbf{a}\otimes\mathbf{b}) &=& \mathbf{a}\cdot\mathbf{b} & \mathrm{tr}\,\mathbf{A}\,\mathbf{B}\,\mathbf{C} &=& \mathrm{tr}\,\mathbf{B}\,\mathbf{C}\,\mathbf{A} = \mathrm{tr}\,\mathbf{C}\,\mathbf{A}\,\mathbf{B}
\end{array}
\tag{A.5}
$$

A.1.2 The Three Scalar Principal Invariants

Scalar product representation:

$$
\begin{array}{rcll}
I_{\mathbf{A}1} &=& \mathbf{A}\cdot\mathbf{I} &= \mathrm{tr}\ \mathbf{A} \\
I_{\mathbf{A}2} &=& \frac{1}{2}\,(I_{\mathbf{A}1}^2-\mathbf{A}\,\mathbf{A}\cdot\mathbf{I}) &= \frac{1}{2}\left[(\mathrm{tr}\ \mathbf{A})^2-\mathrm{tr}\ (\mathbf{A}\,\mathbf{A})\right] \\
I_{\mathbf{A}3} &=& \frac{1}{6}\,I_{\mathbf{A}1}^3-\frac{1}{2}\,I_{\mathbf{A}1}^2(\mathbf{A}\,\mathbf{A}\cdot\mathbf{I})+\frac{1}{3}\,\mathbf{A}^T\mathbf{A}^T\cdot\mathbf{A} &= \det\ \mathbf{A}
\end{array}
\tag{A.6}
$$

Eigenvalue representation:

$$
\begin{aligned}
I_{\mathbf{A}1} &= \lambda_{\mathbf{A}1}+\lambda_{\mathbf{A}2}+\lambda_{\mathbf{A}3} \\
I_{\mathbf{A}2} &= \lambda_{\mathbf{A}1}\,\lambda_{\mathbf{A}2}+\lambda_{\mathbf{A}2}\,\lambda_{\mathbf{A}3}+\lambda_{\mathbf{A}3}\,\lambda_{\mathbf{A}1} \\
I_{\mathbf{A}3} &= \lambda_{\mathbf{A}1}\,\lambda_{\mathbf{A}2}\,\lambda_{\mathbf{A}3}
\end{aligned}
\tag{A.7}
$$

For deformation tensors of the solid phase φ^S $(\mathbf{C}_S, \mathbf{B}_S; \mathbf{F}_S)$:

$$\begin{array}{lllllll} (I_{S1} \equiv) & I_1 & = & \operatorname{tr} \mathbf{C}_S & = & \operatorname{tr} \mathbf{B}_S & = & \mathbf{F}_S \cdot \mathbf{F}_S \\ (I_{S2} \equiv) & I_2 & = & \operatorname{tr} (\operatorname{cof} \mathbf{C}_S) & = & \operatorname{tr} (\operatorname{cof} \mathbf{B}_S) & = & \operatorname{cof} \mathbf{F}_S \cdot \operatorname{cof} \mathbf{F}_S \\ (I_{S3} \equiv) & I_3 & = & \det \mathbf{C}_S & = & \det \mathbf{B}_S & = & (\det \mathbf{F}_S)^2 \end{array} \tag{A.8}$$

A.1.3 The Basic Scalar Invariants

The three scalar principal invariants from Section A.1.2 can also be expressed in terms of the so-called basic invariants. The basic invariants are defined as the traces of the power of a tensor $\mathbf{A}$, i. e.,

$$\begin{aligned} J_{\mathbf{A}1} &= I_{\mathbf{A}1}\,, \\ J_{\mathbf{A}2} &= \operatorname{tr} (\mathbf{A}^2) = I_{\mathbf{A}1}^2 - 2I_{\mathbf{A}2}\,, \\ J_{\mathbf{A}3} &= \operatorname{tr} (\mathbf{A}^3) = I_{\mathbf{A}1}^3 - 3I_{\mathbf{A}1}I_{\mathbf{A}2} + 3I_{\mathbf{A}3}\,. \end{aligned} \tag{A.9}$$

Additional invariants, the so-called mixed invariants, to the invariants of a single tensor $\mathbf{A}$ for two symmetric second order tensors $\mathbf{A}$ and $\mathbf{B}$ are

$$\begin{array}{lll|lll} J_{\{\mathbf{A},\mathbf{B}\}4} & = & \operatorname{tr} (\mathbf{A}\,\mathbf{B})\,, & J_{\{\mathbf{A},\mathbf{B}\}6} & = & \operatorname{tr} (\mathbf{A}\,\mathbf{B}^2)\,, \\ J_{\{\mathbf{A},\mathbf{B}\}5} & = & \operatorname{tr} (\mathbf{A}^2\,\mathbf{B})\,, & J_{\{\mathbf{A},\mathbf{B}\}7} & = & \operatorname{tr} (\mathbf{A}^2\,\mathbf{B}^2)\,. \end{array} \tag{A.10}$$

If $\mathbf{B}$ is of rank one and $\|\mathbf{B}\| = 1$, then $J_{\{\mathbf{A},\mathbf{B}\}4} \equiv J_{\{\mathbf{A},\mathbf{B}\}6}$ and $J_{\{\mathbf{A},\mathbf{B}\}5} \equiv J_{\{\mathbf{A},\mathbf{B}\}7}$. Note that, consequently, the higher principal invariants of $\mathbf{B}$ are then equal to zero, i. e., $I_{\mathbf{B}2} = I_{\mathbf{B}3} = 0$; the only remaining basic invariant $I_{\mathbf{B}1}$ is in this case constant.

A.1.4 *Cardano*'s Method

The solution of a characteristic polynomial

$$\lambda^3 - I_1\lambda^2 + I_2\lambda - I_3 = 0 \tag{A.11}$$

can be found by

$$\lambda_i = \frac{1}{3}\left\{ I_1 + 2\sqrt{I_1^2 - 3\,I_2}\,\cos\left[\frac{1}{3}(\theta + 2\,\pi\,i)\right]\right\} \quad \text{with} \quad \theta = \arccos\frac{2\,I_1^3 - 9\,I_1 I_2 + 27\,I_3}{2\,(I_1^2 - 3\,I_2)^{3/2}}\,. \tag{A.12}$$

A.2 Tensor Analysis

A.2.1 Co- and Contravariant Transport of Tensors

First-order tensors (vectors):

$$\mathbf{h}_{Sk} \underset{\mathbf{F}_S^{-1}(\cdot)}{\overset{\mathbf{F}_S(\cdot)}{\rightleftarrows}} \mathbf{a}_{Sk} \qquad \mathbf{h}_S^k \underset{\mathbf{F}_S^{T}(\cdot)}{\overset{\mathbf{F}_S^{T-1}(\cdot)}{\dashrightarrow\!\!\!\dashleftarrow}} \mathbf{a}_S^k$$

Second-order tensors:

$$\mathbf{h}_{Sk}\otimes\mathbf{h}_{S\ell} \underset{\mathbf{F}_S^{-1}(\cdot)\,\mathbf{F}_S^{T-1}}{\overset{\mathbf{F}_S(\cdot)\,\mathbf{F}_S^{T}}{\rightleftarrows}} \mathbf{a}_{Sk}\otimes\mathbf{a}_{S\ell} \qquad \mathbf{h}_S^k\otimes\mathbf{h}_S^\ell \underset{\mathbf{F}_S^{T}(\cdot)\,\mathbf{F}_S}{\overset{\mathbf{F}_S^{T-1}(\cdot)\,\mathbf{F}_S^{-1}}{\dashrightarrow\!\!\!\dashleftarrow}} \mathbf{a}_S^k\otimes\mathbf{a}_S^\ell$$

Legend:

— : covariant transport

– – : contravariant transport

→ : push-forward

← : pull-back

A.2.2 Selected Rules for the Operators $\operatorname{grad}(\cdot)$ and $\operatorname{div}(\cdot)$

$$\begin{aligned}
\operatorname{grad}(\phi\,\psi) &= \phi\operatorname{grad}\psi + \psi\operatorname{grad}\phi \\
\operatorname{grad}(\phi\,\mathbf{b}) &= \mathbf{b}\otimes\operatorname{grad}\phi + \phi\operatorname{grad}\mathbf{b} \\
\operatorname{grad}(\phi\,\mathbf{T}) &= \mathbf{T}\otimes\operatorname{grad}\phi + \phi\operatorname{grad}\mathbf{T} \\
\operatorname{div}(\mathbf{a}\otimes\mathbf{b}) &= \mathbf{a}\operatorname{div}\mathbf{b} + (\operatorname{grad}\mathbf{a})\,\mathbf{b} \\
\operatorname{div}(\phi\,\mathbf{b}) &= \mathbf{b}\cdot\operatorname{grad}\phi + \phi\operatorname{div}\mathbf{b} \\
\operatorname{div}(\phi\,\mathbf{T}) &= \mathbf{T}\operatorname{grad}\phi + \phi\operatorname{div}\mathbf{T} \\
\operatorname{div}(\mathbf{T}\,\mathbf{b}) &= (\operatorname{div}\mathbf{T}^T)\cdot\mathbf{b} + \mathbf{T}^T\cdot\operatorname{grad}\mathbf{b} \\
\operatorname{div}(\operatorname{grad}\mathbf{b})^T &= \operatorname{grad}\operatorname{div}\mathbf{b}
\end{aligned} \tag{A.13}$$

Appendix B: Mechanical Details

B.1 Co- and Contravariational Framework

The concept of the co- and contravariational framework can be best introduced by regarding a corresponding example. Bodies with curved boundaries need a "natural" coordinate system, i. e., curvilinear coordinates, see Figure B.1. For the following discussion on natu-

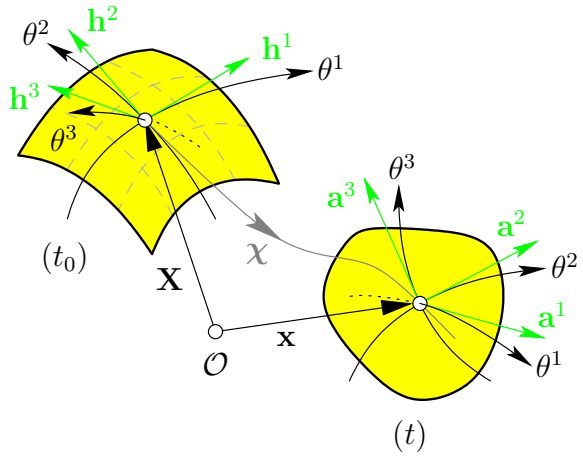

$\theta^i;\ i = 1,2,3$	:	natural coordinates $\rightarrow$ curvilinear $\rightarrow$ contravariant
$\mathbf{X} = \mathbf{X}(\theta^i)$	:	reference position vector
$\mathbf{x} = \mathbf{x}(\theta^i, t)$	:	actual position vector
$\boldsymbol{\chi} = \boldsymbol{\chi}(\theta^i(\mathbf{X}), t)$	:	placement funtion

Figure B.1: Natural (curvilinear) coordinate system in actual and referential configuration.

ral (or fundamental) covariant basis systems, general, non-orthogonal and non-normalised local base vectors are firstly introduced as

$$\boxed{\mathbf{g}_i := \frac{\partial \mathbf{x}}{\partial \theta^i}}\,. \qquad \text{(B.1)}$$

(covariant frame)

Note that the length of $\mathbf{g}_i$ is proportional to the length of an infinitesimal line element in θ^i-direction. Covariant basis vectors in a configurational framework are then defined as

$$\mathbf{h}_i = \frac{\partial \mathbf{X}}{\partial \theta^i}\,, \quad \mathbf{a}_i = \frac{\partial \mathbf{x}}{\partial \theta^i}\,. \qquad \text{(B.2)}$$

Therein, $\mathbf{h}_i$ denote the basis vectors in the referential configuration, and $\mathbf{a}_i$ the basis vectors in the actual configuration. Each triple of them span a tangential space in the corresponding configuration. For measuring vector-based physical quantities (force, displacement, strains, stresses, etc.) in a unique "metric" system, metric coefficients need to

be associated to base vectors, e. g.,

$$\begin{aligned} \mathbf{f} &= f^i\,\mathbf{g}_i \;:\; \text{force vector}\,, \\ \mathbf{u} &= u^i\,\mathbf{g}_i \;:\; \text{displacement vector}\,, \\ W &= \mathbf{f}\cdot\mathbf{u} \;:\; \text{work (expressed by scalar product)}\,. \end{aligned} \tag{B.3}$$

In this example, the vector coefficients f^i and u^i are constitutive denoted by a superscript index, in contrast to the subscript index of their base vectors. This notation will be clarified in the succeeding illustration. Because the base vectors $\mathbf{g}_i$ change their length along coordinate lines by design (recall, the base vectors are not normalised or even constant along the infinitesimal line elements), the components of the coefficients must adjust analogously; otherwise the physical quantities would become position dependent. See Figure B.2 for a 2-d illustration of the above given example $(\text{B.3})_3$ on the computation of work by a corresponding scalar product. The metric coefficients g_{ij} are the abstraction

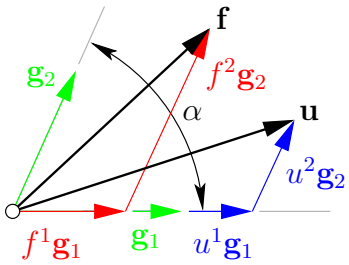

$$\begin{aligned} W &= \mathbf{f}\cdot\mathbf{u} = f^i u^i\,\mathbf{g}_i\cdot\mathbf{g}_i \\ &= f^1u^1\,\mathbf{g}_1\cdot\mathbf{g}_1 + f^1u^2\,\mathbf{g}_1\cdot\mathbf{g}_2 + \\ &\quad f^2u^1\,\mathbf{g}_2\cdot\mathbf{g}_1 + f^2u^2\,\mathbf{g}_2\cdot\mathbf{g}_2 \\ \text{with}\quad &\begin{cases} \mathbf{g}_i\cdot\mathbf{g}_j &= |\mathbf{g}_i|\,|\mathbf{g}_j|\cos(\alpha_{ij}) =: g_{ij} \\ \cos(\alpha_{ii}) &= 1 \end{cases} \\ W &= g_{ij}f^iu^j \neq f^iu^i \end{aligned}$$

Figure B.2: 2-d illustration of variant scalar product.

of distance and the cause for a variant result of the scalar product. This is the consequence of the mixed terms g_{ij} for $i \neq j$. For example, if $|\mathbf{g}_i| = 1$, the corresponding work yields $\rightsquigarrow W = f^1u^1 + (f^1u^2 + f^2u^1)\cos(\alpha) + f^2u^2$. In order to obtain a scalar product that is independent (invariant) of base vectors for the determination of physical quantities by multiplication of their components, a contravariant basis formulation with following orthogonality condition is introduced:

$$\mathbf{g}^j\cdot\mathbf{g}_i = \delta_i^j \quad \text{with} \quad \begin{cases} |\mathbf{g}^j| \neq 1, |\mathbf{g}_i| \neq 1 \\ \mathbf{g}^1 \perp \mathbf{g}_2, \mathbf{g}_3\,,\ \mathbf{g}^2 \perp \mathbf{g}_3, \mathbf{g}_1\,,\ \mathbf{g}^3 \perp \mathbf{g}_1, \mathbf{g}_2 \\ \delta_i^j = 1,\ \text{if } i = j \\ \delta_i^j = 0,\ \text{if } i \neq j \end{cases} \tag{B.4}$$

This orthogonality condition can be alternatively defined by

$$\boxed{\mathbf{g}^j := \frac{\partial \theta^j}{\partial \mathbf{x}} := \operatorname{grad} \theta^j} \quad \text{(contravariant frame)} \tag{B.5}$$

The following relations hold:

$$\left.\begin{aligned} g_{ij}\,\mathbf{g}^j &= \mathbf{g}_i \\ g^{ij}\,\mathbf{g}_j &= \mathbf{g}^i \end{aligned}\right\} \; g_{ij}\,\mathbf{g}^{jk} = \delta_i^k \,. \tag{B.6}$$

With this co- and contravariational framework, the previously stated scalar product example can be solved with resulting coefficients which are invariant to the base vectors, see Figure B.3.

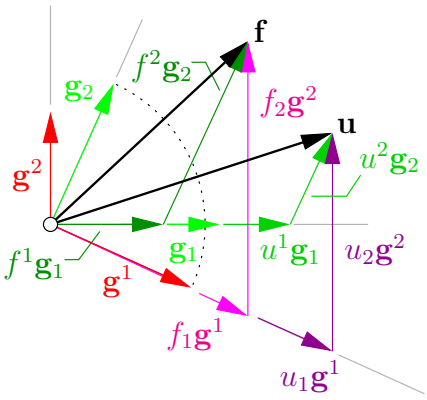

$$\begin{aligned} \mathbf{f} &= f^i\,\mathbf{g}_i = f_i\,\mathbf{g}^i \\ \mathbf{u} &= u^j\,\mathbf{g}_j = u_j\,\mathbf{g}^j \\ W &= \mathbf{f}\cdot\mathbf{u} = f^i\,\mathbf{g}_i \cdot u_j\,\mathbf{g}^j \\ &= f^1 u_1\,\mathbf{g}_1\cdot\mathbf{g}^1 + f^1 u_2\,\mathbf{g}_1\cdot\mathbf{g}^2 + \\ &\quad\; f^2 u_1\,\mathbf{g}_2\cdot\mathbf{g}^1 + f^2 u_2\,\mathbf{g}_2\cdot\mathbf{g}^2 \\ &= f^i u_i \quad \surd \end{aligned}$$

Figure B.3: 2-d illustration of invariant scalar product.

B.2 Plasticity

In this section, geometrically linear elasto-viscoplastic material behaviour is introduced for single-phase materials. Note in passing that in the following only non-α-indexed equations and physical quantities appear because of the restriction to single-phase materials. Nevertheless, the governing equations and mechanical quantities are in principle identical to that of the mixture, recall *Truesdell*'s metaphysical principle $(2.35)_3$. For a comprehensive introduction on plastic material behaviour within a standard continuum-mechanical and an extended TPM framework, the interested reader is referred to *Simo & Hughes* [170], *Naghdi* [143], *Haupt* [97], *Miehe et al.* [137], *Wieners* [192], *Mahnkopf* [132], *Ehlers* [59], and citations therein; also, take note on the remark at the end of this subsection.

The momentum balance $(2.41)_2$ is simplified by assuming quasi-static conditions ($\ddot{\mathbf{x}} = \mathbf{0}$) and vanishing body-force densities ($\mathbf{b} = \mathbf{0}$). For the modelling of the inelastic material behaviour, a viscoplastic *Perzyna*-type regularisation is considered. It is assumed that the *Green-Lagrange*an strain tensor is geometrically linear, recall (2.25). As a result, the in Section 2.4 introduced stress tensors are taken to be approximately identical: $\mathbf{T} \approx \boldsymbol{\tau} \approx \mathbf{P} \approx \mathbf{S} =: \boldsymbol{\sigma}$. These assumptions lead to the equilibrium equations

$$\begin{aligned} \operatorname{div} \boldsymbol{\sigma}(\mathbf{x},t) &= \mathbf{0} && \text{with} \quad (\mathbf{x},t) \in \Omega(t) \times [0,T]\,, \\ \boldsymbol{\sigma}(\mathbf{x},t)\,\mathbf{n}(\mathbf{x}) &= \mathbf{t}(\mathbf{x},t) && \text{with} \quad (\mathbf{x},t) \in \Gamma_N(t) \times [0,T]\,, \end{aligned} \tag{B.7}$$

where $\mathbf{n}(\mathbf{x})$ is the outward-oriented unit surface normal. Furthermore, let $[0,T]$ be a fixed time interval, let $\Omega_0 \subset \mathbb{R}^d$ be the reference configuration of the domain Ω with the spatial dimension d, and let the domain surface be decomposed into a *Dirichlet* Γ_D and a *Neumann* Γ_N boundary such that $\Gamma_D(t=0) \cup \Gamma_N(t=0) = \partial\Omega_0$. Details on the domain surface decomposition can be found in Section 2.6.4. The geometrically linear strain tensor $\boldsymbol{\varepsilon}$ is described as $\boldsymbol{\varepsilon} = \frac{1}{2}[\operatorname{Grad}\mathbf{u} + (\operatorname{Grad}\mathbf{u})^T]$. Due to the small-strain approach, $\boldsymbol{\varepsilon}$ can be decomposed additively into an elastic part $\boldsymbol{\varepsilon}_e$ and a plastic part $\boldsymbol{\varepsilon}_p$, such that

$$\boldsymbol{\varepsilon} = \boldsymbol{\varepsilon}_e + \boldsymbol{\varepsilon}_p\,. \tag{B.8}$$

Regarding *Hooke*'s law, $\boldsymbol{\sigma} = 2\,\mu\,\boldsymbol{\varepsilon}_e + \lambda\,(\boldsymbol{\varepsilon}_e \cdot \mathbf{I})\,\mathbf{I}$, for the linear elastic material response depending on the *Lamé* constants μ and λ, the constitutive stress-strain relation is introduced via

$$\boldsymbol{\sigma} \;=\; \overset{4}{\boldsymbol{\mathcal{C}}}\,[\,\boldsymbol{\varepsilon} - \boldsymbol{\varepsilon}_p\,]\,. \tag{B.9}$$

Therein, $\overset{4}{\boldsymbol{\mathcal{C}}} = 2\mu\,(\mathbf{I}\otimes\mathbf{I})^{\overset{23}{T}} + \lambda\,(\mathbf{I}\otimes\mathbf{I})$ is the symmetric, fourth-order elastic material tangent. The elastic material behaviour, limited by the equivalent stress σ_0, is enveloped by a convex scalar-based yield function F which, for the present purpose, is set to a *von Mises*[1]-type yield function

$$F(\boldsymbol{\sigma};\kappa) = |\boldsymbol{\sigma}^D| \; - \sqrt{\frac{2}{3}}\,\kappa = 0 \quad \text{with} \quad \left\{ \begin{aligned} \boldsymbol{\sigma}^D &= \boldsymbol{\sigma} - \tfrac{1}{3}(\boldsymbol{\sigma}\cdot\mathbf{I})\,\mathbf{I}\,, \\ |\boldsymbol{\sigma}^D| &= \sqrt{(\boldsymbol{\sigma}^D \cdot \boldsymbol{\sigma}^D)}\,. \end{aligned} \right. \tag{B.10}$$

Therein, $\boldsymbol{\sigma}^D$ is the deviatoric part of the stress tensor, and $|\boldsymbol{\sigma}^D|$ is the *Frobenius*[2] norm. As an example for isotropic softening behaviour, it is assumed that $\kappa = \overset{*}{\kappa}\,(\varepsilon_{pv})$ depends

[1] *Richard Edler von Mises* (1883–1953): Austrian mathematician who worked in several engineering disciplines. His main area of work was the numerical mathematics. Therein, he is most famous for the "von Mises yield criterion". [WIKIPEDIA]

[2] *Ferdinand Georg Frobenius* (1849–1917): German mathematician who's algorithm on "Gruppencharaktere" is of particular importance in the field of quantum mechanics. [Neue deutsche Biographie **5** (1961), 641.]

on the accumulated plastic strain

$$\varepsilon_{pv} = \sqrt{\frac{2}{3}} \int_0^{\bar{t}} |\dot{\boldsymbol{\varepsilon}}_p| \, \mathrm{d}t \,. \tag{B.11}$$

The isotropic softening behaviour is postulated as

$$\overset{*}{\kappa} (\varepsilon_{pv}) = \kappa_0 \left\{ 1 - h_{sat} [1 - \exp(-h_e \, \varepsilon_{pv})] \right\}, \tag{B.12}$$

i. e., the progression of the material softening can be controlled by two material parameters, h_{sat} and h_e. The initial stress parameter κ_0 is related to the equivalent stress σ_0 as $\sigma_0 \equiv \kappa_0$. The softening behaviour that is given here is comparable to *Engelen et. al* [69]. Note that the underlying mathematical problem of plastic material behaviour is ill-posed. As a consequence, the following boundary-value problem looses ellipticity, cf. *Lourenco et. al* [130]. Thus, all deformation tends to localise into a zone of zero width. One possible remedy to this problem is the application of a regularisation technique, e. g., the elasto-viscoplasticity approach discussed here. In order to complete the momentum balance, the plastic strain rate $\dot{\boldsymbol{\varepsilon}}_p$ needs to evolve from the plastic flow rule $\dot{\boldsymbol{\varepsilon}}_p = \Lambda \boldsymbol{\zeta}$. The non-negative parameter Λ is, in general, known as the plastic multiplier or the consistency parameter, cf. *Simo & Hughes* [170]. In this context, the parameter Λ specifies the magnitude of the plastic strain rate, while $\boldsymbol{\zeta}$ determines its direction. For associated plasticity, $\boldsymbol{\zeta}$ is perpendicularly oriented on the yield surface $F(\boldsymbol{\sigma}; \kappa) \equiv 0$. Thus, $\boldsymbol{\zeta}$ can be derived according to

$$\boldsymbol{\zeta} \;=\; \frac{\partial F(\boldsymbol{\sigma}; \kappa)}{\partial \boldsymbol{\sigma}} \,. \tag{B.13}$$

For a viscoplastic model of *Perzyna*-type [155], the viscoplastic multiplier is given by

$$\Lambda \;:=\; \frac{1}{\eta} \left\langle \frac{F(\boldsymbol{\sigma}; \kappa)}{\sigma_0} \right\rangle^r , \qquad \text{where} \quad \eta > 0 \text{ and } r \geq 1 \,. \tag{B.14}$$

Through the viscoplastic multiplier Λ, the relaxation time η controls the evolution of plastic strains and the amount of viscosity, respectively. Furthermore, r is the viscoplastic exponent, and the *Macaulay*[3] brackets $\langle \cdot \rangle$ are defined by $\langle x \rangle = \max\{0, x\}$. Taking the preceding considerations into account, the plastic flow rule can be evaluated as

$$\dot{\boldsymbol{\varepsilon}}_p \;=\; \frac{1}{\eta} \left\langle \frac{F(\boldsymbol{\sigma}; \kappa)}{\sigma_0} \right\rangle^r \frac{\partial F(\boldsymbol{\sigma}; \kappa)}{\partial \boldsymbol{\sigma}} \,. \tag{B.15}$$

[3] *William Herrick Macaulay* (1853 – 1936): British mathematician and engineer who is usually given credit for introducing singularity functions in the context of beam deflections. Before *Macaulay* [131], the equation for the deflection of beams could not be found in closed form. This finding of the closed form is also referred to as "*Macaulay*'s method".

Remark: In contrast to the preceding discussion on non-porous materials, a major characteristic of porous materials is that they can undergo plastic deformations under purely hydrostatic loading conditions, see Figure B.4(a). Furthermore, the volume change of porous materials under plastic loading can be contractant or dilatant. A non-associated flow direction $\dot{\boldsymbol{\varepsilon}}_p \rightsquigarrow (\boldsymbol{\varepsilon}_{Sp})'_S$ is then the consequence, see Figure B.4(b). In this context,

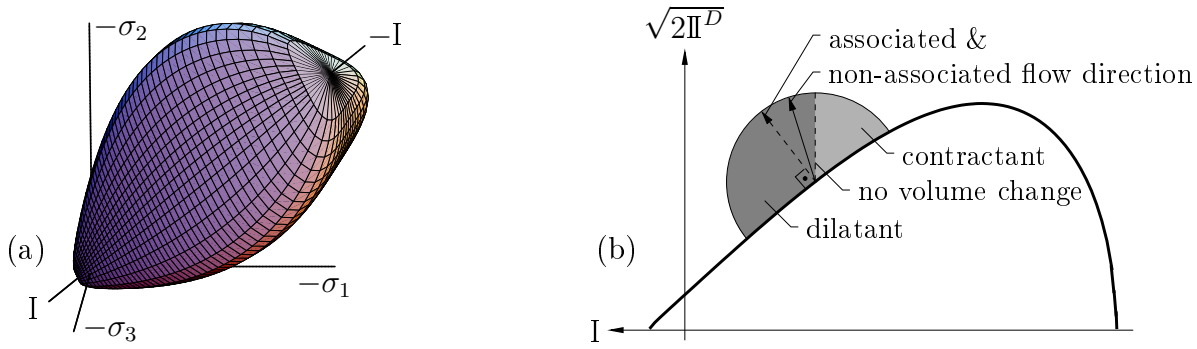

Figure B.4: Example of single-surface yield criterion F for frictional materials in (a) principal stress space (tension positive), and (b) in hydrostatic plane, see *Ehlers* [55, 56]

porous materials are also called frictional materials. Thus, a more complex yield criterion than (B.10) is needed for the proper representation of these special characteristics of porous materials. As an example of a sophisticated single-surface yield criterion for frictional materials, *Ehlers* [55] is cited:

$$F = \Phi^{1/2} + \beta\,\mathrm{I} + \epsilon\,\mathrm{I}^2 - \kappa = 0 \quad \text{with} \quad \left\{ \begin{array}{rcl} \Phi & = & \mathrm{II}^D(1+\gamma\,\vartheta)^m + \dfrac{1}{2}\,\alpha\,\mathrm{I}^2 + \delta^2\,\mathrm{I}^4\,, \\ \vartheta & = & \mathrm{III}^D/(\mathrm{II}^D)^{3/2}\,. \end{array} \right. \tag{B.16}$$

Furthermore, for the correct determination of non-associated plasticity, a plastic potential, cf. *Mahnkopf* [132], must be defined:

$$\left. \begin{array}{l} G = \Gamma^{1/2} + \psi_2\,\mathrm{I} + \epsilon\,\mathrm{I}^2\,, \\ \Gamma = \psi_1\,\mathrm{II}^D + \dfrac{1}{2}\,\alpha\,\mathrm{I}^2 + \delta^2\,\mathrm{I}^4\,, \end{array} \right\} \quad \rightsquigarrow \quad (\boldsymbol{\varepsilon}_{Sp})'_S = \Lambda\,\frac{\partial G(\boldsymbol{\sigma}^S_E)}{\partial \boldsymbol{\sigma}^S_E}\,. \tag{B.17}$$

In the above equations, I represents the first principal invariant of $\boldsymbol{\sigma}^S_E$ ($\rightsquigarrow \boldsymbol{\sigma}$) and II^D, III^D the (negative) second and third invariants of $(\boldsymbol{\sigma}^S_E)^D$ ($\rightsquigarrow \boldsymbol{\sigma}^D$). The seven material parameters $\{\alpha,\ \beta,\ \delta,\ \epsilon,\ \kappa,\ \gamma,\ m\}$, govern the shape of the yield surface. The dilatation angles ψ_1 and ψ_2 need to be measured from experimental data. For details, see *Ehlers & Avci* [61]. □

B.3 Introduction to Configurational Forces

The following introduction to configurational forces is restricted to isothermal processes for elastic – single phase – homogeneous materials within the geometrically linear theory. The derivation process is based on handwritten notes from *Ehlers*. For more details on this topic, the interested reader is referred to, e.g., *Kienzler & Herrmann* [117], *Müller et al.* [142] and *Miehe & Gürses* [136]. With the aforementioned restrictions, the *Clausius-Duhem* inequality reduces to an energy equation, viz.

$$\boldsymbol{\sigma}\cdot\dot{\boldsymbol{\varepsilon}}-\rho_0\dot{\psi}\geq 0 \quad\rightsquigarrow\quad \dot{\mathcal{W}}-\boldsymbol{\sigma}\cdot\dot{\mathbf{H}}=0 \quad\text{with}\quad \left\{\begin{array}{rcl}\mathcal{W} &:=& \rho_0\psi\,,\\ \mathbf{H} &:=& \operatorname{Grad}\mathbf{u}\,.\end{array}\right. \tag{B.18}$$

After a *Legendre*-transformation ($\zeta := \mathcal{W}-\boldsymbol{\sigma}\cdot\mathbf{H}$), the energy equation reads

$$\dot{\mathcal{W}}-(\boldsymbol{\sigma}\cdot\mathbf{H})^{\cdot}+\dot{\boldsymbol{\sigma}}\cdot\mathbf{H}=0\,. \tag{B.19}$$

Time integration and the vector derivative $\big(\nabla(\,\cdot\,):=\operatorname{grad}(\,\cdot\,)\big)$ of (B.19) yields

$$\begin{array}{rcl}\mathcal{W}-\boldsymbol{\sigma}\cdot\mathbf{H}+\displaystyle\int\dot{\boldsymbol{\sigma}}\cdot\mathbf{H}\,\mathrm{d}t &=& 0\,,\\ \nabla\mathcal{W}-\nabla(\boldsymbol{\sigma}\cdot\mathbf{H})+\displaystyle\int\nabla(\dot{\boldsymbol{\sigma}}\cdot\mathbf{H})\,\mathrm{d}t &=& 0\,.\end{array} \tag{B.20}$$

This can be reformulated[4] as

$$\operatorname{div}\underbrace{(\mathcal{W}\mathbf{I}-\mathbf{H}^T\boldsymbol{\sigma})}_{=:\,\boldsymbol{\mathcal{E}}}+\mathbf{H}^T\operatorname{div}\boldsymbol{\sigma}-(\nabla\boldsymbol{\sigma})^{\overset{13}{T}}\mathbf{H}^T+\int\nabla(\dot{\boldsymbol{\sigma}}\cdot\mathbf{H})\,\mathrm{d}t=0\,. \tag{B.21}$$

[4] Note the transformations:

$$\begin{array}{rcccccl}\nabla(\boldsymbol{\sigma}\cdot\mathbf{H}) &=& (\nabla\boldsymbol{\sigma})^{\overset{13}{T}}\mathbf{H}^T &+& (\nabla\mathbf{H})^{\overset{13}{T}}\boldsymbol{\sigma}^T &=& \nabla(\mathbf{H}^T\boldsymbol{\sigma}\cdot\mathbf{I})\,,\\ \operatorname{div}(\mathbf{H}^T\boldsymbol{\sigma}) &=& (\nabla\mathbf{H}^T)\,\boldsymbol{\sigma} &+& \mathbf{H}^T\operatorname{div}\boldsymbol{\sigma} &=& \nabla(\mathbf{H}^T\boldsymbol{\sigma})\,\mathbf{I}\,.\end{array}$$

With $\boldsymbol{\sigma}=\boldsymbol{\sigma}^T$ and $\nabla\mathbf{H}=(\nabla\mathbf{H})^{\overset{23}{T}}$ following holds:

$$\begin{array}{rcl}(\nabla\mathbf{H}^T)\boldsymbol{\sigma} &=& (\nabla\mathbf{H})^{\overset{13}{T}}\boldsymbol{\sigma}^T\\ \rightarrow\quad \nabla(\boldsymbol{\sigma}\cdot\mathbf{H}) &=& \operatorname{div}(\mathbf{H}^T\boldsymbol{\sigma})-\mathbf{H}^T\operatorname{div}\boldsymbol{\sigma}+(\nabla\boldsymbol{\sigma})^{\overset{13}{T}}\mathbf{H}^T\,.\end{array}$$

Furthermore, it is:

$$\nabla\mathcal{W}=\operatorname{div}(\mathcal{W}\mathbf{I})\,.$$

Therein, the *Eshelby* or configurational stress tensor $\boldsymbol{\mathcal{E}}$, respectively, can be identified. Insertion of the equilibrium condition $\operatorname{div}\boldsymbol{\sigma}+\mathbf{b}=\mathbf{0}\rightarrow\operatorname{div}\boldsymbol{\sigma}=-\mathbf{b}$ into (B.21) yields

$$\operatorname{div}\boldsymbol{\mathcal{E}}-\mathbf{H}^T\mathbf{b}\underbrace{-(\nabla\boldsymbol{\sigma})\overset{13}{}^T\mathbf{H}^T+\int\nabla(\dot{\boldsymbol{\sigma}}\cdot\mathbf{H})\,\mathrm{d}t}_{=:\,A,\text{ see footnote}^5}=0\,. \tag{B.22}$$

Application of $(\text{B.18})_2$ results for (B.22) in

$$\begin{aligned}\operatorname{div}\boldsymbol{\mathcal{E}}-\mathbf{H}^T\mathbf{b}+(\nabla\mathbf{H})\overset{13}{}^T\boldsymbol{\sigma}^T-\int\nabla\dot{\mathcal{W}}\,\mathrm{d}t &= 0\,,\\ \operatorname{div}\boldsymbol{\mathcal{E}}\underbrace{-\mathbf{H}^T\mathbf{b}+(\nabla\mathbf{H})\overset{13}{}^T\boldsymbol{\sigma}^T-\nabla\mathcal{W}}_{=:\,\mathbf{f}} &= 0\,.\end{aligned} \tag{B.23}$$

Finally, the configurational force vector $\mathbf{f}$ is identified and the final form of the configurational force equilibrium is:

$$\operatorname{div}\boldsymbol{\mathcal{E}}+\mathbf{f}=\mathbf{0}\,. \tag{B.24}$$

B.4 Modified *Reynolds* Transport Theorem

$$\frac{\mathrm{d}_\alpha}{\mathrm{d}t}\int_{\mathcal{B}}\boldsymbol{\Psi}^\alpha\,\mathrm{d}v=\int_{\mathcal{B}}[(\boldsymbol{\Psi}^\alpha)'_\alpha\,\mathrm{d}v+\boldsymbol{\Psi}^\alpha(\,\mathrm{d}v)'_\alpha]\quad\text{with}\quad\left\{\begin{aligned}(\boldsymbol{\Psi}^\alpha)'_\alpha &= \frac{\partial\boldsymbol{\Psi}^\alpha}{\partial t}+(\operatorname{grad}\boldsymbol{\Psi}^\alpha)\,\mathbf{x}'_\alpha\,,\\ (\,\mathrm{d}v)'_\alpha &= \operatorname{div}\mathbf{x}'_\alpha\,\mathrm{d}v\,,\end{aligned}\right. \tag{B.25}$$

[5] Separate investigation of the substitution A, B, respectively:

$$A=-\int\{\underbrace{[(\nabla\boldsymbol{\sigma})\overset{13}{}^T\mathbf{H}^T]^{\cdot}-\nabla(\dot{\boldsymbol{\sigma}}\cdot\mathbf{H})}_{=:\,B}\}\,\mathrm{d}t=-\int\{\nabla(\boldsymbol{\sigma}\cdot\dot{\mathbf{H}})-[(\nabla\mathbf{H})\overset{13}{}^T\boldsymbol{\sigma}^T]^{\cdot}\}\,\mathrm{d}t=(\nabla\mathbf{H})\overset{13}{}^T\boldsymbol{\sigma}^T-\int\nabla(\boldsymbol{\sigma}\cdot\dot{\mathbf{H}})\,\mathrm{d}t$$

$$\begin{aligned}B &= (\dot{\boldsymbol{\sigma}})\overset{13}{}^T\mathbf{H}^T+(\nabla\boldsymbol{\sigma})\overset{13}{}^T(\dot{\mathbf{H}})^T-(\dot{\boldsymbol{\sigma}})\overset{13}{}^T\mathbf{H}^T-(\nabla\mathbf{H})\overset{13}{}^T(\dot{\boldsymbol{\sigma}})^T\\ &= \underbrace{(\nabla\boldsymbol{\sigma})\overset{13}{}^T(\dot{\mathbf{H}})^T+(\nabla\,\dot{\mathbf{H}})\overset{13}{}^T\boldsymbol{\sigma}^T}_{\nabla(\boldsymbol{\sigma}\cdot\dot{\mathbf{H}})}\underbrace{-(\nabla\,\dot{\mathbf{H}})\overset{13}{}^T\boldsymbol{\sigma}^T-(\nabla\mathbf{H})\overset{13}{}^T(\dot{\boldsymbol{\sigma}})^T}_{-[(\nabla\mathbf{H})\overset{13}{}^T\boldsymbol{\sigma}^T]^{\cdot}}\end{aligned}$$

The general *Reynolds* transport theorem is extended for a singular surface $\bar{\mathcal{S}}(\bar{\mathbf{n}}^{\mathcal{S},+}\,\mathrm{d}a^{\mathcal{S}}, \bar{\mathbf{n}}^{\mathcal{S},+}\,\mathrm{d}a^{\mathcal{S}})$ intersecting a body $\mathcal{B}$, see Figure B.5. The surface splits the body into the two parts, $\mathcal{B}^+$ and $\mathcal{B}^-$. Let the surface move with the velocity $\overset{\prime}{\mathbf{x}}_{\bar{\mathcal{S}}}$. All continuum-mechanical field functions are assumed to be continuous within each body part and on the surface itself. Due to the singular design of the surface $\bar{\mathcal{S}}$, discontinuities in the field functions over the surface are possible. The interested reader is referred to *Mahnkopf* [132] for more details on the following derivation. Starting from the total, material time derivation of a vector-valued physical quantity $\boldsymbol{\Psi}^\alpha$ integrated over the overall body $\mathcal{B}$, see (2.14), viz.

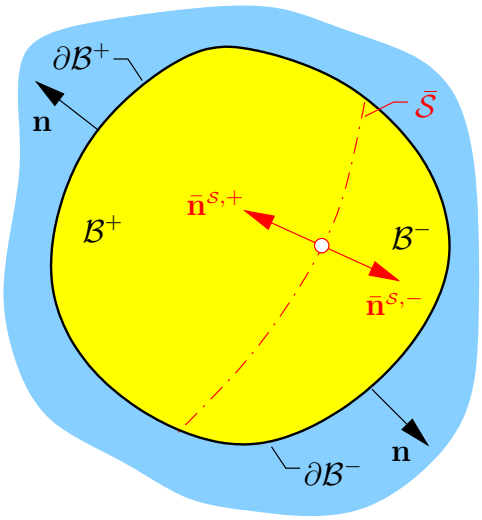

Figure B.5: Surface intersected body.

leads to

$$\begin{aligned}
\frac{\mathrm{d}_\alpha}{\mathrm{d}t}\int_{\mathcal{B}} \boldsymbol{\Psi}^\alpha\,\mathrm{d}v &= \int_{\mathcal{B}} \Big[\,\frac{\partial \boldsymbol{\Psi}^\alpha}{\partial t} + \underbrace{(\operatorname{grad}\,\boldsymbol{\Psi}^\alpha)\,\overset{\prime}{\mathbf{x}}_\alpha + \boldsymbol{\Psi}^\alpha \operatorname{div}\overset{\prime}{\mathbf{x}}_\alpha}_{\operatorname{div}\,(\boldsymbol{\Psi}^\alpha \otimes \overset{\prime}{\mathbf{x}}_\alpha)}\,\Big]\,\mathrm{d}v\,, \\
&= \int_{\mathcal{B}} \frac{\partial \boldsymbol{\Psi}^\alpha}{\partial t}\,\mathrm{d}v + \int_{\mathcal{B}} \operatorname{div}\,(\boldsymbol{\Psi}^\alpha \otimes \overset{\prime}{\mathbf{x}}_\alpha)\,\mathrm{d}v\,, \\
&= \int_{\mathcal{B}} \frac{\partial \boldsymbol{\Psi}^\alpha}{\partial t}\,\mathrm{d}v + \int_{\partial\mathcal{B}} (\boldsymbol{\Psi}^\alpha \otimes \overset{\prime}{\mathbf{x}}_\alpha)\,\mathrm{d}\mathbf{a}\,.
\end{aligned} \tag{B.26}$$

With this, regarding now two motion functions $\boldsymbol{\chi}_\alpha \to \overset{\prime}{\mathbf{x}}_\alpha$ and $\boldsymbol{\chi}_\beta \to \overset{\prime}{\mathbf{x}}_\beta$, the following relation is obtained:

$$\begin{aligned}
(i) \qquad &: \frac{\mathrm{d}_\alpha}{\mathrm{d}t}\int_{\mathcal{B}} \boldsymbol{\Psi}^\alpha\,\mathrm{d}v = \int_{\mathcal{B}} \frac{\partial \boldsymbol{\Psi}^\alpha}{\partial t}\,\mathrm{d}v + \int_{\partial\mathcal{B}} (\boldsymbol{\Psi}^\alpha \otimes \overset{\prime}{\mathbf{x}}_\alpha)\,\mathrm{d}\mathbf{a}\,, \\
(ii) \qquad &: \frac{\mathrm{d}_\beta}{\mathrm{d}t}\int_{\mathcal{B}} \boldsymbol{\Psi}^\alpha\,\mathrm{d}v = \int_{\mathcal{B}} \frac{\partial \boldsymbol{\Psi}^\alpha}{\partial t}\,\mathrm{d}v + \int_{\partial\mathcal{B}} (\boldsymbol{\Psi}^\alpha \otimes \overset{\prime}{\mathbf{x}}_\beta)\,\mathrm{d}\mathbf{a}\,, \\
(i)-(ii) \qquad &: \frac{\mathrm{d}_\alpha}{\mathrm{d}t}\int_{\mathcal{B}} \boldsymbol{\Psi}^\alpha\,\mathrm{d}v = \frac{\mathrm{d}_\beta}{\mathrm{d}t}\int_{\mathcal{B}} \boldsymbol{\Psi}^\alpha\,\mathrm{d}v + \int_{\partial\mathcal{B}} [\boldsymbol{\Psi}^\alpha \otimes (\overset{\prime}{\mathbf{x}}_\alpha - \overset{\prime}{\mathbf{x}}_\beta)]\,\mathrm{d}\mathbf{a}\,.
\end{aligned} \tag{B.27}$$

Because the total, material time derivation in $(\text{B.27})_3$ is not necessarily limited to be composed by the constituents motion functions, the second velocity $\overset{\prime}{\mathbf{x}}_\beta$ can be substituted

by $\overset{\prime}{\mathbf{x}}_{\bar{s}}$. The separate evaluation of (B.27)$_3$ for the two body parts then reads

$$\text{for } \mathcal{B}^+ : \quad \frac{\mathrm{d}_\alpha}{\mathrm{d}t}\int\limits_{\mathcal{B}^+} \boldsymbol{\Psi}^\alpha \,\mathrm{d}v \;=\; \frac{\mathrm{d}_{\bar{s}}}{\mathrm{d}t}\int\limits_{\mathcal{B}^+} \boldsymbol{\Psi}^\alpha \,\mathrm{d}v \;+\; \int\limits_{\partial\mathcal{B}^+} \left[\boldsymbol{\Psi}^\alpha \otimes (\overset{\prime}{\mathbf{x}}_\alpha - \overset{\prime}{\mathbf{x}}_{\bar{s}})\right] \mathrm{d}\mathbf{a} + \int\limits_{\bar{\mathcal{S}}} \left\{(\boldsymbol{\Psi}^\alpha)^+ \otimes \left[(\overset{\prime}{\mathbf{x}}_\alpha)^+ - \overset{\prime}{\mathbf{x}}_{\bar{s}}\right]\right\} (-\bar{\mathbf{n}}^{\mathcal{S},+})\,\mathrm{d}a^{\mathcal{S}}\,, \tag{B.28}$$

$$\text{for } \mathcal{B}^- : \quad \frac{\mathrm{d}_\alpha}{\mathrm{d}t}\int\limits_{\mathcal{B}^-} \boldsymbol{\Psi}^\alpha \,\mathrm{d}v \;=\; \frac{\mathrm{d}_{\bar{s}}}{\mathrm{d}t}\int\limits_{\mathcal{B}^-} \boldsymbol{\Psi}^\alpha \,\mathrm{d}v \;+\; \int\limits_{\partial\mathcal{B}^-} \left[\boldsymbol{\Psi}^\alpha \otimes (\overset{\prime}{\mathbf{x}}_\alpha - \overset{\prime}{\mathbf{x}}_{\bar{s}})\right] \mathrm{d}\mathbf{a} + \int\limits_{\bar{\mathcal{S}}} \left\{(\boldsymbol{\Psi}^\alpha)^- \otimes \left[(\overset{\prime}{\mathbf{x}}_\alpha)^- - \overset{\prime}{\mathbf{x}}_{\bar{s}}\right]\right\} (-\bar{\mathbf{n}}^{\mathcal{S},-})\,\mathrm{d}a^{\mathcal{S}}\,. \tag{B.29}$$

Therein, quantities denoted by $(\,\cdot\,)^{+/-}$ represent the corresponding limiting values of the two sides of the surface $\bar{\mathcal{S}}$. The normal vectors of the two sides of the surface $\bar{\mathcal{S}}$ are in each case reciprocally oriented to the normal vector of the surfaces $\partial\mathcal{B}^{+/-}$, thus, $\mathbf{n} = -\bar{\mathbf{n}}^{\mathcal{S},+}$ and $\mathbf{n} = -\bar{\mathbf{n}}^{\mathcal{S},-}$. Defining a single surface normal vector for $\bar{\mathcal{S}}$ as $\bar{\mathbf{n}}^{\mathcal{S},+} = -\bar{\mathbf{n}}^{\mathcal{S},-} =: \bar{\mathbf{n}}^{\mathcal{S}}$, and taking into account that $\mathcal{B} = \mathcal{B}^+ \cup \mathcal{B}^-$, as well as $\partial\mathcal{B} = \partial\mathcal{B}^+ \cup \partial\mathcal{B}^-$, leads together with (B.26) and the definition of general jump quantities (3.37) to the final form of the modified *Reynolds* transport theorem for a moving discontinuity in a body:

$$\rightsquigarrow \frac{\mathrm{d}_\alpha}{\mathrm{d}t}\int\limits_{\mathcal{B}} \boldsymbol{\Psi}^\alpha \,\mathrm{d}v = \int\limits_{\mathcal{B}} \frac{\partial \boldsymbol{\Psi}^\alpha}{\partial t}\,\mathrm{d}v + \int\limits_{\partial\mathcal{B}} (\boldsymbol{\Psi}^\alpha \otimes \overset{\prime}{\mathbf{x}}_\alpha)\,\mathrm{d}\mathbf{a} - \int\limits_{\bar{\mathcal{S}}} [\![\boldsymbol{\Psi}^\alpha \otimes (\overset{\prime}{\mathbf{x}}_\alpha - \overset{\prime}{\mathbf{x}}_{\bar{s}})]\!]\, \bar{\mathbf{n}}^{\mathcal{S}}\,\mathrm{d}a^{\mathcal{S}} \tag{B.30}$$

Appendix C: Numerical Details

C.1 *Householder-QL* Algorithm

One of the most efficient techniques for the numerical computation of eigenvalues and eigenvectors of real symmetric matrices $\boldsymbol{A} \in \mathbb{R}^{m\times m}$ is their QL-decomposition following after a *Householder* transformation. For the purpose of this monograph, the *Householder-QL* algorithm is only applied to 3×3 matrices ($m = 3$). The *Householder* transformation reduces a symmetric matrix $\boldsymbol{A}$ to tridiagonal form $\boldsymbol{P}$ by an orthogonal transformation

$$\boldsymbol{P} := \text{tridiag}\,(\boldsymbol{A}) = \boldsymbol{Q}_H^T\,\boldsymbol{A}\,\boldsymbol{Q}_H\,, \tag{C.1}$$

where $\boldsymbol{Q}_H$ is symmetric ($\boldsymbol{Q}_H = \boldsymbol{Q}_H^T$). The basic idea behind the QL-decomposition is that any real matrix can be decomposed in the form $\boldsymbol{P}= \boldsymbol{Q}\boldsymbol{L}$, where $\boldsymbol{Q}$ is orthogonal ($\boldsymbol{Q}^{-1} = \boldsymbol{Q}^T$) and $\boldsymbol{L}$ is lower triangular. The columns of $\boldsymbol{Q}$ then represent the eigenvectors $\boldsymbol{m}_{\mathbf{A}i}$, and the diagonal elements of $\boldsymbol{L}$ represent the eigenvalues $\lambda_{\mathbf{A}i}$ of $\boldsymbol{A}$. The *Householder-QL* algorithm can then be constructed as follows:

`IN)` $\boldsymbol{A} = [\,a_{ij}\,]$ with $i, j = 1, 2, 3\,.$

`S0)` If $a_{13} = 0$ then $\boldsymbol{Q}_H = \mathbf{I} \rightsquigarrow \boldsymbol{P} \equiv \boldsymbol{A}\,.$

`S1)` If $a_{13} \neq 0$ then $\boldsymbol{Q}_H = \begin{bmatrix} 1 & 0 & 0 \\ 0 & u & v \\ 0 & v & -u \end{bmatrix} \rightsquigarrow \boldsymbol{P} = \begin{bmatrix} a_{11} & \ell & 0 \\ \ell & a_{22} + v\,w & a_{23} - u\,w \\ 0 & a_{23} - u\,w & a_{33} - v\,w \end{bmatrix}$

with $\ell = \sqrt{a_{12}\,a_{12} + a_{13}\,a_{13}}, \quad u = \dfrac{a_{12}}{\ell}, \quad v = \dfrac{a_{13}}{\ell}, \quad w = 2\,a_{23}\,u + v\,(a_{33} - a_{22})\,.$

`S2)` For $(s = 0;\ s < 3;\ s = s + 1)$, decompose $\boldsymbol{P}_s = \boldsymbol{Q}_s\,\boldsymbol{L}_s$
with $\boldsymbol{P}_{s+1} = \boldsymbol{L}_s\,\boldsymbol{Q}_s\ (= \boldsymbol{Q}_s^T\,\boldsymbol{P}_s\,\boldsymbol{Q}_s)\,.$

`OUT)` $\boldsymbol{Q} = [\,q_{ij}\,] \rightsquigarrow \boldsymbol{m}_{\boldsymbol{A}1} = [\,q_{i1}\,], \boldsymbol{m}_{\mathbf{A}2} = [\,q_{i2}\,], \boldsymbol{m}_{\mathbf{A}3} = [\,q_{i3}\,]$ with $i, j = 1, 2, 3\,,$

$\boldsymbol{L} = [\,l_{ij}\,] \rightsquigarrow \lambda_{\mathbf{A}i} = l_{ii}$ with $i, j = 1, 2, 3\,.$

Table C.1: *Householder-QL* algorithm for the numerical computation of eigenvalues $\lambda_{\mathbf{A}i}$ and eigenvectors $\boldsymbol{m}_{\mathbf{A}i}$ of real symmetric matrices $\boldsymbol{A} \in \mathbb{R}^{3\times3}$ $(i = 1, 2, 3)$.

C.2 *Newton* Algorithm with Radial Return

The following scheme shows a generalised *Newton* algorithm for the displacement with local nonlinear radial return at all integration points. The *Newton* iteration index is denoted m, the actual time-step index is n. For a stable performance, this algorithm should be extended by a time-step control and a damping strategy for the *Newton* update. Note that for the sake of clarity the general notation of the *Runge-Kutta* intermediate steps is waived herein. Consequently, the corresponding variables are substituted, viz. $\mathbf{u} := \triangle \boldsymbol{u}$ and $\triangle \mathbf{u} := \boldsymbol{\Delta}$.

`S0)` Set $\mathbf{u}_0^h = \mathbf{0}$, $\boldsymbol{\varepsilon}_{p,0} = \mathbf{0}$, $\varepsilon_{pv,0}^h = 0$ and $n = 1$.

`S1)` In time step n, choose a start value $\mathbf{u}_n^{h,0} \in \mathcal{A}^{\mathbf{u},h}(t_n)$ satisfying the *Dirichlet* boundary conditions and set $m = 0$.

`S2)` Compute the trial stress $\boldsymbol{\sigma}_{\text{trial},n}^{h,m} = \boldsymbol{\sigma}_{\text{trial},n}^h(\mathbf{u}_n^{h,m}, \boldsymbol{\varepsilon}_{p,n-1}^h)$, $s_n^{h,m} = \left|(\boldsymbol{\sigma}_{\text{trial},n}^{h,m})^D\right|$ and $\Lambda_n^{h,m} = \Lambda_n^h\big(s_n^{h,m}\big)$ by solving the equation (4.33) in every integration point. Compute the residual

$$R_n^{h,m}(\delta\mathbf{u}^h) = \int_{\Omega^h} \mathbb{S}_n^h\left(\boldsymbol{\varepsilon}(\mathbf{u}_n^{h,m}), \boldsymbol{\varepsilon}_{p,n-1}^h\right) \cdot \boldsymbol{\varepsilon}(\delta\mathbf{u}^h)\, \mathrm{d}v - \int_{\Gamma_N^{\mathbf{t},h}} \bar{\mathbf{t}}_n^h \cdot \delta\mathbf{u}^h\, \mathrm{d}a\,, \quad \delta\mathbf{u}^h \in \mathcal{T}^{\mathbf{u},h}\,.$$

`S3)` If the residual is small enough, set $\mathbf{u}_n^h = \mathbf{u}_n^{h,m}$ and update the inner variables by $\boldsymbol{\varepsilon}_{p,n}^h = \mathbb{R}_n^h(\boldsymbol{\sigma}_{\text{trial},n}^h)$ and $\varepsilon_{pv,n}^h = \varepsilon_{pv,n-1}^h + \sqrt{\frac{2}{3}}|\triangle\boldsymbol{\varepsilon}_{p,n}^h|$. Set $n := n+1$ and go to `S1)`.

`S4)` For every integration point compute the consistent tangent $\boldsymbol{\mathcal{S}}_n^{h,m}$ by

$$\boldsymbol{\mathcal{S}}_n^{h,m}\boldsymbol{\varepsilon} = \begin{cases} \overset{4}{\boldsymbol{\mathcal{C}}}\,\boldsymbol{\varepsilon} & \text{if} \quad f_n^h(s_n^{h,m}, \Lambda_n^{h,m}) \le 0\,, \\ \overset{4}{\boldsymbol{\mathcal{C}}}\,\Big(\boldsymbol{\varepsilon} - 2\mu\,\partial\Lambda_n^{h,m}\,\boldsymbol{\varepsilon}\cdot\boldsymbol{\zeta}_n^{h,m}\boldsymbol{\zeta}_n^{h,m} - \\ \qquad -\dfrac{2\mu\Lambda_n^{h,m}}{s_n^{h,m}}\big(\boldsymbol{\varepsilon}^D - \boldsymbol{\varepsilon}\cdot\boldsymbol{\zeta}_n^{h,m}\boldsymbol{\zeta}_n^{h,m}\big)\Big) & \text{if} \quad f_n^h(s_n^{h,m}, \Lambda_n^{h,m}) > 0\,, \end{cases}$$

with $\boldsymbol{\zeta}_n^{h,m} = \frac{1}{s_n^{h,m}}(\boldsymbol{\sigma}_{\text{trial},n}^{h,m})^D$ and the derivative of the return parameter $\partial\Lambda_n^{h,m} = \frac{\partial\Lambda_n^h(s_n^{h,m})}{\partial s}$. Let $\triangle\mathbf{u}_n^{h,m} \in \mathcal{T}^{\mathbf{u},h}$ be the solution of the linear variational problem

$$\int_{\Omega^h} \boldsymbol{\mathcal{S}}_n^{h,m}\boldsymbol{\varepsilon}(\triangle\mathbf{u}_n^{h,m}) \cdot \boldsymbol{\varepsilon}(\delta\mathbf{u}^h)\, \mathrm{d}v = R_n^{h,m}(\delta\mathbf{u}^h)\,, \quad \delta\mathbf{u}^h \in \mathcal{T}^{\mathbf{u},h}\,.$$

Compute the *Newton* update $\mathbf{u}_n^{h,m+1} = \mathbf{u}_n^{h,m} - \triangle\mathbf{u}_n^{h,m}$, set $m := m+1$ and go to `S1)`.

C.3 *Newton* Algorithm without Radial Return

The following scheme shows a generalised *Newton* algorithm for the coupled system for displacement and plastic strain avoiding a local nonlinear radial return. The *Newton* iteration index is denoted m, the actual time-step index is n. Note that for the sake of clarity the general notation of the *Runge-Kutta* intermediate steps is waived herein. Consequently, the corresponding variables are substituted, viz. $\{\mathbf{u}, \boldsymbol{\varepsilon}_p\} := \{\triangle \boldsymbol{u}, \triangle \boldsymbol{e}\}$ and $\{\triangle\mathbf{u}, \triangle\boldsymbol{\varepsilon}_p\} := \{\boldsymbol{\Delta}_{\boldsymbol{u}}, \boldsymbol{\Delta}_{\boldsymbol{e}}\}$.

`S0)` Set $\mathbf{u}_0^h = \mathbf{0}$, $\boldsymbol{\varepsilon}_{p,0} = \mathbf{0}$, $\varepsilon_{pv,0}^h = 0$ and $n = 1$.

`S1)` In time step n, choose start values $\{\mathbf{u}_n^{h,0}, \boldsymbol{\varepsilon}_{p,n}^{h,0}\} \in \{\mathcal{A}^{\mathbf{u},h}(t_n), \mathcal{A}^{\boldsymbol{\varepsilon},h}(t_n)\}$ and set $m = 0$.

`S2)` Compute the stress $\boldsymbol{\sigma}_n^{h,m} = \overset{4}{\boldsymbol{\mathcal{C}}} \left[\boldsymbol{\varepsilon}_n(\mathbf{u}_n^{h,m}) - \boldsymbol{\varepsilon}_{p,n}^{h,m} \right]$, its second invariant $s_n^{h,m} = |(\boldsymbol{\sigma}_n^{h,m})^D|$, the equivalent plastic strain $\varepsilon_{pv,n}^{h,m} = \varepsilon_{pv,n-1}^h + \sqrt{\frac{2}{3}} |\boldsymbol{\varepsilon}_{p,n}^{h,m} - \boldsymbol{\varepsilon}_{p,n-1}^h|$, the return parameter $\Lambda_n^{h,m} = \Lambda_n^h\big(s_n^{h,m}, \varepsilon_{pv,n}^{h,m}\big)$, the flow direction $\boldsymbol{\zeta}_n^{h,m} = \frac{1}{s_n^{h,m}} (\boldsymbol{\sigma}_n^{h,m})^D$ and compute the residual

$$
\begin{aligned}
R_{\mathrm{mod},n}^{h,m}(\delta\mathbf{u}^h, \delta\boldsymbol{\varepsilon}_p^h) \;=\; & \int_{\Omega^h} \boldsymbol{\sigma}_n^{h,m} \cdot \boldsymbol{\varepsilon}(\delta\mathbf{u}^h) \, \mathrm{d}v - \int_{\Gamma_N^{\mathbf{t},h}} \bar{\mathbf{t}}_n \cdot \delta\mathbf{u}^h \, \mathrm{d}a + \\
& + \int_{\Omega^h} \big(\boldsymbol{\varepsilon}_{p,n}^{h,m} - \boldsymbol{\varepsilon}_{p,n-1}^h - \Lambda_n^{h,m} \boldsymbol{\zeta}_n^{h,m} \big) \cdot \delta\boldsymbol{\varepsilon}_p^h \, \mathrm{d}v \,.
\end{aligned}
$$

`S3)` If the residual is small enough, set $(\mathbf{u}_n^h, \boldsymbol{\varepsilon}_{p,n}^h, \varepsilon_{pv,n}^h) = (\mathbf{u}_n^{h,m}, \boldsymbol{\varepsilon}_{p,n}^{h,n}, \varepsilon_{pv,n}^{h,m})$. Set $n := n+1$ and go to `S1)`.

`S4)` For every integration point compute $f_n^{h,m} = \tilde{F}(s_n^{h,m}, \varepsilon_{pv,n}^{h,m})$ and the generalised derivatives

$$
\frac{\partial \Lambda_n^{h,m}}{\partial s} = \left\{ \begin{array}{r|l|l} 0 & f_n^{h,m} \le 0 & 0 \\ \dfrac{r \triangle t_n}{\eta} \left(f_n^{h,m}\right)^{r-1} \dfrac{\partial \tilde{F}}{\partial s} & f_n^{h,m} > 0 & \dfrac{r \triangle t_n}{\eta} \left(f_n^{h,m}\right)^{r-1} \dfrac{\partial \tilde{F}}{\partial \varepsilon_p} \end{array} \right\} = \frac{\partial \Lambda_n^{h,m}}{\partial \varepsilon_p} \,.
$$

Let $\{\triangle\mathbf{u}_n^{h,m}, \triangle\boldsymbol{\varepsilon}_{p,n}^{h,m}\} \in \{\mathcal{T}^{\mathbf{u},h}, \mathcal{T}^{\boldsymbol{\varepsilon},h}\}$ be the solution of the linear variational system

$$
\begin{aligned}
& \int_{\Omega^h} \triangle\boldsymbol{\sigma}_n^{h,m} \cdot \boldsymbol{\varepsilon}(\delta\mathbf{u}^h) \, \mathrm{d}v + \int_{\Omega^h} \triangle\boldsymbol{\varepsilon}_{p,n}^{h,m} \cdot \delta\boldsymbol{\varepsilon}_p^h \, \mathrm{d}v - \\
& - \int_{\Omega^h} \Big(\frac{\partial \Lambda_n^{h,m}}{\partial s} \triangle\boldsymbol{\sigma}_n^{h,m} \cdot \boldsymbol{\zeta}_n^{h,m} + + \frac{\partial \Lambda_n^{h,m}}{\partial \varepsilon_p} \frac{2}{3} \frac{\triangle\boldsymbol{\varepsilon}_{p,n}^{h,m} \cdot \big(\boldsymbol{\varepsilon}_{p,n}^{h,m} - \boldsymbol{\varepsilon}_{p,n-1}^h\big)}{|\boldsymbol{\varepsilon}_{p,n}^{h,m} - \boldsymbol{\varepsilon}_{p,n-1}^h|} \Big) \delta\boldsymbol{\varepsilon}_p^h \cdot \boldsymbol{\zeta}_n^{h,m} \, \mathrm{d}v -
\end{aligned}
$$

$$-\int_{\Omega^h} \frac{\Lambda_n^{h,m}}{s_n^{h,m}} \Big(\triangle \boldsymbol{\sigma}_n^{h,m} \cdot \delta \boldsymbol{\varepsilon}_p^h - (\triangle \boldsymbol{\sigma}_n^{h,m} \cdot \boldsymbol{\zeta}_n^{h,m})(\delta \boldsymbol{\varepsilon}_p^h \cdot \boldsymbol{\zeta}_n^{h,m}) \Big) \, \mathrm{d}v = R_{\mathrm{mod},n}^{h,m}(\delta \mathbf{u}^h, \delta \boldsymbol{\varepsilon}_p^h)$$

with $\triangle \boldsymbol{\sigma}_n^{h,m} = \overset{4}{\boldsymbol{\mathcal{C}}} \left[\boldsymbol{\varepsilon}_n(\triangle \mathbf{u}_n^{h,m}) - \triangle \boldsymbol{\varepsilon}_{p,n}^{h,m} \right]$. Finally, compute the *Newton* update $\{\mathbf{u}_n^{h,m+1}, \boldsymbol{\varepsilon}_{p,n}^{h,m+1}\} = \{\mathbf{u}_n^{h,m}, \boldsymbol{\varepsilon}_{p,n}^{h,m}\} - \{\triangle \mathbf{u}_n^{h,m}, \triangle \boldsymbol{\varepsilon}_{p,n}^{h,m}\}$, set $m := m + 1$ and go to `S1)`.

C.4 Area of a 2-d Polygon

The following program computes the area of an arbitrary shaped 2-d polygon. This function is also valid for the area computation of triangle or rectangular finite-elements.

```
#!/usr/bin/env python

# --- import external libraries
from math import *

# --- global vars
X = 0; Y = 1

# --- polygon example
p1 = [+1.0,+0.0]; p5 = [+2.0,+1.0]
p2 = [+3.0,+0.0]; p6 = [+1.0,+4.0]
p3 = [+4.0,+4.0]; p7 = [+0.0,+4.0]
p4 = [+3.0,+4.0]; p8 = [+1.0,+0.0]
polygon = [p1, p2, p3, p4, p5, p6, p7, p8]

# --- compute area of a 2-d polygon
def Area2DPolygon(polygon):
  area = 0.0
  j = 2; k = 0; n = len(polygon)
  polygon.append(polygon[0])
  polygon.append(polygon[1])
  for i in range(1,n+1):
    area += (polygon[i][X]*(polygon[j][Y]-polygon[k][Y]))
    j += 1; k += 1
  return area/2.

# --- start program
```

```
28 if __name__ == '__main__':
29   # --- compute polygon area
30   print Area2DPolygon(polygon)
```

The function[1] `Area2DPolygon()` decomposes a 2-d polygon into triangles. The included summation of the area of these triangles is preferred for efficiency. But to avoid any overhead from computing the index i, one must extend the polygon array up to `polygon[n] = polygon[0]` and `polygon[n+1] = polygon[1]` with n representing the number of the nodes of the polygon. This computation gives a signed area for a polygon; and similar to the signed area of a triangle, it is positive when the vertices are oriented counterclockwise around the polygon and negative when oriented clockwise. Thus, this function could also be used to efficiently test a polygon's global orientation.

C.5 Volume of a 3-d Mesh

The following program computes the volume of an arbitrary shaped 3-d object that consists of a surface mesh made up from triangles. The procedure is also valid for the volume computation of tetrahedron and hexahedron finite-elements. For hexahedron based finite-elements the six surfaces need to be triangulated. Therein, it is crucial to take the orientation of the triangulated surfaces into account.

```
1  #!/usr/bin/env python
2
3  # --- import external libraries
4  from math import *
5
6  # --- global vars
7  X = 0; Y = 1; Z = 2
8
9  # --- hexahederon example
10 p1 = [-0.5,-1.0,+1.5]; p5 = [+0.5,-1.0,+1.5]
11 p2 = [-0.5,+1.2,+1.7]; p6 = [+0.5,+1.0,+1.5]
12 p3 = [-0.5,+1.0,-1.5]; p7 = [+0.5,+2.2,-1.5]
13 p4 = [-0.8,-1.0,-1.5]; p8 = [+0.5,-1.0,-1.5]
14 hex_sur1 = [p1, p2, p3, p4]; hex_sur4 = [p3, p7, p8, p4]
15 hex_sur2 = [p1, p5, p6, p2]; hex_sur5 = [p1, p4, p8, p5]
16 hex_sur3 = [p5, p8, p7, p6]; hex_sur6 = [p2, p6, p7, p3]
17 hex_elem = [hex_sur1, hex_sur2, hex_sur3,
18              hex_sur4, hex_sur5, hex_sur6]
19
20 # --- triangle -> tetrahedron volume
21 def SignedVolumeOfTriangle(p1, p2, p3):
22   v321 = p3[X]*p2[Y]*p1[Z]
```

[1] The original idea for this function is based on `http://goo.gl/8Gkm0`.

```
23    v231 = p2[X]*p3[Y]*p1[Z]
24    v312 = p3[X]*p1[Y]*p2[Z]
25    v132 = p1[X]*p3[Y]*p2[Z]
26    v213 = p2[X]*p1[Y]*p3[Z]
27    v123 = p1[X]*p2[Y]*p3[Z]
28    return (1.0/6.0)*(-v321+v231+v312-v132-v213+v123)
29
30  # --- volume of triangle based surface mesh
31  def VolumeOfMesh(mesh):
32    volume = 0.0
33    for tri in mesh:
34      volume += SignedVolumeOfTriangle(tri[X],tri[Y],tri[Z])
35    return abs(volume)
36
37  # --- start program
38  if __name__ == '__main__':
39    mesh = []
40    # --- triangulation hexaedron surfaces
41    for surf in hex_elem:
42      tri1 = [surf[0], surf[1], surf[2]]
43      tri2 = [surf[2], surf[3], surf[0]]
44      mesh.append(tri1)
45      mesh.append(tri2)
46    # --- compute mesh volume
47    print VolumeOfMesh(mesh)
```

The function[2] `SignedVolumeOfTriangle()` calculates the signed volume of a tetrahedron based on a single surface triangle and topped off at the origin. The sign of the volume comes from whether the triangle is pointing in the direction of the origin. The normal of the triangle is itself dependent upon the order of the vertices or nodes, respectively.

C.6 Marching Cubes Algorithm (MCA)

The MCA[3] uses an index to a pre-calculated array of 256 possible polygon configurations ($2^8 = 256$) within a cube. The iso-level (levelset value) of each nodal scalar value of the cube is interpreted as a bit in an 8-bit integer. For nodal values higher than the levelset value, the appropriate bit is set to one, lower values result in a zero bit. The binary sum of all eight element edges indicates the polygon configuration. The intersection position of the cube edges with the corresponding triangles is computed by a linear interpolation of the nodal scalar values.

```
1  #!/usr/bin/env python
```

[2] The original idea for this function is based on `http://goo.gl/YOFFp`.
[3] The implementation of the MCA is based on `http://goo.gl/lGnOC` and `http://goo.gl/lGnOC`.

```
2
3  # --- iso-level (levelset value)
4  level = 0.0
5
6  # --- hexahederon example
7  n0 = [+1, -1, -1]; n1 = [+1, +1, -1];
8  n2 = [+1, +1, +1]; n3 = [+1, -1, +1];
9  n4 = [-1, -1, -1]; n5 = [-1, +1, -1];
10 n6 = [-1, +1, +1]; n7 = [-1, -1, +1]
11 elem_hex = [n0, n1, n2, n3, n4, n5, n6, n7]
12 elem_val = [-1.1, +1.2, +1.3, -1.4, +1.1, +1.2, +1.3, +1.]
13
14 # --- MCA: edge table
15 edgeTable =  [
16 0x0  , 0x109, 0x203, 0x30a, 0x406, 0x50f, 0x605, 0x70c,
17 0x80c, 0x905, 0xa0f, 0xb06, 0xc0a, 0xd03, 0xe09, 0xf00,
18 0x190, 0x99 , 0x393, 0x29a, 0x596, 0x49f, 0x795, 0x69c,

                                ...

45 0x69c, 0x795, 0x49f, 0x596, 0x29a, 0x393, 0x99 , 0x190,
46 0xf00, 0xe09, 0xd03, 0xc0a, 0xb06, 0xa0f, 0x905, 0x80c,
47 0x70c, 0x605, 0x50f, 0x406, 0x30a, 0x203, 0x109, 0x0]
48
49 # --- MCA: triangle table
50 m = -1; triTable = [
51 [m, m, m, m, m, m, m, m, m, m, m, m, m, m, m, m],
52 [0, 8, 3, m, m, m, m, m, m, m, m, m, m, m, m, m],
53 [0, 1, 9, m, m, m, m, m, m, m, m, m, m, m, m, m],

                                ...

304 [0, 9, 1, m, m, m, m, m, m, m, m, m, m, m, m, m],
305 [0, 3, 8, m, m, m, m, m, m, m, m, m, m, m, m, m],
306 [m, m, m, m, m, m, m, m, m, m, m, m, m, m, m, m]]
307
308 # --- linear interpolation of edge intersection
309 def interpolate(p1, p2, valp1, valp2):
310     if abs(level-valp1) < 0.000000000001: return p1
311     if abs(level-valp2) < 0.000000000001: return p2
312     if abs(valp1-valp2) < 0.0000000001: return p1
313     mu = (level-valp1)/(valp2-valp1)
314     p = (p1[0] + mu * (p2[0] - p1[0]),
```

```
315             p1[1] + mu * (p2[1] - p1[1]),
316             p1[2] + mu * (p2[2] - p1[2]))
317     return p
318 
319 # --- MCA: intersection surface (triangles)
320 def cube(pos, val):
321     cubeIdx = 0
322 
323     pnts = [[0.0, 0.0, 0.0] for i in range(12)]
324     if val[0] < level: cubeIdx|=1
325     if val[1] < level: cubeIdx|=2
326     if val[2] < level: cubeIdx|=4
327     if val[3] < level: cubeIdx|=8
328     if val[4] < level: cubeIdx|=16
329     if val[5] < level: cubeIdx|=32
330     if val[6] < level: cubeIdx|=64
331     if val[7] < level: cubeIdx|=128
332 
333     et = edgeTable[cubeIdx]
334     vi = interpolate
335 
336     if et==0:   return 0
337     if et&1:    pnts[0]  = vi(pos[0],pos[1],val[0],val[1])
338     if et&2:    pnts[1]  = vi(pos[1],pos[2],val[1],val[2])
339     if et&4:    pnts[2]  = vi(pos[2],pos[3],val[2],val[3])
340     if et&8:    pnts[3]  = vi(pos[3],pos[0],val[3],val[0])
341     if et&16:   pnts[4]  = vi(pos[4],pos[5],val[4],val[5])
342     if et&32:   pnts[5]  = vi(pos[5],pos[6],val[5],val[6])
343     if et&64:   pnts[6]  = vi(pos[6],pos[7],val[6],val[7])
344     if et&128:  pnts[7]  = vi(pos[7],pos[4],val[7],val[4])
345     if et&256:  pnts[8]  = vi(pos[0],pos[4],val[0],val[4])
346     if et&512:  pnts[9]  = vi(pos[1],pos[5],val[1],val[5])
347     if et&1024: pnts[10] = vi(pos[2],pos[6],val[2],val[6])
348     if et&2048: pnts[11] = vi(pos[3],pos[7],val[3],val[7])
349 
350     ntriangle = 0
351     tt = triTable[cubeIdx]
352     triangles = []
353     for i in range(0,16,3):
354         if tt[i]!= -1:
355             triangles.append((pnts[tt[i]],
356                               pnts[tt[i+1]],
357                               pnts[tt[i+2]]))
358             ntriangle+=1
359     return ntriangle, triangles, cubeIdx
```

```
360
361 # --- start program
362 if __name__ == '__main__':
363   # --- compute intersection surface (triangles)
364   print cube(elem_hex,elem_val)
```

Bibliography

[1] Alexander, R.: Diagonally implicit Runge-Kutta methods for stiff O.D.E.'s. *SIAM Journal on Numerical Analysis* **14** (1977), 1006–1021.

[2] Ammann, M.: *Parallel finite element simulations of localization phenomena in porous media.* Dissertation, Bericht Nr. II-11 aus dem Institut für Mechanik (Bauwesen), Universität Stuttgart 2005.

[3] Apel, N.: *Approaches to the Description of Anisotropic Material Behaviour at Finite Elastic and Plastic Defomations - Theory and Numerics.* Dissertation, Bericht Nr. I-12 aus dem Institut für Mechanik (Bauwesen), Universität Stuttgart 2004.

[4] Areias, P. M. A. & Belytschko, T.: A comment on the article "A finite element method for simulation of strong and weak discontinuities in solid mechanics" by A. Hansbo and P. Hansbo [Comput. Methods Appl. Mech. Engrg. 193 (2004) 3523-3540]. *Computer Methods in Applied Mechanics and Engineering* **195** (2006), 1275–1276.

[5] Armero, F. & Garikipati, K.: An analysis of strong discontinuities in multiplicative finite strain plasticity and their relation with the numerical simulation of strain localization in solids. *International Journal of Solids and Structures* **33** (1996), 2863–2885.

[6] Baković, D.; Valic, Z.; Eterović, D.; Vuković, I.; Obad, A.; Marinović-Terzić, I.; & Željko Dujić: Spleen volume and blood flow response to repeated breath-hold apneas. *Journal of Applied Physiology* **95** (2003), 14460–1466.

[7] Barenblatt, G. I.: The mathematical theory of equilibrium of cracks in brittle fracture. *Advances in Applied Mechanics* **7** (1962), 55–129.

[8] Bathe, K. J.: *Finite-Elemente-Methoden.* Springer-Verlag, Berlin 1990.

[9] Becker, M. & Miehe, C.: Incompatibility induced nonlocal crystal plasticity. *Proceedings in Applied Mathematics and Mechanics (PAMM)* **5** (2005), 259–260.

[10] Belytschko, T. & Black, T.: Elastic crack growth in finite elements with minimal remeshing. *International Journal for Numerical Methods in Engineering* **45** (1999), 601–620.

[11] Bilby, B. A.: John Douglas Eshelby. 21 December 1916-10 December 1981. *Biographical Memoirs of Fellows of the Royal Society* **36** (1990), 126–150.

[12] Biot, M. A.: General theory of three dimensional consolidation. *Journal of Applied Physics* **12(1)** (1941), 155–164.

[13] Bishop, A. W.: The effective stress principle. *Teknisk Ukeblad* **39** (1959), 859–863.

[14] Blome, K.-P.: *Ein Mehrphasen-Stoffmodell für Böden mit Übergang auf Interface Gesetze*. Dissertation, Bericht Nr. II-10 aus dem Institut für Mechanik (Bauwesen), Universität Stuttgart 2003.

[15] Boehler, J. P.: Introduction of the invariant formulation of anisotropic constitutive equations. In Boehler, J. P. (ed.): *Applications of Tensor Functions in Solid Mechanics*. Springer-Verlag, Wien 1987, CISM Courses and Lectures No. 292, pp. 13–30.

[16] de Boer, R.: Highlights in the historical development of porous media theory: toward a consistent macroscopic theory. *Applied Mechanics Review* **49** (1996), 201–262.

[17] de Boer, R.: *Theory of Porous Media*. Springer-Verlag, Berlin 2000.

[18] de Boer, R. & Ehlers, W.: *Theorie der Mehrkomponentenkontinua mit Anwendungen auf bodenmechanische Probleme*. Forschungsberichte aus dem Fachbereich Bauwesen, Heft 40, Universität-GH-Essen 1986.

[19] Boer, R. & Ehlers, W.: The development of the concept of effective stresses. *Acta Mechanica* **83** (1990), 77–92.

[20] de Boer, R.; Ehlers, W.; Kowalski, S. & Plischka, J.: *Porous media, a survey of different approaches*. Forschungsbericht aus dem Fachbereich Bauwesen, Heft 54, Universität-GH-Essen 1991.

[21] de Borst, R.: *Non-linear analysis of frictional materials*. Dissertation, Delft University of Technology 1986.

[22] de Borst, R.: Numerical aspects of cohesive-zone models. *Engineering Fracture Mechanics* **70** (2003), 1743–1757.

[23] de Borst, R.; Remmers, J. J. & Needleman, A.: Mesh-independent discrete numerical representations of cohesive-zone models. *Engineering Fracture Mechanics* **73** (2006), 160–177.

[24] Borst, R. d.; Gutièrrez, M. A.; Wells, G. N.; Remmers, J. J. C. & Askes, H.: Cohesive-zone models, higher-order continuum theories and reliability methods for computational failure analysis. *International Journal for Numerical Methods in Engineering* **60** (2004), 289–315.

[25] Borst, R. d.; Remmers, J. J. C.; Needleman, A. & Abellan, M.-A.: Discrete vs smeared crack models for concrete fracture: bridging the gap. *International Journal for Numerical and Analytical Methods in Geomechanics* **28** (2004), 583–607.

[26] Bowen, R. M.: Theory of mixtures. In Eringen, A. C. (ed.): *Continuum Physics*. Academic Press, Vol. III, New York 1976, pp. 1–127.

[27] Bowen, R. M.: Incompressible porous media models by use of the theory of mixtures. *International Journal of Engineering Science* **18** (1980), 1129–1148.

[28] Bowen, R. M.: Compressible porous media models by use of the theory of mixtures. *International Journal of Engineering Sciences* **20** (1982), 697–735.

[29] Braess, D.: *Finite Elemente*. Springer-Verlag, Berlin 1997.

[30] Braess, D.: *Finite Elements: Theory, Fast Solvers, and Applications in Solid Mechanics*. 3rd edn. Cambridge University Press, Cambridge 2007.

[31] Brezzi, F. & Fortin, M.: *Mixed and Hybrid Finite Element Methods*. Springer-Verlag, New York 1991.

[32] Butcher, J. C.: *Numerical methods for ordinary differential equations*. 2nd edn., John Wiley & Sons Inc. 2008.

[33] Callari, C.; Armero, F. & Abati, A.: Strong discontinuities in partially saturated poroplastic solids. *Computer Methods in Applied Mechanics and Engineering* **199** (2010), 1513–1535.

[34] Cash, J. R.: Diagonally implicit Runge-Kutta formulae with error estimates. *IMA Journal of Applied Mathematics* **24** (1979), 293–301.

[35] Cervera, M. & Chiumenti, M.: Mesh objective tensile cracking via a local continuum damage model and a crack tracking technique. *Computer Methods in Applied Mechanics and Engineering* **196(1-3)** (2006), 304–320.

[36] Chadwick, P.: *Continuum Mechanics: Concise Theory and Problems*. Dover Publications, Mineola (NY) 1999.

[37] Cheng, A. H.-D. & Cheng, D. T.: Heritage and early history of the boundary element method. *Engineering Analysis with Boundary Elements* **29** (2005), 268–302.

[38] Coleman, B. D. & Noll, W.: The thermodynamics of elastic materials with heat conduction and viscosity **13** (1963), 167–178.

[39] Cotterell, B.: The past, present, and future of fracture mechanics. *Engineering Fracture Mechanics* **69** (2002), 533–553.

[40] Cowin, S. C.: How Is a Tissue Built? *ASME Journal of Biomechanical Engineering* **122** (2000), 553–569.

[41] Cutnell, J. D. & Johnson, K. W.: *Physics*. 4th edn., John Wiley & Sons Inc. 1997.

[42] Delesse, A.: Pour déterminer la composition des roches. *Annales des mines, 4. séries* **13** (1848), 379–388.

[43] Diebels, S.: A micropolar theory of porous media: Constitutive modelling. *A Micropolar Theory of Porous Media: Constitutive Modelling* **34** (1999), 193–208.

[44] Diebels, S.: *Mikropolare Zweiphasenmodelle: Formulierung auf der Basis der Theorie Poröser Medien*. Habilitation, Bericht Nr. II-4 aus dem Institut für Mechanik (Bauwesen), Universität Stuttgart 2000.

[45] Diebels, S. & Ehlers, W.: Dynamic analysis of a fully saturated porous medium accounting for geometrical and material non-linearities. *International Journal for Numerical Methods in Engineering* **39** (1996), 81–97.

[46] Diebels, S.; Ehlers, W. & Markert, B.: Neglect of the fluid extra stresses in volumetrically coupled solid-fluid problems. *Zeitschrift für Angewandte Mathematik und Mechanik (ZAMM)* **81** (2001), 521–522.

[47] Diebels, S.; Ellsiepen, P. & Ehlers, W.: Error-controlled Runge-Kutta time integration of a viscoplastic hybrid two-phase model. *Technische Mechanik* **19** (1999), 19–27.

[48] Dolbow, J.: *An extended finite element method with discontinuous enrichment for applied mechanics*. Ph. D. thesis, Theoretical and Applied Mechanics, Northwestern University, Evanston (IL) 1999.

[49] Dugdale, D. S.: Yielding of steel sheets containing slits. *Journal of the Mechanics and Physics of Solids* **8** (1960), 100–104.

[50] Dumstorff, P.: *Modellierung und numerische Simulation von Rissfortschritt in spröden und quasi-spröden Materialien auf Basis der Extended Finite Element Method*. Dissertation, Institut für Konstruktiven Ingenieurbau, Ruhr-Universität Bochum 2006.

[51] Dumstorff, P. & Meschke, G.: Crack propagation criteria in the framework of X-FEM-based structural analyses. *International Journal for Numerical and Analytical Methods in Geomechanics* **31** (2007), 239–259.

[52] Ehlers, W.: On thermodynamics of elasto-plastic porous media. *Archives of Mechanics* **41** (1989), 73–93.

[53] Ehlers, W.: *Poröse Medien – ein kontinuumsmechanisches Modell auf der Basis der Mischungstheorie*. Habilitation, Forschungsberichte aus dem Fachbereich Bauwesen, Heft 47, Universität-GH-Essen 1989.

[54] Ehlers, W.: Compressible, incompressible and hybrid two-phase models in porous media theories. In Angel, Y. C. (ed.): *Anisotropy and Inhomogeneity in Elasticity and Plasticity*. ASME, New York 1993, AMD-Vol. 158, pp. 25–38.

[55] Ehlers, W.: Constitutive equations for granular materials in geomechanical context. In Hutter, K. (ed.): *Continuum Mechanics in Environmental Sciences and Geophysics*. Springer-Verlag, Wien 1993, CISM Courses and Lecture Notes No. 337, pp. 313–402.

[56] Ehlers, W.: A single-surface yield function for geomaterials. *Archive of Applied Mechanics* **65** (1995), 246–259.

[57] Ehlers, W.: *Vector and Tensor Calculus: An Introduction*. Lecture notes, Institute of Applied Mechanics (Chair of Continuum Mechanics), Universität Stuttgart 1995–2011, URL http://www.mechbau.uni-stuttgart.de/ls2.

[58] Ehlers, W.: Grundlegende Konzepte in der Theorie Poröser Medien. *Technische Mechanik* **16** (1996), 63–76.

[59] Ehlers, W.: Foundations of multiphasic and porous materials. In Ehlers, W. & Bluhm, J. (eds.): *Porous Media: Theory, Experiments and Numerical Applications.* Springer-Verlag, Berlin 2002, pp. 3–86.

[60] Ehlers, W.: Challenges of porous media models in geo- and biomechanical engineering including electro-chemically active polymers and gels. *International Journal of Advances in Engineering Sciences and Applied Mathematic* **1** (2009), 1–24.

[61] Ehlers, W. & Avci, O.: Experimental and computational issues in the mechanics of multi-physical unsaturated soil. In Borja, R. I. & Wu, W. (eds.): *Multiscale and Multiphysics Processes in Geomechanics.* Springer Berlin Heidelberg 2011, ISBN 978-3-642-19630-0, pp. 125–128.

[62] Ehlers, W.; Diebels, S.; Mahnkopf, D. & Ellsiepen, P.: *Theoretische und numerische Studien zur Lösung von Rand- und Anfangswertproblemen in der Theorie poröser Medien.* Forschungsbericht zum DFG-Projekt Eh 107/6-1, Universität Stuttgart 1996.

[63] Ehlers, W.; Ellsiepen, P.; Blome, P.; Mahnkopf, D. & Markert, B.: *Theoretische und numerische Studien zur Lösung von Rand- und Anfangswertproblemen in der Theorie Poröser Medien, Abschlußbericht zum DFG-Forschungsvorhaben Eh 107/6-2.* Bericht Nr. 99-II-1 aus dem Institut für Mechanik (Bauwesen), Universität Stuttgart 1999.

[64] Ehlers, W. & Markert, B.: A linear viscoelastic biphasic model for soft tissues based on the Theory of Porous Media. *ASME Journal of Biomechanical Engineering* **123** (2001), 418–424.

[65] Ehlers, W.; Markert, B. & Karajan, N.: A coupled FE analysis of the intervertebral disc based on a multiphasic TPM formulation. In Holzapfel, G. A. & Ogden, R. W. (eds.): *Mechanics of Biological Tissue.* Springer 2006, pp. 373–386.

[66] Eipper, G.: *Theorie und Numerik finiter elastischer Deformationen in fluidgesättigten porösen Festkörpern.* Dissertation, Bericht Nr. II-1 aus dem Institut für Mechanik (Bauwesen), Universität Stuttgart 1998.

[67] Ellsiepen, P.: *Zeit- und ortsadaptive Verfahren angewandt auf Mehrphasenprobleme poröser Medien.* Dissertation, Bericht Nr. II-3 aus dem Institut für Mechanik (Bauwesen), Universität Stuttgart 1999.

[68] Ellsiepen, P. & Hartmann, S.: Remarks on the interpretation of current non-linear finite element analyses as differential-algebraic equations. *International Journal for Numerical Methods in Engineering* **51** (2001), 679–707.

[69] Engelen, R. A. B.; Geers, M. G. D. & Baaijens, F. P. T.: Nonlocal implicit gradient-enhanced elasto-plasticity for the modelling of softening behaviour. *International Journal of Plasticity* **19** (2003), 403–433.

[70] Erdogan, F. & Sih, G.: On the crack extension in plates under plane loading and transverse shear. *Journal of Basic Engineering* **85** (1963), 519–527.

[71] Eriksson, K.: Decomposition of Eshelby's energy momentum tensor and application to path and domain independent integrals for the crack extension force of a plane circular crack in Mode III loading. *International Journal of Fracture* **144** (2007), 215–225.

[72] Eshelby, J. D.: The force on an elastic singularity. *Royal Society of London Philosophical Transactions Series A* **244** (1951), 87–112.

[73] Feist, C. & Hofstetter, G.: An embedded strong discontinuity model for cracking of plain concrete. *Computer Methods in Applied Mechanics and Engineering* **195(52)** (2007), 7115–7138.

[74] Fillunger, P.: Das Delesse'sche Gesetz. *Monatsheft für Mathematik und Physik* **42** (1935), 87 – 96.

[75] Fosdick, R. & Truskinovsky, L.: About Clapeyron's theorem in linear elasticity. *Journal of Elasticity* **72** (2003), 145–172.

[76] Fries, T.-P.: A corrected XFEM approximation without problems in blending elements. *International Journal For Numerical Methods in Engineering* **75** (2008), 503–532.

[77] Frijns, A. J. H.; Huyghe, J. M. & Janssen, J. D.: A validation of the quadriphasic mixture theory for intervertebral disc tissue. *International Journal of Engineering Science* **35** (1997), 1419–1429.

[78] Fritzen, P.: *Numerische Behandlung nichtlinearer Probleme der Elastizitäts- und Plastizitätstheorie*. Dissertation, TU Darmstadt 1997.

[79] Fung, Y. C.: *Biomechanics: Mechanical Properties of Living Tissues*. Springer-Verlag, New-York 1981.

[80] Gander, M. J. & Wanner, G.: From Euler, Ritz and Galerkin to Modern Computing (2010), URL http://www.unige.ch/~gander/Preprints/Ritz.pdf, to appear in SIREV 2011.

[81] Garden, R. S.: Low-angle fixation in fractures of the femoral neck. *The Journal of Bone and Joint Surgery* **43** (1961), 647–663.

[82] Gasser, T. C. & Auer, M.: Numerical prediction of the 3D fracture propagation in the proximal femur. In *ECCOMAS Thematic conference MHM2007 (Modeling*

of Heterogeneous Materials with Applications in Construction and Biomedical Engineering), Prague, 2007, URL http://www-old.hallf.kth.se/~tg/cv/papers/TCG_MA_prag2007.pdf.

[83] Gasser, T. C. & Holzapfel, G. A.: Geometrically non-linear and consistently linearized embedded strong discontinuity models for 3D problems with an application to the dissection analysis of soft biological tissues. *Computer Methods in Applied Mechanics and Engineering* **192** (2003), 5059–5098.

[84] Gehrlicher, S.: *Kontinuumsmechanische Modellierung und numerische Simulation von 3-d Rissausbreitung auf Basis des „Global Tracking Algorithm“ und der XFEM.* Diplomarbeit, Bericht Nr. 11-II-3 aus dem Institut für Mechanik (Bauwesen), Universität Stuttgart 2011.

[85] Graf, T.: *Multiphasic Flow Processes in Deformable Porous Media under Consideration of Fluid Phase Transitions.* Dissertation, Bericht Nr. II-17 aus dem Institut für Mechanik (Bauwesen), Universität Stuttgart 2008.

[86] Griffith, A. A.: The phenomena of rupture and flow in solids. *Philosophical Transactions of the Royal Society of London* **221** (1921), 163–198.

[87] Griffith, A. A.: The theory of rupture. In Biezeno, C. B. & Burgers, J. M. (eds.): *Proceedings of the First International Congress for Applied Mechanics.* Delft 1924, pp. 55–63.

[88] Gross, D. & Seelig, T.: *Bruchmechanik.* Springer-Verlag, Berlin 1996.

[89] Gürses, E.: *Aspects of Energy Minimization in Solid Mechanics: Evolution of Inelastic Microstructures and Crack Propagation.* Dissertation, Bericht Nr. I-19 aus dem Institut für Mechanik (Bauwesen), Universität Stuttgart 2007.

[90] Gürses, E. & Miehe, C.: A computational framework of three-dimensional configurational-force-driven brittle crack propagation. *Computer Methods in Applied Mechanics and Engineering* **198** (2009), 1413–1428.

[91] Gurtin, M. E.: *An Introduction to Continuum Mechanics.* Academic Press, Boston 1981.

[92] Hahn, H. G.: *Bruchmechanik.* B. G. Teugner Stuttgart 1976.

[93] Hansbo, A. & Hansbo, P.: An unfitted finite element method, based on Nitsche's method, for elliptic interface problems. *Computer Methods in Applied Mechanics and Engineering* **191** (2002), 5537–5552.

[94] Hansbo, A. & Hansbo, P.: A finite element method for the simulation of strong and weak discontinuities in solid mechanics. *Computer Methods in Applied Mechanics and Engineering* **193** (2004), 3523–3540.

[95] Hassanizadeh, S. M. & Gray, W. G.: General conservation equations for multi-phase systems: 1. Averaging procedure. *Advances in Water Resources* **2** (1979), 25–40.

[96] Hassanizadeh, S. M. & Gray, W. G.: High velocity flow in porous media. *Transport in Porous Media* **2** (1987), 521–531.

[97] Haupt, P.: On the concept of an intermediate configuration and its application to a representation of viscoelastic-plastic material behavior. *International Journal of Plasticity* **1** (1985), 303–316.

[98] Haupt, P.: Foundation of continuum mechanics. In Hutter, K. (ed.): *Continuum Mechanics in Environmental Sciences and Geophysics*. Springer-Verlag, Wien 1993, CISM Courses and Lectures No. 337, pp. 1–77.

[99] Haupt, P.: *Continuum Mechanics and Theory of Materials*. 2nd ed., Springer-Verlag, Berlin 2002.

[100] Hayes, W. C. & Bodine, A. J.: Flow-independent viscoelastic properties of articular cartilage matrix. *Journal of Biomechanics* **11** (1978), 407–419.

[101] Herres, O. M.; Suiker, A. S. J. & de Borst, R.: A comparison between the Perzyna viscoplastic model and the Consistency viscoplastic model. *European Journal of Mechanics A/Solids* **21** (2002), 1–12.

[102] Herrmann, N.: *Höhere Mathematik für Ingenieure, Physiker und Mathematiker*. Oldenburg Verlag, München 2007.

[103] Hettich, T. M.: *Diskontinuierliche Modellierung zur Versagensanalyse von Verbundmaterialien*. Dissertation, Bericht Nr. 50, Institut für Baustatik und Baudynamik, Universität Stuttgart 2007.

[104] Holzapfel, G.; Gasser, T. C. & Ogden, R. W.: A new constitutive framework for arterial wall mechanics and a comparative study of material models. *Journal of Elasticity* **61** (2000), 1–48.

[105] Holzapfel, G. A.; Schulze-Bauer, C. A. J.; Feigl, G. & Regitnig, P.: Mono-lamellar mechanics of the human lumbar anulus fibrosus. *Biomechanics and Modeling in Mechanobiology* **3** (2005), 125–140.

[106] Huang, M.; Yue, Z. Q.; Tham, L. G. & Zienkiewicz, O. C.: On the stable finite element procedures for dynamic problems of saturated porous media. *International Journal for Numerical Methods in Engineering* **62** (2004), 1421–1450.

[107] Huber, O.; Nickel, J. & Kuhn, G.: On the decomposition of the J-integral for 3D crack problems. *International Journal of Fracture* **64** (1993), 339–348.

[108] Inglis, C. E.: Stresses in a plate due to the presence of cracks and sharp corners. *Transactions of the Rocal Institution of Naval Architects* **55** (1913), 219–230.

[109] Irwin, G. R.: Fracture dynamics. In *Fracturing of metals: a seminar on the fracturing of metals held during the Twenty-ninth National Metal Congress and Exposistion*. American Society for Metals 1948, pp. 147–166.

[110] Irwin, G. R.: Analysis of stresses and strains near the end of a crack traversing. *Journal of Applied Mechanics* **24** (1957), 361–364.

[111] Irwin, G. R.: Fracture. In Flügge, S. (ed.): *Handbuch der Physik, Vol. VI.* Springer-Verlag Berlin 1958, pp. 551–590.

[112] Jäger, P.: *Theory and numerics of three-dimensional strong discontinuities at finite strains.* Dissertation, Lehrstuhl für Technische Mechanik, Technische Unverstität Kaiserslautern 2009.

[113] Jäger, P.; Steinmann, P. & Kuhl, E.: Modeling three-dimensional crack propagation – A comparison of crack path tracking strategies. *International Journal for Numerical Methods in Engineering* **76** (2008), 1328–1352.

[114] Jäger, P.; Steinmann, P. & Kuhl, E.: Towards the treatment of boundary conditions for global crack path tracking in three-dimensional brittle fracture. *Computational Mechanics* **45** (2009), 91–107.

[115] Kahn, A. S. & Huang, S.: *Continuum Theory of Plasticity.* John Wiley & Sons, New York 1995.

[116] Karajan, N.: *An Extended Biphasic Description of the Inhomogeneous and Anisotropic Intervertebral Disc.* Dissertation, Bericht Nr. II-19 aus dem Institut für Mechanik (Bauwesen), Universität Stuttgart 2009.

[117] Kienzler, R. & Herrmann, G.: *Mechanics in material space: with applications to defect and fracture mechanics.* Springer-Verlag, Berlin 2000.

[118] Kies, J. A. & Smith, H. L.: Toughness testing of hot-stretched acrylics. In *Aircraft Industries Association and Air Development Command, Dayton (OH)*, 1955.

[119] Koch, D.: *Vektorwertige Levelset-Funktionenen zur Beschreibung von Diskontinuitäten.* Entwurfsarbeit, Institut für Mechanik (Bauwesen), Universität Stuttgart 2008.

[120] Koch, D.: *Kontinuumsmechanische Modellierung und numerische Simulation von Rissen.* Diplomarbeit, Bericht Nr. 09-II-1 aus dem Institut für Mechanik (Bauwesen), Universität Stuttgart 2009.

[121] Krabbenhoft, K.; Lyamin, A. V.; Sloan, S. W. & Wriggers, P.: An interior-point algorithm for elastoplasticity. *International Journal for Numerical Methods in Engineering* **69** (2007), 592–626.

[122] Krause, R.; Markert, B. & Ehlers, W.: A porous media model for the description of adaptive bone remodelling. *PAMM* **10** (2010), 79–80.

[123] Kreyszig, E.: *Advanced Engineering Mathematics.* 9th edn., John Wiley & Sons Inc. 2006.

[124] Kulkarni, D. V.; Tortorelli, D. A. & Wallin, M.: A Newton-Schur alternative to the consistent tangent approach in computational plasticity. *Computer Methods in Applied Mechanics and Engineering* **196** (2007), 1169–1177.

[125] Lai, W. M.; Hou, J. S. & Mow, V. C.: A triphasic theory for the swelling and deformation behaviours of articular cartilage. *ASME Journal of Biomechanical Engineering* **113** (1991), 245–258.

[126] Lemaitre, J. & Chaboche, J.-L.: *Mechanics of Solid Materials*. Cambridge University Press, Cambridge 1994.

[127] Liebe, T. & Steinmann, P.: Theory and numerics of a thermodynamically consistent framework for geometrically linear gradient plasticity. *International Journal for Numerical Methods In Engineering* **51** (2001), 1437–1467.

[128] Linder, C.; Rosato, D. & Miehe, C.: New finite elements with embedded strong discontinuities for the modeling of failure in electromechanical coupled solids. *Computer Methods in Applied Mechanics and Engineering* **200** (2010), 141–161.

[129] Lorensen, W. E. & Cline, H. E.: Marching cubes: A high resolution 3D surface construction algorithm. *Proceedings of the 14th annual conference on Computer graphics and interactive techniques* (1987), pp. 163–169, SIGGRAPH '87.

[130] Lourenco, P. B.; de Borst, R. & Rots, J. G.: A plane stress softening plasticity model for orthotropic materials. *International Journal for Numerical Methods in Engineering* **40** (1997), 4033–4057.

[131] Macaulay, W. H.: Note on the deflection of the beams. *Messenger of Mathematics* **48** (1919), 129–130.

[132] Mahnkopf, D.: *Lokalisierung fluidgesättigter poröser Festkörper bei finiten elastoplastischen Deformationen*. Dissertation, Bericht Nr. II-5 aus dem Institut für Mechanik (Bauwesen), Universität Stuttgart 2000.

[133] Malvern, L. E.: *Introduction to the Mechanics of a Continuous Medium*. Prentice-Hall, Englewood Cliffs (NJ) 1969.

[134] Markert, B.: *Porous Media Viscoelasticity with Application to Polymeric Foams*. Dissertation, Bericht Nr. II-12 aus dem Institut für Mechanik (Bauwesen), Universität Stuttgart 2005.

[135] Maugin, G. A.: *The Thermomechanics of Plasticity and Fracture*. Cambridge University Press, Cambridge 1992.

[136] Miehe, C. & Gürses, E.: A robust algorithm for configurational-force-driven brittle crack propagation with r-adaptive mesh alignment. *A robust algorithm for configurational-force-driven brittle crack propagation with R-adaptive mesh alignment* **72** (2007), 127–155.

[137] Miehe, C.; Schröder, J. & Schotte, J.: Computational homogenization analysis in finite plasticity simulation of texture development in polycrystalline materials. *Computer Methods in Applied Mechanics and Engineering* **171** (1999), 387–418.

[138] Moës, N. & Belytschko, T.: Extended finite element method for cohesive crack growth. *Engineering Fracture Mechanics* **69** (2002), 813–833.

[139] Moës, N.; Dolbow, J. & Belytschko, T.: A finite element method for crack growth without remeshing. *International Journal for Numerical Methods in Engineering* **46** (1999), 131–150.

[140] Mow, V. C.; Gibbs, M. C.; Lai, W. M.; Zhu, W. B. & Athanasiou, K. A.: Biphasic indentation of articular cartilage - II. A numerical algorithm and an experimental study. *Journal of Biomechanics* **22** (1989), 853–861.

[141] Mow, V. C.; Kuei, S. C.; Lai, W. M. & Armstrong, C. G.: Biphasic creep and stress relaxation of articular cartilage in compression: Theory and experiments. *ASME Journal of Biomechanical Engineering* **102** (1980), 73–84.

[142] Müller, R.; Kolling, S. & Gross, D.: On configurational forces in the context of the finite element method. *International Journal for Numerical Methods in Engineering* **53** (2002), 1557–1572.

[143] Naghdi, P. M.: A critical review of the state of finite plasticity. *Zeitschrift für Angewandte Mathematik und Physik (ZAMP)* **41** (1990), 315–394.

[144] Neff, P.: *The Cosserat or micropolar model*. 2010, URL http://www.uni-due.de/mathematik/ag_neff/cosserat.

[145] Noll, W.: A mathematical theory of the mechanical behavior of continous media. *Archives for Rational Mechanics and Analysis* **2** (1958), 197–226.

[146] O'Brien, J. F. & Hodgins, J. K.: Graphical modeling and animation of brittle fracture. *Proceedings of the 26th annual conference on Computer graphics and interactive techniques* (1999), pp. 137–146, SIGGRAPH '99.

[147] O'Connor, J. J. & Robertson, E. F.: *Gabriel Lamé*. MacTutor History of Mathematics archive, University of St. Andrews 2000, URL http://www-history.mcs.st-andrews.ac.uk/Biographies/Lame.html.

[148] Ogden, R. W.: Large deformation isotropic elasticity – On the correlation of theory and experiment for compressible rubberlike solids. *Proceedings of the Royal Society of London* **328** (1972), 323–338.

[149] Ogden, R. W.: *Nonlinear Elastic Deformations*. Ellis Harwood, Chichester 1984.

[150] Oliver, J.; Huespe, A. E.; Samaniego, E. & Chaves, E. W. V.: On strategies for tracking stong discontinuities in computational failure mechanics. In *Proceedings of the Fifth World Congress on Computational Mechanics (WCCM V)*. 2002, ISBN 3-9501554-0-6.

[151] Oliver, J.; Huespe, A. E.; Samaniego, E. & Chaves, E. W. V.: Continuum approach to the numerical simulation of material failure in concrete. *International Journal for Numerical and Analytical Methods in Geomechanics* **28** (2004), 609–632.

[152] Orowan, E.: Energy criteria of fracture. *Welding Journal Research Supplement* **34** (1955), 157–160.

[153] Osher, S. & Fedkiw, R.: *Level Set Methods and Dynamic Implicit Surfaces*. Springer-Verlag New York 2003.

[154] Pauwels, F.: *Der Schenkelhalsbruch: ein mechanisches Problem*. Ferdinand Enke, Stuttgart 1935.

[155] Perzyna, P.: Fundamental problems in viscoplasticity. *Advances in Applied Mechanics* **9** (1966), 243–377.

[156] Remmers, J. J. C.: *Discontinuities in materials and structures: a unifying computational approach*. Ph. D. thesis, Delft University of Technology 2006.

[157] Rempler, H.-U.: *Visualisierung von Ergebnissen aus numerischen Berechnungen*. Diplomarbeit, Bericht Nr. 04-II-13 aus dem Institut für Mechanik (Bauwesen), Universität Stuttgart 2004.

[158] Rempler, H.-U.; Wieners, C. & Ehlers, W.: Efficiency comparison of an augmented finite element formulation with standard return mapping algorithms for elastic-inelastic materials. *Computational Mechanics* **48** (2011), 551–562.

[159] Rice, J. R.: A Path Independent Inegral and the Approximate Analysis of Strain Concentration by Notches and Cracks. *Journal of Applied Mechanics* **35** (1968), 379–386.

[160] Riddle, L. H.: *Biographies of Women Mathematicians*. 2010, URL http://www.agnesscott.edu/lriddle/women/ladyzhen.htm.

[161] Rooke, D. P.: *Compendium of stress intensity factors*. H.M.S.O. 1976.

[162] Sailer, H.: *Messung viskoelastischer Gewebeeigenschaften in vivo*. Master's thesis, Fachhochschule Furtwangen (2001).

[163] Samaniego, E. A.: *Contributions to the continuum modelling of strong discontinuities in two-dimensional solids*. Ph. D. thesis, Departament de Resistència de Materials i Estructures a l'Enginyeria, Universitat Politècnica de Catalunya 2003.

[164] Schlote, K.-H. (ed.): *Chronologie der Naturwissenschaften: Der Weg der Mathematik und der Naturwissenschaften von den Anfängen in das 21. Jahrhundert*. Verlag Harri Deutsch 2002.

[165] Scholz, B.: *Application of a micropolar model to the localization phenomena in granular materials*. Dissertation, Bericht Nr. II-15 aus dem Institut für Mechanik (Bauwesen), Universität Stuttgart 2007.

[166] Schröder, J.: *Theoretische und algorithmische Konzepte zur phänomenologischen Beschreibung anisotropen Materialverhaltens.* Dissertation, Bericht Nr. I-1 aus dem Institut für Mechanik (Bauwesen), Universität Stuttgart 1996.

[167] Schröder, J. & Neff, P.: Invariant formulation of hyperelastic transverse isotropy based on polyconvex free energy functions. *International Journal of Solids and Structures* **40** (2003), 401–445.

[168] Schröder, J.; Neff, P. & Balzani, D.: A variational approach for materially stable anisotropic hyperelasticity **42** (2005), 4352–4371.

[169] Schwarz, H. R.: *Methode der finiten Elemente.* Teubner, Stuttgart 1991.

[170] Simo, J. & Hughes, T. J. R.: *Computational Inelasticity.* Springer-Verlag, Berlin 1998.

[171] Simo, J. C.; Kennedy, J. G. & Govindjee, S.: Non-smooth multisurface plasticity and viscoplasticity. Loading/unloading conditions and numerical algorithms. *International Journal for Numerical Methods in Engineering* **26** (1988), 2161–2185.

[172] Simo, J. C.; Oliver, J. & Armero, F.: An analysis of strong discontinuities induced by strain-softening in rate-independent inelastic solids. *Computational Mechanics* **12** (1993), 277–296.

[173] Simo, J. C. & Rifai, M. S.: A class of mixed assumed strain methods and the method of incompatible modes. *International Journal for Numerical Methods in Engineering* **29** (1990), 1595–1638.

[174] Simo, J. C. & Taylor, R. L.: Consistent tangent operators for rate-independent elastoplasticity. *Computer Methods in Applied Mechanics and Engineering* **48** (1985), 101–118.

[175] Skempton, A. W.: Significance of Terzaghi's concept of effective stress (Terzaghi's discovery of effective stress). In Bjerrum, L.; Casagrande, A.; Peck, R. B. & Skempton, A. W. (eds.): *From Theory to Practice in Soil Mechanics.* Wiley, New York 1960, pp. 42–53.

[176] Steinmann, P. & Betsch, P.: A localization capturing FE-interface based on regularized strong discontinuities at large inelastic strains. *International Journal of Solids and Structures* **37** (2000), 4061–4082.

[177] Stolarska, M.; Chopp, D. L.; Moës, N. & Belytschko, T.: Modelling crack growth by level sets in the extended finite element method. *International Journal for Numerical Methods in Engineering* **51** (2001), 943–960.

[178] Strouboulis, T.; Babuska, I. & Copps, K.: The design and analysis of the generalized finite element method. *Computer Methods in Applied Mechanics and Engineering* **181** (2000), 43–69.

[179] Sukumar, N.; Moës, N.; Moran, B. & Belytschko, T.: Extended finite element method for three-dimensional crack modelling. *International Journal for Numerical Methods in Engineering* **48** (2000), 1549–1570.

[180] Taylor, C. & Hood, P.: A numerical solution of the Navier-Stokes equations using the finite element technique. *Computers and Fluids* **1** (1973), 73–100.

[181] Terzaghi, K.: *Erdbaumechanik auf bodenphysikalischer Grundlage.* Franz Deuticke, Leipzig and Wien 1925.

[182] Truesdell, C.: *A new definition of a fluid, II. The Maxwellian fluid.* Report P-3553, **S** 19, US Naval Research Laboratory 1949.

[183] Truesdell, C.: *Rational Thermodynamics.* 2nd ed., Springer-Verlag, New York 1984.

[184] Truesdell, C. & Noll, W.: The nonlinear field theories of mechanics. In Flügge, S. (ed.): *Handbuch der Physik.* Band III/3, Springer-Verlag, Berlin 1965.

[185] Truesdell, C. & Toupin, R. A.: The classical field theories. In Flügge, S. (ed.): *Handbuch der Physik.* Band III/1, Springer-Verlag, Berlin 1960.

[186] Ventura, G.; Budyn, E. & Belytschko, T.: Vector level sets for description of propagating cracks in finite elements. *International Journal for Numerical Methods in Engineering* **58** (2003), 1571–1592.

[187] Ventura, G.; Xu, J. X. & Belytschko, T.: A vector level set method and new discontinuity approximations for crack growth by EFG. *International Journal for Numerical Methods in Engineering* **54** (2002), 923–944.

[188] Wells, A. A.: Application of fracture mechanics at and beyond general yielding. *British Welding Journal* **10** (1963), 563–570.

[189] Wells, G. N.: *Discontinuous modelling of strain localisation and failure.* Ph. D. thesis, Delft University of Technology 2001.

[190] Wells, G. N.; de Borst, R. & Sluys, L. J.: A consistent geometrically non-linear approach for delamination. *International Journal for Numerical Methods in Engineering* **54** (2002), 1333–1355.

[191] Westergaard, H. M.: Bearing pressures and cracks. *Journal of Applied Mechanics* **6** (1939), 49–53.

[192] Wieners, C.: Nonlinear solution methods for infinitesimal perfect plasticity. *Zeitschrift für Angewandte Mathematik und Mechanik (ZAMM)* **87** (2007), 636–660.

[193] Wieners, C.; Ammann, M.; Diebels, S. & Ehlers, W.: Parallel 3-d simulations for porous media models in soil mechanics. *Computational Mechanics* **29** (2002), 75–87.

[194] Wu, X.-R. & Carlsson, A. J.: *Weight Functions and Stress Intensity Factor Solutions*. Pergamon Press, Oxford 1991.

[195] Yarema, S. Y.: On the contribution of G. R. Irwin to fracture mechanics. *Materials Science* **31** (1996), 617–623.

[196] Yau, J. F.; Wang, S. S. & Corten, H. T.: A mixed-mode crack analysis of isotropic solids using conservation laws of elasticity. *Journal of Applied Mechanics* **47** (1980), 335–341.

[197] Zi, G. & Belytschko, T.: New crack-tip elements for XFEM and applications to cohesive cracks. *International Journal for Numerical Methods in Engineering* **57** (2003), 2221–2240.

[198] Zienkiewicz, O. C. & Taylor, R. L.: *The Finite Element Method for Solid and Structural Mechanics*. 6th ed., Elsevier 2005.

Curriculum Vitae

Personal Data

Name:	Hans-Uwe Rempler
Date of birth:	June 23, 1976
Place of birth:	Mediasch, Romania
Nationality:	German
Marital status:	married

Résumé

since 10/2011	**Robert Bosch GmbH** Simulation engineer
02/2003 – 09/2011	**Universität Stuttgart, Institute of Applied Mechanics** Doctoral student, research associate, assistant lecturer
02/2010 – 05/2010	Stay abroad at Stanford University, USA
from 04/2009	Doctoral student in graduate school "Simulation Technology"
from 01/2005	Research associate, assistant lecturer
until 12/2004	Student research assistant
07/2001 – 08/2006	**Creamos GbR mbH** Internet services and consulting as self-employment
10/1998 – 01/2003	**MetaComp GmbH** IT specialised tradesman for logistics as employee and IT-technician, -sales and -purchasing as freelancer
01/1997 – 12/1998	**Steim Architekten** Internship and engineering draughtsman as freelancer
08/1996 – 12/1996	**Bauunternehmung Alber** Internship

Education

10/1997 – 10/2004	**Universität Stuttgart, Civil Engineering** Stuttgart, major subject: "Allgemeines Bauingenieurwesen", degree: "Diplom-Ingenieur (Dipl.-Ing.)"
10/1995 – 07/1996	**Military Service** Ulm, Stabskompanie Führungsunterstützungsbrigade 2
09/1982 – 06/1995	**Elementary & Secondary Academic School** Stuttgart, degree: "Abitur"

Released Report Series

II-1 Gernot Eipper: *Theorie und Numerik finiter elastischer Deformationen in fluidgesättigten porösen Festkörpern*, 1998.

II-2 Wolfram Volk: *Untersuchung des Lokalisierungsverhaltens mikropolarer poröser Medien mit Hilfe der Cosserat-Theorie*, 1999.

II-3 Peter Ellsiepen: *Zeit- und ortsadaptive Verfahren angewandt auf Mehrphasenprobleme poröser Medien*, 1999.

II-4 Stefan Diebels: *Mikropolare Zweiphasenmodelle: Formulierung auf der Basis der Theorie Poröser Medien*, 2000.

II-5 Dirk Mahnkopf: *Lokalisierung fluidgesättigter poröser Festkörper bei finiten elastoplastischen Deformationen*, 2000.

II-6 Heiner Müllerschön: *Spannungs-Verformungsverhalten granularer Materialien am Beispiel von Berliner Sand*, 2000.

II-7 Stefan Diebels (Ed.): *Zur Beschreibung komplexen Materialverhaltens: Beiträge anläßlich des 50. Geburtstages von Herrn Prof. Dr.-Ing. Wolfgang Ehlers*, 2001.

II-8 Jack Widjajakusuma: *Quantitative Prediction of Effective Material Parameters of Heterogeneous Materials*, 2002.

II-9 Alexander Droste: *Beschreibung und Anwendung eines elastisch-plastischen Materialmodells mit Schädigung für hochporöse Metallschäume*, 2002.

II-10 Peter Blome: *Ein Mehrphasen-Stoffmodell für Böden mit Übergang auf Interface-Gesetze*, 2003.

II-11 Martin Ammann: *Parallel Finite Element Simulations of Localization Phenomena in Porous Media*, 2005.

II-12 Bernd Markert: *Porous Media Viscoelasticity with Application to Polymeric Foams*, 2005.

II-13 Saeed Reza Ghadiani: *A Multiphasic Continuum Mechanical Model for Design Investigations of an Effusion-Cooled Rocket Thrust Chamber*, 2005.

II-14 Wolfgang Ehlers & Bernd Markert (Eds.): *Proceedings of the 1st GAMM Seminar on Continuum Biomechanics*, 2005.

II-15 Bernd Scholz: *Application of a Micropolar Model to the Localization Phenomena in Granular Materials: General Model, Sensitivity Analysis and Parameter Optimization*, 2007.

II-16 Wolfgang Ehlers & Nils Karajan (Eds.): *Proceedings of the 2nd GAMM Seminar on Continuum Biomechanics*, 2007.

II-17 Tobias Graf: *Multiphasic Flow Processes in Deformable Porous Media under Consideration of Fluid Phase Transitions*, 2008.

II-18 Ayhan Acartürk: *Simulation of Charged Hydrated Porous Materials*, 2009.

II-19 Nils Karajan: *An Extended Biphasic Description of the Inhomogeneous and Anisotropic Intervertebral Disc*, 2009.

II-20 Bernd Markert: *Weak or Strong – On Coupled Problems In Continuum Mechanics*, 2010.

II-21 Wolfgang Ehlers & Bernd Markert (Eds.): *Proceedings of the 3rd GAMM Seminar on Continuum Biomechanics*, 2012.

II-22 Wolfgang Ehlers: *Poröse Medien – ein kontinuumsmechanisches Modell auf der Basis der Mischungstheorie*, 2012. Nachdruck der Habilitationsschrift aus dem Jahr 1989 (Forschungsberichte aus dem Fachbereich Bauwesen der Universität-GH-Essen 47, Essen 1989).

II-23 Hans-Uwe Rempler: *Damage in Multi-Phasic Materials Computed with the Extended Finite-Element Method*, 2012.

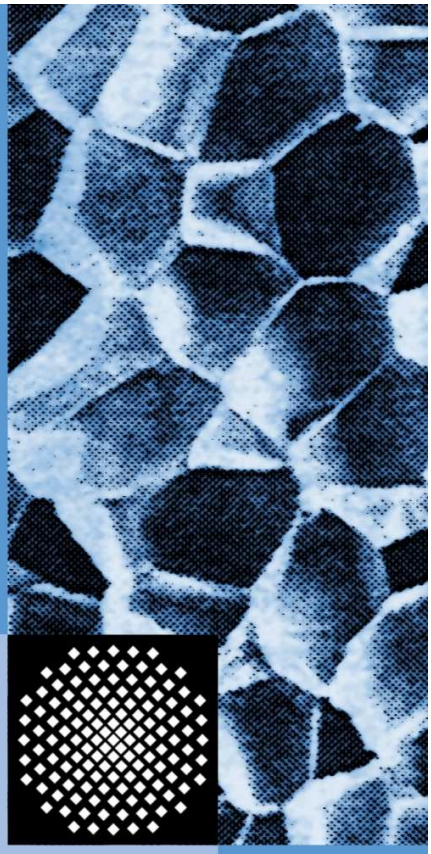

ISBN 3–937399–24–0
(D 93 – Dissertation, Universität Stuttgart)